Fotonische bouwblokken en subsystemen voor microgolffotonica
in heterogene siliciumtechnologie

Heterogeneous Silicon Photonic Devices and Subsystems for Microwave Photonics

Kasper Van Gasse

UNIVERSITEIT
GENT

Dankwoord

Doctoreren in de fotonica, hoe begin je daar eigenlijk aan? Voor mij is het allemaal begonnen toen ik een master thesis wou kiezen in de master Engineering Physics. Een van de onderwerpen was het ontwikkelen van een mid-infrarooddetector gebaseerd op collodale quantum dots, wat naast een sensationele titel mij ook een erg interessant onderwerp leek. Daarenboven werd de thesis begeleid door twee gedreven professoren: Zeger Hens en Gunther Roelkens, de keuze was snel gemaakt.

Een onderzoeker in de groep van Zeger Hens raadde mij toen ook aan om het vak microfotonica te volgen, omdat dat wel interessant zou zijn voor mijn thesis. Na het volgen van microfotonica en het afwerken van mijn thesis, onder begeleiding van de immers energieke Chen Hu, wist ik dat fotonica mijn ding was. Na een gesprek met Roel en Gunther was ik klaar voor een duik in het fotonisch onderzoek.

De eerste dag in het technicum werd ik ontvangen door Gunther die me begeleide naar een bureau op het einde van de gang. Daar kwam ik terecht naast (ondertussen professor) Bart Kuyken, die naast kampioen in het verzamelen van titels en beurzen ook een uitstekende coach was voor mij en andere (toen nog) jonge doctoraatsstudenten Koen en Utsav. Koen, die op dezelfde dag begon, kreeg het bureau naast mij toegewezen en is meer dan vier jaar mijn buur en collega geweest tot zijn vertrek naar het zonnige California. Naast een goede collega was Koen ook altijd klaar om een sportief avontuur te ondernemen, van roeien tot skateboarden. Ook met niet-lineaire expert Utsav heb ik vele jaren met veel plezier het bureau gedeeld, tot hij vertrokken is naar het (minder zonnige) New York. Een ander kantoor genoot die mij vele jaren heeft vergezeld is Pieter Wuytens, die toen nog een dynamisch Raman verstrooier was maar ondertussen vertrokken is naar het (zonnige?) imec. Alsook Herbert De Heer, die met zijn subtiele humor de sfeer wist te verblijden. Tenslotte, de senior van ons kantoor Stephan Clemmen, die in tegenstelling tot Koen en Utsave van Amerika naar Gent is gekomen. Beste Koen, Bart, Pieter, Utsav, Stephane en Herbert ik zou jullie dan ook erg willen bedanken voor het heel prettig samenwerken tijdens

de voorbije jaren! Naast een goede sfeer op het kantoor waren er ook veel mooie momenten na de werkuren. Hoogtepunten zoals de roei-initiatie met Koen en Sren zal ik waarschijnlijk nooit vergeten, ook omdat een deel van de initiatie gefilmd werd door een enthousiaste omstaander. Ook de Age of Empires II avonden met pizza zullen me altijd bijblijven als erg plezierige momenten.

De groep is natuurlijk groter dan het kantoor op het einde van de gang in het technicum. Bijvoorbeeld Anton, Frederik en Sarvagya waren altijd klaar om elkaar een poets te bakken en moppen te tappen na de uren met Alfonso. And ofcourse a special thanks to Frederik, Floris, Alejandro, Saurav, Sulakshna, Sren and many others for the fun evenings in the plansjee and the Latin quarter. Of de vaste klanten van de Verloren Kost zoals Eva, Thijs en Raphael. Ook de journal club georganiseerd door Dr. Van Laer (natuurlijk weer vergezeld van pizza) waren erg leuke momenten die sterk bijdroegen tot de sfeer. Onbegrijpelijk dat dit initiatief slechts een kort leven was beschoren. Zeker na de fantastische presentatie van Amin over de mogelijke vervalsing van de maanlanding.

In het technicum maakte ik ook kennis met de mensen van IDlab design (toen nog INTEC Design). Gezien ik vaak experimenten wou opzetten waar ik al eens drie RF-generatoren voor nodig had, kwam ik geregeld wat materiaal lenen. Het voordeel van materiaal in een ander labo te lenen is dat je ook veel leuke mensen leert kennen. Veel van die mensen kom ik nog steeds tegen als ik materiaal ga lenen (ondertussen op het twaalfde verdiep) zoals Jochem (werk jij ondertussen niet ergens anders?), Joris Van Kerrebrouck, Laurens Breyne, Laurens Bogaerts, Guy Torfs, Scott, Bart moeneclaey, Hoalin Li, Hannes, Joris Lambrecht. Bedankt voor alle hulp!

Een groot deel van mijn doctoraat heb ik gewerkt aan een project van het European Space Agency. Dit project werd begeleid door Gunther en Dr. Zhechao Wang, die ondertussen ook naar Amerika is vertrokken. We werkten ook samen met Antwerp Space waar ik kennis maakte met een echte veteraan van de RF-wereld: Jules Marin. Ook mijn thesis student Bert De Deckere besloot het space team te versterken. Zelfs Hakimeh, een visiting scientist van Aarhus University, besloot om de in de wereld van de space photonics te duiken.

Met Zhechao heb ik vele avonturen beleeft zoals meetings in ESTEC, een prachtige conferentie in Cyprus en slapen in een hotel op de markt in Eindhoven terwijl PSV kampioen speelt. Samen met Zhechao heb ik vele maskers gemaakt en vele lasers en modulators uitgemeten. Thanks Zhechao for the great collaboration and teaching me about research and device fabrication!

Gepulste lasers zijn echter erg gecompliceerde dingen en Gunther stelde voor om de metingen te ondernemen in Eindhoven. De laser groep in Eindhoven onder leiding van Erwin Bente had immers erg veel ervaring met het uitmeten van gepulste lasers. In het labo van Eindhoven heb ik dan enorm veel geleerd over de theorie en het uitmeten van gepulste lasers. Dit vooral

dankzij Erwin Bente, Dr. Sylwester Latkowksi en Dr. Valentina Moskalenko. Many thanks to all of you! Het is ook hier dat ik niet alleen mijn passie voor lasers heb ontdekt maar ook mijn vriendin hebt ontmoet, de multi-getalenteerde Valentina Moskalenko!

In Eindhoven hebben we een erg goed werkende laser kunnen karakteriseren. Deze resultaten hebben geleid tot een mooie publicatie en een trip naar een conferentie in Kobe, Japan (ISLC 2016). Deze conferentie was een van de leukste van mijn doctoraat. Mede dankzij het gezelschap van Geert Morthier, Amin abasi, Erwin Bente en Stefanos Andreou. In KObe hebben we ook vele leuke avonden beleefd met doctoraats studenten van over de hele wereld. Het kennismaken met mensen van over heel de wereld is ongetwijfeld een van de leukste kanten van conferenties. Na de conferentie heb ik samen met Amin in Japan rondgetrokken en hebben we samen Kyoto en Nara (de oude hoofdstad van Japan bezocht). Thank you Amin for the many years of working together and the great memories! Ondertussen zijn we al enkele jaren naar de iGent toren verhuisd, waar mijn bureau nu meer en meer bevolkt wordt door de volgende generatie: Camiel, Isaac, Stijn, Zuyang, Nina, Lukas en Maximillien. Thank you all for being such great office colleagues! Ook zijn er vele nieuwe mensen bij gekomen zoals Ewoud en Emmauel. Zij hebben broodjes halen bij Allys om twaalf uur tot een ware traditie verheven. Tot ongenoegen van Dr. Dhoore die al enkele maanden (zonder succes) een brunch tracht te implementeren.

Ik zou ook graag Sarah willen bedanken voor de vele interessante III-V-gesprekken en de hulp bij het uitmeten van de mode-locked lasers toen ik pas begon.

Andreas zou ik ook willen bedanken voor de vele goede raad, maar natuurlijk ook voor de uitstekende begeleiding van zijn werknemers bij Brolis.

I would also like to thank Jing Zhang, one of the most passionate III-V-on-silicon researchers I met. Your dedication has shaped many masks, lasers and technology used by almost all of Gunthers students.

And of course also Grigorij, for his passionate transfer printing and polarization (in)sensitive adventures.

And a special thank you for Haolan for the great fashion advice!

Given that we currently have 53 PhD students and 16 post-docs it is rather challenging to thank everyone individually. So therefore, I would like to thank all students and post-docs for creating such a good atmosphere in the group, coffee room and work environment!

Naast de studenten zou ik ook graag de vaste medewerkers willen bedanken voor hun harde werk, engelengeduld en ondersteuning. Bedankt Jasper, Michael, Ilse Meersman, Mike, Kristien en Ilse Van Royen! En ook een extra dankjewel aan Antonio, die al jaren hoogstaand onderzoek weet te combineren met het helpen managen van de IT-infrastructuur. Natuurlijk ook de mensen van de clean room die het mogelijk maken om elke dag chips te maken, bedankt Steven en Liesbeth!

Dit brengt mij bij het academisch c-level: de professoren.

Eerst en vooral zou ik Roel willen bedanken, het kloppende hart van de Photonics Research Group. Ik denk niet dat ik ooit iemand heb ontmoet die even oprecht en gedreven is. Het is ongelooflijk hoe je onderzoek op het hoogste niveau weet te combineren met het creëren van een aangename sfeer waar mensen zich kunnen ontwikkelen. Bedankt om mij de kans te geven om onderzoek te mogen doen in je groep!

Maar de PRG is vooral ook een team en dat voel je ook aan alle professoren die altijd bereid zijn om studenten bij te staan. Zoals Wim Bogaerts die altijd klaar staat om iedereen zijn ipkiss problemen op te lossen en structuur aan te brengen in de soms chaotische academische wereld. Geert Morthier die alijd klaar staat om mensen met laser vraagstukken te helpen. Nicolas Le Thomas die me vele malen heeft laten zien hoe je free space optics gebruikt in het labo. Dries Van Thourhout die de clean room in de running houdt desondanks vele machines die het al eens opgeven zonder goede reden. En Peter Bienstman die onevenaarbaar elke groep meeting op schema weet te houden.

Er resten mij nog drie professoren die ik in het bijzonder zou willen bedanken:

Bart Kuyken, die me sinds mijn eerste dag altijd heeft bijgestaan met goede raad en als geen andere de nuances van het onderzoek verstaat. Maar die me ook geïnspireerd heeft met zijn passie voor optische frequentie kammen. (Er bestaat zelfs ergens een foto van Bart met Nobelprijswinnaar Theodor Hänsch!)

Mijn promotor Johan Bauwelinck die altijd paraat stond om mij te helpen met mijn hoge-snelheids elektronische vragen en het begeleiden van de vlotte samenwerking tussen de design en fotonica groep.

Maar vooral mijn promotor Gunther die me de kans heeft gegeven te experimenteren met alle mogelijke technologien en devices. Jaren hebben we geëxperimenteerd met alle mogelijke lasers, modulators en systemen. Wat ooit begonnen is met ring resonatoren waar we chemisch gedopeerde quantum dots gingen op deponeren is geindigd met gepulste lasers, electro-fotonische mixers, resonante modulatoren en versterkers. Het zijn niet enkel ingewikkelde termen, het was ook een groot avontuur. Desondanks alle stress, deadlines en ups en downs is Gunther vooral altijd een erg menselijk mens geweest met een groot hart en vooral een passie voor onderzoek. Ik denk dat ik nergens zoveel had kunnen leren als de voorbije jaren bij Gunther.

Dit brengt mij bij de meer persoonlijke rubriek:

Ik wil mijn vriendin Valentina bedanken om me veel te leren over gepulste lasers en het woelige leven in het onderzoek. Maar vooral om altijd naar mij te luisteren en mij te ondersteunen. Maar natuurlijk ook om mij te introduceren tot de wereld van het (ijs)rotsklimmen. Ik had nooit verwacht om zoveel avontuurlijk trips te maken, maar ben erg blij dat je mij mee op avontuur hebt genomen. Dankzij jou werd ook Eindhoven een beetje mijn tweede thuis. Waar ik veel leuke nieuwe mensen heb leren kennen. Ten-

slotte, hoop ik dat je er snel aan zult wennen dat je niet langer de enige Dr. zult zijn :).

Tenslotte, mijn ouders Anne en Dirk, die me door de vele jaren altijd zijn blijven steunen. Ik ben erg zeker dat het zonder jullie niet gelukt was. Ik ben jullie enorm dankbaar voor alles! Dit doctoraat is natuurlijk niet enkel het resultaat van de voorbije vier jaar, maar van een heel leven bijleren en werken. Zonder de mogelijkheden die jullie me gegeven hebben had ik nooit mijn talenten kunnen ontwikkelen om dit doctoraat te behalen. Naast mijn oneindige dankbaarheid zal ik jullie de komende jaren kunnen verblijden met vele weetjes over lasers en telecommunicatie.

En natuurlijk een fascinerend boek dat begint op de volgende pagina!

Gent, Mei 2019
Kasper Van Gasse

Table of Contents

List of Figures

List of Tables

List of Acronyms

ASE	Amplified spontaneous emission
a.u.	Arbitrary units
AWG	Arbitrary waveform generator
BER	Bit-error rate
CMOS	Complementary metal-oxide-semiconductor
CMP	Chemical mechanical polishing
CVD	Chemical vapor deposition
dc	Direct current
DBR	Distributed Bragg reflector
DFB	Distributed feedback (laser)
EAM	Electro-absorption modulator
EDFA	Erbium-doped fiber amplifier
ESA	Electrical spectrum analyzer
EVM	Error vector magnitude
FBG	Fiber Bragg grating
FDTD	Finite-Difference Time-Domain method
FFT	Fast Fourier transform
FIB	Focused ion beam
FPC	Fiber polarization controller
FSR	Free-spectral range
GC	Grating coupler
HD-FEC	Hard-decision forward error coding
IMWP	Integrated microwave photonics
IR	Infrared
LO	Local oscillator
MLL	Mode-locked laser
MMI	Multi-mode interferometer
MOCVD	Metal-organic chemical vapor deposition
MOS	Metal-oxide-semiconductor
MWP	Microwave photonics
MZI	Mach-Zehnder interferometer
MZM	Mach-Zehnder modulator
NRZ	Non-return-to-zero
OSA	Optical spectrum analyzer

OTF	Optical tunable filter
PD	Photodiode
PECVD	Plasma-enhanced chemical vapor deposition
PIC	Photonics integrated circuit
Q factor	Quality factor
QAM	Quadrature amplitude modulation
RF	Radio frequency
RIE	Reactive ion etching
rms	Root-mean-square
rpm	Revolutions per minute
SA	Saturable absorber
SEM	Scanning electron microscopy
SMF	Single mode fiber
SMSR	Side-mode suppression ratio
SOA	Semiconductor optical amplifier
SOI	Silicon-on-insulator
TE	Transverse electric
TPA	Two-photon absorption
UV	Ultraviolet
VECSEL	Vertical external-cavity surface-emitting laser
VNA	Vector network analyzer
VOA	Variable optical attenuator
WDM	Wavelength-division multiplexing

Samenvatting

De impact van telecommunicatie op de maatschappij is niet te onderschatten. In 1997 verstuurden we -wereldwijd- 100 gigabyte per minuut naar elkaar terwijl dit in 2017 al 45000 gigabyte per seconde was. Mensen zijn tegenwoordig altijd en overal met elkaar verbonden via het internet en mobiele telefonie. Het zijn echter niet enkel mensen die met elkaar verbonden zijn. In de toekomst zullen ook toestellen steeds meer met elkaar verbonden zijn. Denk maar aan het snel ontwikkelende internet der dingen. Om al deze mensen en toestellen met elkaar te verbinden ligt de nadruk steeds vaker op mobiele netwerken. Het mobiele netwerk van de toekomst (5G) is in volle ontwikkeling, maar het implementeren van dit netwerk bevat vele uitdagingen. Een van de grootste uitdagingen is het neerzetten van een Radio Access Network dat in staat is om het steeds toenemende aantal gebruikers te voorzien van een hoog datadebiet. Het is erg belangrijk in deze netwerken dat glasvezelverbindingen efficiënt kunnen interfacen met hoge-snelheid elektronica en draadloze zender-ontvangers. In het verleden werd de ontwikkeling van optische en elektronische technologie vaak gescheiden. Om nieuwe en snellere opto-elektronische systemen te ontwikkelen is er steeds meer nood aan nauwe co-ontwikkeling van fotonische en elektronische componenten. Door deze toenemende belangstelling in hoogperformante mobiele netwerken en elektronisch/fotonisch co-design is het onderzoeksveld van microgolffotonica en meer bepaald geïntegreerde microgolffotonica ontstaan.

Doelstelling en motivatie

De doelstelling van dit proefschrift is het onderzoeken van heterogene III-V-op-silicium fotonische bouwblokken en elektronische/fotonische subsystemen die toepassingen hebben in de microgolffotonica. De focus ligt vooral op toepassingen in het gebied van draadloze communicatie zoals "Radio-over-Fiber"-verbindingen en RF frequentie-omzetting. Voor deze toepassingen gebruiken we ook optische bouwblokken gerealizeerd op het imec siliciumfotonica platform.

Resultaten

Zoals beoogd, hebben we verschillende III-V-op-silicium fotonische componenten ontwikkeld. De voornaamste resultaten zijn verkregen bij het ontwikkelen van mode-locked lasers, fasedraaiers en optische versterkers. We hebben echter ook silicium fasedraaiers en germanium elektro-absorptiemodulatoren ontworpen en gebruikt voor een aantal subsystemen. Verder hebben we op basis van deze componenten analoge fotonische communicatiekanalen onderzocht en gedemonstreerd. In een eerste demonstratie hebben we met behulp van een direct gemoduleerde III-V-op-silicium DFB-laser en een golfgeleidergekoppelde germanium fotodiode een hoogfrequent analoog signaal over vijf kilometer glasvezel verstuurd. De prestaties van deze link werden verder verbeterd door het co-integreren van een SiGe BiCMOS transimpedantieversterker met de germanium fotodiode. In het laatste onderdeel van deze thesis stellen we het ontwerp, de fabricage en karakterisatie van een geïntegreerde fotonische sampler voor.

III-V-op-silicium bouwblokken

De ontwikkeling van III-V-op-silicium fotonische geïntegreerde circuits heeft grote vooruitgang gekend in de voorbije jaren. Men heeft niet enkel verschillende lasers met hoogwaardige eigenschappen ontwikkeld op dit platform, maar ook fasedraaiers en fotodiodes. De technologie leent zich ook sterk tot het ontwikkelen van microgolffotonische toepassingen. In deze thesis ligt de nadruk op de ontwikkeling van een gepulste laser (mode-locked laser) en een hoogvermogen optische versterker. De gepulste laser werd ontwikkeld met het oog op geïntegreerde fotonische sampling en microgolffotonische frequentieconversie. De versterker werd ontwikkeld omwille van de hoge optische vermogens nodig in analoge fotonische links.

Geïntegreerde mode-locked lasers

Mode-locked lasers vormen een brug tussen de wereld van de microgolven en optica en zijn een essentiële component van vele microgolffotonische systemen. De meeste mode-locked lasers, zoals glasvezel- en vaststoflasers, zijn echter gebaseerd op grote en dure componenten die niet integreerbaar zijn. Dit zorgt ervoor dat deze systemen niet op grote schaal kunnen gebruikt worden. Een halfgeleider mode-locked laser kan echter wel geïntegreerd worden en kan in grote volumes geproduceerd worden maar mist voorlopig de hoogwaardige prestaties van de glasvezel- en vastestoflasers. Wij hebben daarom een nieuwe III-V-op-silicium mode-locked laser ontwikkeld met ongevenaarde microgolf en optische prestaties. Deze eigenschappen werden verkregen door het combineren van een InP/InGaAsP versterker en een passieve caviteit gevormd door (37 mm lange) laag-verlies silicium optische golfgeleiders op dezelfde chip. In Fig. 1(a) is een microscoopbeeld van de

(a)

(b)

(c)
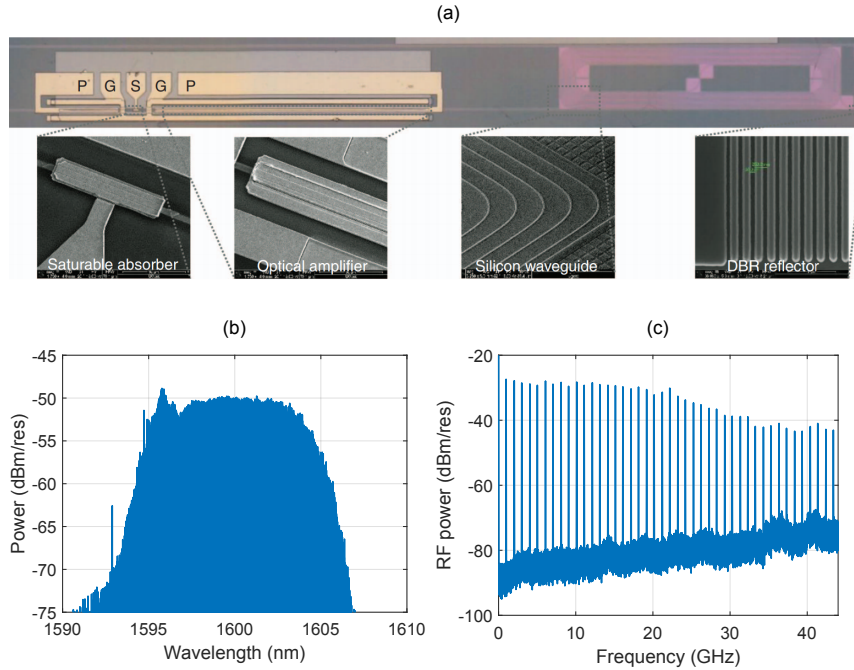
Figuur 1: (a) Microscoopbeeld van een III-V-op-silicium mode-locked laser. De zwart-wit beelden tonen SEM opnames van verschillende details van de laser. (b) Optisch spectrum gegenereerd door de mode-locked laser dat breder is dan 10 nm en meer dan 1400 longitudinale modes bevat. (c) De door de gepulste laser gegenereerde RF-frequentiekam gemeten met een elektrische spectrum analyzer. De RF-toon bij 1 GHz heeft een record lage lijnbreedte van 0.8 kHz.

III-V-op-silicium laser weergegeven. In dezelfde figuur worden enkele details van de laser met elektronenmicroscoopbeelden weergegeven. In Fig. 1(b) wordt het brede optische spectrum (10 nm) van de laser, dat meer dan 1400 longitudinale modes bevat, weergegeven. De lijnbreedte van de individuele longitudinale optische modes is minder dan 250 kHz, wat erg nauw is in vergelijking met de optische lijnbreedte van de meeste geïntegreerde mode-locked lasers zonder passieve caviteit (1-10 MHz). Het microgolfspectrum geproduceerd door de laser is weergegeven in Fig. 1. De 1 GHz toon heeft een erg nauwe lijnbreedte van minder dan 1 kHz en de vlakke microgolf-frequentiekam toont stabiele en coherente mode-locking aan. Dit is een van de eerste demonstraties van een geïntegreerde mode-locked laser die een breed optisch spectrum, stabiele microgolfgeneratie en nauwe optisch lijnbreedte combineert.

Silicium fotonische modulatoren

In deze thesis ligt de focus op silicium fotonische modulatoren voor smalbandige en analoge modulatie. Ook verschillende resonante structuren met transmissielijn-gebaseerde impedantieafstemming werden onderzocht. Er werd ook een reflectieve push-pull MZM onderzocht, die niet-gecentreerd werd gevoed om impedantie-afstemming te bekomen. Tenslotte hebben we een III-V-op-silicium fasedraaier ontwikkeld met als doelstelling deze te integreren op een enkele fotonische chip met een mode-locked laser en een optische versterker.

Geïntegreerde optische versterker

In analoge optische links is optische versterking essentieel voor het verkrijgen van een goede signaalkwaliteit. Op dit moment zijn de meeste optische versterkers echter vezelgebaseerd en niet integreerbaar. Optische versterkers met een hoog uitgangsvermogen en veel versterking vereisen een speciaal ontwerp. In deze thesis tonen we aan dat een versterker met een hoog uitgangsvermogen en veel versterking kan gefabriceerd worden met III-V-op-silicium technologie door gebruik te maken van een brede passieve siliciumgolfgeleider onder de versterker. Verder kan met deze aanpak zo een versterker samen met een direct gemoduleerde laser of mode-locked laser gefabriceerd worden op dezelfde chip, met hetzelfde III-V halfgeleidermateriaal. Het ontwerp van de versterker-golfgeleider is weergegeven in Fig. 2(a) en het gesimuleerde hybride modeprofiel in Fig. 2(b). Omdat de versterker bedoeld is om te werken in een geïntegreerd circuit is een transitie ontwikkeld tussen de versterker-golfgeleider en een monomodale siliciumgolfgeleider. Een schematisch bovenaanzicht van het versterkerontwerp is weergegeven Fig. 2(c). Een microscoopbeeld van de gefabriceerde chip die versterkers met verschillende lengtes en teststructuren bevat is weergegeven in Fig. 2(d). Zoals weergegeven in Fig. 2(e) hebben zowel de 1.2 mm als 1.45 mm lange versterkers een maximaal uitgangsvermogen van meer dan 50 mW (17 dBm). Dit is het hoogste uitgangsvermogen gemeten voor dit soort versterker.

Silicium fotonische analoge links

We hebben in dit werk ook transmissie-experimenten uitgevoerd met state-of-the-art geïntegreerde fotonische componenten. Er zijn reeds verschillende hoogwaardige III-V-op-silicium en germanium-op-silicium modulatoren en detectoren ontwikkeld. Verschillende fotodetectoren en elektroabsorptiemodulatoren gebaseerd op germanium dat gegroeid is op silicium zijn aangetoond in de literatuur. Door gebruik te maken van zo een germanium elektroabsorptiemodulator hebben we experimenteel een hoogfrequente analoge optisch link gedemonstreerd. Niet enkel externe modulatoren maar ook direct-gemoduleerde III-V-op-silicium lasers met bandbreedtes beter dan
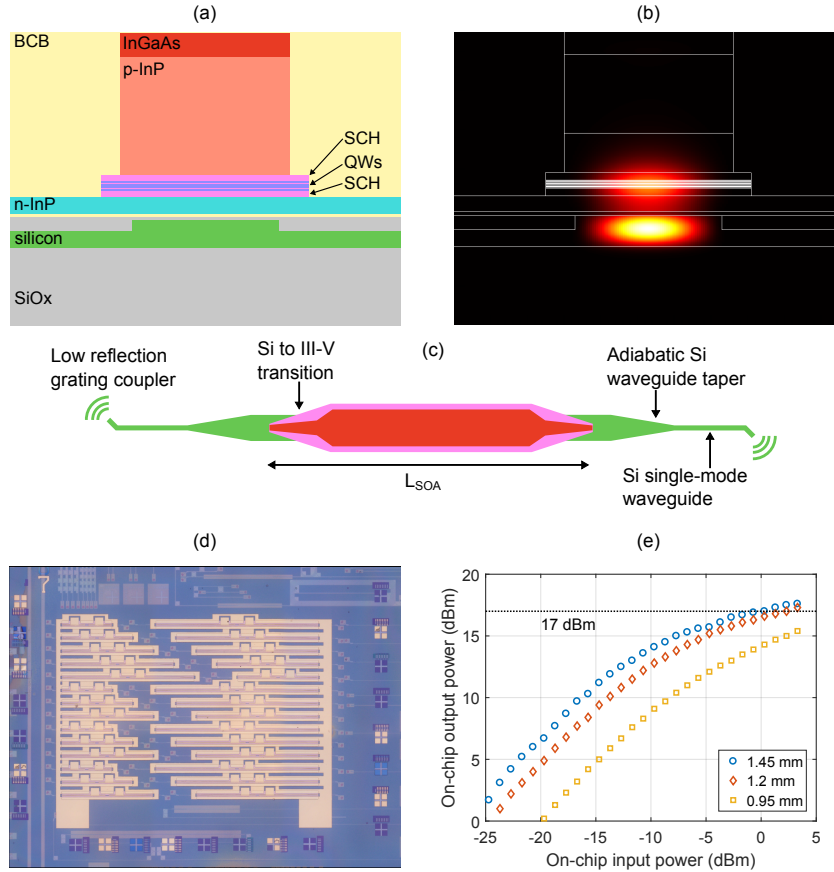
Figuur 2: (a) Schematische voorstelling van de versterker golfgeleiderdoorsnede. (b) Het (in FIMMWave) gesimuleerde hybride modeprofiel. (c) Bovenaanzicht van het versterkerontwerp. (d) Microscoopbeeld van de geïntegreerde fotonische chip die versterkers met verschillende lengtes en teststructuren bevat. (e) Het optisch uitgangsvermogen (in de golfgeleider) van de versterker als functie van het ingangsvermogen voor versterkers met verschillende lengte.

30 GHz zijn aangetoond. In het verleden zijn deze lasers vooral gebruikt voor digitale transmissie, terwijl we in dit werk de lasers gebruiken voor het versturen van analoge signalen.

Radio-over-Fiber links gebaseerd op siliciumfotonica

Met behulp van een direct-gemoduleerde III-V-op-silicium laser en een silicium fotonische ontvanger hebben we experimenteel een 4G LTE (Long Term Evolution) en een 5G Radio-over-Fiber link aangetoond. Voor de 4G link hebben we een golfgeleider-gekoppelde germanium lawine fotodi-

ode geïntegreerd met een SiGe BiCMOS transimpedantieversterker. Met deze opstelling was het mogelijk om een LTE-type signaal op een 3.5 en 5 GHz drager te versturen over 5 km single-mode vezel met een lage rms error vector magnitude (EVM) (1.7 %). De rms EVM (%) en fotostroom bij de ontvanger als functie van de fotodiodespanning is weergegeven in Fig. 3(a). Het lawinemechanisme is een laagvermogen versterkingsmechanisme dat hoogwaardige transmissie toe laat met slechts -16 dBm ontvangen optisch vermogen. In een tweede link hebben we een hoge-bandbreedte golfgeleider-gekoppelde germanium fotodiode geïntegreerd met een hogebandbreedte SiGe BiCMOS transimpedantieversterker gebruikt. Door gebruik te maken van deze componenten zijn we erin geslaagd om 16 Gb/s (16-QAM) data te versturen over 5 km single-mode glasvezel. De rms EVM (%) en bit-error rate (BER) zijn getoond in Fig. 3(b). Een microscoopbeeld van de ontvanger die een fotonisch geïntegreerd circuit en een SiGe BiCMOS transimpedantieversterker bevat is weergegeven in Fig. 3(c).
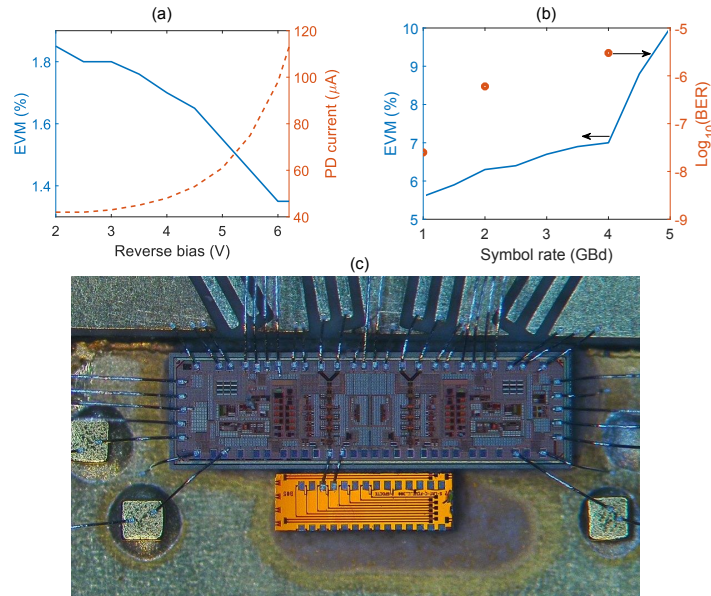
Figuur 3: (a) De rms EVM (%) en fotostroom als functie van de spanning over de lawinefotodiode. Het verbeteren van de EVM met de toenemende spanning illustreert het voordeel van het lawine-effect. (b) De rms EVM (%) en gemeten BER als functie van de symbol rate. (c) Microscoopbeeld van de (kleine chip) golfgeleider-gekoppelde germanium fotodiode op een silicium geïntegreerde fotonische chip en een hoge-bandbreedte SiGe BiCMOS TIA (grote chip) geïntegreerd op een PCB met gebruik van korte draadverbindingen.

Geïntegreerde elektroabsorptie-gebaseerde mixer en zender

We hebben experimenteel een microgolf-fotonische mixer-zender aangetoond door gebruik te maken van twee elektroabsorptiemodulatoren in een MZI-configuratie op een geïntegreerde fotonische chip. Dit soort van microgolf-fotonische mixertopologie waar gebruik gemaakt wordt van LiNbO3 MZMs is reeds uitgebreid bestudeerd in de literatuur, maar het is nog nooit aangetoond door gebruik te maken van hoge-snelheid elektroabsorptiemodulatoren. Met behulp van een Vector Network Analyzer hebben we de klein signaal bandbreedte van de EAM gemeten. Een 3 dB bandbreedte groter dan 67 GHz werd gemeten. Door gebruik te maken van een parallelle weerstand op de chip konden we een breedbandige impedantie-afstemming implementeren. Met behulp van deze afstemming hebben we een reflectiecoëfficiënt van minder dan -10 dB bereikt over het volledig frequentiebereik van 0 tot 67 GHz. We hebben zo een mixer met vlakke respons aangetoond door 10 MBd 64-QAM-data op een 1.5 GHz IF drager omhoog te mixen naar dragerfrequenties van 6 tot 25 GHz met minder dan 3 dB variatie in conversie-efficiëntie. Met deze structuur hebben we 1.3 Gb/s (64-QAM) data op een 3.5 GHz IF-drager geconverteerd naar een 28 GHz drager en dit signaal verzonden over 2 km single-mode glasvezel. Een overzicht van de mixer/zenderstructuur is weergegeven in Fig. 4.
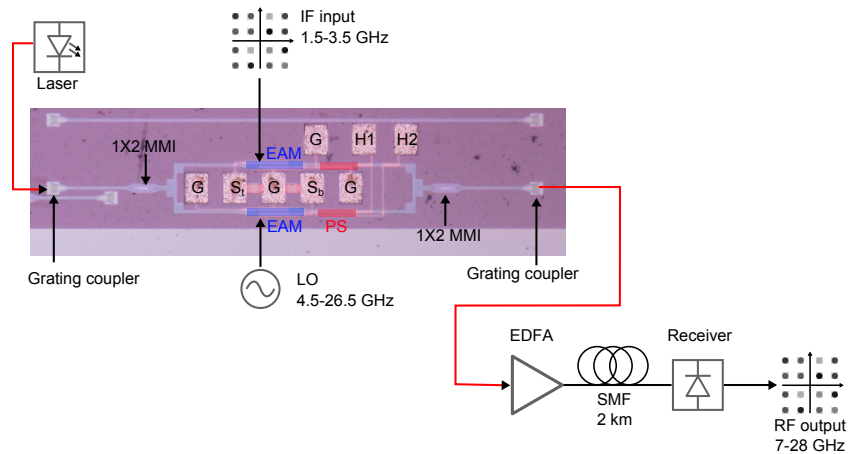
Figuur 4: Overzicht van de GeSi elektroabsorptiemodulator gebaseerde mixer-zender link die gebruikt wordt om 64-QAM-data van een 1.5 GHz drager om te zetten naar een 28 GHz drager en te verzenden over 2 km monomode-glasvezel.

III-V-op-silicium fotonische sampler

Tenslotte hebben we een onderbemonsterde analoge link gebaseerd op III-V-op-silicium fotonische componenten ontwikkeld. De onderbemonsterde link is ontworpen in twee versies. De eerste is volledig geïntegreerd op een enkele chip met enkel elektrische ingangen en uitgangen. De tweede versie bevat een aparte mode-locked laser chip die pulsen levert aan verschillende sampler chips. De bemonsteringscircuits zijn ontworpen in twee verschillende uitvoeringen. In een eerste uitvoering zijn zowel de fasedraaier als de fotodiode gerealiseerd met behulp van III-V-op-silicium componenten. In de tweede uitvoering wordt de fasedraaier gerealiseerd met silicium depletiemodulatoren, gecombineerd met een germanium lawinefotodiode. De specificaties van het systeem werden afgestemd op het gebruik in communicatiesatellieten. Dit werd gedaan in het kader van het European Space Agency ARTES Electro-Photonic Frequency Converter project. De mode-locked laser werd zodanig ontworpen dat de pulsfrequentie toelaat vijf kanalen vanuit de Ka-band naar de L-band te mixen. Een extra laagfrequente lokale oscillator werd toegevoegd om flexibele kanaalselectie te bekomen. Met behulp van discrete commerciële componenten hebben we de systeemarchitectuur geverifieerd en een omzettingsefficiëntie van -20 dB aangetoond. Vervolgens hebben we een gelijkaardig experiment uitgevoerd met geïntegreerde componenten en met succes vijf kanalen van de Ka-band naar de L-band omlaag geconverteerd. Gebaseerd op deze resultaten hebben we een simulatiemodel gebouwd met behulp van de VPITransmissionmaker software. Dit simulatiemodel werd gebruikt voor het systeemontwerp van een volledig geïntegreerde fontonische sampler. In samenwerking met Antwerp Space werd een prototype ontwikkeld en getest.

Conclusie en toekomstvisie

In dit werk hebben we het potentieel van geïntegreerde heterogene (III-V-op-silicium en silicium) bouwblokken en subsystemen voor microgolf fotonica gedemonstreerd. Verder hebben we twee III-V-op-silicium bouwblokken gerealiseerd met prestaties die beter zijn dan de state-of-the-art. De mode-locked laser levert uitstekende prestaties en de lijnbreedte van de gegenereerde fundamentele RF-toon is de nauwste tot nog toe gerapporteerd. Ook de optische lijnbreedte van de laser is erg nauw (400 kHz) wat de laser geschikt maakt voor coherente optische communicatie en dubbele-kam spectroscopie. Verder geeft het brede optische spectrum aan dat de pulsduur sterk verkort zou kunnen worden met behulp van pulscompressie. Het brede optische spectrum in combinatie met de lage pulsfrequentie laat toe hoogfrequente signalen rechtstreeks naar de 1 GHz band te converteren. Tenslotte is dit de eerste keer dat een geïntegreerde passieve mode-locked laser in staat is om zo een lage pulsfrequentie te produceren. In parallel heb-

ben we ook een hoogvermogen halfgeleider optische versterker ontwikkeld
die een record uitgangsvermogen van 50 mW kan produceren. Dit uitgangs-
vermogen is erg interessant voor gebruik in analoge optische links waar het
vermogen erg belangrijk is. Verder is ook de klein-signaal versterking van
27 dB erg relevant voor analoge optische links, omdat op die manier zwakke
signalen met een enkele versterker kunnen worden versterkt. Tenslotte zou
het erg interessant zijn om in de toekomst deze versterker te integreren me
(gepulste) lasers op dezelfde chip. Zeker in gepulste lasers zou dit toe laten
om grotere puls energieën te genereren wat interessant zou zijn voor vele
toepassingen. De experimenteel aangetoonde Radio-over-Fiber links vor-
men interessante elementen voor toekomstige radiotoegangsnetwerk. Het
gebruik van een direct gemoduleerde III-V-op-silicium laser als zender is
een interessante aanpak omdat hierbij geen externe modulatie benodigd
is. Zeker in combinatie met golfgeleider-gekoppelde germanium fotodiodes,
omdat zo een analoge link met enkel geïntegreerde optisch componenten ge-
realiseerd wordt. De prestaties van de link werden nog verder verbeterd door
de co-integratie van een SiGe BiCMOS transimpedantieversterker. Ook de
GeSi elektroabsorptiemodulatoren zijn erg beloftevolle componenten voor
5G analoge links, gezien hun bandbreedte ze in staat stelt te opereren in
de nieuwe 5G banden (30-60 GHz). Verder hebben we microgolf fotonische
frequentie-omzetting kunnen demonstreren door deze modulatoren in een
MZI-structuur te plaatsen. Tenslotte hebben we een geïntegreerde onder-
bemonsteraar ontworpen, gefabriceerd en getest. Dit geïntegreerd fotonisch
circuit werd ontwikkeld om gebruikt te worden in communicatiesatellieten.

Summary

The evolution of telecommunication in the last decades has had an enormous impact on society. For example, since 1997 the internet traffic has increased from 100 gigabytes per minute to more than 45 terabytes per second in 2017. Not only are people everywhere and always connected, also machines are becoming more and more interconnected. One of the main evolutions is the development of mobile connectivity, which is becoming one of the main sources of data traffic. To service all these mobile users and devices the next generation mobile networks (5G) are in full development. One of the main challenges in 5G networks will be to deploy a radio access network capable of servicing an ever increasing number of users while also increasing data rates by a tenfold. In such radio access networks fiber optic connections, high speed analogue electronics and wireless transceivers have to be efficiently interfaced. While in the past these technologies were often considered different disciplines, the increased co-integration has driven the research of microwave photonics and more specifically integrated microwave photonics.

Goals and Motivation

In this work we aim to investigate heterogeneous III-V-on-silicon photonic and all-silicon (including Ge-based) devices and links for applications in microwave photonics. This work is focused on technologies enabling the optical distribution and processing of wireless communication signals.

Results

In this work we developed both new heterogeneous III-V-on-silicon and all-silicon devices and demonstrated microwave photonics subsystems based on these devices. A large portion of the device development is focused on III-V-on-silicon mode-locked lasers, phase-shifters and amplifiers. Also silicon carrier-depletion phase-shifter based MZMs and Ge EAM-based devices were investigated. In a second part of the thesis we investigated analogue

photonic links based on both germanium-on-silicon and III-V-on-silicon devices. We first demonstrate that a high-frequency Radio-over-Fiber link can be realized using a III-V-on-silicon directly modulated DFB laser and a waveguide-coupled germanium-on-silicon photodiode. The link was further enhanced by co-integrating a SiGe BiCMOS TIA with the high-bandwidth germanium photodiode. We then further investigated the use of microwave photonic up-conversion in an analogue photonic link based on GeSi EAMs. And finally we designed, fabricated and characterized a III-V-on-silicon photonic sampling circuit.

III-V-on-silicon devices

The development of heterogeneous III-V-on-silicon PICs has seen a great advancement in the last decade. Several types of high-performance integrated lasers have been demonstrated on this platform, as well as phase shifters and photodiodes. Not only are there many promising devices developed, devices and circuits for integrated microwave photonics have received quite some attention in the last years. We focused mainly on the development of a pulsed laser and a high-power amplifier. The pulsed laser was developed for the use in integrated optical sampling microwave frequency converters. The amplifier was developed to integrate the necessary gain in an analogue photonic link.

Integrated mode-locked laser

Mode-locked lasers form an interesting link between the optical and microwave domain and are an essential component of several microwave photonic systems. However, fiber or solid-state mode-locked lasers are bulky and expensive and cannot be integrated. On the other hand, integrated semiconductor mode-locked lasers offer easy integration and scalable fabrication but lack the performance of their table-top counterparts. We demonstrated a novel III-V-on-silicon mode-locked laser with best-in-class optical and microwave performance. By combining an InP/InGaAsP gain section with a long (37 mm) low-loss silicon on-chip extended cavity, an excellent optical linewidth and RF stability is achieved. In Fig. 1(a) a microscope image of the III-V-on-silicon laser is shown with scanning electron microscope images of essential parts of the laser. In Fig. 1(b) the wide optical spectrum (10 nm) containing more than 1400 longitudinal modes is shown. The individual optical linewidths are approximately 250 kHz, which is very narrow compared to the optical linewidths (1-10 MHz) found in all-active semiconductor mode-locked lasers. Furthermore, across the entire spectrum no mode with an optical linewidth broader than 400 kHz was found. The RF spectrum generated by the pulsed laser output incident on a photodiode is shown in Fig. 1(c). The 1 GHz RF tone has a record low linewidth below 1 kHz and the flat RF frequency comb indicates stable and coherent mode-

(a)

(b)   (c)
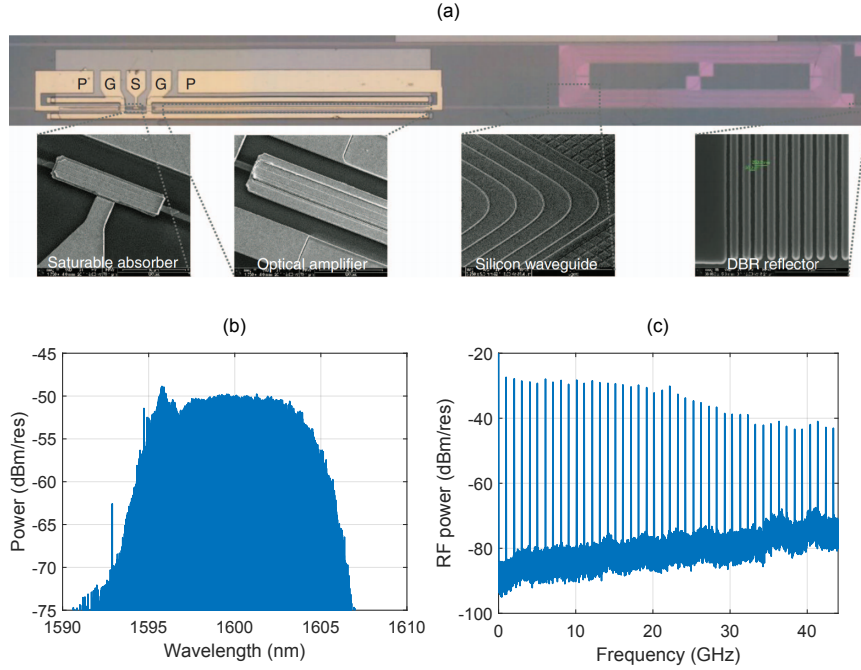
Figure 1: (a) Microscope image of a III-V-on-silicon mode-locked laser. The inset images show scanning electron microscope images of various constituent parts of the laser. (b) Optical spectrum generated by the mode-locked laser, spanning over 10 nm and containing more than 1400 longitudinal modes. (c) Generated RF frequency comb by the pulsed laser. The RF tone at 1 GHz has a record narrow 10 dB linewidth of 0.8 kHz.

locking. This is one of the first demonstrations of an integrated mode-locked laser combining a wide optical spectrum, stable RF generation and narrow optical linewdith.

Silicon photonic modulators

In this work we focused on the development of silicon photonic modulators for narrow-band and analogue modulation. Several resonant structures with on-chip stub matching were investigated. Furthermore a push-pull reflective MZM was studied and off-center feeding was used to achieve narrow-band impedance matching. Finally a III-V-on-silicon phase shifter was developed which can be co-integrated on a single III-V-on-silicon PIC with a mode-locked laser, semiconductor optical amplifier and photodiode.

Integrated semiconductor optical amplifier

Optical amplification is an essential part of most analogue photonic links. However, common amplifiers such as erbium doped fiber amplifiers are bulky and cannot be integrated into a photonic circuit. High-power and high-gain optical amplifiers often require a dedicated design. Here we show that a high-power high-gain amplifier can be realized in III-V-on-silicon by making use of a wide silicon waveguide in the gain section. With this approach the high-power amplifier can be fabricated on the same chip (with the same III-V material) as a high-speed directly modulated laser or mode-locked laser. The design of the gain waveguide is shown in Fig. 2(a) and the simulated hybrid optical mode profile is shown in Fig. 2(b). Because the amplifier is meant to be integrated into a photonic integrated circuit with other devices, a taper structure from the gain waveguide to a single silicon waveguide was implemented. A schematic top view of the amplifier design is shown in Fig. 2(c). A microscope image of the fabricated chip containing SOAs with the hybrid gain waveguide design in different lengths and several test structures is shown in Fig. 2(d). As can be seen in Fig. 2(e) both the 1.45 and 1.2 mm long devices achieve over 50 mW on-chip output power, the highest reported to the best of our knowledge for a III-V-on-silicon optical amplifier.

Silicon photonics analogue links

Not only did we investigate the development of novel devices, we also experimentally demonstrated the use of state-of-the-art integrated photonic components in analogue photonic links. Many high performance modulators and detectors were developed on the silicon photonic platform. For example, using the epitaxial growth of germanium on silicon high-bandwidth photodetectors and electro-absorption modulators have been realized. Using such germanium EAMs we experimentally demonstrated a high-performance analogue photonic link. Not only external modulators but also directly modulated lasers with a modulation bandwidth beyond 30 GHz have been demonstrated in III-V-on-silicon, with promising results for digital data transmission. In this work we also explore its use for analogue transmission.

Heterogeneous silicon photonics Radio-over-fiber link

Using a directly modulated III-V-on-silicon DFB laser and a silicon photonic receiver we experimentally demonstrated both a 4G LTE and 5G Radio-over-Fiber link. In the 4G link a waveguide-coupled germanium avalanche photodiode co-integrated with a SiGe BiCMOS TIA was used as a receiver. This enabled the transmission of an LTE-type signal on a 3.5 and 5 GHz carrier over 5 km of single mode fiber with a low rms EVM (1.7 %). The rms EVM (%) and receiver photocurrent as a function of the
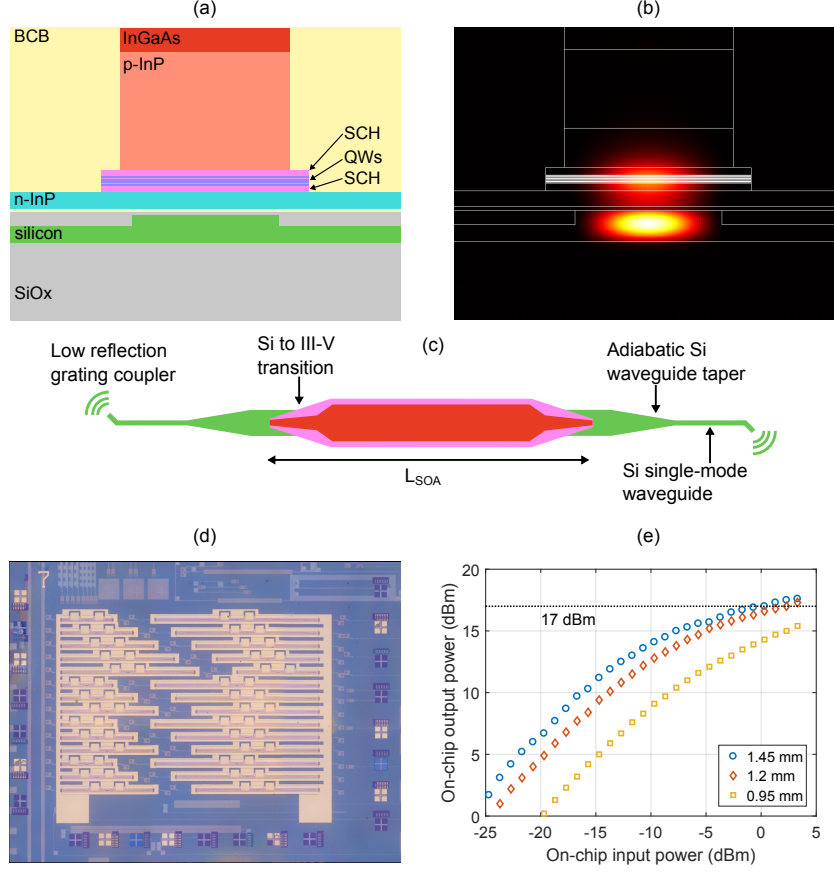
Figure 2: (a) Schematic of the gain waveguide cross-section with different layers denoted. (b) Modal simulation (FIMMWave) of the gain waveguide. (c) Top-view of the amplifier design. (d) Microscope image of the fabricated III-V-on-silicon PIC containing amplifiers in different lengths and reference waveguides. (e) On-chip output power as a function of the input power for different amplifier lengths.

avalanche photodiode reverse bias are shown in Fig. 3(a). The low power consumption avalanche gain mechanism enables high-quality transmission with only -16 dBm of received optical power. In a second link we use a high-bandwidth waveguide-coupled germanium photodiode co-integrated with a high-bandwidth SiGe BiCMOS TIA. Using these integrated photonic components we demonstrated the transmission of 16 Gb/s (16-QAM) data over 5 km of standard single mode fiber. The rms EVM (%) and bit error rate are shown in Fig. 3(b). A micrograph of the receiver containing the photonic integrated circuit and a SiGe BiCMOS TIA chip is shown in Fig. 3(c).
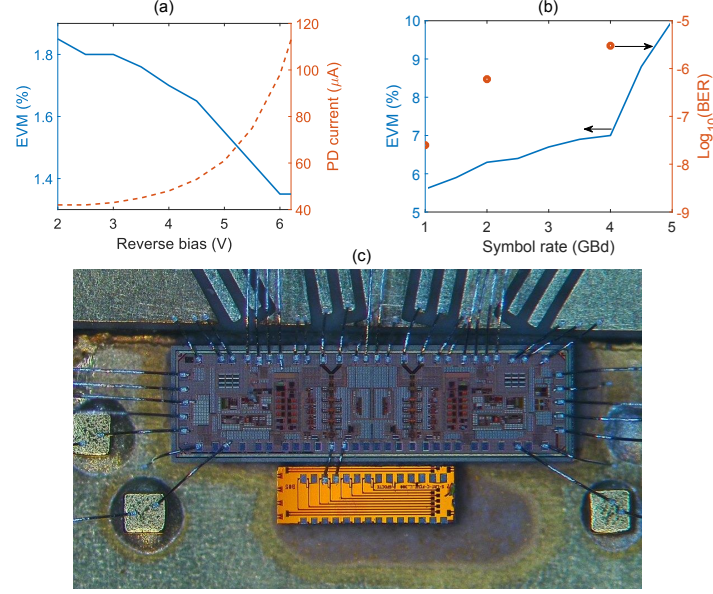
Figure 3: (a) The rms EVM (%) and photocurrent as a function of the reverse bias over the avalanche photodiode. The improving EVM and increasing photocurrent illustrate the benefits of the avalanche gain mechanism. (b) The rms EVM (%) and measured bit error rate as a function of the symbol rate. (c) Microscope image of the (small die) waveguide-coupled germanium photodiode on a silicon PIC and high-bandwidth SiGe BiCMOS TIA (large die) co-integrated on a PCB using wire-bonds.

Integrated EAM-based mixer and transmitter

We demonstrated a microwave-photonic up-converter-transmitter based on two GeSi EAMs in a MZI structure on a silicon PIC. This type of microwave photonic mixer topology has been widely investigated using $LiNbO_3$ Mach-Zehnder modulators but was never before demonstrated using high-bandwidth integrated EAMs. Using a vector network analyzer we characterized the EAM and found a 3 dB modulation bandwidth exceeding 67 GHz. Furthermore, by using a on-chip parallel resistor, wide-band matching is achieved with a return loss better 10 dB from 0 to 67 GHz. We demonstrate an extremely flat-band mixer behaviour by up-converting a 1.5 GHz IF signal with 10 MBd of 64-QAM data to carrier frequencies from 6 to 25 GHz with less than 3 dB ripple. Using this structure we up-converted 1.3 Gb/s (64-QAM) data on a 3.5 GHz IF carrier to a 28 GHz carrier and successfully transmitted it over 2 km of single mode fiber. An overview of the full link together with a colorized micorscope image of the photonic integrated circuit is shown in Fig. 4.
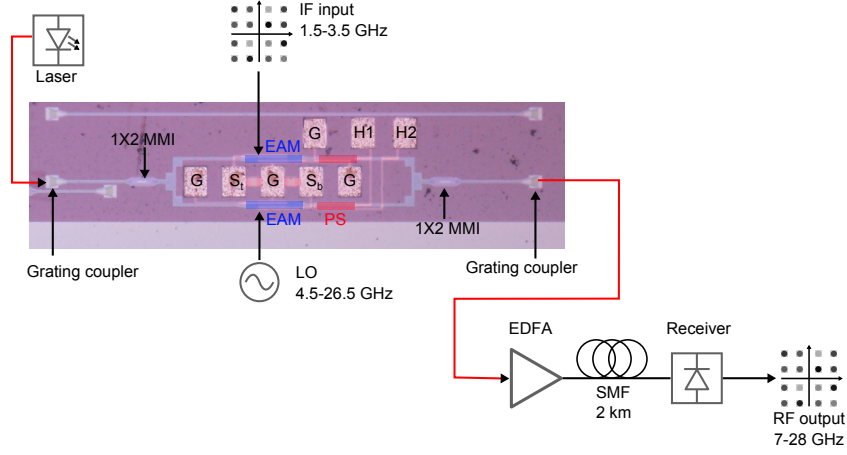
Figure 4: Overview of the GeSi EAM-based up-converter-transmitter link used to up-convert 64-QAM data on 1.5-3.5 GHz carriers to 6-28 GHz carriers and transmit it over 2 km of single mode fiber.

III-V-on-silicon sub-sampler

Finally we developed a sub-sampled analog link based on heterogeneous silicon photonic devices. The sub-sampled link is designed in two flavors, one is a fully integrated version where the full subsystem is contained in a single chip with only electrical inputs and outputs. In the alternative version a separate mode-locked laser chip is developed that is used to distribute the optical pulses to several different sampler chips. The sampler circuits were designed both using III-V-on-silicon phase shifters (combined with III-V-on-silicon photodiodes) and silicon carrier-depletion phase-shifters (combined with germanium avalanche photodiodes). The specifications of the fabricated systems were geared towards the implementation in a communication satellite. This was done within the framework of the European Space Agency ARTES project Electro-Photonic Frequency Converter (EPFC). The repetition rate of the mode-locked laser was chosen such that five channels with 500 MHz bandwidth can be down-converted from the Ka-band to the L-band. An additional low-frequency oscillator was added to the scheme to enable flexible channel selection. We used commercial discrete components to validate the system design and demonstrated a conversion efficiency of -20 dB. We then demonstrated the same systems using an individual mode-locked laser and modulator chip and successfully down-converted five channels from Ka- to L-band. Based on this experimental demonstration the system was modelled using VPITransmissionmaker. Based on the results of this simulation a fully integrated photonic sub-sampling down-converter system was designed. A prototype was designed, assembled and tested in

collaboration with Antwerp Space.

Conclusion and outlook

In this work we have demonstrated the potential of silicon devices (III-V-on-silicon and all-silicon) and subsytems for applications in integrated microwave photonics. We demonstrated two III-V-on-silicon devices with beyond state-of-the-art performance designed for integrated microwave photonic applications. The mode-locked laser has excellent performance and especially the linewidth of the fundamental RF tone is the narrowest reported to the best of our knowledge. Furthermore, the optical linewidth of the individual modes is less than 400 kHz over the entire output spectrum, making it suitable for coherent communication and dual-comb spectroscopy. Furthermore, the wide optical spectrum generated by the laser indicates that with suitable compression techniques extremely short pulses can be achieved. The wide optical spectrum in combination with a low repetition rate allows to down-sample very high-frequency signals straight to the 1 GHz band. This is also the first time an integrated mode-locked laser that can passively mode-lock at such a low-repetition rates is demonstrated. In parallel we developed a high-power amplifier which produced a record on-chip output power for a III-V-on-silicon amplifier of more than 50 mW. This output power is very interesting for amplification in the output stage of an analogue transmitter in a radio-over-fiber link. Even more so because the amplifier also has a small-signal gain of 27 dB, which allows to amplify rather weak signals to high output powers. It would also be interesting to integrate such a high-power amplifier in integrated mode-locked lasers to increase the pulse energy and further improve the performance.

The demonstrated Radio-over-Fiber links are a promising approach for future radio access networks. The use of a directly modulated III-V-on-silicon laser as transmitter is an interesting approach as no external modulation is needed. However, the extremely high bandwidth of the GeSi EAMs make them an excellent candidate for the high-frequency (60 GHz bands) signals in future 5G Radio Access Networks. Therefore we demonstrated for the first time the integration of wide-band microwave photonic up-conversion on-chip using GeSi EAMs. Finally, the use of germanium waveguide-coupled photodiodes is also an interesting approach for the receiver side. Especially when co-designed with a SiGe BiCMOS TIA a high-performance and compact solution can be realized. Finally, the integrated photonic sampling circuits designed and fabricated in this work show promising results. We demonstrated an optical sub-sampling system using both commercial components and photonic integrated circuits designed for operation in communication satellites.

Chapter 1

Introduction

This dissertation details the research of integrated optical circuits, using silicon photonic technology, for the processing and transmission of microwave signals. In this introductory chapter we give the context for the work that is reported in the following chapters. The state-of-the-art regarding III-V-on-silicon, microwave photonics and integrated microwave photonics is given followed by an outline of the dissertation.

1.1 Silicon photonic integrated circuits

One of the most seminal discoveries of the last century must be the integrated electronic circuit. The ability to integrate electronic components on a millimeter-sized chip has reshaped the way we live. Every aspect of our life has become intertwined with integrated electronics, from driving a car to interacting with friends and family, or even a visit to the hospital. Not just our life, but our society has been undergoing a digital revolution. At the core of all this lies the CMOS industry which produces the integrated circuits (ICs) in extremely large quantities, necessary to fuel this revolution. Today, when everyone is becoming connected with everyone, a technology complementing electronics has taken the stage: photonics. Photonics is a research field and technology that has grown out of classical optics and is focused on the generation and manipulation of light. Moreover, one topic lies at the heart of photonics: optical communication. Thanks to the development of optical fiber and the semiconductor laser, we are capable of being interconnected with the entire world. Due to the ever increasing number of connected devices and people, the requirements on photonic components and systems has also dramatically increased. This ushered in the development of integrated photonics, where optical devices and circuits can be

integrated on a semiconductor chip. In the last decades there has been an explosive growth in integrated photonic technologies and Photonic Integrated Circuits (PICs) can be fabricated in many different materials such as silicon or indium phosphide. However, silicon photonics is the only technology that can directly benefit from the CMOS industry. These silicon photonic circuits are made on silicon-on-insulator, a material platform used for high-performance CMOS circuits.

This photonic SOI platform is based on the use of a high refractive index material (silicon) on top of a low refractive index material (SiO_2) to create dielectric waveguides. These waveguides can have very small cross sections, for example 220 by 450 nm, and have excellent confinement allowing for small bend radii. The small size of the waveguides and small bend radii allow a very large number of components to be combined on a single PIC. Not only do these waveguides have good confinement, they can also be fabricated with relatively low-loss (less than 1 dB/cm). If very low losses are needed rib-waveguides can be used to achieve losses smaller than 0.5 dB/cm [1, 2]. Furthermore, easy interfacing with cleaved single mode fibers can be achieved using vertical chip-to-fiber grating couplers [3]. Not only waveguides but also components such as high-Q ring filters have been realized on the silicon photonic platform [4]. Also Mach-Zehnder Interferometers (MZIs) [5] and more complex filters with a wide range of applications have been developed [6]. In many telecommunication applications, the multiplexing or de-multiplexing of different wavelengths is an essential function. This can be implemented in a very compact fashion using silicon Arrayed Waveguide Gratings (AWGs) [7].

Several silicon photonic platforms have been developed that offer not only passive but also active components such as photodiodes (PDs), thermo-optic phase shifters, Electro Absorption Modulators (EAMs) and carrier-based phase shifters. For example, imec offers a silicon photonic platform (iSiPP50G) with many advanced devices geared toward 50 Gb/s communication and beyond. A key component of this platform is a high-speed waveguide-coupled GeSi photodiode with an analogue bandwidth exceeding 67 GHz [8]. Furthermore, GeSi EAMs with similar analogue bandwith are available on the same platform and have been used for the transmission of 100 Gb/s NRZ and 128 Gb/s PAM-4 data [9, 10]. Apart from the germanium-based devices, carrier-depletion and carrier-injection-based phase shifters have been realized in silicon [11–13]. Using carrier-depletion phase shifters in a MZI structure, Mach-Zehnder modulators (MZMs) with an Electro-Optic (EO) bandwidth exceeding 40 GHz have been demonstrated [13]. However, the demand for ever higher bandwidths has pushed research beyond single devices and electronic/photonic co-design has be-

come an important evolution. By designing electronic circuits, such as modulator drivers, specifically for silicon photonic components the performance can be further optimized and the power consumption reduced [14, 15].

1.2 III-V-on-silicon photonics

Although silicon photonics has many advantages, the downside is that no light sources can be directly integrated without the use of foreign materials. The semiconductors of choice for light generation, especially for laser sources used in telecommunication, are the so called III-V materials. An example of a much used III-V material in the semiconductor industry is InP. For example InP/InGaAsP and InP/AlGaInAs epitaxial layer structures are heavily used for semiconductor lasers in the telecom wavelength window of 1.3 and 1.55 μm.

1.2.1 Monolithic InP PICs

An alternative to silicon photonics are monolithic InP PICs, where the light source can be directly integrated and the passive waveguides are also realized in a III-V material instead of silicon. For example the SMART InP platform offers gain sections, passive waveguides and phase shifters on one monolithic chip through an epitaxial regrowth process [16, 17]. Several high performance devices such as narrow linewidth lasers [18], tunable lasers [19], short-wave infrared lasers [20], modulators [21] and even optical phase-locked loops for THz generation [22] have been demonstrated using this technology. This approach has the advantage of full integration of all components on a monolithic chip, however the many regrowth steps can make the fabrication complex and challenging. Furthermore, the passive waveguides have higher losses and larger bend radii when compared to silicon or silicon nitride platforms. A possible alternative approach is the IMOS (InP membrane on silicon) platform where the InP circuit is created in a thin InP membrane wafer-bonded on top of a silicon wafer. This has the advantage that the index contrast in the InP waveguides is strongly increased allowing for more compact devices and higher integration density [23].

1.2.2 Hybrid integration

Next to monolithic InP PICs, many hybrid integration approaches have been developed for specific applications. For example, to create a chip-scale narrow linewidth laser an on-chip low-loss cavity is needed. In this case, the low-optical losses of a silicon or silicon nitride (SiN) waveguide are ideally suited. Using butt-coupling, an active InP chip can be optically
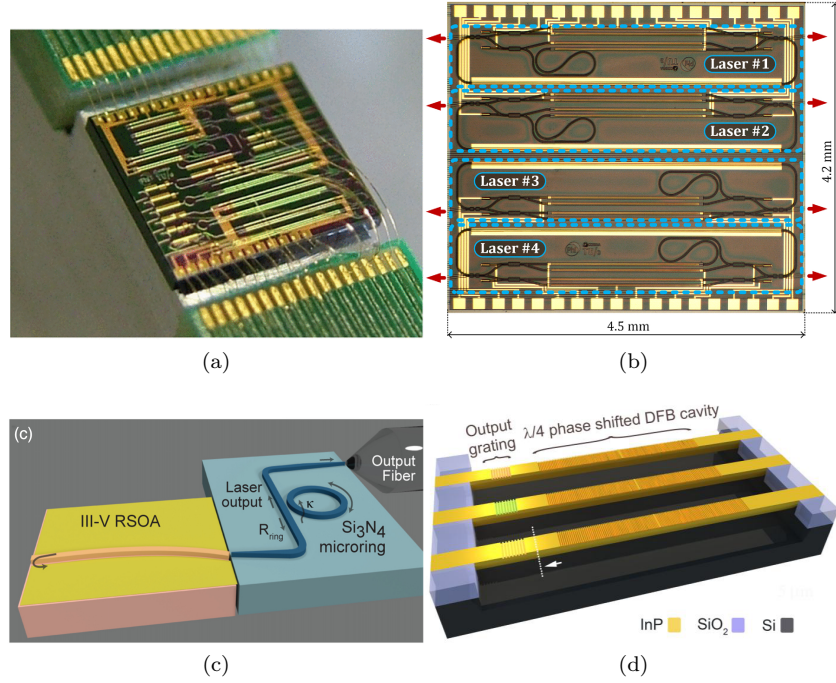
Figure 1.1: Overview of lasers realized in different active/passive photonic platforms. (a) An InP 4.7 x 4.1 mm PIC containing several tunable lasers, wire-bonded to a PCB [19]. (b) Micrograph of InP PIC with four widely tunable 2 μm lasers [20]. (c) Schematic of a butt-coupled hybrid III-V/SiN laser [24]. (d) Three dimensional rendering of monolithically integrated InP DFB lasers on silicon [25].

connected to a silicon cavity, creating an integrated external cavity laser. For example, a widely tunable laser was realized by butt-coupling a GaSb Semiconductor Optical Amplifier (SOA) chip to a silicon photonic external cavity chip and resulted in a laser with a tuning range of > 50 nm and a Side-Mode Suppression Ratio (SMSR) of > 50 dB [26]. Not only silicon chips can be used as external cavities, compact narrow-linewidth lasers have been fabricated by butt-coupling an SOA chip to a silicon nitride external cavity PIC. For example, a chip-based laser with a (Lorentzian) optical linewidth of 87 kHz was achieved by butt-coupling a Reflective SOA (RSOA) to a SiN PIC with a ring-based reflector [27]. More recently, a commercially available RSOA butt-coupled to a SiN high-Q ring resonator achieved a narrow optical (Lorentzian) linewidth of 13 kHz [24].

Although the performance of these devices is excellent, while maintaining a compact form factor, it is not possible to manufacture these devices

on a wafer scale. Every device has to be assembled with great precision, because the butt-coupling requires time-consuming alignment with tolerances often below 1 μm. The wafer-scale integration of InP on silicon is a very interesting alternative and could offer a scalable platform for the fabrication of high-performance active/passive PICs. A lot of ongoing research is dedicated to the direct epitaxial growth of InP on silicon wafers. Although many promising results have been reported, it is a very challenging approach [25, 28, 29]. Currently no electrically injected InP-on-Si or GaAs-on-Si laser which is coupled to a silicon waveguide has been demonstrated, to the best of our knowledge. Moreover, due to the challenging nature of growing InP materials on Si this process greatly increases the complexity of manufacturing when compared to "regular" silicon photonics.

1.2.3   Die-to-wafer bonding

A very interesting alternative to the direct growth on silicon, is the use of die-to-wafer bonding of InP material on a processed silicon photonics wafer [30–32]. With the use of industrial collective die-to-wafer bonding, scalable and low-cost fabrication is within reach [33, 34]. The passive silicon PICs can be fabricated on 200 mm or 300 mm wafers and can be processed using CMOS manufacturing technology, which allows for low-cost and high-volume manufacturing. At the same time the III-V material can be grown on its native substrate, which allows for high-quality material with minimal complexity. Suitably-sized dies of InP can then be bonded to a silicon PIC or wafer depending on the goal.

Many high-performance devices and circuits have been demonstrated using the die-to-wafer bonding approach. For example, a very large variety of III-V-on-silicon lasers have been reported, ranging from widely tunable lasers with a narrow optical linewidth to high-bandwidth directly modulated lasers. A tunable III-V-on-silicon laser, using ring filters, achieved a tuning range of more than 50 nm and an optical linewidth of 50 kHz [35]. A DFB laser, with an InP/AlGaInAs MQW as active material, has shown small-signal bandwidths up to 34 GHz allowing for 56 Gb/s data transmission [36]. The design of this laser allowed to co-integrate an EAM by electrically isolating a part of the gain section. Using such a laser-EAM, 56 Gb/s NRZ data was transmitted over 2 km of on-zero dispersion-shifted fiber [36] and 100 Gb/s of electrical duobinary optical data was transported over 100 m of single mode fiber [37].

Not only telecom lasers have been demonstrated, also longer wavelength III-V-on-silicon lasers have been reported. These are very interesting for the use in gas-spectroscopy and sensing, as the molecular fingerprint absorption becomes stronger in the mid-infrared. An array of III-V-on-silicon
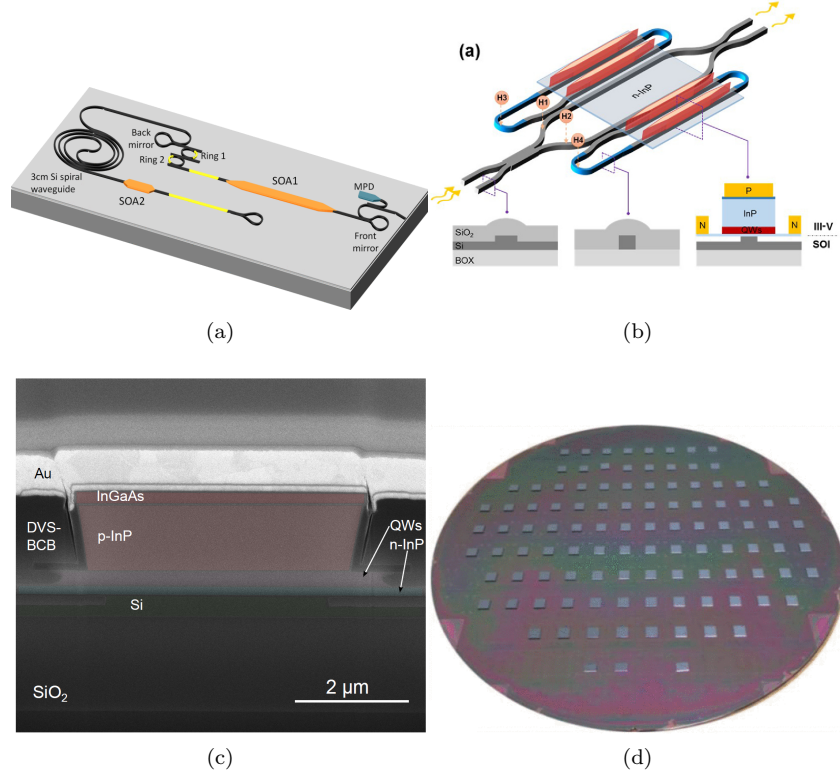
Figure 1.2: (a) Schematic of a III-V-on-silicon tunable laser [35]. (b) Schematic of a III-V-on-silicon ultralinear MZM [38]. (c) Cross-section of InP/InGaAsP-on-silicon SOA waveguide. (d) Photograph of a processed 8 inch silicon wafer with over 100 InP dies bonded on it [34].

DFB lasers with an emission wavelength around 2.3 μm has been demonstrated using a W-shaped InGaAs/GaAsSb Type II active region [39]. The advantage of using III-V-on-silicon is that the output of all lasers in the array can be multiplexed using compact and high performance silicon photonic components. Even interband cascade lasers on silicon, emitting beyond 3 μm, have been demonstrated [40]. The combination of high-quality gain waveguides with low-loss passive cavities has also enabled the fabrication of high-performance integrated pulsed lasers [41]. A more extensive discussion of the state-of-the-art can be found in chapter 2.

Many other devices such as phase shifters have also been demonstrated in III-V-on-silicon. Not only modulators for digital data transmission [42] have been reported, but also ultra-high linearity modulators for microwave

photonic (MWP) applications have been demonstrated [38, 43].

1.3 Microwave photonics

Not only the integration of optical circuits has evolved dramatically in the past decades. Also the use of optical methods for the processing and transmission of microwave signals has seen intensive development in the recent past. The interest in electro-optic systems for the transmission and processing of microwave signals stems from their wide-band operation and flexibility. Furthermore, electro-optic systems are capable of transmitting high-bandwidth signals over very long distances with very low loss compared to copper cables. This growing popularity has led to the development of the research area known as microwave photonics (MWP) [44]. One of the earliest and most important topics within MWP is the development of analogue photonic links. Using optical fiber it is possible to transport high frequency microwave signals over a distance of several kilometers, which is unimaginable using metallic waveguides or coaxial cable. These analogue links, also referred to as Radio-over-Fiber (RoF) links, have been intensively investigated and have been demonstrated for a large variety of microwave frequencies and fiber lengths [45]. With the advent of next generation mobile networks (5G) RoF links have gained further interest as they could play an enabling role in cloud-radio access networks (C-RAN) [46].

An interesting advantage of using analogue RoF links, is that frequency conversion from IF to RF can be realized in the optical domain instead of using an electronic mixer. This has the advantage of very flexible and wide-band operation. Extensive research on this topic has been performed and many different architectures have been proposed using commercial LiNbO$_3$ MZMs. Although serial MZM topologies have been investigated [47], a parallel MZM topology, where 2 MZMs or phase shifters are placed in a MZI structure, has shown optimal performance [48, 49]. More complex and advanced systems have been developed, including a parallel MZM mixer with a tunable RF phase shift [50–52]. Even more complex mixers using polarization multiplexing and up to 4 MZMs [53] and fiber Sagnac loops have been demonstrated [54]. Furthermore, RoF links with photonic up-conversion have not only been demonstrated using MZMs but also using EAMs [55].

Microwave photonic systems are not limited to the transmission or mixing of microwave signals, but find many other applications such as the generation of very stable or complex microwave signals. A first example of microwave signal generators are opto-electronic oscillators (OEOs). These systems use optical fiber to create long delay lines unachievable using pure

microwave technologies [56]. Another approach to generate very pure microwave signals, is to translate the relative stability of a narrow-linewidth laser from the optical to the microwave domain. This approach was used to generate photonic microwave signals, with zeptosecond timing jitter, by locking an optical frequency comb to an ultra-stable laser [57]. More complex signals, necessary for radar systems, can also be photonically generated which increases the flexibility and bandwidth of the system [58]. The field of MWP has grown so much and covers so many topics that a full review of all advances is outside the scope of this introduction. However, it is interesting to note that in recent years a lot of focus within MWP is towards integration. This has led to a vibrant research domain referred to as Integrated Microwave Photonics (IMWP).

1.4   Integrated microwave photonics

The use of PICs in microwave photonics is essential to increase the cost-efficiency and scalability of microwave photonics for real-world applications. Due to the strong development of MWP and integrated photonic technologies, the research effort in IMWP has surged in the past years and many exhilarating advances have been made [59, 60]. For example, in [61] a programmable Bragg grating is demonstrated on a silicon PIC. This is achieved by inserting multiple carrier-based phase shifters in a silicon waveguide grating. One of the most salient results of the past few years is the development of programmable microwave photonic processors [62–64]. These photonic processors can be thought of as the equivalent of a Field Programmable Gate Array (FPGA) used in electronics. In [64] a SiN (TriPlex) PIC is demonstrated which contains a reprogrammable square coupler mesh that is used to implement several microwave photonic filter functions. In [62] a hexagonal mesh is implemented on a silicon PIC and is used to demonstrate a wide variety of signal processing functionalities.

Although the functionality of these chips is very impressive, they are not truly integrated solutions as an external laser, modulator and detector is needed for operation. Although InP has some disadvantages when compared to silicon photonics, the technology allows to combine all components on a single PIC. For example, a monolithic InP re-configurable microwave photonic filter containing a laser, single side-band modulator, lattice-filter and photodetector was reported in [65]. Furthermore, a fully integrated microwave photonic frequency down-converter was also demonstrated on a single InP PIC [66].

As described above, III-V-on-silicon is an attractive technology which allows to combine all the benefits of silicon photonics with the monolithic

(a) (b)

(c) (d)
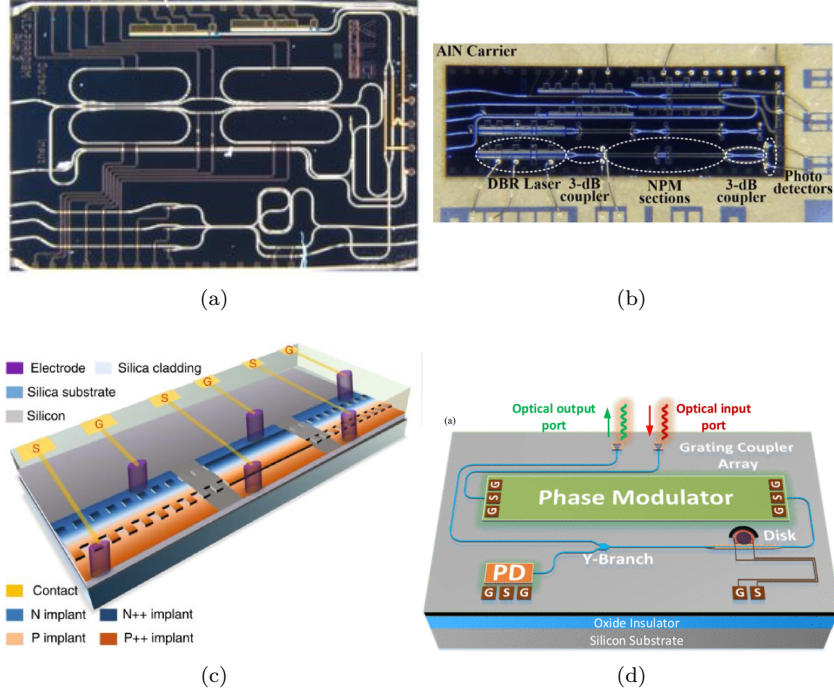
Figure 1.3: (a) Microscope image of a InP PIC containing a fully integrated microwave photonic filter [65]. (b) Microscope image of a microwave photonic down-conversion PIC [66]. (c) Schematic of a silicon photonic reconfigurable Bragg Grating for flexible microwave photonic signal processing [61]. (d) Schematic of a silicon photonics based OEO [67].

integration of active devices. This technology is therefore ideally suited for IMWP, as demonstrated by the ultra-linear MZM reported in [38]. Not only single devices but also complex IMWP circuits such as tunable microwave synthesizers have been realized on the platform [68]. Recently, even a fully integrated millimeter-wave tracker has been demonstrated in III-V-on-silicon [69]. Although many high-performance circuits and devices have already been demonstrated on III-V-on-silicon PICs there is still much room for innovation.

1.5   Overview of the work presented in this thesis

The work presented in this thesis can be divided in three main parts. In the first part we developed (III-V-on-)silicon photonic devices specifically for IMWP applications. The second part consist of MWP system experiments with existing state-of-the-art photonic devices. In the final part we develop a more complex III-V-on-silicon subsystem containing several active devices on a single PIC, an Electro-Photonic Frequency Converter. Although this dissertation is divided in three main themes, some themes contain several chapters. Several devices were developed and characterized. The first device is a III-V-on-silicon mode-locked laser that is detailed in chapter 2. In chapter 3 we investigated and compared several MZMs. In chapter 4 we develop a high-power high-gain III-V-on-silicon amplifier, which is essential for future integrated photonic links. In the second part of the dissertation we investigate analogue links based on existing photonic components. In chapter 5 we demonstrate and characterize radio-over-fiber links using heterogeneous silicon photonic components. In chapter 6 we demonstrate a silicon photonic EAM up-converter/transmitter. Chapter 7 reports the development of an Electro-Photonic Frequency Converter. In chapter 8 a conclusion and outlook on future developments is presented.

1.6 Publications and awards

1.6.1 Publications in international journals

K. Van Gasse, J. Verbist, H. Li, G. Torfs, J. Bauwelinck and G. Roelkens, *Silicon Photonics Radio-Over-Fiber Transmitter Using GeSi EAMs for Frequency Up-Conversion*, IEEE Photonics Technology Letters, vol. 31, no. 2, pp. 181-184, 2019
doi: 10.1109/LPT.2018.2889537

G. Muliuk, **K. Van Gasse**, J. Van Kerrebrouck, A. J. Trindade, B. Corbett, D. Van Thourhout, G. Roelkens, *4x25 Gb/s Polarization Diversity Silicon Photonics Receiver With Transfer Printed III-V Photodiodes*, IEEE Photonics Technology Letters, vol. 31, no. 4, pp. 287-290, 2019
doi: 10.1109/LPT.2018.2889901

K. Van Gasse, R. Wang, G. Roelkens, *27 dB gain III-V-on-silicon semiconductor optical amplifier with > 50 mW output power*, Optics Express, vol. 27, no. 1, pp.293-302, 2019

L. Bogaert, **K. Van Gasse**, T. Spuesens, G. Torfs, J. Bauwelinck, G. Roelkens, *Silicon Photonics Traveling Wave Photodiode with Integrated Star Coupler for High-Linearity mmWave Applications*, Optics Express, vol. 26, no. 26, pp. 34753-34765, 2018

K. Van Gasse, L. Bogaert, L. Breyne, J. Van Kerrebrouck, S. Dhoore, C. Op de Beeck, A. Katumba, C.Y. Wu, H. Li, J. Verbist, A. Rahim, A. Abbasi, B. Moeneclaey, Z. Wang, H. Chen, J. Van Campenhout, X. Yin, B. Kuyken, G. Morthier, J. Bauwelinck, G. Torfs, G. Roelkens, *Analog radio-over-fiber transceivers based on III-V-on-silicon photonics*, **(invited)** IEEE Photonics Technology Letters, vol. 30, no. 21, pp. 1818-1821, 2018
doi: 10.1109/LPT.2018.2867930

K. Van Gasse, J. Van Kerrebrouck, A. Abbasi, J. Verbist, G. Torfs, G. Morthier, X. Yin, J. Bauwelinck, G. Roelkens, *III-V-on-Silicon Photonic Transceivers for Radio-over-Fiber links*, Journal of Lightwave Technology, vol. 36, no. 19, pp. 4438-4444, 2018
doi: 10.1109/JLT.2018.2845743

K. Van Gasse, Z. Wang, S. Uvin, B. De Deckere, J. Marien, L. Thomassen, G. Roelkens, *Ka-band to L-band frequency down-conversion based on III-V-on-silicon photonic integrated circuits*, CEAS Space Journal, vol. 9, no. 4,

pp. 531-541, 2017
doi: 10.1007/s12567-017-0179-z

Z. Wang*, **K. Van Gasse***, Valentina Moskalenko, Sylwester Latkowski,
Erwin Bente, B. Kuyken, G. Roelkens, *A III-V-on-Si ultra dense comb laser*,
Light: Science & Applications, vol. 6, no. 5, p.e16260, 2017
*These authors contributed equally.
doi: 10.1038/lsa.2016.260

Z. Wang, A. Abbasi, U.D. Dave, A. De Groote, S. Kumari, B. Kunert, C.
Merckling , M. Pantouvaki, Y. Shi, B. Tian, **K. Van Gasse**, J. Verbist,
R. Wang, W. Xie, J. Zhang, Y. Zhu, J. Bauwelinck, X. Yin, Z. Hens, J.
Van Campenhout, B. Kuyken, R. Baets, G. Morthier, D. Van Thourhout,
G. Roelkens, *Novel light source integration approaches for silicon photonics*,
Laser & Photonics Reviews, vol. 11, no. 4, pp. 1700063-1700084, 2017
doi: 10.1002/lpor.201700063

G. Roelkens, A. Abbasi, P. Cardile, U.D. Dave, A. De Groote, Y. De Kon-
inck, S. Dhoore, X. Fu, A. Gassenq, N. Hattasan, Q. Huang, S. Kumari,
S. Keyvaninia, B. Kuyken, L. Li, P. Mechet, M. Muneeb, D. Sanchez, H.
Shao, T. Spuesens, A. Subramanian, S. Uvin, M. Tassaert, **K. Van Gasse**,
J. Verbist, R. Wang, Z. Wang, J. Zhang, J. Van Campenhout, Y. Xin, J.
Bauwelinck, G. Morthier, R. Baets, D. Van Thourhout, *III-V-on-silicon
photonic devices for optical communication and sensing*, Photonics (**in-
vited**), vol. 2, no. 3, pp. 969-1004, 2015
doi: 10.3390/photonics2030969

1.6.2   Publications in national and international conferences

Abdul Rahim, Amin Abbasi, Mahmoud Shahin, Nuno Sequeira André,
André Richter, Joris Van Kerrebrouck, **Kasper Van Gasse**, Andrew Ka-
tumba, Bart Moeneclaey, Xin Yin, Geert Morthier, Roel Baets, Gunther
Roelkens, *50 Gb/s DMT and 120 Mb/s LTE signal transmission over 5 km
of optical fiber using a silicon photonics transceiver*, Advanced Photonics
Congress, Switzerland, 2018
doi: 10.1364/IPRSN.2018.IW1B.4

K. Van Gasse, Z. Wang, B. De Deckere, G. Roelkens, *Heterogeneous Sili-
con Photonic Devices for Wireless Communication Systems*, 2018 2nd URSI

Atlantic Radio Science Meeting (AT-RASC), **(invited)**, Spain, 2018
doi: 10.23919/URSI-AT-RASC.2018.8471380

G. Muliuk, **K. Van Gasse**, M. Shahin, J. Verbist, A. J. Trindade, B. Corbett, D. Van Thourhout, G. Roelkens, *4x25Gbit/s Silicon Photonics Tunable Receiver using Transfer Printed III-V Photodiodes*, IEEE Photonics Conference, United States, 2018

L. Bogaert, **K. Van Gasse**, G. Torfs, J. Bauwelinck, G. Roelkens, *High-power traveling wave photodetector in silicon photonics with monolithically integrated optical power splitter*, 22nd Annual Symposium of the IEEE Photonics Society Benelux Chapter, Proceedings, Netherlands, p.74-77, 2017

K. Van Gasse, J. Van Kerrebrouck, A. Abbasi, G. Torfs, J. Bauwelinck, G. Roelkens, *16 Gb/s RoF Link at 20 GHz Carrier Frequency using a Silicon Photonics Transmitter and Receiver*, The 2017 International Topical Meeting on Microwave Photonics (MWP 2017), China, pp. 1-4, 2017 doi: 10.1109/MWP.2017.8168728

K. Van Gasse, J. Van Kerrebrouck, A. Abbasi, G. Morthier, J. Bauwelinck, G. Roelkens, *26 GHz Carrier Frequency 10 Gbit/s Radio-over-Fiber Link based on a Directly Modulated III-V/Si DFB Laser*, European Conference on Integrated Optics (ECIO), Netherlands, T3.4, 2017

A. Rahim, A. Abbasi, Nuno Sequeira André, A. Katumba, Hadrien Louchet, **K. Van Gasse**, R. Baets, G. Morthier, G. Roelkens, *69 Gb/s DMT Transmission Using Directly Modulated Heterogeneously Integrated InP-on-Si DFB*, Optical Fiber Communication Conference and Exhibition (OFC) , United States, paper Th1B5, 2017

J. Sarmiento-Merenguel, J. Verbist, **K. Van Gasse**, J. Zhang, B. Moeneclaey, J. Bauwelinck, X. Yin, R. Halir, A. Ortega-Monux, I, Molina-Fernandez, G. Roelkens, *Demonstration of Silicon-on-insulator coherent receiver for radio-over-fiber applications*, European Conference on Integrated Optics (ECIO), Netherlands, p.M7.4, 2017

K. Van Gasse, J. Van Kerrebrouck, A. Abbasi, G. Torfs, H. Chen, X. Yin, J. Bauwelinck, G. Roelkens, *480Mbps/1 Gb/s radio-over-fiber link based on a directly modulated III-V-on-Silicon DFB laser*, IEEE topical meeting on Microwave Photonics 2016, United States, pp.328-331, 2016
doi: 10.1109/MWP.2016.7791272

K. Van Gasse, Z. Wang, S. Uvin, J. Marien, L. Thomassen, G. Roelkens, *Ka-to-L-band frequency down-conversion using a micro-photonic IIIV-on-silicon mode-locked laser and Mach-Zehnder modulator*, International Conference on Space Optics, France, 2016
doi: 10.1117/12.2296159

K. Van Gasse, Z. Wang, V. Moskalenko, S. Latkowski, B. Kuyken, E. Bente, G. Roelkens, *Passively mode-locked III-V-on-silicon laser with 1 GHz repetition rate*, The 25th International conference Semiconductor Laser Conference (ISLC 2016), Japan, paper ThB6 (2 pages), 2016

G. Roelkens, U.D. Dave, S. Keyvaninia, F. Leo, S. Uvin, **K. Van Gasse**, Z. Wang, S. Latkowski, E. Bente, B. Kuyken, *Frequency comb generation in III-V-on-silicon photonic integrated circuits*, Advanced Photonics Congress - IPR, **(invited)**, Canada, paper IM2A.5, 2016
doi: 10.1364/IPRSN.2016.IM2A.5

G. Roelkens, A. Abbasi, S. Keyvaninia, S. Uvin, **K. Van Gasse**, Z. Wang, U.D. Dave, B. Kuyken, G. Morthier, D. Van Thourhout, *III-V-on-silcon photonic integrated circuits for communication and sensing applications*, 28th IEEE Photonics Conference (IPC 2015), **(invited)**, United States, pp.593-594, 2015
doi: 10.1109/IPCon.2015.7323470

G. Roelkens, S. Keyvaninia, Y. De Koninck, S. Uvin, A. Abbasi, **K. Van Gasse**, Z. Wang, G. Morthier, D. Van Thourhout, R. Baets, *III-V-on-silicon photonic integrated circuits for optical interconnects*, IEEE Summer Topicals, **(invited)**, Bahamas, paper TuC2.1, 2015
doi: 10.1109/PHOSST.2015.7248237

1.6.3 Awards

Best student paper award honorable mention
International Semiconductor Laser Conference (ISLC 2016)
12-15 September 2016, Kobe, Japan
For the paper: K. Van Gasse, Z. Wang, V. Moskalenko, S. Latkowski, B. Kuyken, E. Bente, G. Roelkens,
"Passively mode-locked III-V-on-silicon laser with 1 GHz repetition rate,"
The 25th International conference Semiconductor Laser Conference (ISLC 2016), Japan, ThB6 (2 pages), 2016

References

[1] P. Dong, W. Qian, S. Liao, H. Liang, C.-C. Kung, N.-N. Feng, R. Shafi-iha, J. Fong, D. Feng, A. V. Krishnamoorthy, and M. Asghari. *Low loss shallow-ridge silicon waveguides.* Optics Express, 18(14):14474, jul 2010.

[2] M. Tran, D. Huang, T. Komljenovic, J. Peters, A. Malik, and J. Bowers. *Ultra-Low-Loss Silicon Waveguides for Heterogeneously Integrated Silicon/III-V Photonics.* Applied Sciences, 8(7):1139, jul 2018.

[3] G. Roelkens, D. Vermeulen, S. Selvaraja, R. Halir, W. Bogaerts, and D. Van Thourhout. *Grating-Based Optical Fiber Interfaces for Silicon-on-Insulator Photonic Integrated Circuits.* IEEE Journal of Selected Topics in Quantum Electronics, 17(3):571–580, may 2011.

[4] W. Bogaerts, P. De Heyn, T. Van Vaerenbergh, K. De Vos, S. Kumar Selvaraja, T. Claes, P. Dumon, P. Bienstman, D. Van Thourhout, and R. Baets. *Silicon microring resonators.* Laser & Photonics Reviews, 6(1):47–73, jan 2012.

[5] S. Dwivedi, A. Ruocco, M. Vanslembrouck, T. Spuesens, P. Bienstman, P. Dumon, T. Van Vaerenbergh, and W. Bogaerts. *Experimental Extraction of Effective Refractive Index and Thermo-Optic Coefficients of Silicon-on-Insulator Waveguides Using Interferometers.* Journal of Lightwave Technology, 33(21):4471–4477, nov 2015.

[6] M. Piekarek, D. Bonneau, S. Miki, T. Yamashita, M. Fujiwara, M. Sasaki, H. Terai, M. G. Tanner, C. M. Natarajan, R. H. Hadfield, J. L. O'Brien, and M. G. Thompson. *High-extinction ratio integrated photonic filters for silicon quantum photonics.* Optics Letters, 42(4):815, feb 2017.

[7] M. Gehl, D. Trotter, A. Starbuck, A. Pomerene, A. L. Lentine, and C. DeRose. *Active phase correction of high resolution silicon photonic arrayed waveguide gratings.* Optics Express, 25(6):6320, mar 2017.

[8] H. Chen, M. Galili, P. Verheyen, P. De Heyn, G. Lepage, J. De Coster, S. Balakrishnan, P. Absil, L. Oxenlowe, J. Van Campenhout, and G. Roelkens. *100-Gbps RZ Data Reception in 67-GHz Si-Contacted Germanium Waveguide p-i-n Photodetectors.* Journal of Lightwave Technology, 35(4):722–726, feb 2017.

[9] J. Verbist, M. Verplaetse, S. A. Srinivasan, J. Van Kerrebrouck, P. De Heyn, P. Absil, T. De Keulenaer, R. Pierco, A. Vyncke, G. Torfs,

X. Yin, G. Roelkens, J. Van Campenhout, and J. Bauwelinck. *Real-Time 100 Gb/s NRZ and EDB Transmission With a GeSi Electroabsorption Modulator for Short-Reach Optical Interconnects.* Journal of Lightwave Technology, 36(1):90–96, jan 2018.

[10] J. Verbist, J. Lambrecht, M. Verplaetse, S. A. Srinivasan, P. De Heyn, T. De Keulenaer, R. Pierco, A. Vyncke, J. Van Campenhout, X. Yin, J. Bauwelinck, G. Torfs, and G. Roelkens. *Real-Time and DSP-free 128 Gb/s PAM-4 Link using a Binary Driven Silicon Photonic Transmitter.* Journal of Lightwave Technology, pages 1–1, 2018.

[11] Q. Xu, S. Manipatruni, B. Schmidt, J. Shakya, and M. Lipson. *125 Gbit/s carrier-injection-based silicon micro-ring silicon modulators.* Optics Express, 15(2):430, jan 2007.

[12] W. M. Green, M. J. Rooks, L. Sekaric, and Y. A. Vlasov. *Ultra-compact, low RF power, 10 Gb/s silicon Mach-Zehnder modulator.* Optics Express, 15(25):17106, 2007.

[13] D. Patel, S. Ghosh, M. Chagnon, A. Samani, V. Veerasubramanian, M. Osman, and D. V. Plant. *Design, analysis, and transmission system performance of a 41 GHz silicon photonic modulator.* Optics Express, 23(11):14263, jun 2015.

[14] H. Ramon, M. Vanhoecke, J. Verbist, W. Soenen, P. De Heyn, Y. Ban, M. Pantouvaki, J. Van Campenhout, P. Ossieur, X. Yin, and J. Bauwelinck. *Low-Power 56Gb/s NRZ Microring Modulator Driver in 28nm FDSOI CMOS.* IEEE Photonics Technology Letters, 30(5):467–470, mar 2018.

[15] M. Vanhoecke, A. Aimone, N. Argyris, S. Dris, R. Vaernewyck, K. Verheyen, M. Gruner, G. Fiol, D. Apostolopoulos, H. Avramopoulos, G. Torfs, X. Yin, and J. Bauwelinck. *Segmented Optical Transmitter Comprising a CMOS Driver Array and an InP IQ-MZM for Advanced Modulation Formats.* Journal of Lightwave Technology, 35(4):862–867, feb 2017.

[16] M. Smit, X. Leijtens, H. Ambrosius, E. Bente, J. van der Tol, B. Smalbrugge, T. de Vries, E.-J. Geluk, J. Bolk, R. van Veldhoven, L. Augustin, P. Thijs, D. D'Agostino, H. Rabbani, K. Lawniczuk, S. Stopinski, S. Tahvili, A. Corradi, E. Kleijn, D. Dzibrou, M. Felicetti, E. Bitincka, V. Moskalenko, J. Zhao, R. Santos, G. Gilardi, W. Yao, K. Williams, P. Stabile, P. Kuindersma, J. Pello, S. Bhat, Y. Jiao, D. Heiss, G. Roelkens, M. Wale, P. Firth, F. Soares, N. Grote,

M. Schell, H. Debregeas, M. Achouche, J.-L. Gentner, A. Bakker, T. Korthorst, D. Gallagher, A. Dabbs, A. Melloni, F. Morichetti, D. Melati, A. Wonfor, R. Penty, R. Broeke, B. Musk, and D. Robbins. *An introduction to InP-based generic integration technology.* Semiconductor Science and Technology, 29(8):83001, 2014.

[17] L. M. Augustin, R. Santos, E. den Haan, S. Kleijn, P. J. A. Thijs, S. Latkowski, D. Zhao, W. Yao, J. Bolk, H. Ambrosius, S. Mingaleev, A. Richter, A. Bakker, and T. Korthorst. *InP-Based Generic Foundry Platform for Photonic Integrated Circuits.* IEEE Journal of Selected Topics in Quantum Electronics, 24(1):1–10, jan 2018.

[18] S. Andreou, K. A. Williams, and E. A. J. M. Bente. *An InP-Based DBR Laser with an Intra-Cavity Ring Resonator with 130 kHz Linewidth and 65 dB SMSR.* In 2018 IEEE International Semiconductor Laser Conference (ISLC), pages 1–2. IEEE, sep 2018.

[19] S. Latkowski, A. Hansel, N. Bhattacharya, T. de Vries, L. Augustin, K. Williams, M. Smit, and E. Bente. *Novel Widely Tunable Monolithically Integrated Laser Source.* IEEE Photonics Journal, 7(6):1–9, dec 2015.

[20] S. Latkowski, A. Hänsel, P. J. van Veldhoven, D. D'Agostino, H. Rabbani-Haghighi, B. Docter, N. Bhattacharya, P. J. A. Thijs, H. P. M. M. Ambrosius, M. K. Smit, K. A. Williams, and E. A. J. M. Bente. *Monolithically integrated widely tunable laser source operating at 2 μm.* Optica, 3(12):1412, dec 2016.

[21] S. Lange, S. Wolf, J. Lutz, L. Altenhain, R. Schmid, R. Kaiser, M. Schell, C. Koos, and S. Randel. *100 GBd Intensity Modulation and Direct Detection With an InP-Based Monolithic DFB Laser MachZehnder Modulator.* Journal of Lightwave Technology, 36(1):97–102, jan 2018.

[22] K. Balakier, H. Shams, M. J. Fice, L. Ponnampalam, C. S. Graham, C. C. Renaud, and A. J. Seeds. *Optical Phase Lock Loop as High-Quality Tuneable Filter for Optical Frequency Comb Line Selection.* Journal of Lightwave Technology, 36(19):4646–4654, oct 2018.

[23] J. J. G. M. van der Tol, Y. Jiao, L. Shen, A. Millan-Mejia, V. Pogoretskii, J. P. van Engelen, and M. K. Smit. *Indium Phosphide Integrated Photonics in Membranes.* IEEE Journal of Selected Topics in Quantum Electronics, 24(1):1–9, jan 2018.

[24] B. Stern, X. Ji, A. Dutt, and M. Lipson. *Compact narrow-linewidth integrated laser based on a low-loss silicon nitride ring resonator.* Optics Letters, 42(21):4541, nov 2017.

[25] Z. Wang, B. Tian, M. Pantouvaki, W. Guo, P. Absil, J. Van Campenhout, C. Merckling, and D. Van Thourhout. *Room-temperature InP distributed feedback laser array directly grown on silicon.* Nature Photonics, 9(12):837–842, dec 2015.

[26] Z. Wang, K. Van Gasse, V. Moskalenko, S. Latkowski, E. Bente, B. Kuyken, and G. Roelkens. *A III-V-on-Si ultra-dense comb laser.* Light: Science & Applications, 6(5):e16260, may 2017.

[27] Y. Fan, J. P. Epping, R. M. Oldenbeuving, C. G. H. Roeloffzen, M. Hoekman, R. Dekker, R. G. Heideman, P. J. M. van der Slot, and K.-J. Boller. *Optically Integrated InPSi$_3$ N$_4$ Hybrid Laser.* IEEE Photonics Journal, 8(6):1–11, dec 2016.

[28] A. Y. Liu and J. Bowers. *Photonic Integration With Epitaxial IIIV on Silicon.* IEEE Journal of Selected Topics in Quantum Electronics, 24(6):1–12, nov 2018.

[29] Y. Shi, Z. Wang, J. Van Campenhout, M. Pantouvaki, W. Guo, B. Kunert, and D. Van Thourhout. *Optical pumped InGaAs/GaAs nano-ridge laser epitaxially grown on a standard 300-mm Si wafer.* Optica, 4(12):1468, dec 2017.

[30] T. Komljenovic, D. Huang, P. Pintus, M. A. Tran, M. L. Davenport, and J. E. Bowers. *Photonic Integrated Circuits Using Heterogeneous Integration on Silicon.* Proceedings of the IEEE, 106(12):2246–2257, dec 2018.

[31] G. Roelkens, A. Abassi, P. Cardile, U. Dave, A. de Groote, Y. de Koninck, S. Dhoore, X. Fu, A. Gassenq, N. Hattasan, Q. Huang, S. Kumari, S. Keyvaninia, B. Kuyken, L. Li, P. Mechet, M. Muneeb, D. Sanchez, H. Shao, T. Spuesens, A. Subramanian, S. Uvin, M. Tassaert, K. van Gasse, J. Verbist, R. Wang, Z. Wang, J. Zhang, J. van Campenhout, X. Yin, J. Bauwelinck, G. Morthier, R. Baets, and D. van Thourhout. *III-V-on-Silicon Photonic Devices for Optical Communication and Sensing.* Photonics, 2(3):969–1004, sep 2015.

[32] Z. Wang, A. Abbasi, U. Dave, A. De Groote, S. Kumari, B. Kunert, C. Merckling, M. Pantouvaki, Y. Shi, B. Tian, K. Van Gasse, J. Verbist, R. Wang, W. Xie, J. Zhang, Y. Zhu, J. Bauwelinck, X. Yin, Z. Hens, J. Van Campenhout, B. Kuyken, R. Baets, G. Morthier,

D. Van Thourhout, and G. Roelkens. *Novel Light Source Integration Approaches for Silicon Photonics.* Laser & Photonics Reviews, 11(4):1700063, jul 2017.

[33] L. Sanchez, F. Fournel, B. Montmayeul, L. Bally, B. Szelag, and L. Adelmini. *Collective Die Direct Bonding for Photonic on Silicon.* ECS Transactions, 86(5):223–231, jul 2018.

[34] X. Luo, Y. Cheng, J. Song, T.-Y. Liow, Q. J. Wang, and M. Yu. *Wafer-Scale Dies-Transfer Bonding Technology for Hybrid III/V-on-Silicon Photonic Integrated Circuit Application.* IEEE Journal of Selected Topics in Quantum Electronics, 22(6):443–454, nov 2016.

[35] T. Komljenovic, S. Srinivasan, E. Norberg, M. Davenport, G. Fish, and J. E. Bowers. *Widely Tunable Narrow-Linewidth Monolithically Integrated External-Cavity Semiconductor Lasers.* IEEE Journal of Selected Topics in Quantum Electronics, 21(6):214–222, nov 2015.

[36] A. Abbasi, B. Moeneclaey, J. Verbist, X. Yin, J. Bauwelinck, G.-H. Duan, G. Roelkens, and G. Morthier. *Direct and Electroabsorption Modulation of a IIIV-on-Silicon DFB Laser at 56 Gb/s.* IEEE Journal of Selected Topics in Quantum Electronics, 23(6):1–7, nov 2017.

[37] A. Abbasi, J. Verbist, L. A. Shiramin, M. Verplaetse, T. De Keulenaer, R. Vaernewyck, R. Pierco, A. Vyncke, X. Yin, G. Torfs, G. Morthier, J. Bauwelinck, and G. Roelkens. *100-Gb/s Electro-Absorptive Duobinary Modulation of an InP-on-Si DFB Laser.* IEEE Photonics Technology Letters, 30(12):1095–1098, jun 2018.

[38] C. Zhang, P. A. Morton, J. B. Khurgin, J. D. Peters, and J. E. Bowers. *Ultralinear heterogeneously integrated ring-assisted MachZehnder interferometer modulator on silicon.* Optica, 3(12):1483, dec 2016.

[39] R. Wang, S. Sprengel, G. Boehm, R. Baets, M.-C. Amann, and G. Roelkens. *Broad wavelength coverage 23 μm III-V-on-silicon DFB laser array.* Optica, 4(8):972, aug 2017.

[40] A. Spott, E. J. Stanton, A. Torres, M. L. Davenport, C. L. Canedy, I. Vurgaftman, M. Kim, C. S. Kim, C. D. Merritt, W. W. Bewley, J. R. Meyer, and J. E. Bowers. *Interband cascade laser on silicon.* Optica, 5(8):996, aug 2018.

[41] S. Keyvaninia, S. Uvin, M. Tassaert, Z. Wang, X. Fu, S. Latkowski, J. Marien, L. Thomassen, F. Lelarge, G. Duan, and Others. *III–V-on-silicon anti-colliding pulse-type mode-locked laser.* Optics letters, 40(13):3057–3060, 2015.

[42] H.-W. Chen, J. D. Peters, and J. E. Bowers. *Forty Gb/s hybrid silicon Mach-Zehnder modulator with low chirp.* Optics Express, 19(2):1455, jan 2011.

[43] C. Zhang, P. A. Morton, J. B. Khurgin, J. D. Peters, and J. E. Bowers. *Highly linear heterogeneous-integrated Mach-Zehnder interferometer modulators on Si.* Optics Express, 24(17):19040, aug 2016.

[44] A. J. Seeds and K. J. Williams. *Microwave Photonics.* Journal of Lightwave Technology, 24(12):4628–4641, dec 2006.

[45] C. Cox, E. Ackerman, G. Betts, and J. Prince. *Limits on the performance of RF-over-fiber links and their impact on device design.* IEEE Transactions on Microwave Theory and Techniques, 54(2):906–920, feb 2006.

[46] J. Bohata, M. Komanec, J. Spáčil, Z. Ghassemlooy, S. Zvánovec, and R. Slavík. *2426 GHz radio-over-fiber and free-space optics for fifth-generation systems.* Optics Letters, 43(5):1035, mar 2018.

[47] G. Gopalakrishnan, W. Burns, and C. Bulmer. *Microwave-optical mixing in LiNbO/sub 3/ modulators.* IEEE Transactions on Microwave Theory and Techniques, 41(12):2383–2391, 1993.

[48] E. H. W. Chan and R. A. Minasian. *Microwave photonic downconverter with high conversion efficiency.* Journal of Lightwave Technology, 30(23):3580–3585, 2012.

[49] B. M. Haas and J. D. McKinney. *Characterization of a Downconverting, Phase-Modulated RF-Over-Fiber Link With a Single Modulator.* IEEE Photonics Journal, 10(4):1–7, 2018.

[50] Y. Wang, J. Li, T. Zhou, D. Wang, J. Xu, X. Zhong, D. Yang, and L. Rong. *All-Optical Microwave Photonic Downconverter With Tunable Phase Shift.* IEEE Photonics Journal, 9(6):1–8, dec 2017.

[51] T. Li, E. H. W. Chan, X. Wang, X. Feng, B.-O. Guan, and J. Yao. *Broadband Photonic Microwave Signal Processor With Frequency Up-/Down Conversion and Phase Shifting Capability.* IEEE Photonics Journal, 10(1):1–12, feb 2018.

[52] T. Jiang, R. Wu, S. Yu, D. Wang, and W. Gu. *Microwave photonic phase-tunable mixer.* Optics Express, 25(4):4519, feb 2017.

[53] W. Zhai, A. Wen, W. Zhang, Z. Tu, H. Zhang, and Z. Xiu. *A Multi-channel Phase Tunable Microwave Photonic Mixer With High Conversion Gain and Elimination of Dispersion-Induced Power Fading.* IEEE Photonics Journal, 10(1):1–10, feb 2018.

[54] Y. Gao, A. Wen, X. Wu, Y. Wang, and H. Zhang. *Efficient Photonic Microwave Mixer With Compensation of the Chromatic Dispersion-Induced Power Fading.* Journal of Lightwave Technology, 34(14):3440–3448, jul 2016.

[55] C. S. Park, C. K. Oh, C. G. Lee, D.-H. Kim, and C.-S. Park. *A photonic up-converter for a WDM radio-over-fiber system using cross-absorption modulation in an EAM.* IEEE photonics technology letters, 17(9):1950–1952, 2005.

[56] O. Lelievre, V. Crozatier, P. Berger, G. Baili, O. Llopis, D. Dolfi, P. Nouchi, F. Goldfarb, F. Bretenaker, L. Morvan, and G. Pillet. *A Model for Designing Ultralow Noise Single- and Dual-Loop 10-GHz Optoelectronic Oscillators.* Journal of Lightwave Technology, 35(20):4366–4374, oct 2017.

[57] X. Xie, R. Bouchand, D. Nicolodi, M. Giunta, W. Hänsel, M. Lezius, A. Joshi, S. Datta, C. Alexandre, M. Lours, P.-A. Tremblin, G. Santarelli, R. Holzwarth, and Y. Le Coq. *Photonic microwave signals with zeptosecond-level absolute timing noise.* Nature Photonics, 11(1):44–47, jan 2017.

[58] P. Ghelfi, F. Laghezza, F. Scotti, G. Serafino, A. Capria, S. Pinna, D. Onori, C. Porzi, M. Scaffardi, A. Malacarne, V. Vercesi, E. Lazzeri, F. Berizzi, and A. Bogoni. *A fully photonics-based coherent radar system.* Nature, 507(7492):341–345, 2014.

[59] D. Marpaung, J. Yao, and J. Capmany. *New opportunities for integrated microwave photonics.* arXiv preprint arXiv:1810.02585, 2018.

[60] D. Marpaung, C. Roeloffzen, R. Heideman, A. Leinse, S. Sales, and J. Capmany. *Integrated microwave photonics.* Laser & Photonics Reviews, 7(4):506–538, jul 2013.

[61] W. Zhang and J. Yao. *A fully reconfigurable waveguide Bragg grating for programmable photonic signal processing.* Nature communications, 9(1):1396, 2018.

[62] D. Pérez, I. Gasulla, L. Crudgington, D. J. Thomson, A. Z. Khokhar, K. Li, W. Cao, G. Z. Mashanovich, and J. Capmany. *Multipurpose silicon photonics signal processor core.* Nature communications, 8(1):636, 2017.

[63] Y. Xie, Z. Geng, L. Zhuang, M. Burla, C. Taddei, M. Hoekman, A. Leinse, C. G. H. Roeloffzen, K.-J. Boller, and A. J. Lowery. *Programmable optical processor chips: toward photonic RF filters with DSP-level flexibility and MHz-band selectivity.* Nanophotonics, 7(2):421–454, 2017.

[64] L. Zhuang, C. G. H. Roeloffzen, M. Hoekman, K.-J. Boller, and A. J. Lowery. *Programmable photonic signal processor chip for radiofrequency applications.* Optica, 2(10):854, oct 2015.

[65] J. S. Fandiño, P. Muñoz, D. Doménech, and J. Capmany. *A monolithic integrated photonic microwave filter.* Nature Photonics, 11:124, dec 2016.

[66] S. Jin, L. Xu, V. Rosborough, J. Klamkin, and Y. Li. *RF Frequency Mixer Photonic Integrated Circuit.* IEEE Photonics Technology Letters, 28(16):1771–1773, aug 2016.

[67] W. Zhang and J. Yao. *Silicon Photonic Integrated Optoelectronic Oscillator for Frequency-Tunable Microwave Generation.* Journal of Lightwave Technology, 2018.

[68] J. Hulme, M. J. Kennedy, R.-L. Chao, L. Liang, T. Komljenovic, J.-W. Shi, B. Szafraniec, D. Baney, and J. E. Bowers. *Fully Integrated Microwave Frequency Synthesizer On Heterogeneous Silicon-III/V.* Opt. Express, 25(3):2422–2431, feb 2017.

[69] R.-L. Chao, L. Liang, J.-W. Shi, T. Komljenovic, J. Hulme, M. J. Kennedy, and J. E. Bowers. *Fully Integrated Photonic Millimeter-Wave Tracking Generators on the Heterogeneous IIIV/Si Platform.* IEEE Photonics Technology Letters, 30(10):919–922, may 2018.

Chapter 2

III-V-on-silicon mode-locked laser

In this chapter we describe the detailed characterization of an integrated III-V-on-silicon mode-locked laser and compare it with state-of-the-art integrated devices. This chapter has been in part published in [1].

2.1 Introduction

Pulsed lasers have become an important component in many branches of science. Although several types of pulsed lasers exist, mode-locked lasers can provide extremely short pulses unachievable using other methods. In a mode-locked laser, short pulses are created by the enforced phase coherence between the different optical modes. The repetition rate of the pulses is determined by the frequency spacing between the locked optical modes. The duration of the pulses becomes shorter as the amount of modes increases. Therefore, very short pulsed lasers have a wide optical spectrum consisting of many equidistant optical modes. Consequently, such a laser can be used as a sort of optical ruler or optical frequency comb. Using an optical frequency comb allowed to perform laser-based spectroscopy with unprecedented precision. This achievement was awarded with the Nobel prize in physics in 2005 [2]. Not only can a mode-locked laser generate a very precise ruler in the frequency domain, it produces an optical pulse train with extreme stability in the time domain. If a photodiode is illuminated with the light of such a laser, very pure microwave signals with frequencies corresponding to integer multiples of the pulse repetition rate are produced. Forming a link between the microwave and optical domain, mode-locked lasers have many applications in microwave photonics. For example, the
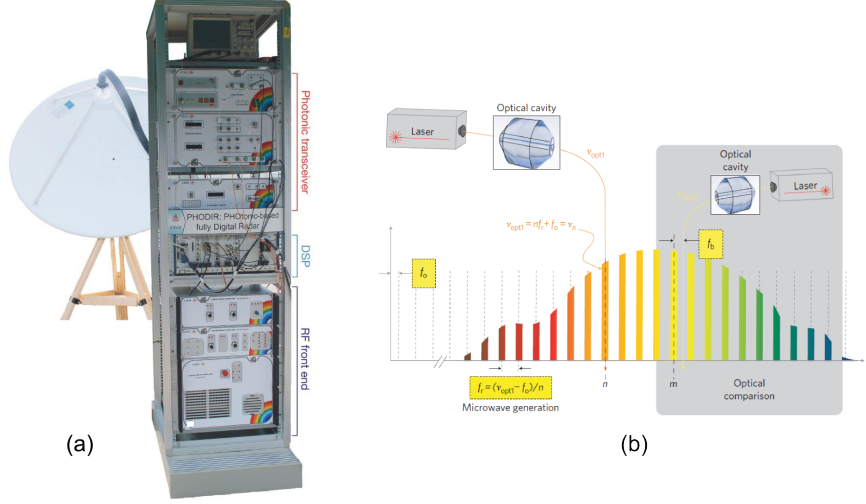
Figure 2.1: (a) Photograph of the mode-locked laser-based photonic coherent radar system [3]. (b) Schematic of ultra-stable microwave signal generation based on the optical frequency division of an ultra-stable laser and mode-locked laser [4].

low timing-jitter pulse train of a commercial mode-locked laser was used to realize a high-performance flexible photonic radar system [3]. In this radar system the mode-locked laser was used for both microwave signal generation and for optical sampling in a photonic ADC. A photograph of the radar set-up is shown in Fig. 2.1(a). Free-running fiber mode-locked lasers can produce extremely stable pulse trains with a timing jitter on the order of 1-10 fs [5]. They can therefore be used to generate extremely stable and low-phase noise microwave signals. Combining such a fiber laser with an advanced phase-detection scheme, microwave generation with sub-femtosecond integrated timing jitter was demonstrated [6]. Some of the most pure and stable microwave signals have been generated using the optical frequency division technique [4, 7]. In this technique a mode-locked laser is used to transfer the fractional frequency stability of an ultra-stable laser to the microwave domain. A schematic overview of the optical frequency division scheme demonstrated in [4] is shown in Fig. 2.1(b). However, the use of a stable optical pulse-train is not limited to sampling in photonic ADCs or microwave signal generation. By combining a mode-locked laser with a high-speed electro-optic modulator, wide-bandwidth and flexible microwave photonic frequency conversion can be achieved. For example, microwave photonic frequency down-conversion was achieved by optically down-sampling a Gaussian minimum-shift keying signal on a 40 GHz carrier with a Er-fiber laser [8]. Furthermore, by combining mode-locked lasers with a dispersive

medium microwave photonic filters can be realized [9]. Finally, they have also enabled the development of photonic RF channelizers [10, 11].

Most of the aforementioned applications rely on bulky and expensive solid-state-based or fiber-based mode-locked lasers. However, most future real-world applications require a compact and scalable pulsed laser source. Integrated semiconductor mode-locked lasers provide an appealing solution to this issue. Several integrated mode-locked lasers have been realized in InP technology and have seen remarkable progress in the past decade [12–19]. Both all-active and active-passive devices have been able to provide impressive results such as sub-picosecond pulses [16, 20]. Integrated semiconductor mode-locked lasers have already seen applications within microwave photonics. For example, a quantum-dash laser was used for the simultaneous microwave up-conversion and Radio-over-Fiber transmission of an OFDM signal [21]. Although all-InP devices have shown great performance, their performance could be further improved by the integration of very low-loss passive waveguides. Several promising devices were realized in III-V-on-silicon, using low-loss silicon waveguides to create an on-chip external cavity [22–24]. Furthermore, a hybrid silicon photonic mode-locked laser was used for the development of a wide-band receiver in an advanced photonic analogue link [25]. A recent extensive review of integrated semiconductor mode-locked lasers can be found in [24].

2.2 Low repetition rate III-V-on-silicon mode-locked laser

However, integrated mode-locked lasers are still far from rivaling their solid-state-based and fiber-based laser counter parts in terms of pulse duration and timing jitter. Consequently the search for methods to improve the timing jitter of on-chip lasers has received much attention. Recently a III-V-on-silicon mode-locked laser with tunable on-chip optical feedback was demonstrated [26]. It was found that using a on-chip delay line with reflector, which serves as optical feedback, could substantially improve the performance of the laser. Since the timing jitter of a pulsed laser defines the quality of the generated microwave signals, low jitter is essential for microwave photonic applications. Although the use of an on-chip optical feedback can improve the laser performance it also increases the footprint and complexity of the device. It is therefore interesting to develop an on-chip mode-locked laser with a very long passive cavity, which translates in a low repetition rate. If a higher repetition rate is wanted, an on-chip pulse-interleaver can be used to create a higher repetition rate pulse train while maintaining the intrinsic qualities of the low-repetition rate laser [27].

To create such a low repetition rate laser, low-loss silicon waveguides are ideally suited. Leveraging the advantages of silicon photonics we designed and fabricated a laser with a record low repetition rate of 1 GHz.

In the rest of this chapter we give a detailed description of the design and implementation of the laser using III-V-on-silicon technology. This is followed by the characterization of the laser when passively mode-locked, i.e. no RF reference is used. We measure the optical spectrum, RF spectrum and the auto-correlation trace of the pulse. A similar study is carried out for hybrid mode-locked operation.

2.3   Implementation

The schematic design of the MLL is shown in Fig. 2.2(a) and Fig. 2.2(b). It consists of a long silicon spiral waveguide, two optical amplifiers (one of which acts as an amplifying spot-size converter to couple the light from the laser into an external silicon waveguide circuit) that are separated by a saturable absorber, and two distributed Bragg reflectors (DBRs), which form the mirrors of the cavity. As shown in Fig. 2.2(a) and (b), by implementing the saturable absorber (SA) above the output DBR reflector, the MLL works in an anti-colliding pulse mode, which promises higher output power, lower timing jitter, and better RF spectral purity [28, 29] than a colliding-pulse MLL. Both optical amplifiers and saturable absorber are realized by heterogeneously integrating an InGaAsP-based multi-quantum well (MQW) epitaxial stack on top of a 400-nm silicon waveguide layer. The details of the epitaxial layer stack can be found in reference [23] and in Chapter 4 which is fully dedicated to III-V-on-silicon semiconductor optical amplifiers (SOAs). A more detailed description of the heterogeneous integration process based on adhesive die-to-wafer bonding can be found in reference [30] and Chapter 4. The device processing was carried out by Dr. Zhechao Wang, while the author took the lead in the design and characterization of the devices. This work was carried out in close collaboration with Dr. Sylwester Latkowski at Eindhoven University of technology. The total length of the optical amplifier is 800 μm, and a 40-μm-long SA is isolated from the amplifier by two 15-μm wide electrically isolating slots in the p-contact layer. Because of the low loss of the passive SOI waveguide ($\approx$0.7 dB cm^{-1}), we can implement a long passive cavity with a length of 37.4 mm, which permits the 1 GHz repetition rate.
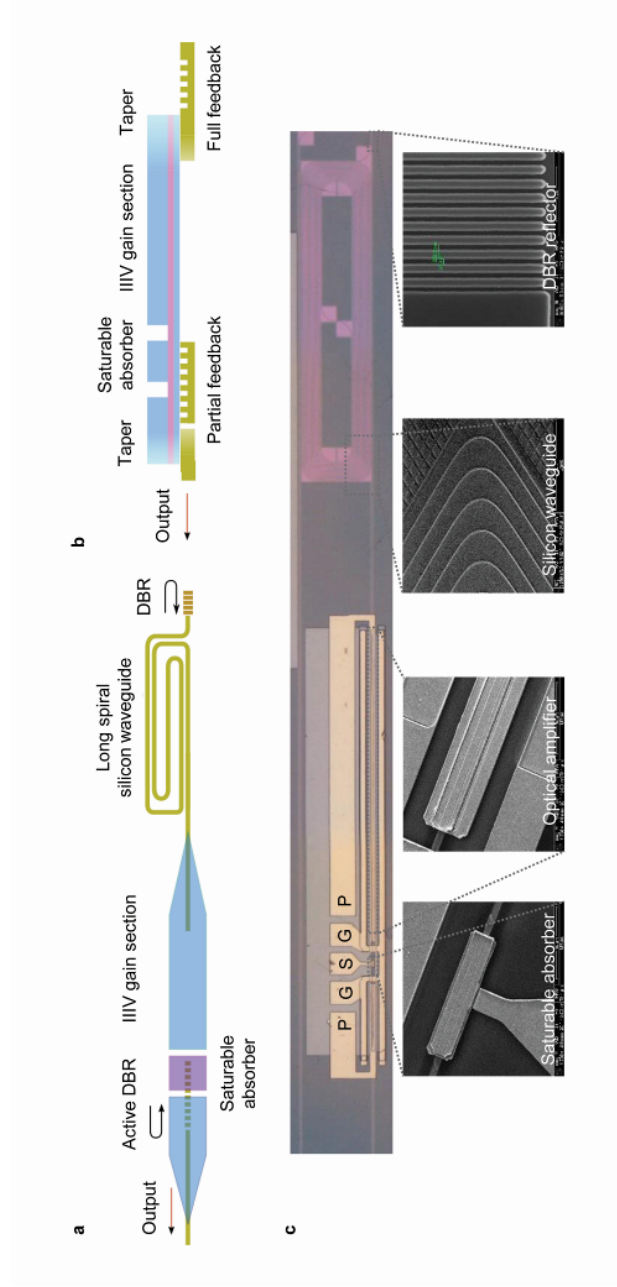
Figure 2.2: (a) Top and (b) side views of the anti-colliding pulse mode-locked laser design. (c) Microscope image of the III-V-on-Si mode-locked laser. The dimensions of the laser are 2.5 mm (saturable absorber to DBR reflector) by 0.3 mm (spiral height). Insets: Scanning electron microscope images of various constituent parts of the laser.
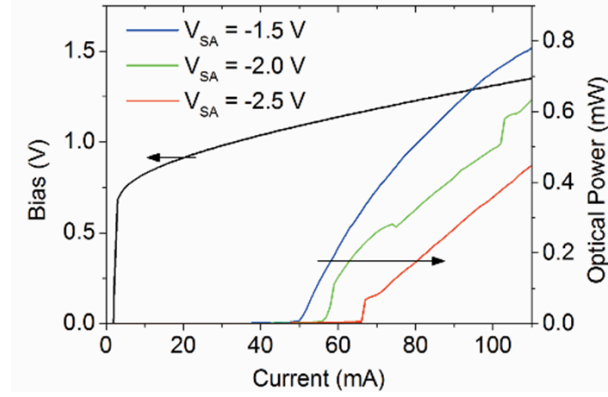
Figure 2.3: Measured Current-Voltage (IV) curve and Light-Current (LI) curves for different SA bias.

2.4   Characterization

The laser characterization results were obtained with the sample on a temperature controlled chuck, which maintained the laser substrate at 20 ^{o}C. The coupling to single-mode optical fiber was realized using a fiber-to-chip grating coupler with a coupling loss of 10 dB. The measured IV and LI curves at different SA bias are plotted in Fig. 2.3. The kinks in the LI curves are attributed to the parasitic reflections from the grating coupler. Because of the low-loss silicon waveguide, a relatively low threshold current (< 60 mA) was achieved even when the SA was under reverse bias.

2.4.1   Passively mode-locked operation

The passive mode-locking operation occurs at an SA bias lower than -2 V. As an example, Fig. 2.4 shows the evolution of the optical spectrum as a function of the injection current of the optical amplifier. Here, the SA was biased at -2.6 V. At this reverse bias, the laser output spectrum was broad even when the device was biased just above treshold. When the current increased, the 3-dB bandwidth of the spectrum significantly broadened and reached a maximum of 10 nm. In Fig 2.5 a map of the optical spectra as a function of the injection current and SA bias is shown. Because the optical spectrum is not always notably flat, it is more practical to measure the 10 dB optical bandwidth [15, 31].

As observed, over a large operation window, the MLL generates a broad optical spectrum of more than 10 nm wide with a maximum bandwidth of 15.8 nm. In the case of a quantum-well semiconductor MLL, the comb span
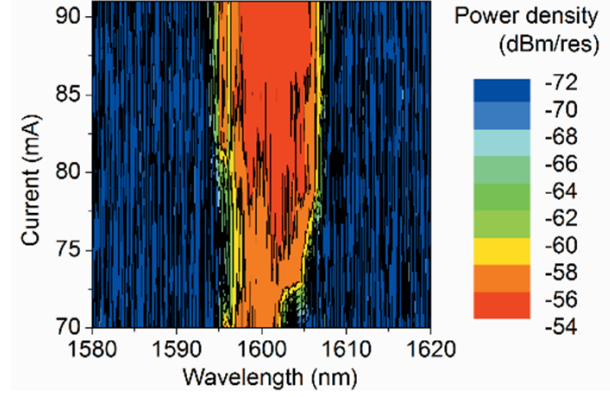
Figure 2.4: Measured optical spectra as a function of current injected in the gain sections, when the SA is biased at -2.6 V.
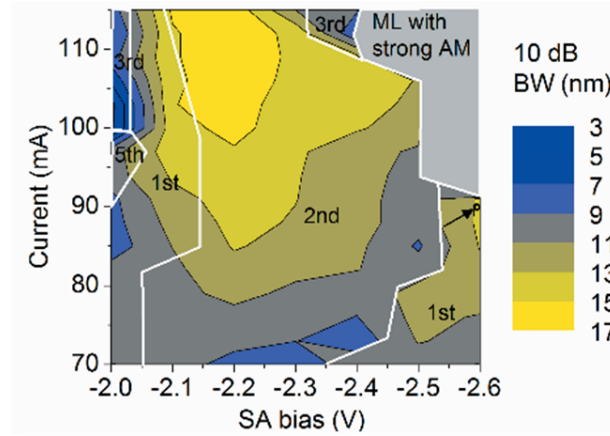
Figure 2.5: Mapping of 10-dB optical bandwidth for different current injection of the optical amplifiers and SA bias. ML: mode-locking. AM: amplitude modulation. Different harmonic mode-locking regions are marked. The black dot indicates the optimal operating point for 1 GHz laser operation.

is mainly determined by the cavity dispersion and gain competition among different optical modes. To broaden the comb span, one may use quantum-dot (QD) or quantum-dash materials, which can provide a broader gain spectrum and suffer less from gain competition. For quantum-well materials, by incorporating an intra-cavity filter to equalize the threshold gain of different longitudinal modes, it is possible to reduce the gain competition between optical modes, and a much wider comb span can be expected [32, 33]. Nonlinear processes in the laser cavity, such as self-phase modulation, can
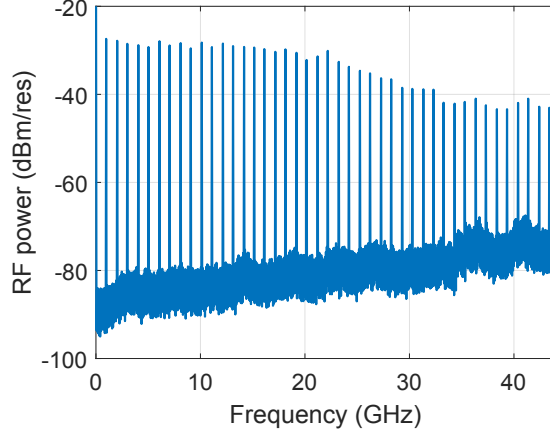
Figure 2.6: RF spectrum of the generated pulse train (RBW 300 kHz, VBW 10 kHz) when the laser is operated at the optimal operation point of Fig 2.5.

also be used to extend the bandwidth [34]. The waveguide dispersion of the current MLL design was not compensated (see more details on the dispersion characterization below). Further optimization of the cavity dispersion can further broaden the comb span.

In Fig. 2.5, different operation regions for different harmonic mode-locking orders are also marked. In a large operation window, the laser is mostly mode-locked at the second harmonic order, that is, with a repetition rate of 2 GHz. The laser can even operate at higher harmonic orders (3rd and 5th) when the injection current is high and the reverse bias is relatively low (Fig. 2.5). When both injection current and reverse bias are large, the lasing spectra significantly shifts to shorter wavelengths, and notably strong amplitude modulations (AM) are found to considerably degrade the mode-locking stability. Fundamental mode-locking occurs only when the injection current is low and the SA reverse bias is high (see the right-bottom corner of Fig. 2.5). Although the laser can be mode-locked at its fundamental repetition rate when the SA is biased at approximately 2 V, modulation on top of the RF spectra occurs because of the relaxation oscillation of the laser. Therefore, in the remainder of this chapter we will focus on the optimal operation point as indicated by the black dot in Fig. 2.5.

In Fig. 2.6 the RF spectrum generated by a photodiode illuminated by the optical pulse train at the optimal laser-operation point is shown (I_{gain}=91 mA, V_{SA}=2.6 V, indicated by the dot in Fig. 2.5) The strong fundamental tone is 55 dB above any spurious peaks or noise floor and indicates that there is notably little residual amplitude modulation of the pulse

train. A more detailed plot of the fundamental tone is shown in Fig 2.7. It
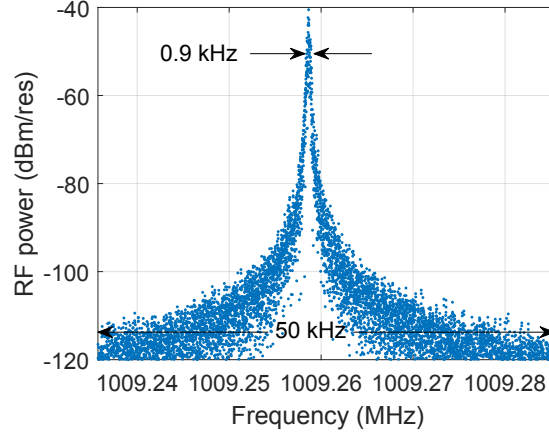
Figure 2.7: Detail of the 1-GHz RF tone (RBW 10 Hz, VBW 10 kHz).

was recorded with a resolution bandwidth of 10 Hz and a video bandwidth of 10 kHz. The exact repetition rate of the MLL is 1009.259 MHz. The 10-dB linewidth measured from the spectrum is below 900 Hz. The laser presents similar noise properties when it is locked at higher-order harmonics, and the measured RF linewidth is in the range of a few kHz.

2.4.2 Optical spectrum measurement

In Fig 2.8 the optical comb spectrum measured by a high-resolution optical spectrum analyzer (5 MHz resolution) is shown. The MLL is set at the identical optimal operation point as indicated in Fig 2.5. A more detailed image of the evenly spaced optical modes is shown in Fig. 2.9. The large optical bandwidth (>10 nm) and the small repetition rate (1 GHz) result in an optical comb with more than 1400 optical lines. The small ripples on top of the optical comb are attributed to the fact that the residual reflections from the fiber-to-chip grating coupler and the III-V-to-silicon taper form a Fabry-Perot cavity, which introduces wavelength-dependent transmission. The origin of the relatively strong peak on the blue side of the comb is under investigation, although it can be attributed to the self-phase modulation process considering the high optical intensity in the highly nonlinear sub-micron silicon waveguides.
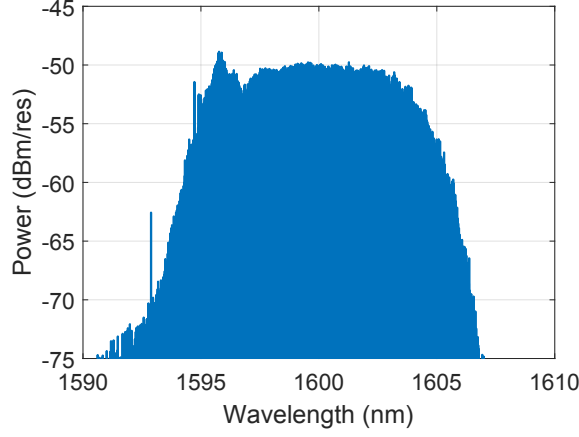
Figure 2.8: An optical comb generated by the passively locked 1 GHz MLL.
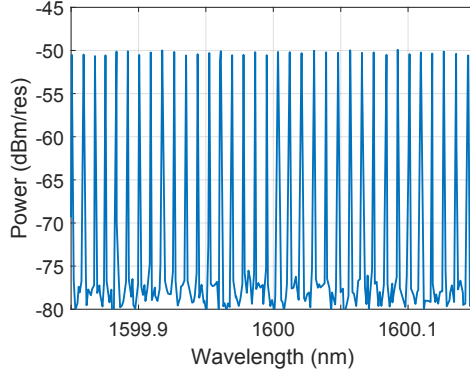
Figure 2.9: Detailed optical spectrum of the optical comb centered at 1600 nm (300 pm span). The individual optical lines show less than 1 dB ripple over the full span.

2.4.3 Optical linewidth measurement

The linewidth of the longitudinal modes of the laser was first measured by heterodyning the output of the MLL with a CW OPO (Argus 2400 sf, 50 kHz linewidth) on a 26-GHz bandwidth photodiode with TIA and analyzing the output with an electrical spectrum analyzer (Keysight EXA N9010). Because of small temeprature drifts during the measurement the frequency of the generated heterodyne beat note slowly drifted. This substantially broadened the measured linewidth as shown in Fig 2.10a. We found that a temperature change of 0.1^{o}C corresponded to an optical frequency shift of

1.5 GHz at 1600 nm. If we would want to stabilize the optical frequency with less than 15 MHz a temperature drift below 0.001^oC would be required. This was not achievable with the used temperature control system. To
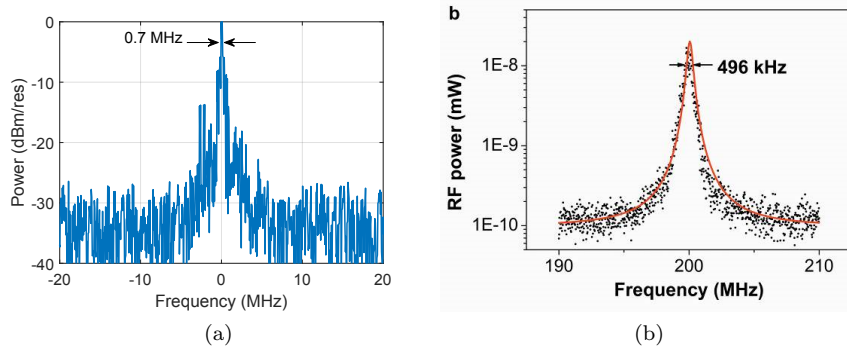
Figure 2.10: (a) Beat note between the optical comb and the tunable laser at a wavelength of 1600 nm. (b) Measured optical linewidth of the MLL using the delayed self-heterodyne method, which indicates an optical linewidth below 250 kHz. The black dots are the measured data, and the red curve is the corresponding Lorentzian fitting.

minimize the influence of the frequency drift on the measurement, the fast-scan-speed setting and low-resolution setting of the spectrum analyzer was used. This allowed to capture an instantaneous image of the drifting beat note. To cancel the effect of such temperature fluctuations, a delayed self-heterodyne method was used. A narrow spectral band of the MLL output (0.5 nm wide optical spectrum centered at 1600 nm) was split into two arms. In one arm, the optical signal went through a 5-km-long single-mode fiber, whereas a 200-MHz frequency shift was introduced in the other arm. The beat note measured by mixing the two optical signals is plotted in Fig 2.10b. A fairly narrow beat note with below-500-kHz 3-dB bandwidth was obtained, which indicates an optical linewidth below 250 kHz. Note that it is not possible to filter out a single longitudinal mode for the linewidth measurement due to the close frequency spacing of the individual modes. Therefore, the current beat note was obtained by beating 60 optical modes (in a 0.5-nm bandwidth). Consequently, the intrinsic optical linewidth of each longitudinal mode may be even smaller. The identical measurement was performed by scanning the central wavelength of the filter from 1598 to 1608 nm. An optical linewidth below 400 kHz was obtained across the entire wavelength range.
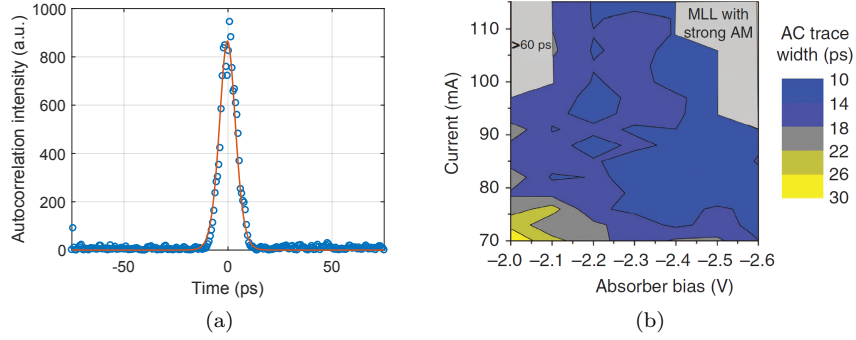
Figure 2.11: (a) An auto-correlation trace and the corresponding fit of the MLL output. (b) Mapping of the auto-correlation trace width over the current injection and SA bias. The arrow indicates the optimal operation point.

2.4.4   Auto-correlation measurement

The pulse width of the laser operated at the optimal point, indicated in Fig. 2.5, was measured using an auto-correlator. The resulting auto-correlation trace is plotted in Fig. 2.11a. The fitted pulse width was ≈ 7 ps, which indicates that the generated pulse was not transform limited. Similar to the technique in reference [35], using a tunable filter and an EDFA, we amplified and fed different slices of the optical comb (with a 1-nm bandwidth) into a high-speed photodiode and recorded the real-time pulse traces using a 160-Giga samples per second real-time oscilloscope. An overall chirp of 2.5 ps nm^{-1} was derived, which also included the chirp introduced by the EDFA (1 ps nm^{-1}, which was measured by using a standard time-of-flight measurement). The pulse duration could be shortened by using external compression using a dispersive element such as fiber. To fully describe the pulse width evolution, we plotted the AC trace width as a function of the injection current and SA bias in Fig 2.11b. The AC trace width was maintained below 15 ps over a large operation window, whereas the pulse width was considerably broader (>60 ps) for the operation region at the top-left corner of the figure, which corresponds to the small optical bandwidths in Fig 2.5.
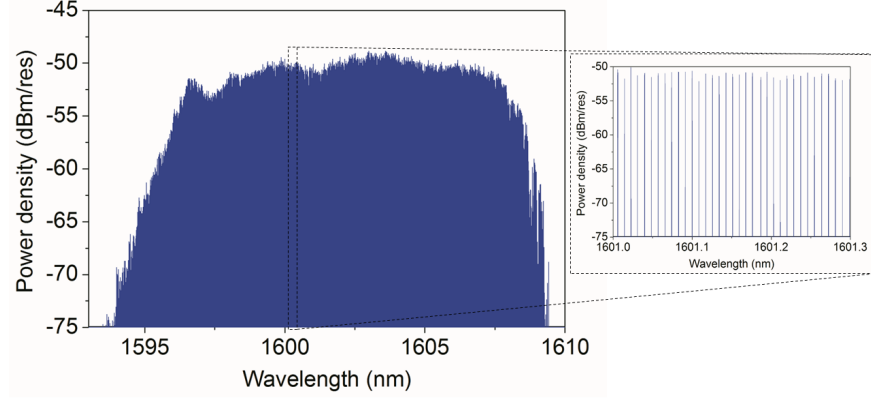
Figure 2.12: High-resolution optical spectrum of the optical comb when the MLL is hybrid mode-locked (inset: magnification of the optical spectrum).

2.4.5 Hybrid mode-locked operation

Two degrees of freedom, that is, the repetition rate and the offset frequency, of the presented mode-locked laser must be stabilized if the laser is to be used as an optical frequency comb. Hybrid mode-locking of the laser was performed by supplying an RF signal to the SA to stabilize the repetition rate. The corresponding optical comb is shown in Fig. 2.12. The MLL operation conditions were 91 mA current injection, 2.6 V SA bias, 1009.30116 MHz RF input frequency and 8 dBm (1.6 V_{pp} in a 50 Ohm system) RF input power. Compared with the optical comb generated by the passive mode-locking (Fig. 2.8), the peak at the blue side of the spectrum was less pronounced when the MLL was hybrid mode-locked (Fig. 2.12). More importantly, the optical comb slightly extended to the red side instead of collapsing into a much narrower comb when the laser was hybrid mode-locked [14]. An analysis of the pulse train in the RF domain (Fig. 2.13) reveals that the FWHM of the fundamental RF tone was sub-Hz, which proves that the line spacing of the optical comb can indeed be well stabilized (see the RF peak in Fig. 2.14).

The AC trace of the output pulse is shown in Fig. 2.15a, which shows a slightly broadened pulse width compared with the passive mode-locking case. In addition, the measured linewidth of the individual comb lines was again less than 1 MHz across the entire comb (Fig. 2.15b), which is comparable to the measured linewidths when the laser was passively mode-locked (Fig. 2.10a).

The measurement results prove that it is indeed possible to stabilize an optical comb without reducing the overall optical bandwidth. In addi-
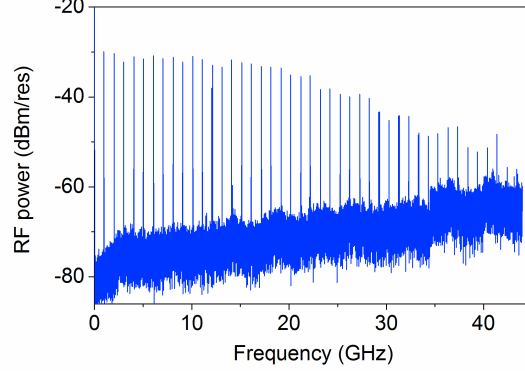
Figure 2.13: RF spectrum of the generated pulse train.
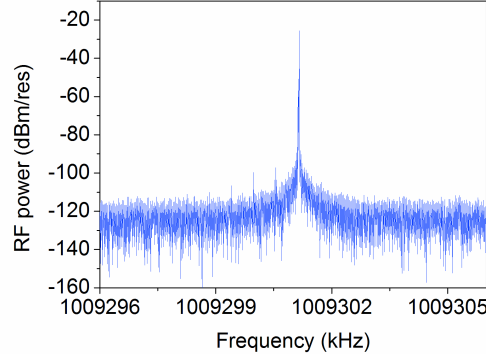
Figure 2.14: Fundamental RF peak over a span of 10 kHz showing that no spurious peaks appear near to the fundamental repetition frequency.

tion to the repetition rate, the other degree of freedom of the laser, which is the offset frequency f_{ceo} [19], must be stabilized. The widely explored self-referencing-based stabilization approach is not feasible here because of the lack of an octave-spanning spectrum without further nonlinear spectral broadening [36, 37]. Furthermore, f_{ceo} can also be stabilized by the electronic feedback modulation of the injected current in the laser using an external reference [38] or by external laser injection [39], as we recently demonstrated. The electronic feedback scheme is more elegant because it is more robust than optical injection locking and does not require optical isolation. Our heterodyne measurements (beating the MLL output with the narrow linewidth emission from a CW OPO) show that the fine tuning of the laser injection current modifies the offset frequency. This would allow the laser to be fully stabilized and operate as an optical frequency comb.

(a)

(b)
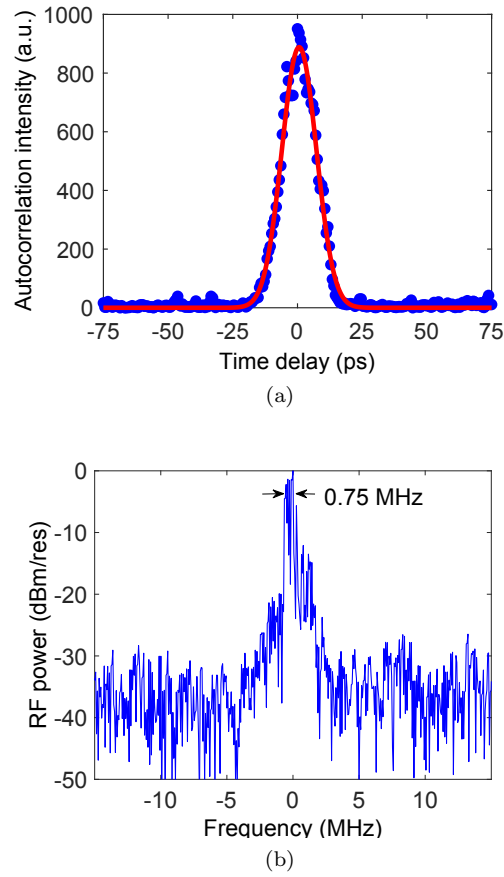
Figure 2.15: (a) Auto-correlation trace of the output pulse when the laser is hybrid mode-locked. (b) Beat note between the optical comb and the tunable laser at a wavelength of 1607 nm, which indicates that the linewidth of the longitudinal mode is smaller than 1 MHz.

2.5   Discussion

For the first time, the demonstrated MLL combines all favored properties in terms of a wide optical spectrum, a low repetition rate, a narrow optical linewidth and a narrow RF linewidth, which can be further stabilized without narrowing the optical spectrum. This is unique, because normally a trade-off exists between certain features. For example, cleaved facet quantum dot lasers can offer very wide optical spectra and narrow RF linewidths but have a less narrow optical linewidth.

The performance of several MLLs with a low-repetition rate or wide optical spectrum is shown in Tab. 2.1. The laser described in [40] is a monolithic InP laser fabricated using the SMART platform and shows a passively mode-locked repetition rate of 1022 MHz. However, no pulse train or auto-correlation trace is presented for the passively mode-locked regime. This makes it hard to assess the performance of the laser. Furthermore, no optical spectrum of the laser is presented when passively mode-locked. Therefore it is not possible to compare the optical spectrum, or number of longitudinal modes, to the laser presented in this chapter. The RF spectrum presented in [40] only shows three beating tones, indicating that only a very limited amount of optical modes are locked or present in the optical spectrum. Furthermore, the reported RF linewidth in [40] of the fundamental RF tone is approximately 400 kHz, indicating a large timing jitter of the pulse train and is considerably higher than the 900 Hz presented in this chapter. Finally, when the laser in [40] is operated in a hybrid mode-locking regime a pulse of 272 ps with a repetition rate of 1 ns is generated.

A second monolithic InP 1 GHz mode-locked laser is demonstrated in [12]. However, this device only shows mode-locked behaviour when an external RF source (20 dBm) is applied. No clear explanation is presented why the laser shows no passive mode-locking behaviour. The laser only operates below room temperature and the shortest produced pulse is 36 ps.

Finally, two low repetition rate III-V-on-silicon mode-locked lasers are reported in [14]. The laser with the lowest repetition rate (930 MHz) is a ring-type laser with a 9 cm long cavity. However, it does not contain a saturable absorber but three SOAs of which one is modulated with an RF signal. Consequently, only hybrid mode-locking is demonstrated with a very narrow optical spectrum (100 pm) and a long pulse duration of 200 ps. Although a long passive cavity is used, the passive waveguide losses are relatively high for silicon waveguides (1.7 dB/cm). In the same publication a 2 GHz ring mode-locked laser is demonstrated. This laser contains a saturable absorber and shows passive mode-locking behaviour. An optical spectrum of 1 nm and an RF linewidth of 14 kHz are demonstrated.

Table 2.1: Overview of semiconductor mode-locked lasers with wide optical spectrum or low repetition rate. Rep. rate: repetition rate; Opt. bw: optical 10 dB bandwidth; Opt. lw: optical 3 dB linewidth; RF lw: 10 dB linewidth of the fundamental RF tone; AC width: width of the auto-correlation trace; No. lines: number of optical modes within the 10 dB optical bandwidth

	Passive/Hybrid	Rep. rate (GHz)	Opt. bw (nm)	Opt. lw (MHz)	RF lw (kHz)	AC width (ps)	No. lines
This work	Passive	1.01	12	0.4	0.9	15	1400
	Hybrid	1.01	13	0.4	0.001	15	1500
[12]	Hybrid	1.03	1	70	500	36	110
[40]	Hybrid	1.0	-	-	-	272	-
	Passive	1.022	-	-	400	-	-
[14]	Hybrid	0.93	0.1	7	-	200	12
	Passive	2	1	-	14	40	126
[17]	Passive	2.5	4	-	18.9	15	210
[15]	Passive	10.2	8.7	-	15	33	110
[16]	Passive	20	15	900	2.4	4	90
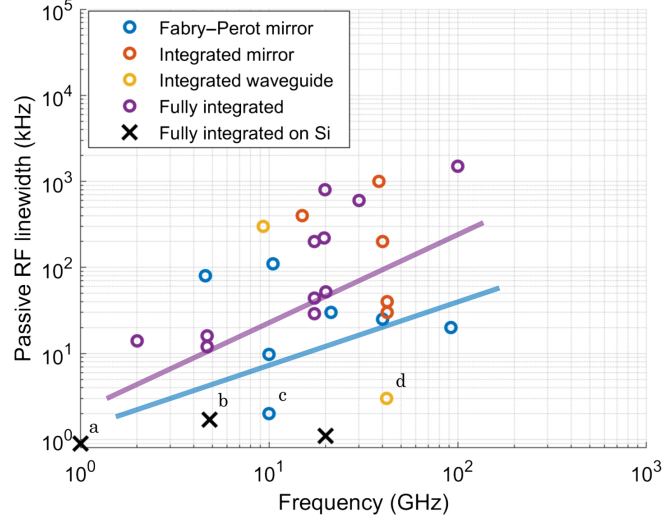
Figure 2.16: 3 dB passively mode-locked RF linewidth of a selection of mode-locked lasers from literature. The laser presented in this chapter is represented by the cross in the left bottom corner of the graph. This figure is reproduced from [24].

To the best of our knowledge, these are the only other 1 GHz integrated mode-locked lasers reported in literature. The performance of the laser presented in this chapter shows improved performance in comparison to the other demonstration. We believe this is due to the low-loss (0.7 dB/cm) waveguides combined with the anti-colliding pulse design.

In Tab. 2.1 also several lasers with a wide optical spectrum, or a large number of optical modes, are listed. For example the device presented in [16] demonstrated a very wide optical comb spanning 15 nm containing 90 optical longitudinal modes. A very interesting property of the laser presented in this chapter is that it combines a low repetition rate with a wide optical spectrum spanning 12 nm. This results in 1400 longitudinal modes, which is an order of magnitude larger than other integrated mode-locked lasers presented in literature. The exact mechanism behind the generation of this wide optical spectrum, and high number of optical modes, is not well understood and requires further investigation.

In Fig. 2.16 an overview of the RF linewidth of several passively mode-locked integrated semiconductor lasers is shown (the figure is reproduced from [24]). All devices which are realized in III-V-on-silicon are denoted with black crosses. From this figure it is clear that the III-V-on-silicon devices present very narrow RF linewidths of the fundamental RF tone

compared to other approaches. As described in [24] the long low-loss silicon waveguide reduces the RF linewidth when compared to all-active devices. The laser denoted by "a" in Fig. 2.16 refers to the laser described in this chapter. As shown in the figure, this laser presents the lowest RF linewidth of the fundamental tone reported for a fully integrated mode-locked laser. This can be understood as this laser also has the longest passive low-loss cavity of all lasers presented in Fig. 2.16. The device referred to with "b" is also a III-V-on-silicon laser developed by the Photonics Research Group of Ghent University and is described in [22]. This is a 5 GHz laser with the same anti-colliding pulse design and low-loss silicon waveguides as used for the laser presented in this chapter. The laser corresponding to "c" is a 10 GHz AlGaInAs all-active laser using uncoated cleaved facets as cavity mirrors and is described in [41]. The laser denoted with "d" is an all-active InP mode-locked laser with an Uni-Travelling Carrier (UTC) photodiode as saturable absorber and a repetition rate of 42 GHz. The use of an UTC layer stack for the saturable absorber reduces the absorption recovery time by almost an order of magnitude [42]. The shorter recovery time can improve timing jitter of the pulse train and shorten pulse duration. The laser denoted by the black cross without a letter is also a III-V-on-silicon mode-locked laser [24] and shows a low RF linewidth of less than 2 kHz. This confirms that the use of low-loss silicon waveguides enables low timing jitter mode-locked lasers. It is interesting to note that the laser described in this chapter and the lasers denoted with "b", "c" and "d" in Fig. 2.16 all have a pulse energy in the order of 500 fJ at the operation point where the narrow RF linewidth is demonstrated. Consequently, further development will be needed to demonstrate a laser which combines low timing jitter with high pulse energy.

2.6 Conclusion

We have successfully demonstrated an integrated III-V-on-silicon mode-locked laser that passively mode-locks at a record-low repetition rate of 1 GHz. Because of the low loss of the passive silicon waveguide, the sub-kHz 10-dB linewidth of the fundamental RF tone indicates low phase noise. The over 10-nm wide optical comb with a line spacing of only 1 GHz consists of more than 1400 densely and evenly spaced optical lines with below 400-KHz optical linewidth. Hybrid mode-locking stabilizes the repetition rate of the optical comb without negatively affecting the bandwidth and linewidth of the individual comb lines. The fully integrated comb laser provides unique advantages of compactness, robustness, power consumption and low cost.

References

[1] Z. Wang, K. Van Gasse, V. Moskalenko, S. Latkowski, E. Bente, B. Kuyken, and G. Roelkens. *A III-V-on-Si ultra-dense comb laser.* Light: Science & Applications, 6(5):e16260, may 2017.

[2] T. W. Hänsch. *Nobel Lecture: Passion for precision.* Reviews of Modern Physics, 78(4):1297–1309, nov 2006.

[3] P. Ghelfi, F. Laghezza, F. Scotti, G. Serafino, A. Capria, S. Pinna, D. Onori, C. Porzi, M. Scaffardi, A. Malacarne, V. Vercesi, E. Lazzeri, F. Berizzi, and A. Bogoni. *A fully photonics-based coherent radar system.* Nature, 507(7492):341–345, 2014.

[4] T. M. Fortier, M. S. Kirchner, F. Quinlan, J. Taylor, J. C. Bergquist, T. Rosenband, N. Lemke, A. Ludlow, Y. Jiang, C. W. Oates, and S. A. Diddams. *Generation of ultrastable microwaves via optical frequency division.* Nature Photonics, 5(7):425–429, 2011.

[5] J. Kim and Y. Song. *Ultralow-noise mode-locked fiber lasers and frequency combs: principles, status, and applications.* Advances in Optics and Photonics, 8(3):465, sep 2016.

[6] Kwangyun Jung, Junho Shin, and Jungwon Kim. *Ultralow Phase Noise Microwave Generation From Mode-Locked Er-Fiber Lasers With Subfemtosecond Integrated Timing Jitter.* IEEE Photonics Journal, 5(3):5500906–5500906, jun 2013.

[7] X. Xie, R. Bouchand, D. Nicolodi, M. Giunta, W. Hänsel, M. Lezius, A. Joshi, S. Datta, C. Alexandre, M. Lours, P.-A. Tremblin, G. Santarelli, R. Holzwarth, and Y. Le Coq. *Photonic microwave signals with zeptosecond-level absolute timing noise.* Nature Photonics, 11(1):44–47, jan 2017.

[8] J. Kim, M. J. Park, M. H. Perrott, and F. X. Kärtner. *Photonic subsampling analog-to-digital conversion of microwave signals at 40-GHz with higher than 7-ENOB resolution.* Optics Express, 16(21):16509, oct 2008.

[9] A. Ortigosa-Blanch, J. Mora, J. Capmany, B. Ortega, and D. Pastor. *Tunable radio-frequency photonic filter based on an actively mode-locked fiber laser.* Optics Letters, 31(6):709, mar 2006.

[10] Xiaojun Xie, Yitang Dai, Kun Xu, Jian Niu, Ruixin Wang, Li Yan, and Jintong Lin. *Broadband Photonic RF Channelization Based on Coherent Optical Frequency Combs and I/Q Demodulators.* IEEE Photonics Journal, 4(4):1196–1202, aug 2012.

[11] X. Xu, J. Wu, T. G. Nguyen, S. T. Chu, B. E. Little, R. Morandotti, A. Mitchell, and D. J. Moss. *Broadband RF Channelizer Based on an Integrated Optical Frequency Kerr Comb Source.* Journal of Lightwave Technology, 36(19):4519–4526, oct 2018.

[12] S. Cheung, J.-H. Baek, R. P. Scott, N. K. Fontaine, F. M. Soares, X. Zhou, D. M. Baney, and S. J. B. Yoo. *1-GHz monolithically integrated hybrid mode-locked InP laser.* IEEE Photonics Technology Letters, 22(24):1793–1795, 2010.

[13] Y. Li, M. Breivik, C. Feng, B. Fimland, and L. F. Lester. *A Low Repetition Rate All-Active Monolithic Passively Mode-Locked Quantum-Dot Laser.* IEEE Photonics Technology Letters, 23(14):1019–1021, 2011.

[14] S. Srinivasan, M. Davenport, M. J. R. Heck, J. Hutchinson, E. Norberg, G. Fish, and J. Bowers. *Low phase noise hybrid silicon mode-locked lasers.* Frontiers of Optoelectronics, 7(3):265–276, sep 2014.

[15] V. Corral, R. Guzmán, C. Gordón, X. J. M. Leijtens, and G. Carpintero. *Optical frequency comb generator based on a monolithically integrated passive mode-locked ring laser with a Mach–Zehnder interferometer.* Optics letters, 41(9):1937–1940, 2016.

[16] V. Moskalenko, S. Latkowski, S. Tahvili, T. de Vries, M. Smit, and E. Bente. *Record bandwidth and sub-picosecond pulses from a monolithically integrated mode-locked quantum well ring laser.* Optics express, 22(23):28865–28874, 2014.

[17] S. Latkowski, V. Moskalenko, S. Tahvili, L. Augustin, M. Smit, K. Williams, and E. Bente. *Monolithically integrated 2.5 GHz extended cavity mode-locked ring laser with intracavity phase modulators.* Optics letters, 40(1):77–80, 2015.

[18] F. Kéfélian, S. O'Donoghue, M. T. Todaro, J. G. McInerney, and G. Huyet. *RF linewidth in monolithic passively mode-locked semiconductor laser.* IEEE Photonics Technology Letters, 20(16):1405–1407, 2008.

[19] B. W. Tilma, M. Mangold, C. A. Zaugg, S. M. Link, D. Waldburger, A. Klenner, A. S. Mayer, E. Gini, M. Golling, and U. Keller. *Recent*

advances in ultrafast semiconductor disk lasers. Light: Science & Applications, 4(7):e310, 2015.

[20] K. Merghem, A. Akrout, A. Martinez, G. Moreau, J.-P. Tourrenc, F. Lelarge, F. Van Dijk, G.-H. Duan, G. Aubin, and A. Ramdane. *Short pulse generation using a passively mode locked single InGaAsP/InP quantum well laser.* Optics Express, 16(14):10675, jul 2008.

[21] M. Huchard, P. Chanclou, B. Charbonnier, F. van Dijk, G.-H. Duan, C. Gonzalez, F. Lelarge, M. Thual, M. Weiss, and A. Stohr. *60 GHz radio signal up-conversion and transport using a directly modulated mode-locked laser.* In 2008 International Topical Meeting on Microwave Photonics jointly held with the 2008 Asia-Pacific Microwave Photonics Conference, pages 333–335. IEEE, sep 2008.

[22] S. Keyvaninia, S. Uvin, M. Tassaert, Z. Wang, X. Fu, S. Latkowski, J. Marien, L. Thomassen, F. Lelarge, G. Duan, and Others. *III–V-on-silicon anti-colliding pulse-type mode-locked laser.* Optics letters, 40(13):3057–3060, 2015.

[23] S. Keyvaninia, S. Uvin, M. Tassaert, X. Fu, S. Latkowski, J. Mariën, L. Thomassen, F. Lelarge, G. Duan, P. Verheyen, G. Lepage, J. Van Campenhout, E. Bente, and G. Roelkens. *Narrow-linewidth short-pulse III-V-on-silicon mode-locked lasers based on a linear and ring cavity geometry.* Optics Express, 23(3):3221, feb 2015.

[24] M. L. Davenport, S. Liu, and J. E. Bowers. *Integrated heterogeneous silicon/IIIV mode-locked lasers.* Photonics Research, 6(5):468, may 2018.

[25] M. S. Eggleston, C.-M. Chang, N. Kaneda, K. Kim, J. H. Sinsky, G. de Valicourt, N. Chimot, F. Lelarge, T. Itoh, M. C. Wu, and Y.-K. Chen. *Silicon Photonics Enabled Hyper-Wideband RF Receiver With >85% Instantaneous Bandwidth.* IEEE Journal of Selected Topics in Quantum Electronics, 24(6):1–8, nov 2018.

[26] S. Liu, T. Komljenovic, S. Srinivasan, E. Norberg, G. Fish, and J. E. Bowers. *Characterization of a fully integrated heterogeneous silicon/III-V colliding pulse mode-locked laser with on-chip feedback.* Optics Express, 26(8):9714, apr 2018.

[27] M.-C. Lo, R. Guzmán, C. Gordón, and G. Carpintero. *Mode-locked laser with pulse interleavers in a monolithic photonic integrated circuit for millimeter wave and terahertz carrier generation.* Optics Letters, 42(8):1532, apr 2017.

[28] J. Javaloyes and S. Balle. *Anticolliding design for monolithic passively mode-locked semiconductor lasers.* Optics letters, 36(22):4407–4409, 2011.

[29] V. Moskalenko, K. A. Williams, and E. A. J. M. Bente. *Integrated Extended-Cavity 1.5-μm semiconductor laser switchable between self- and anti-colliding pulse passive mode-locking configuration.* IEEE Journal of Selected Topics in Quantum Electronics, 21(6):40–45, 2015.

[30] G. Roelkens, A. Abassi, P. Cardile, U. Dave, A. de Groote, Y. de Koninck, S. Dhoore, X. Fu, A. Gassenq, N. Hattasan, Q. Huang, S. Kumari, S. Keyvaninia, B. Kuyken, L. Li, P. Mechet, M. Muneeb, D. Sanchez, H. Shao, T. Spuesens, A. Subramanian, S. Uvin, M. Tassaert, K. van Gasse, J. Verbist, R. Wang, Z. Wang, J. Zhang, J. van Campenhout, X. Yin, J. Bauwelinck, G. Morthier, R. Baets, and D. van Thourhout. *III-V-on-Silicon Photonic Devices for Optical Communication and Sensing.* Photonics, 2(3):969–1004, sep 2015.

[31] J. S. Parker, R. S. Guzzon, E. J. Norberg, A. Bhardwaj, P. R. A. Binetti, and L. A. Coldren. *Theory and design of THz intracavity gain-flattened filters for monolithically integrated mode-locked lasers.* IEEE Journal of Quantum Electronics, 48(2):114–122, 2012.

[32] J. S. Parker, A. Bhardwaj, P. R. A. Binetti, Y.-J. Hung, and L. A. Coldren. *Monolithically integrated gain-flattened ring mode-locked laser for comb-line generation.* IEEE Photonics Technology Letters, 24(2):131–133, 2012.

[33] M. M. Mielke, G. A. Alphonse, and P. J. Delfyett. *Multiwavelength modelocked semiconductor lasers for photonic access network applications.* IEEE Journal on Selected Areas in Communications, 25(3), 2007.

[34] V. Moskalenko, J. Koelemeij, K. Williams, and E. Bente. *Study of extra wide coherent optical combs generated by a QW-based integrated passively mode-locked ring laser.* Optics letters, 42(7):1428–1431, 2017.

[35] M. S. Tahvili, L. Du, M. J. R. Heck, R. Nötzel, M. K. Smit, and E. Bente. *Dual-wavelength passive and hybrid mode-locking of 3, 4.5 and 10 GHz InAs/InP (100) quantum dot lasers.* Optics express, 20(7):8117–8135, 2012.

[36] A. Klenner, A. S. Mayer, A. R. Johnson, K. Luke, M. R. E. Lamont, Y. Okawachi, M. Lipson, A. L. Gaeta, and U. Keller. *Gigahertz frequency comb offset stabilization based on supercontinuum generation in silicon nitride waveguides.* Optics express, 24(10):11043–11053, 2016.

[37] P. Brochard, N. Jornod, S. Schilt, V. J. Wittwer, S. Hakobyan, D. Waldburger, S. M. Link, C. G. E. Alfieri, M. Golling, L. Devenoges, and Others. *First investigation of the noise and modulation properties of the carrier-envelope offset in a modelocked semiconductor laser.* Optics letters, 41(14):3165–3168, 2016.

[38] A. Apolonski, A. Poppe, G. Tempea, C. Spielmann, T. Udem, R. Holzwarth, T. W. Hänsch, and F. Krausz. *Controlling the phase evolution of few-cycle light pulses.* Physical Review Letters, 85(4):740, 2000.

[39] S. Uvin, S. Keyvaninia, F. Lelarge, G.-H. Duan, B. Kuyken, and G. Roelkens. *Narrow line width frequency comb source based on an injection-locked III–V-on-silicon mode-locked laser.* Optics express, 24(5):5277–5286, 2016.

[40] R. Guzmán, C. Gordon, L. Orbe, and G. Carpintero. *1 GHz InP on-chip monolithic extended cavity colliding-pulse mode-locked laser.* Optics Letters, 42(12):2318, jun 2017.

[41] L. Hou, M. Haji, B. Qiu, J. Akbar, A. C. Bryce, and J. H. Marsh. *10-GHz AlGaInAs/InP 1.55-μm Passively Mode-Locked Laser With Low Divergence Angle and Timing Jitter.* IEEE Photonics Technology Letters, 23(15):1079–1081, aug 2011.

[42] R. Scollo, H.-J. Lohe, F. Robin, D. Erni, E. Gini, and H. Jackel. *Mode-Locked InP-Based Laser Diode With a Monolithic Integrated UTC Absorber for Subpicosecond Pulse Generation.* IEEE Journal of Quantum Electronics, 45(4):322–335, apr 2009.

Chapter 3

Silicon photonic modulators

In this chapter we present the design, fabrication and characterization of several silicon photonic modulators. We investigated Mach-Zehnder modulators both using silicon carrier-depletion phase-shifters and III-V-on-silicon phase-shifters. We designed and characterized a silicon carrier-depletion dual-parallel Mach-Zehnder modulator that can be used for microwave photonic applications such as microwave photonic frequency conversion. As microwave systems often operate in a 50 Ohm environment, we investigated advanced electrode design to provide on-chip impedance matching without the use of resistive elements. Both stub-matching and off-center-fed electrodes were designed and characterized. Finally we developed a III-V-on-silicon modulator that can be integrated with other active devices on a microwave photonic chip.

3.1   Introduction

Over the last years a great amount of research has been dedicated to the development of high-bandwidth optical modulators on integrated photonic platforms, such as silicon photonics, InP photonics and hybrid InP/Si photonics. Mach-Zehnder Modulators (MZMs) based on pn-doped silicon waveguide phase-shifters have seen tremendous progress in recent years. Although both carrier-injection [1, 2] and carrier-depletion phase-shifters have been investigated, carrier-depletion has shown great promise for high-bandwidth applications [3, 4]. Using a single travelling-wave modulator, on-off keying data rates of 70 Gb/s were achieved [3]. By using advanced modulation formats and multi-electrode structures, data rates exceeding 100

Gb/s have been successfully demonstrated with these devices [5, 6]. Furthermore, IQ-modulators can be implemented by placing two parallel MZMs in a Mach-Zehnder Interferometer (MZI) structure. Such modulators are also referred to as dual-parallel MZMs and they can be used for complex modulation formats used in coherent communication, such as 16-QAM. The use of dual-parallel MZMs is also of great interest to the microwave photonics community, as they can be used for microwave photonic frequency conversion and single-sideband modulation. Especially in Radio-over-Fiber links single-sideband modulation can be of great interest to mitigate fiber-dispersion induced fading.

For digital communication, broadband matching is needed to ensure minimal distortion of the modulated signal. Silicon photonic modulators for digital data transmission often use a travelling-wave electrode in combination with an on-chip 50 Ohm termination to achieve wide-band impedance matching [7]. Although this is an effective approach, the use of resistive impedance matching also has drawbacks. For example, the static bias needed for proper operation of a carrier-depletion phase-shifter will cause constant power dissipation in the 50 Ohm termination [7]. For narrow band applications, such as Radio-over-Fiber, broad-band matching is not needed and non-resistive matching can be used. For example, stub-matching or off-center feeding can be used for narrow-band matching of phase-shifter electrodes. The use of stub-matching for optical modulators was already explored for LiNbO$_3$ [8, 9] and promising narrow-band performance was demonstrated.

Although carrier-depletion phase-shifters have many advantages, there are also limitations intrinsic to the technology. One of the main drawbacks of using all-silicon carrier-depletion phase-shifters is the low efficiency, which translates itself into large voltage-length products ranging from 1 to 2 Vcm. One of the most promising approaches to create a more efficient integrated phase-shifter, is by integrating III-V materials on a silicon chip. For example, using III-V-on-silicon technology a phase-shifter with a voltage-length product of 0.2 Vcm was demonstrated [10], an order of magnitude more efficient than all-silicon phase-shifters.

In this chapter we will discuss the design and characterization of several types of silicon carrier-depletion MZMs and a III-V-on-silicon MZM. The modulators were designed in the framework of the European Space Agency ARTES project Electro-Photonic Frequency Converter (EPFC), in collaboration with Antwerp Space. We implemented several designs using an iSiPP25G Multi-Project Wafer run, provided by imec. The photonic technology developed by imec was oriented towards 25 Gb/s data transmission and was therefore called iSiPP25G. We used this technology to develop
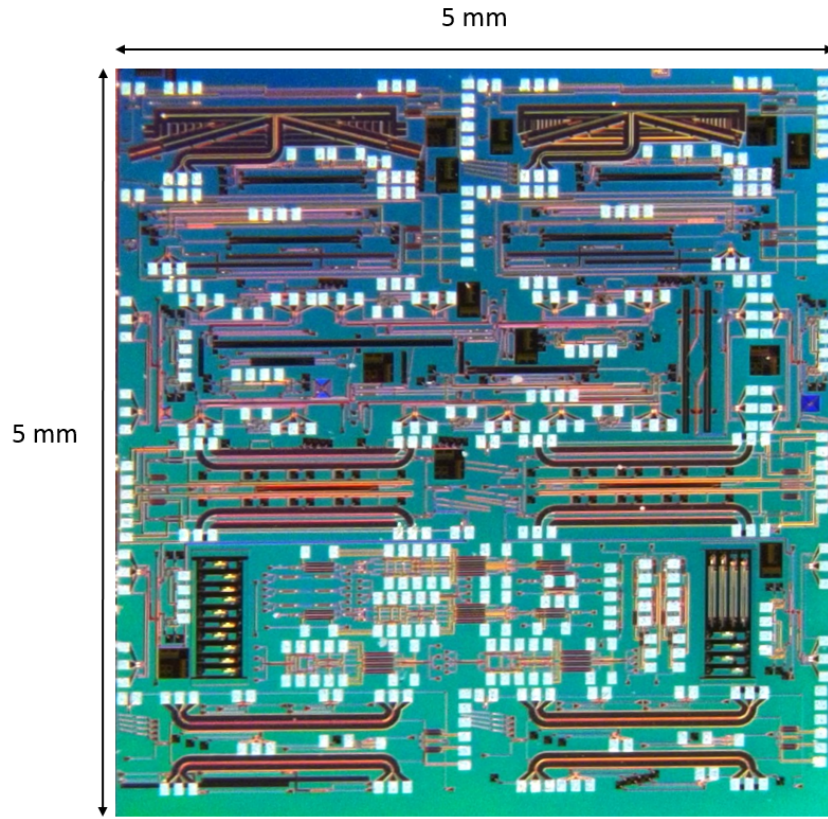
Figure 3.1: Microscope image of a chip containing several silicon carrier-depletion phase-shifters and MZMs. The chip was fabricated on a imec iSiPP25G technology multi-project-wafer run.

a dual-parallel MZM capable of microwave photonic frequency conversion. Furthermore, we designed and tested a narrow-band stub-matched phase shifter and an off-center fed push-pull MZM. A microscope image of the iSiPP25G chip containing several silicon MZMs is shown in Fig. 3.1. Finally we developed a III-V-on-silicon phase-shifter with the specific intent of integrating it with other III-V-on-silicon components on a single chip.
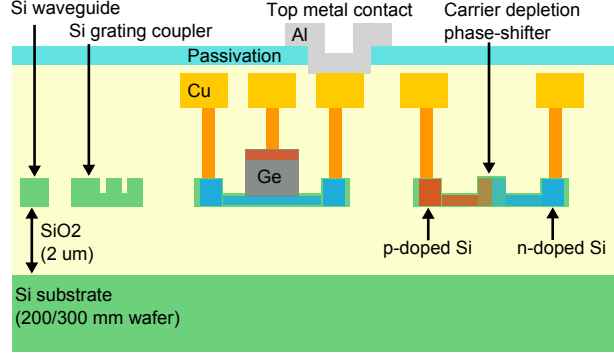
Figure 3.2: Schematic cross-section of imec's silicon photonics platform, indicating basic passive and active devices. This figure was reproduced based on a figure found in [11].

3.2 The iSiPP25G platform

Silicon photonics has the great advantage it can be fabricated using technologies developed by the CMOS industry. A 200 mm silicon photonics pilot line was set up at imec based on a 130 nm CMOS node. This platform was named iSiPP25G at the time the modulators described in this chapter were developed. However, the platform has evolved to iSiPP50G by the end of this work and MZMs enabling bit-rates up to 50 Gb/s are now available as basic building blocks. A schematic representation of the iSiPP25G platform is shown in Fig. 3.2 [11]. The advanced silicon photonic platform (iSIPP25G) developed by imec offers high-performance devices such as photodiodes, phase-shifters, grating couplers and passives. Photonic integrated circuits can be designed using a Process Design Kit (PDK) and fabricated on a Multi-Project Wafer run. One of the basic building blocks in the platform is a phase-shifter based on a laterally pn-doped silicon waveguide as illustrated in Fig. 3.2. Two types of phase-shifters were offered in the iSiPP25G PDK, one with a lumped 500 μm electrode and one with a 1500 μm travelling wave electode. The $V_\pi L_\pi$ of the pn-doped waveguide is approximately 1 Vcm and the passive optical losses of the pn-doped waveguide are approximately 3 dB/mm. Both devices had a 3 dB modulation bandwidth of approximately 10-15 GHz, depending on the reverse bias over the pn-junction. In this work we focus on high-efficiency modulation and impedance matching in a narrow frequency band. Such modulators were not available in the PDK and were developed using the available pn-doped waveguide and metal layer. All designs in the following sections are custom designs.

3.3 Silicon dual-parallel MZM

Dual-parallel MZMs, two MZMs placed in a MZI structure, have many interesting applications such as coherent optical communication and single-sideband modulation. Such optical IQ-modulators are commercially available based on $LiNbO_3$. For example, a high performance microwave photonic mixer was demonstrated using a $LiNbO_3$ dual-parallel MZM [12].

We developed a silicon photonic dual-parallel MZM using the iSiPP25G carrier-depletion phase-shifters discussed in the previous section. The design of the individual MZMs is based on the push-pull design reported in [4]. A schematic layout of the design is shown in Fig. 3.3a. In this layout the different components are denoted together with a cross-section of the phase-shifting waveguides. In this design two pn-doped waveguides are placed closely together and driven using a single travelling wave electrode. The pn-doped waveguides from the iSiPP25G PDK have a voltage-length product of approximately 1 Vcm and an optical loss of 3 dB/mm. Given that the effective length of the phase-shifter is 1 mm, the resulting V_π is approximately 10 V and the insertion loss due to the doped waveguides is approximately 3 dB. By electrically connecting the n-doped regions of the two phase-shifters the capacitances of the depletion regions are connected in series. This reduces the capacitance and the microwave propagation losses [4]. A fabrication layout (gds file) of the modulator and a simplified equivalent electrical circuit are shown in Fig. 3.3b. Furthermore, the doping was segmented to reduce possible parasitic transmission line losses as shown in the inset of Fig. 3.3b. This approach is similar to the work presented in [4] and avoids current parasitic current in the doped silicon. The optical structure of the MZMs and the MZI were realized using 2 by 2 MMIs. This allowed the output to be split between a grating coupler and a high speed on-chip germanium photodiode. The photodiode enabled the chip to work as a stand-alone photonic sampler, as will be discussed in chapter 7. A thermo-optic phase shifter was added to each individual MZM and the MZI structure. These extra phase shifters are used to provide a static bias to the MZMs and MZI that is needed for IQ-modulation. This is necessary because in the push-pull configuration it is inefficient to provide each pn-junction with an individual static bias. An on-chip 50 Ohm resistor was added to terminate the transmission line electrodes to avoid unwanted reflections and excessive ripple in the modulation response. To provide a static bias on the pn-junctions a separate biasing contact is implemented using a long metal trace, that acts as an RF choke. This way a static bias can be provided without drawing current through the 50 Ohm resistor. The high-frequency inputs for the modulators are on opposite sides of the chip

so that they can be easily contacted with RF probes. Chip-to-fiber grating couplers were used for optical I/O using a cleaved single-mode fiber. Finally, all electrical dc connections for heaters and biasing were grouped on the left side of the PIC so that these contacts can be easily wire-bonded (see Fig. 3.3b). A microscope image of the fabricated PIC is shown in Fig. 3.3c.

To assess the performance of the individual modulators a small-signal measurement was performed using a Keysight PNA-X Vector Network Analyzer. It was found that the modulation shows less than 3 dB ripple up to 30 GHz. The measured small-signal modulation response, for different bias-voltages across the pn-junction, is shown in Fig. 3.4a. When the pn-junction is forward biased the modulator operates in the carrier injection regime and the bandwidth is severely limited. The flat response with reverse bias makes the modulator well suited for both digital and analogue modulation. A measurement of the return loss was performed using the Keysight PNA-X Vector Network Analyzer and the resulting S11 is shown in Fig. 3.4b. From the measurement we can deduce that at very low frequencies good matching is achieved with the on-chip resistor that has a targeted resistance of 50 Ohm. However, for frequencies above 500 MHz the return loss deteriorates to approximately 8.5 dB. As can be seen in the Smith chart in Fig. 3.4c, for low frequencies the input impedance is lower than 50 Ohms. This indicates that the impedance of the on-chip resistor deviates from the designed value. The return loss can be further improved in future designs by using measured values for the modulator electrode impedance and on-chip resistors.

(a)

(b)

(c)
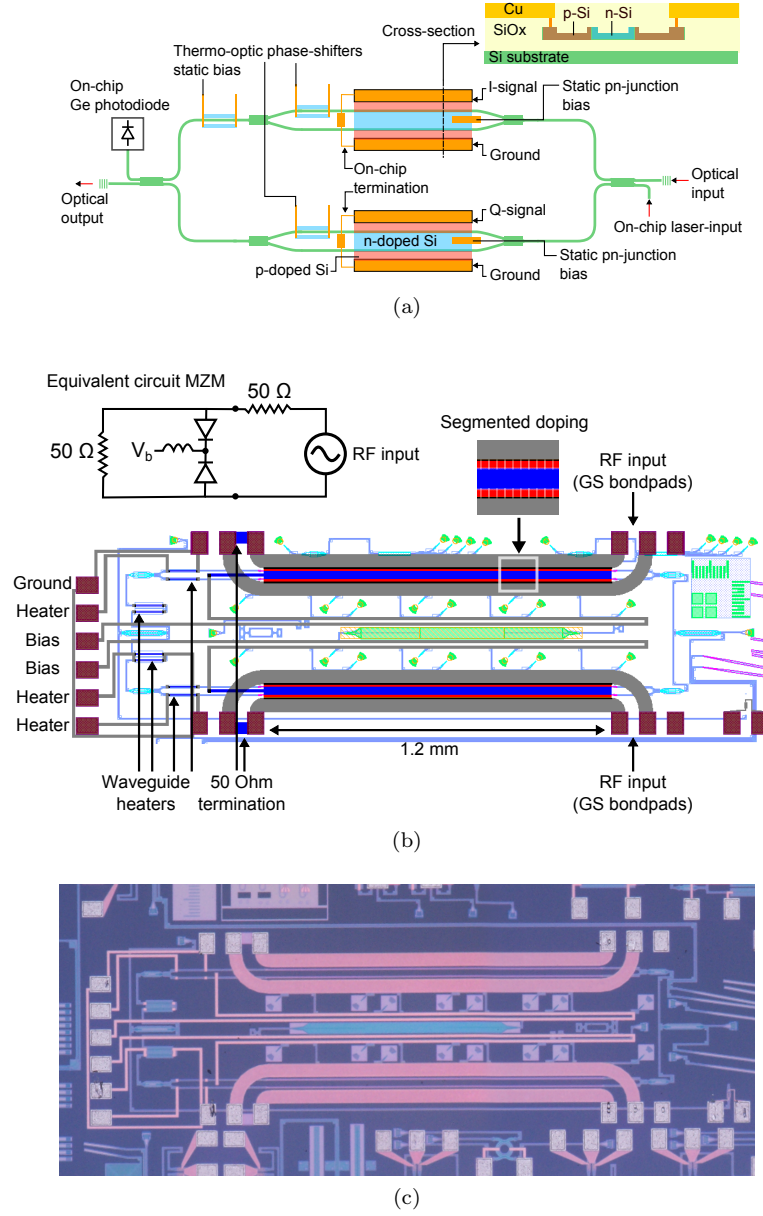
Figure 3.3: (a) Schematic layout (not to scale) of the iSiPP25 IQ-modulator. The inset shows a cross-section of the doped silicon phase-shifter waveguides. (b) Fabrication layout of the IQ-modulator with indication of the different parts and simplified equivalent circuit of a single push-pull MZM. (c) Micrograph of a silicon photonic IQ-modulator realized on the iSiPP25G platform.

(a)

(b)   (c)
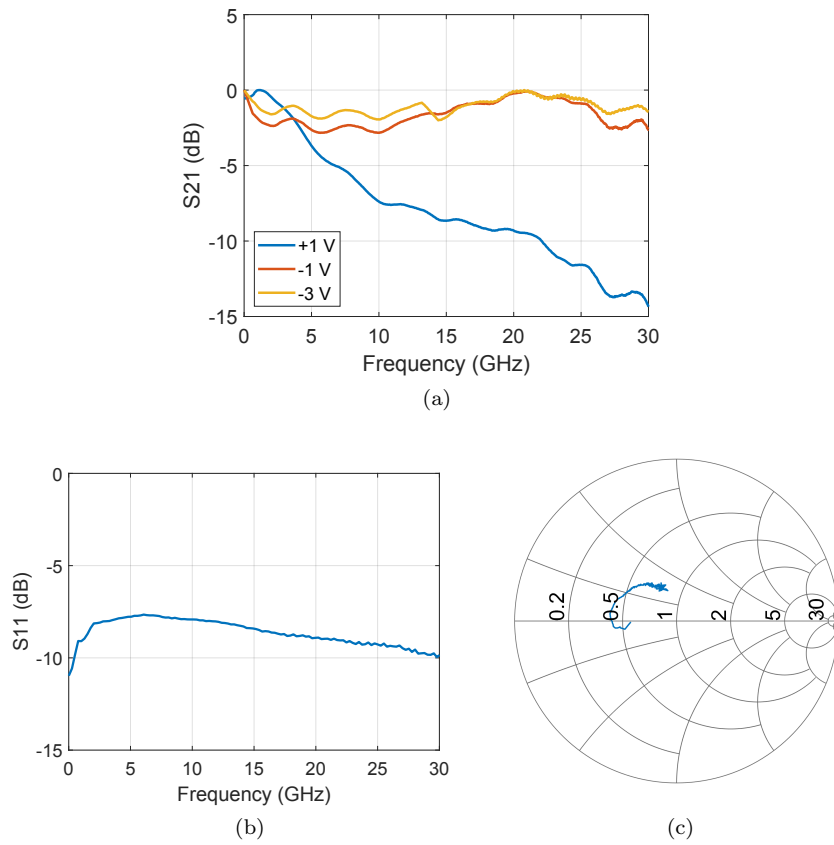
Figure 3.4: (a) The small-signal transmission of a push-pull MZM at different pn-junction bias voltages. (b) The S11 of the push-pull modulator terminated with an on-chip 50 Ohm resistor. (c) The measured reflection coefficient of the push-pull modulator terminated with an on-chip 50 Ohm resistor plotted in a Smith Chart.

3.4 Off-center-fed reflective MZM based transceiver

In Radio Access Networks it can be interesting to have a low cost and simple remote antenna unit. An interesting way to realize this, is by eliminating the light source from the transceiver at the remote antenna unit. This can be realized by using a reflective modulator combined with a high-performance light source at the base-station. However, reflective modulators have seen less development when compared to their single-pass counterparts. This is in part because most silicon single-pass modulators employ travelling-wave electrodes to achieve high-bandwidth operation. Although travelling-wave electrodes have many benefits, they modulate the light only efficiently for one propagation direction at high microwave frequencies. This makes them less interesting to be used in a reflective architecture. Using a Michelson-Morley configuration a reflective silicon photonic modulator using lumped carrier-depletion phase shifters has been demonstrated [13]. However, the lumped phase-shifters do not have any impedance matching and strong RF reflections occur. An interesting solution to reduce the RF reflections is the narrow-band matching of the electrode by using off-center feeding. This has been previously demonstrated with the electrode of a LiNbO$_3$ modulator [8, 14].

We have designed a reflective silicon photonic modulator based on a push-pull carrier-depletion MZM, identical to the one discussed in the previous section. To make it operate as a reflective modulator we placed it in a Sagnac loop and used a lumped electrode. The modulator was designed to be part of a transceiver which also contains a high-speed photodiode and un-balanced MZI-based wavelength de-multiplexer, enabling full duplex operation by WDM. A schematic layout of the reflective MZM and full transceiver PIC is shown in Fig. 3.5a. The inset in Fig. 3.5a shows the layer stack of the second generation iSiPP25G technology, that provides two metal layers instead of one. The use of two metal layers allowed to contact the phase-shifter electrode in a straightforward way (as illustrated in Fig. 3.5a). A fabrication layout (gds file) of the transceiver PIC with reflective modulator is shown in Fig. 3.5b.

Because the transceiver was designed with 5G RANs in mind, we wanted to achieve 50 Ohm matching in the 28 GHz band. The input impedance of the lumped phase-shifter electrode can be tuned by changing the position of the feedpoint. To design the electrode and MZM we used a transmission line equivalent circuit as demonstrated in [8, 14]. The transmission line parameters of the phase-shifter were determined using a electro-magnetic field-solver simulation. The input impedance at the feed point can be cal-

culated using a formula based on the transmission line equivalent circuit.

$$Z_{in} = \frac{Z_0}{\tanh(\gamma L_1) + \tanh(\gamma L_2)} \qquad (3.1)$$

Where Z_{in} the input impedance at the feedpoint, Z_0 is the characteristic impedance of the push-pull transmission line, γ is the complex propagation constant and $L_{1,2}$ are the lengths of the push-pull electrodes. To achieve optimal matching the total length of the phase-shifter was chosen to be 1.3 mm, resulting in a V_π of 7.7 V and a doped-waveguide insertion-loss of 4 dB. The measured effective V_π at 28 GHz is about 60 V and sufficient electrical amplification of the input signal is needed for efficient operation. The lengths L_1 (0.45 mm) and L_2 (0.95 mm) are indicated in the design layout shown in Fig. 3.5b. The S11 (10 MHz-40 GHz) of the modulator was measured by contacting it with an RF probe and measuring the reflection with a PNA-X Vector Network Analyzer. The resulting S11 and Smith chart are shown in Fig. 3.5c and Fig. 3.5d. As can be seen in Fig. 3.5c, the return loss is better than 10 dB from 26 to 31 GHz. From the Smith chart it is clear that at low frequencies the modulator behaves as a capacitor and approaches 50 Ohm for higher frequencies. From this we can conclude that the off-center feeding is an interesting approach for narrow-band impedance matching.

(a)

(b)

(c)

(d)
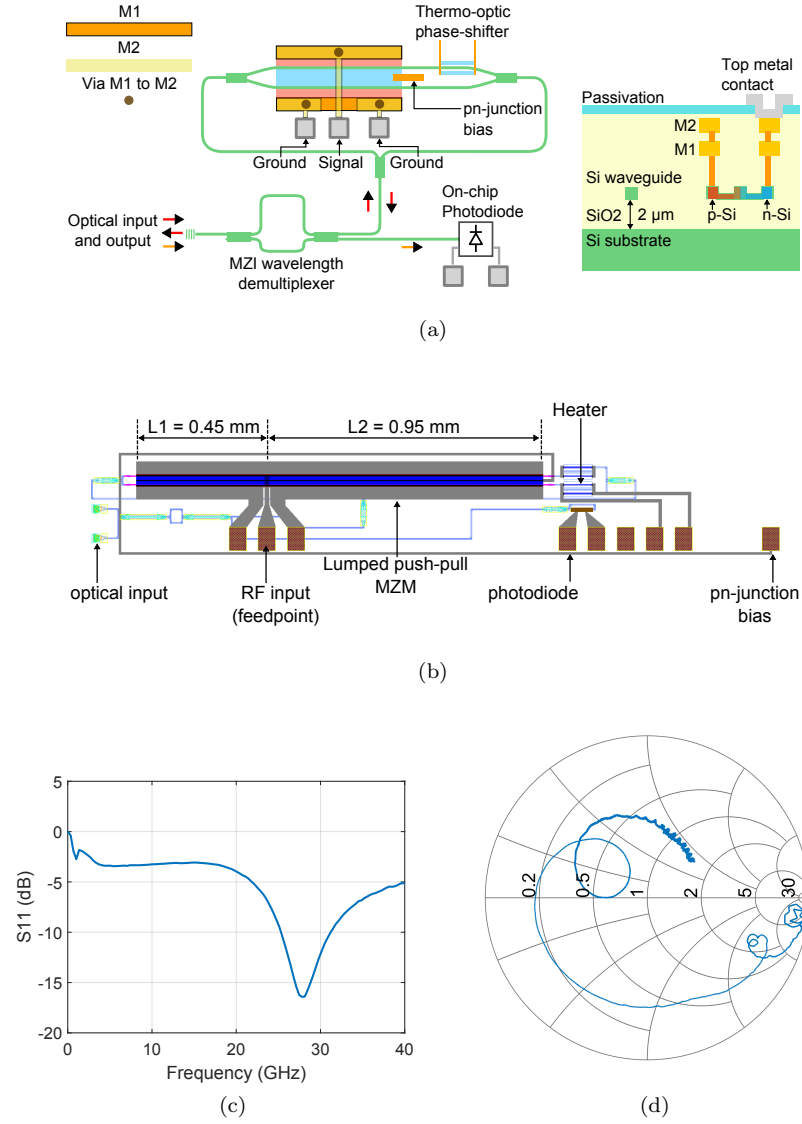
Figure 3.5: (a) Schematic layout of the reflective Mach-Zehnder modulator with off-center-fed electrode, and the transceiver structure in which it is embedded. (b) Fabrication layout of the reflective Mach-Zehnder modulator with off-center-fed phase-shifter electrode. (c) The measured S11 of the off-center fed electrode for a reverse bias of 1.5 V over the pn-junctions. (d) Plot of the S11 from 10 MHz to 67 GHz in a Smith chart of the off-center fed electrode MZM.

3.5 Narrow-band stub-matched silicon MZM

As discussed in the previous section, narrow-band impedance matching can be achieved avoiding the use of on-chip resistors. This is interesting as resistive matching dissipates power when compared to pure reactive matching. For example, stub-matching can provide low-loss narrow-band impedance matching. Stubs are short pieces of transmission line which are connected on one side to the feed transmission line. The use of stubs is a well known matching technique used in microwave and RF engineering. An extensive discussion of this subject can be found in most handbooks on microwave engineering [15]. The use of stub-matching has been previously demonstrated for narrow-band impedance matching of resonant $LiNbO_3$ electrodes [8, 16]. With this approach excellent matching was achieved for frequencies higher than 20 GHz. However, to the best of our knowledge this approach has never been implemented in silicon photonics. The imec iSiPP25G platform offers a metal layer (Cu damascene) which allows for the design of microwave transmission lines. This allowed to implement a phase shifter electrode with on-chip stub-matching. Based on the designs previously reported in [8] and [17] we chose to develop a phase-shifter with open-ended electrode and open ended stubs connected at the feed point. A schematic layout of the implementation of such a modulator on the iSiPP25G platform is shown in Fig. 3.6a. As demonstrated in [17], a stub-matched MZM electrode can be approximated using an equivalent transmission line circuit. The transmission line equivalent circuit corresponding to an open-ended electrode configuration is shown in Fig. 3.6b. Using this equivalent circuit the input impedance at the feed point can be calculated with the following formula:

$$Z_{\mathrm{in}} = \frac{1}{2}\frac{Z_1 Z_2}{Z_1 \tanh(\gamma_2 L_2) + Z_2 \tanh(\gamma_1 L_1)} \tag{3.2}$$

Where Z_{in} is the input impedance at the feed point, Z_1 is the characteristic impedance of the phase shifter transmission line, Z_2 is the characteristic impedance of the stubs, γ_1 and γ_2 are the propagation constants of the phase-shifter transmission line and stubs respectively. The length of a single side of the phase-shifter corresponds to L_1 and L_2 corresponds to the length of the stubs. The co-planar transmission lines for the stubs were designed with Keysight Advanced Design System (ADS). The phase-shifter transmission line is a co-planar waveguide of which one of the slots is loaded with the pn-doped silicon waveguide and was taken from the iSiPP25G PDK. The transmission line parameters of the phase-shifter were determined using an electro-magnetic field-solver simulation. The structure was designed to have an input impedance of 50 Ohm for a frequency of 28 GHz. The resulting length for the phase-shifter is 1.6 mm ($L_1 = 0.8$ mm), resulting

in a static V_π of 6.3 V and a phase-shifter insertion loss of 5 dB. Matching was achieved using stubs of (L_2) 0.8 mm long. A microscope image of the fabricated modulator is shown in Fig. 3.6c.

To investigate the impedance matching we performed a S11 measurement of the structure using a Keysight PNA-X vector network analyzer. In Fig. 3.7a the return loss is shown as function of the frequency. A resonance in the reflection coefficient is seen between 15 and 25 GHz, which deviates from the design target of 28 GHz. Furthermore, the 3 dB bandwidth of the S11 resonance is relatively broad (8 GHz) resulting in a low Q-factor (~ 3). The reflection coefficient plotted in a Smith chart is shown in Fig. 3.7b. As expected, for low frequencies the input impedance resembles that of a capacitor and approaches 50 Ohm at higher frequencies. Finally we measured the S21 of the phase-shifter placed in a MZI structure, the result is shown in Fig. 3.7c. Due to the strong roll-off of the modulator as a whole, it is difficult to distinguish the resonant behaviour in the S21 graph.

For further designs it would be preferable to first develop a reproducible transmission line so that further designs can be based on empirical results. The simulation of the phase-shifter transmission line is not accurate as the exact doping-profile and doping-concentrations of the the phase-shifter were not available.

(a)

(b)

(c)
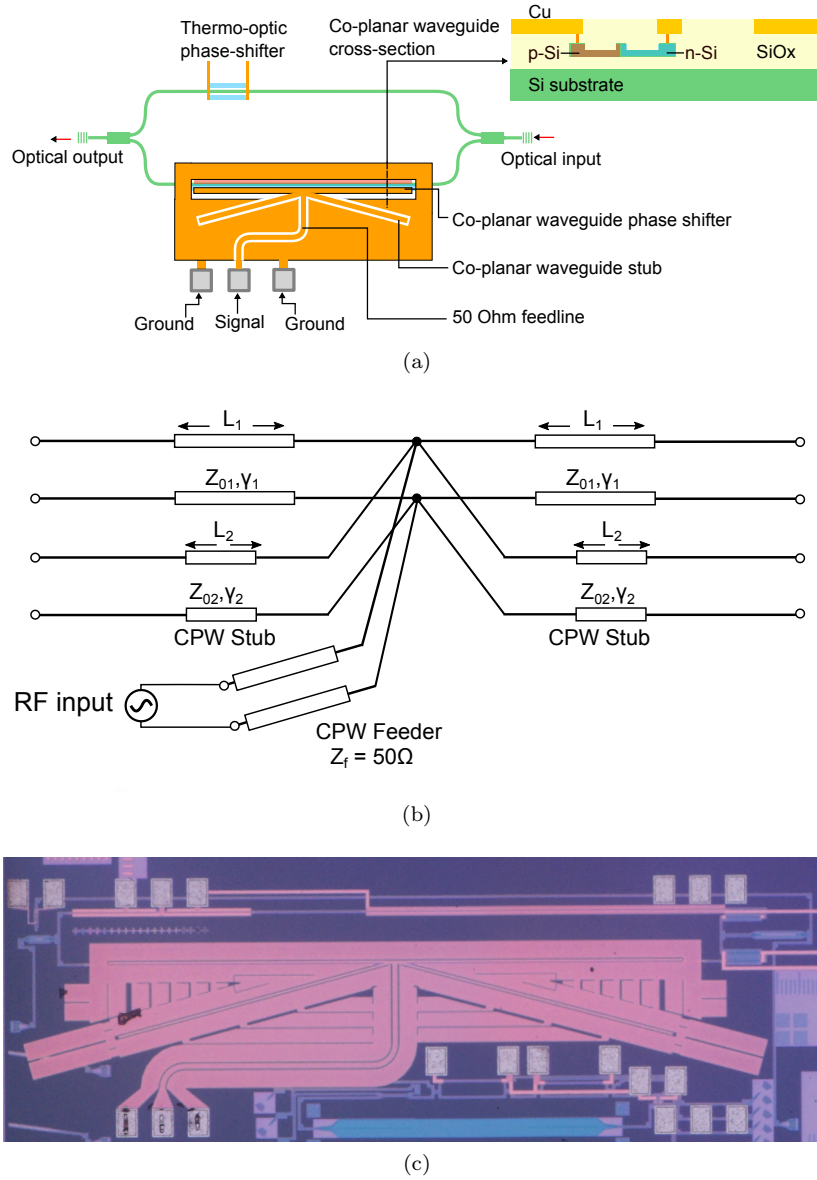
Figure 3.6: (a) Schematic layout of the stub-matched MZM. The inset shows a cross-section of the co-planar waveguide phase shifter. (b) Transmission-line-based equivalent circuit of a stub-matched silicon photonic phase-shifter electrode. (c) Microscope picture of the fabricated device.
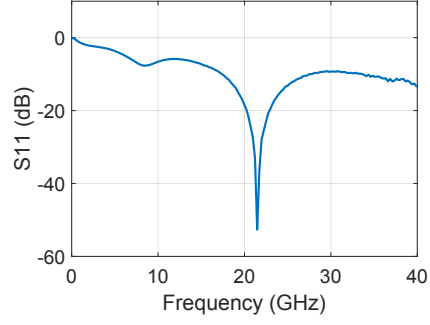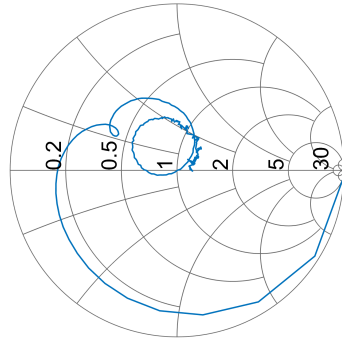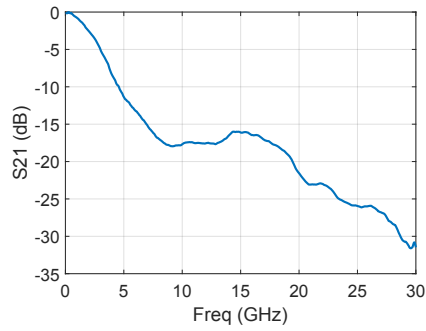
Figure 3.7: (a) Measured S11 of the stub-matched open ended silicon phase-shifter. The resonance has a Q-factor of ~ 3. (b) Reflection coefficient of the stub-matched silicon phase-shifter plotted in a Smith chart. (c) The measured small-signal modulation response (S21) of the stub-matched open ended silicon phase-shifter placed in a MZI.

3.6   III-V-on-silicon phase-shifter

Although silicon carrier-depletion phase-shifters are widely used and investigated, their efficiency is limited to voltage-length products in the order of 1-2 Vcm. For a realistic modulator length of 2 mm this results in a V_π of 5-10 V, which is rather high for many applications. An interesting alternative is the use of III-V-on-silicon, where a III-V material can be used as phase-shifter. It has been demonstrated that using an InP/AlGaInAs material a voltage-length product of 2 Vmm can be achieved [10]. This is almost an order of magnitude more efficient than a silicon carrier-depletion phase-shifter. This high efficiency was achieved by creating a material architecture where several electro-optic effects such as carrier-depletion, Pockels effect and quantum confined Stark effect are combined. Using this approach a III-V-on-silicon modulator with an analogue bandwidth of 27 GHz capable of transmitting 40 Gb/s was demonstrated [18]. A second advantage of using III-V-on-silicon is that several materials can be bonded on a single passive silicon PIC. For example, using different III-V materials a III-V-on-silicon PIC containing lasers, phase shifters and photodiodes was demonstrated [19]. We wanted to develop a phase-shifter which can be integrated on the same PIC as the III-V-on-silicon mode-locked laser described in the previous chapter to realize a fully integrated optical sampler. Therefore we developed a phase shifter similar to the design described in [10]. We developed a similar hybrid co-planar waveguide structure adapted for the integration with a mode-locked laser on the same chip. The layer stack of the epitaxy is shown in the table below.

Layer type	Material	Thickness (nm)	Carrier density (cm^{-3})
P-doped contact	InGaAs	300	$1.5 \cdot 10^{-19}$
P-doped transition	InGaAsP	20	$5 \cdot 10^{18} \rightarrow 7 \cdot 10^{18}$
P-doped cladding	InP	1500	$2 \cdot 10^{18} \rightarrow 1 \cdot 10^{18}$
15 QWs and SCH	AlGaInAs	350	$3 \cdot 10^{18} \rightarrow 1 \cdot 10^{17}$
N-doped contact	InP	190	$3 \cdot 10^{18}$

Using this phase-shifter we designed a MZM containing two individually addressable phase-shifters. Bondpads in a Ground-Signal-Ground (GSG) arrangement with a 100 μm pitch were used so that the device can be contacted using a RF probe or wire-bonds. The optical MZI structure was realized using a 2 by 2 MMI, both for the optical input and output. A thermo-optic phase-shifter was included to provide a static bias of the MZM. A micrograph of the III-V-on-silicon MZM is shown in Fig. 3.8. The
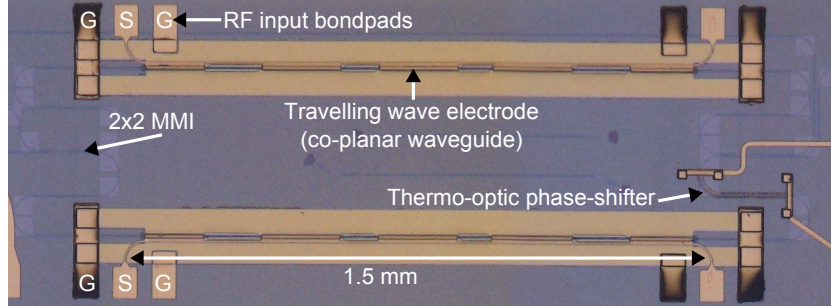
Figure 3.8: Microscope image of the III-V-on-silicon MZM containing two individual III-V-on-silicon phase-shifters and a thermo-optic phase-shifter.

design of the optical waveguide cross-section with electrode is shown in Fig. 3.9a. The device was fabricated by Dr. Zhechao Wang and mask-design and characterization was performed by the author. A cross-section of the fabricated phase-shifter (made with focused ion beam milling) was imaged using SEM and the resulting image is shown in Fig. 3.9b. To characterize the performance of the III-V-on-silicon modulator, we placed the PIC on a temperature-controlled vacuum chuck. Light was coupled in and out of the chip using vertical grating couplers and cleaved single mode fibers. The static transmission was characterized as a function of the bias on a single III-V-on-silicon phase-shifter. The result of this measurement is shown in Fig. 3.9c. From the measurement a V_π of 2.1 V and an insertion loss of 7 dB were determined. Given that the effective phase-shifter is approximately 1.5 mm long, a voltage-length product of 3.15 Vmm is found. A small-signal modulation response measurement was performed and the results are shown in Fig. 3.9d. The measurement was performed using a 40 GHz RF probe to drive a single phase-shifter. From the results plotted in Fig. 3.9d we see that the 3 dB modulation bandwidth of the phase-shifter is limited to 3-4 GHz. The reason for this very low modulation bandwidth is a bad contact between the p-doped InGaAs layer and the Ti/Au metal layer. In a separate measurement it was found that the InGaAs/metal contact behaves as a high resistance Ohmic contact at low frequencies. However, at high frequencies the contact shows a much lower impedance which we believe to be due to capacative coupling. As can be seen in Fig. 3.9b the metal layer seems to show cracking close to the InGaAs layer. However, even with the poor high-frequency operation the III-V-on-silicon modulator still has a reasonable performance even at higher frequencies due to the low V_π.
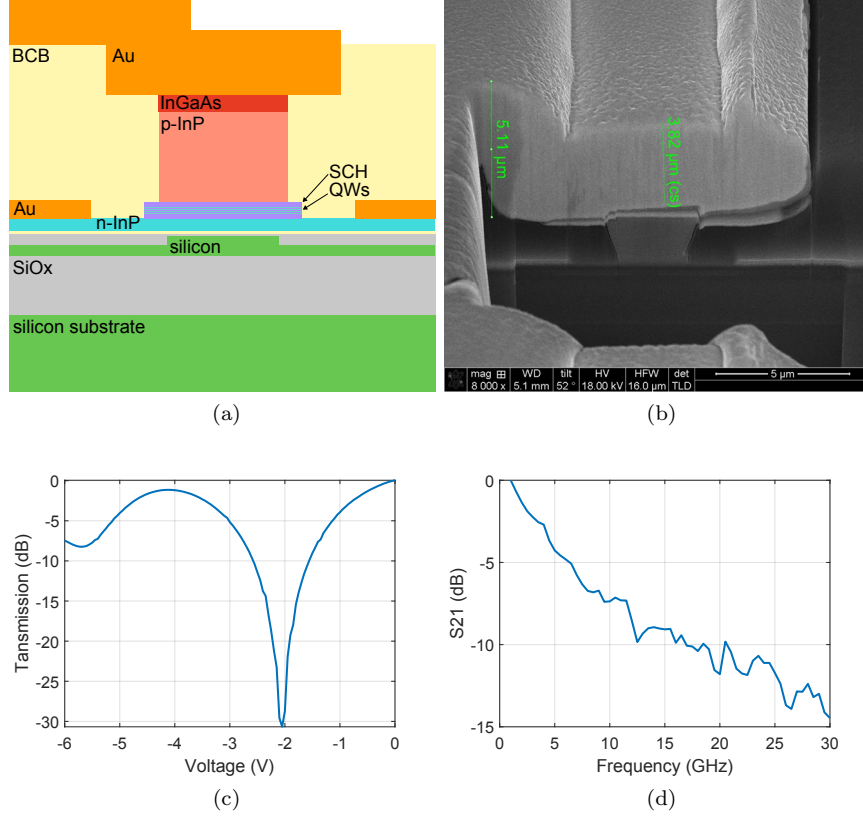
Figure 3.9: (a) Schematic cross-section of the phase-shifter with different material layers indicated. (b) SEM image of the cross-section of the III-V-on-silicon phase-shifter with thickness of the electrode indicated. (c) Normalized static transmission characteristic of the III-V-on-silicon MZM as a function of the static voltage applied across the phase shifter. (d) Small-signal modulation characteristic of the MZM.

3.7 Conclusion

In summary, we developed several phase-shifters and MZMs both using the iSiPP25G and III-V-on-silicon technology. The IQ-modulator shows promising performance and can be used for many applications. The non-resistive matching is a promising approach, but further development of transmission line modeling and characterization is needed to provide more reliable design methodologies. Finally, we successfully developed a III-V-on-silicon phase-shifter with moderate performance.

References

[1] W. M. Green, M. J. Rooks, L. Sekaric, and Y. A. Vlasov. *Ultra-compact, low RF power, 10 Gb/s silicon Mach-Zehnder modulator.* Optics Express, 15(25):17106, 2007.

[2] T. Baba, S. Akiyama, M. Imai, and T. Usuki. *25-Gb/s broadband silicon modulator with 031-V·cm VπL based on forward-biased PIN diodes embedded with passive equalizer.* Optics Express, 23(26):32950, dec 2015.

[3] D. Patel, S. Ghosh, M. Chagnon, A. Samani, V. Veerasubramanian, M. Osman, and D. V. Plant. *Design, analysis, and transmission system performance of a 41 GHz silicon photonic modulator.* Optics Express, 23(11):14263, jun 2015.

[4] A. Samani, M. Chagnon, D. Patel, V. Veerasubramanian, S. Ghosh, M. Osman, Q. Zhong, and D. V. Plant. *A Low-Voltage 35-GHz Silicon Photonic Modulator-Enabled 112-Gb/s Transmission System.* IEEE Photonics Journal, 7(3):1–13, jun 2015.

[5] A. Samani, D. Patel, M. Chagnon, E. El-Fiky, R. Li, M. Jacques, N. Abadía, V. Veerasubramanian, and D. V. Plant. *Experimental parametric study of 128 Gb/s PAM-4 transmission system using a multi-electrode silicon photonic Mach Zehnder modulator.* Optics Express, 25(12):13252, jun 2017.

[6] E. El-Fiky, A. Samani, M. Sowailem, M. Osman, M. Jacques, D. Patel, M. G. Saber, L. Xu, Z. Xing, M. Xiang, and D. V. Plant. *Dual Parallel Multielectrode Traveling Wave MachZehnder Modulator for 200 Gb/s Intra-datacenter Optical Interconnects.* IEEE Photonics Journal, 11(1):1–9, feb 2019.

[7] M. Pantouvaki, S. A. Srinivasan, Y. Ban, P. De Heyn, P. Verheyen, G. Lepage, H. Chen, J. De Coster, N. Golshani, S. Balakrishnan, P. Absil, and J. Van Campenhout. *Active Components for 50 Gb/s NRZ-OOK Optical Interconnects in a Silicon Photonics Platform.* Journal of Lightwave Technology, 35(4):631–638, feb 2017.

[8] R. Krahenbuhl and M. Howerton. *Investigations on short-path-length high-speed optical modulators in LiNbO with resonant-type electrodes.* Journal of Lightwave Technology, 19(9):1287–1297, 2001.

[9] R. Krahenbuhl, J. Cole, R. Moeller, and M. Howerton. *High-speed optical modulator in LiNbO with cascaded resonant-type electrodes.* Journal of Lightwave Technology, 24(5):2184–2189, may 2006.

[10] H.-W. Chen, Y.-h. Kuo, and J. E. Bowers. *High speed hybrid silicon evanescent Mach-Zehnder modulator and switch.* Optics Express, 16(25):20571, dec 2008.

[11] P. P. Absil, P. De Heyn, H. Chen, P. Verheyen, G. Lepage, M. Pantouvaki, J. De Coster, A. Khanna, Y. Drissi, D. Van Thourhout, and J. Van Campenhout. *Imec iSiPP25G silicon photonics: a robust CMOS-based photonics technology platform.* page 93670V, feb 2015.

[12] E. H. W. Chan and R. A. Minasian. *Microwave photonic downconverter with high conversion efficiency.* Journal of Lightwave Technology, 30(23):3580–3585, 2012.

[13] D. Patel, V. Veerasubramanian, S. Ghosh, A. Samani, Q. Zhong, and D. V. Plant. *High-speed compact silicon photonic Michelson interferometric modulator.* Optics Express, 22(22):26788, nov 2014.

[14] T. Kawanishi, S. Oikawa, K. Higuma, M. Sasaki, and M. Izutsu. *Design of LiNbO 3 Optical Modulator with an Asymmetric Resonant Structure.* IEICE Transactions on Electronics, 85(1):150–155, 2002.

[15] D. M. Pozar. *Microwave engineering.* John Wiley & Sons, 2009.

[16] S. Oikawa, T. Kawanishi, K. Higuma, Y. Matsuo, and S. Member. *Double-Stub Structure for Resonant-Type Optical Modulators Using 20-m-Thick Electrode.* 15(2):2002–2004, 2003.

[17] S. Oikawa, T. Kawanishi, K. Higuma, Y. Matsuo, and M. Izutsu. *Double-stub structure for resonant-type optical modulators using 20-μm-thick electrode.* IEEE Photonics Technology Letters, 15(2):221–223, feb 2003.

[18] H.-W. Chen, J. D. Peters, and J. E. Bowers. *Forty Gb/s hybrid silicon Mach-Zehnder modulator with low chirp.* Optics Express, 19(2):1455, jan 2011.

[19] C. Zhang, P. A. Morton, J. B. Khurgin, J. D. Peters, and J. E. Bowers. *Ultralinear heterogeneously integrated ring-assisted MachZehnder interferometer modulator on silicon.* Optica, 3(12):1483, dec 2016.

Chapter 4

High-power III-V-on-silicon semiconductor optical amplifier

In this chapter we present the design, fabrication and characterization of a high-saturation power and high-gain III-V-on-silicon semiconductor optical amplifier. The material presented in this chapter has in part been published in [1].

4.1 Introduction

Photonic Integrated Circuits (PICs) have been rapidly developing in the last years and have seen an increasing number of applications. Because of the advancing maturity of photonic technology platforms, such as silicon photonics, complex PICs such as coherent solid-state LIDAR have been demonstrated [2]. Even a fully integrated III-V-on-silicon two dimensional optical beam scanner was realized containing more than 100 integrated optical components including lasers and amplifiers [3]. Not only LIDAR subsystems have been implemented using (III-V-on-)silicon photonics, but also integrated microwave photonic synthesizer circuits have been demonstrated in III-V-on-silicon [4, 5]. However, the performance of these circuits is often limited by the availability of high-gain and high-output power optical amplifiers that can be integrated in such a PIC [6]. This issue is not limited to LIDAR PICs, but is shared by analogue transceivers, coherent transceivers

and integrated microwave photonic circuits. In analogue links, such as described in Chapter 5, the optical power levels often dominate the link gain and high-output power amplifiers can significantly improve transmission quality [7].

Although several semiconductor optical amplifiers (SOAs) have been developed, both on the InP platform and the hybrid III-V-on-silicon platform, achieving high gain and high output power remains challenging. The highest output power from a C-band InP discrete SOA was achieved using a slab coupled optical waveguide (SCOW) design [8]. Although this design provides watt-level output power, this type of amplifier demands a dedicated layer stack and an amplifier length of 1 cm, making the co-integration with other photonic components not straightforward. A chip saturation output power of 19.6 dBm and a gain of >15 dB was reported for a discrete InP/InGaAsP SOA with 3 quantum wells [9]. Again, in monolithic integration many different components have to be integrated together and specific integration for high-power SOAs is not trivial [10, 11]. SOAs have also been developed on the III-V-on-silicon platform, both using direct die-to-wafer bonding and divinylsiloxane-bis-benzocyclobutene (DVS-BCB) adhesive die-to-wafer bonding. In the latter approach the bonding is facilitated by spin-coating a thin layer (40-100 nm) of DVS-BCB, a planarizing spin-on polymer, on the silicon PIC. In [12] III-V/Si SOA designs are presented where the wall-plug efficiency is optimized for 10 dB gain SOAs with 13 dBm of on-chip output power. A packaged III-V-on-silicon amplifier with 28 dB gain is demonstrated in [13], but the saturation power is not discussed and the highest mentioned on-chip output power is 12 dBm. More recently III-V-on-silicon SOAs using direct die-to-wafer bonding were fabricated with 14 dB gain and 16.8 dBm saturation power [6]. This was achieved with a 2 mm long amplifier, using a 3 quantum well material. The power consumption of the device was approximately 640 mW.

In this chapter we present the design, fabrication and characterization of an array of hybrid III-V-on-silicon SOAs. The array consists of 5 SOAs with identical cross-section but with different lengths, ranging from 0.95 to 1.85 mm. This enables to assess the impact of the device length on the amplifier performance, as well as to enable loss measurements (internal loss of the amplifier and the loss of the III-V/silicon transition sections). A 1.45 mm long SOA was measured to have an unsaturated gain of 27 dB and an on-chip amplified output signal of 17.5 dBm. This result was achieved at a current density of 4.9 kA/cm^2 and a power consumption of 540 mW. The 1.2 mm long SOA provides 24.7 dB of gain and a maximum on-chip output power of 17.2 dBm at the same current density (power consumption of 410 mW).

4.2 Design

As discussed in the previous section, there are several approaches to achieve an integrated high-output-power amplifier. However, the two main strategies are to either have low confinement in the active region or having a large cross-section active region. This is illustrated by the formula for the saturation power P_s [6], which is defined as the optical power for which the gain coefficient g is halved:

$$P_s = \frac{hc}{\lambda} \frac{\sigma_{xy}}{a\tau\Gamma_{xy}}, \quad g = \frac{g_0}{1 + P/P_s} \tag{4.1}$$

Where h is the Planck constant, c is the speed of light, λ is the wavelength in vacuum, σ_{xy} is the cross-sectional area of the active material, a is the differential gain, τ is the carrier lifetime, Γ_{xy} is the confinement factor of the optical mode in the active region, g_0 is the maximum gain coefficient and P is the optical power. The expression for P_s and g can be derived from the basic rate equations for a semiconductor optical amplifier. The optical input power $P_{in} = P(z = 0)$ and output power $P_{out} = P(z = L)$ are related to each other through the amplifier equation:

$$\frac{dP}{dz} = P\frac{g_0}{1 + P/P_s}. \tag{4.2}$$

For further details on saturation effects of optical amplifiers we refer to existing literature [14].

Using a hybrid III-V-on-silicon mode is an appealing strategy to lower the confinement factor, similar to the slab coupled SOA [8]. Furthermore, it is beneficial to realize the amplifier using the same fabrication process and material that can also be used for other active devices to form complex photonic integrated circuits. While other high-output power amplifiers had few quantum wells to optimize output power, it is appealing to implement a high saturation power amplifier using III-V epitaxial material that can also be used for the realization of advanced laser sources on the same circuit, such as directly modulated lasers for example, which typically require more quantum wells [15].

Therefore, the epitaxial layer stack used in this work consists of a 6 quantum well active region, consisting of InGaAsP quantum wells (1.55 μm wavelength, 7 nm thick) and InGaAsP barriers (bandgap wavelength of 1.17 μm, 9 nm thick). A 100 nm thick separate confinement heterostructure above and below the active region is realized using InGaAsP (bandgap wavelength of 1.17 μm). The top p-contact consists of a highly doped InGaAs layer (300 nm thick) and the p-type cladding consists of a gradient p-doped InP layer (1500 nm thick). A 200 nm thick n-doped InP layer

is used for the n-contact. A cross-section of the III-V waveguide with the different layers indicated is shown in Fig. 4.1(a).

The silicon rib waveguide underneath the III-V is realized in a 400 nm thick silicon device layer on a 2 μm thick buried oxide layer, by a 180 nm partial etch. The silicon rib waveguide is 4 μm wide, while the III-V mesa is 5 μm wide. The mode is laterally confined by the mesa and the silicon waveguide. The active region is 0.5 μm wider than the p-InP mesa to reduce the interaction between the guided mode and the sidewalls. A simulated hybrid mode-profile is shown in Fig. 4.1(b). The mode-profile was simulated using FIMMwave and an optical confinement of 0.7 % per well is found for this waveguide design. Simulation of the mode-profile without a silicon waveguide underneath the InP waveguide results of a confinement of 1.5 % per well. This illustrates that the silicon waveguide can be used to considerably reduce the mode confinement in the active region.

Since the amplifier is meant to be used in a photonic circuit, tapering to a single-mode 650 nm wide silicon rib waveguide is implemented. As shown in Fig. 4.1(c) the transition from the single mode waveguide to the amplifier happens in two steps: first the silicon waveguide is adiabatically tapered from 650 nm to 4 μm over a length of 150 μm. Then the III-V waveguide structure is tapered, which is shown in detail in Fig. 4.1(d). The III-V waveguide tapers in two parts from 0.6 μm to 5 μm, the first part tapers from 0.6 μm to 1 μm over a length of 80 μm. The narrow III-V waveguide width is achieved using an anisotropic etch of the p-type InP cladding, creating a V-shaped waveguide as described in [16]. In the second part of the taper the III-V waveguide widens from 1 to 5 μm over a distance of 100 μm. However, the active region is kept wider than the cladding layer to minimize interaction between the confined optical mode and the sidewalls. Due to the large confinement in the silicon waveguide, the mode mismatch between the silicon waveguide and the hybrid III-V-on-silicon amplifier is small. The coupling efficiency of the taper and back-reflections of the taper-tip were simulated using FIMMWave and FIMMprop software. It was found that the reflections at the III-V taper tip are below -40 dB and coupling losses are < 0.5 dB per taper.

4.3   Fabrication

The fabrication of the amplifiers was achieved using DVS-BCB bonding of the above discussed III-V material, as described with more detail in [17]. The fabrication of this device was carried out by Dr. Ruijun Wang, while the design, simulation and characterization was performed by the author. A bonding layer thickness of 40 nm was used. First a SiN hard mask is defined
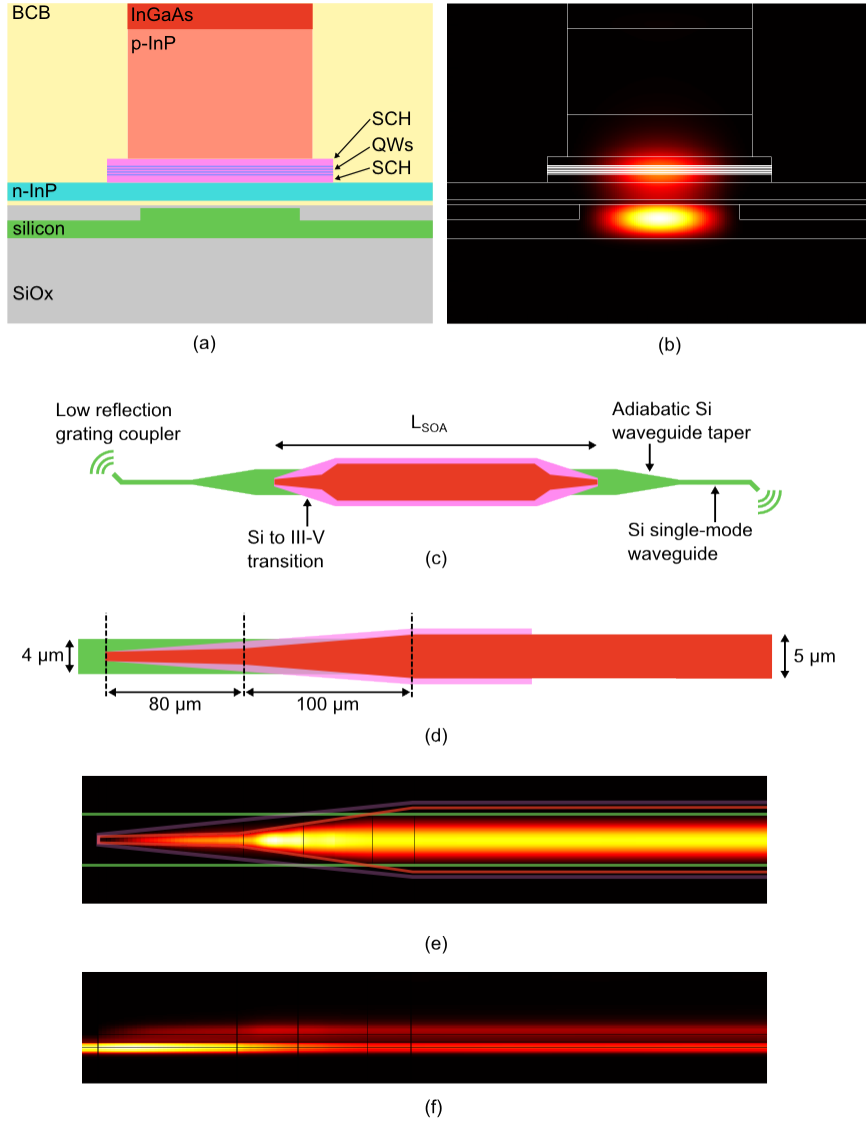
Figure 4.1: (a) Cross-section of the amplifier waveguide. (not to scale) (b) Hybrid optical mode in the amplifier, simulated using FIMMwave. (c) Top-view of the silicon waveguide, p-InP mesa and active region. (d) Detailed schematic of the silicon to hybrid III-V-on-silicon waveguide taper. (e) Simulated propagation of the optical coupling from the silicon waveguide to the gain waveguide (top view). Only the intensity in the active layer is shown. The silicon waveguide, p-InP mesa and active area are indicated with colored lines. (f) Side-view of the simulated coupling from the silicon waveguide to the gain waveguide.

to etch the InP mesa. Then the heavily p-doped InGaAs contact layer is dry-etched, after which the p-InP cladding layer is wet etched in diluted HCl. This anisotropic wet-etch creates the V-shape of the cladding layer. A second nitride hard mask was then deposited to perform a wet-etch of the active region using a $H_2SO_4 : H_2O_2 : H_2O$ solution. Then 30-20-50 nm of Ni-Ge-Au is deposited on the n-InP to create metallic n-contacts. Finally the n-InP is etched again using diluted HCl. Once the III-V waveguides are formed the structures are passivated and planarized using DVS-BCB. To electrically contact the III-V waveguide the DVS-BCB is etched back to reveal the top InGaAs contact and vias are etched in the DVS-BCB such that the metallic n-contacts are exposed. In a final step 40-800 nm Ti-Au is deposited using a lift-off process to form the final contact layer and to define contact pads, which allow for easy electrical probing.

The array of 5 SOAs with different lengths was fabricated on a PIC together with several test-structures and other devices. A microscope image of the fabricated sample is shown in Fig. 4.2. The amplifier lengths are varied from 0.95 mm to 1.85 mm, including two 0.18 mm long tapers. A cross-section of the III-V-on-silicon amplifier structure is shown in Fig. 4.3.
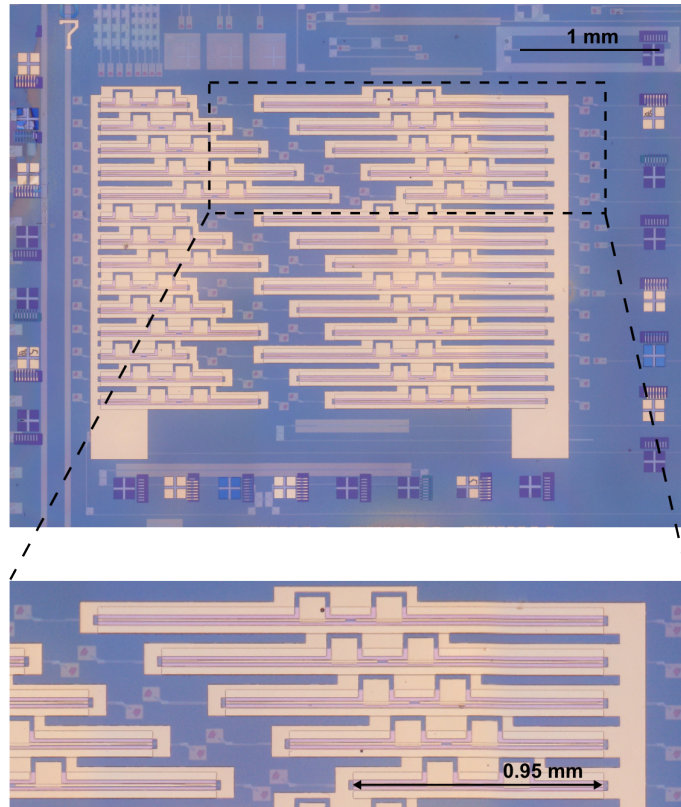
Figure 4.2: Microscope image of the III-V-on-silicon PIC with a zoom-in of the five high-power SOAs.
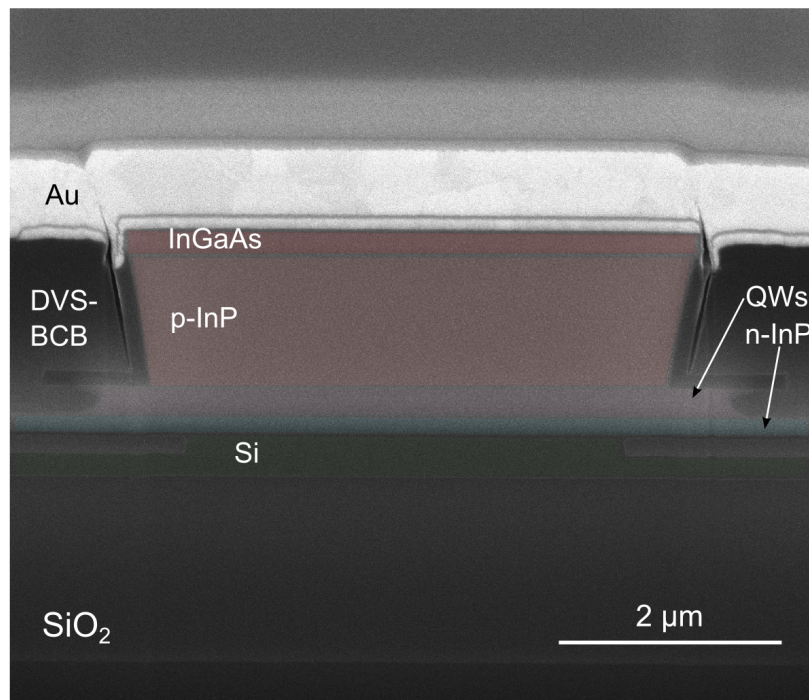
Figure 4.3: SEM image of the gain waveguide cross section.

4.4 Gain characterization

The III-V-on-silicon SOA PIC was placed on a temperature-controlled stage and kept at a constant 20ºC for all measurements. The device under test is optically probed using cleaved standard single mode fibers on a fiber stage. Reflectionless grating couplers with a simulated back-reflection below -40 dB were used [18]. The amplifiers were electrically contacted using probe needles. The SOAs have a differential resistance ranging from 3.4 Ω (3630 μm^2 surface area) to 1.7 Ω (8630 μm^2 surface area), for the 0.95 mm to 1.85 mm long SOAs respectively. This is similar to the differential resistance found for a full InP SOA (6300 μm^2 surface area) [9]. The differential resistance was determined for an injection current density of 4.9 kA/cm^2 for all amplifiers. The three shortest amplifiers were biased at 175 mA (1.57 V), 237 mA (1.74 V) and 300 mA (1.8 V) for a length of 0.95 mm, 1.2 mm and 1.45 mm respectively. The two longest amplifiers were biased at 362 mA (1.97 V) and 425 mA (1.79 V) for a length of 1.6 mm and 1.85 mm respectively. The good electrical characteristics of the amplifier enables high current injection with low self-heating, which is essential for high-power operation.

To characterize the on-chip gain of the amplifier, the grating coupler losses must be accurately known as a function of wavelength. Therefore, reference passive silicon waveguides were placed on the chip, in between the amplifiers, such that the reference waveguides undergo the same processing as the passive waveguides and couplers of the SOAs. The losses of the grating couplers were determined using a tunable laser (Santec TSL-510) and an optical spectrum analyzer (Anritsu OSA MS9740A), as shown in Fig. 4.4. As the gain peak of the III-V material is approximately 1575 nm, the angle of the fiber holders was optimized so that the wavelength of maximum transmission coincides with the gain peak. At this optimum angle the grating couplers have a loss of 9.5 dB per coupler at a wavelength of 1575 nm. The grating couplers were optimized for low reflection and in future applications could be replaced by high-efficiency edge-couplers [19]. To determine the gain of the amplifiers, the same measurement set-up was used. The output power of the SOA was measured with the OSA, in a 1 nm band centered at the input laser wavelength. This ensures that the measured output power is not distorted by the amplified spontaneous emission (ASE).

It was found that all amplifiers, except for the shortest, could generate an on-chip output power exceeding 17 dBm, for an on-chip optical input power of 3 dBm. However, the 1.6 and 1.85 mm long amplifier didn't achieve higher output power or gain than the 1.45 mm. Furthermore, for the two longest amplifiers parasitic lasing occurred for on-chip optical input powers
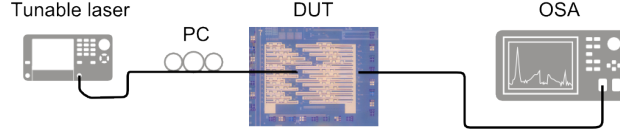
Figure 4.4: Schematic overview of the measurement set-up. PC: polarization controller; DUT: device under test; OSA: optical spectrum analyzer.

smaller than -10 dBm. From the free spectral range of the lasing modes it was deduced that the lasing is due to parasitic reflections of the cleaved single mode fibers. Optimum gain and output power characteristics were found for the amplifiers with a length of 1.2 and 1.45 mm. Furthermore, a current density of 4.9 kA/cm^2 was chosen, as further increasing the gain current did not improve the output power at high input powers. The on-chip output power as a function of the on-chip input power for the three shortest SOAs is shown in Fig. 4.5. The shortest amplifier, 0.95 mm long, provides 20 dB of small-signal gain and 16 dBm of maximum output power. The two amplifiers with length 1.2 mm and 1.45 mm show over 17 dBm of maximum output power and 14 dB of gain for 3 dBm on-chip input power. To accurately determine the small-signal gain G_0 and gain saturation power P_s of the 1.2 mm and 1.45 mm SOA, we use the same method as described in [6]. Using the methods described in [6] allows us to provide a direct comparison between the performance of the devices. This is implemented by varying the input power of the tunable laser between -15 and +13 dBm while monitoring the SOA output power on the OSA. Both amplifiers were biased at an injection current density of 4.9 kA/cm^2 corresponding to 300 mA for the 1.45 mm SOA and 237 mA for the 1.2 mm long SOA. For this injection current the power consumption of the 1.45 mm SOA is 540 mW and that of the 1.2 mm SOA is 410 mW. The corresponding gain as a function of input power is shown in Fig. 4.6a, for a wavelength of 1575 nm, corresponding with the material gain peak in this experiment. This result is fitted with a formula used in [6] relating the gain G to the input power P_{in}, gain saturation power P_s and small-signal gain G_0:

$$G(P_{in}) = G_0 \frac{1 + P_{in}/P_s}{1 + G_0 P_{in}/P_s} \tag{4.3}$$

The small signal gain is found to be 27 dB for the 1.45 mm SOA and 25 dB for the 1.2 mm SOA. The saturation power P_s was determined from the fit procedure and was found to be 17.24 dBm for the 1.45 mm SOA and
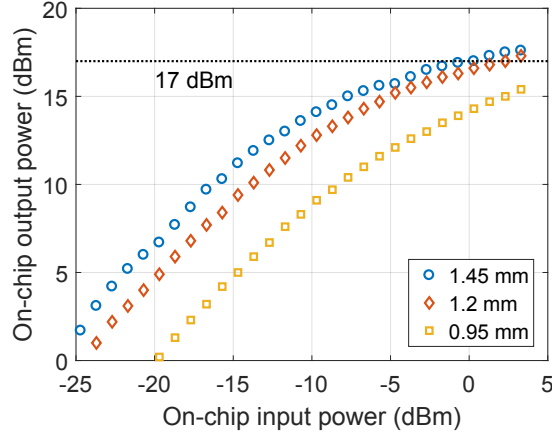
Figure 4.5: The on-chip output power as a function of the input power for three different SOA lengths.

16.72 dBm for the 1.2 mm SOA. In principle the saturation power should be identical for both amplifiers, since it only depends on the waveguide cross-section. However, since the discrepancy is small it can be explained by measurement accuracy and fabrication tolerances. To assess the optical bandwidth of the amplifiers we measured the small-signal gain as a function of wavelength of the 1.2 mm long SOA. This was achieved by sweeping the wavelength of the tunable laser from 1550 to 1610 nm with a constant output power of -10 dBm. The output power at the signal wavelength was measured with the OSA, and the transmission spectrum of the grating couplers was de-embedded to calculate the on-chip gain. As described in [20], the gain G as a function of wavelength λ can be described with the following formula:

$$G(\lambda) = G_p \exp\big[- A(\lambda - \lambda_p)^2\big]. \tag{4.4}$$

Where G_p is the peak value of the gain, λ_p is the wavelength at which the maximum gain occurs and A is a factor which determines the gain bandwidth. The gain as a function of wavelength is shown in Fig. 4.6b for a current density of 4.9 kA/cm^2. The fit gives a 1 dB small-signal gain bandwidth of 20 nm. It is of course also essential to investigate the gain at very high output powers. Therefore we analyzed the gain of the 1.45 mm amplifier in a 20 nm band centered at 1575 nm. The gain as a function of wavelength for the 1.45 mm SOA is shown in Fig. 4.6c. We see that for an input power of 3 dBm, corresponding to an output power of > 17 dBm, the gain ripple is less than 1 dB over a 20 nm span. Furthermore the gain ripple is similar for an input power of -12.5 dBm.

(a)

(b)

(c)
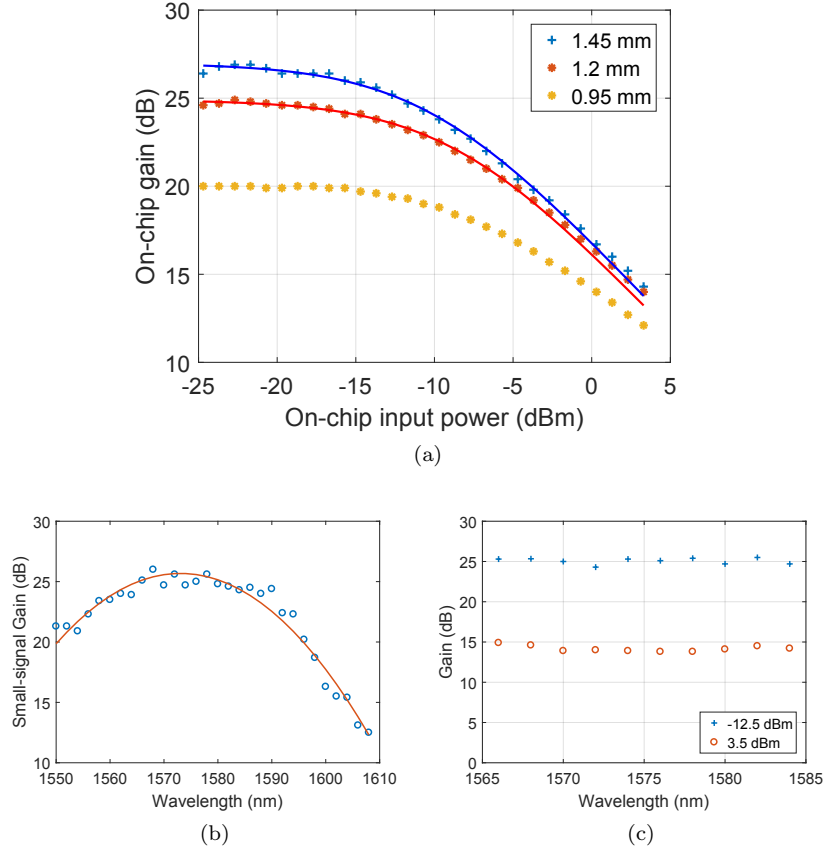
Figure 4.6: (a) The gain as a function of on-chip optical input power for three SOAs with different lengths. The points are measured values, the line was fitted. (b) Small-signal gain as a function of the wavelength of the 1.2 mm long SOA, for a current density of 4.9 kA/cm^2. The circles represent the measured values, the full line is a fitted curve. (c) The on-chip gain as a function of the wavelength for an injection current of 4.9 kA/cm^2 for the 1.45 mm long SOA. The gain was measured for both 3.5 dBm on-chip optical input power and -12.5 dBm on-chip optical input power.

Figure 4.7: Overview of the set-up used for the measurement of the transparency current density.
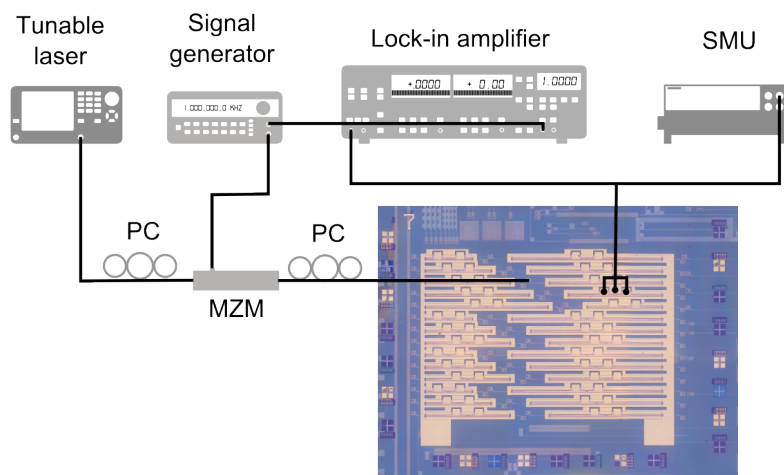
4.5 Transparency current measurement and loss characterization

The passive losses of the optical mode shown in Fig. 4.1(a) and the tapers shown in Fig. 4.1(d) can be determined by performing a cutback measurement while the amplifiers are biased at transparency current density. At transparency current the quantum wells neither absorb or amplify, therefore any measured losses are caused by the passive waveguide layers (including free carrier losses). To measure the transparency current density of the amplifiers the method described in [21] was used. This method relies on measuring the voltage drop over the amplifier when it is being operated at constant current. If we inject the amplifier with the modulated output of a tunable laser, the voltage drop across the amplifier will also be modulated. If the modulation of the voltage drop across the amplifier is detected using a lock-in amplifier the phase can also be measured. If either the wavelength or the injection current is swept, the modulation will change sign for a given wavelength and current. This occurs at transparency because at that point the modulated laser output does not affect the carrier density or the voltage drop over the amplifier. The transparency current density was determined for all 5 SOAs. The result is plotted as a function of wavelength in Fig. 4.8. As can be seen in the plot, the transparency current density varies slightly
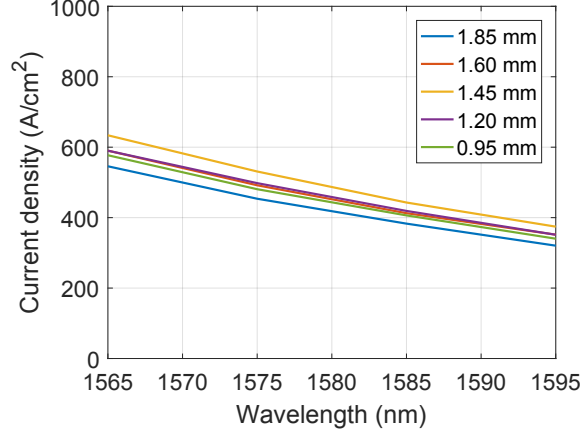
Figure 4.8: Transparency current density measurement as a function of wavelength for all 5 SOAs of different lengths.

but is not correlated to the length of the amplifier. In previous SOA designs we found that the taper introduced substantial surface recombination and the transparency current density depended on the amplifier to taper length ratio. From this we conclude that the taper design with wider quantum wells reduces this problem.

Using the measured transparency current of the amplifiers shown in Fig. 4.8, the passive losses of the amplifiers can be determined with a cut-back measurement. We find a III-V-on-silicon waveguide loss of 18 cm^{-1} and a taper loss of approximately 0.5 dB per taper at a wavelength of 1575 nm.

4.6   Noise figure measurement

To assess the on-chip noise figure (NF) we used the optical method detailed in [22, 23]. We chose to evaluate the on-chip NF instead of the external NF, as the amplifier was designed for implementation in a photonic circuit and not as a separate packaged device. However, if low-loss edge couplers would be used the amplifier could be envisioned to be used in a similar fashion as demonstrated in [13]. To determine the NF we use the OSA to measure the ASE for a given input power. Once the on-chip ASE power P_{ASE} in a band B_0 is determined together with the on-chip gain G, the on-chip NF can be determined using the following formula:

$$NF = 10 \cdot \log_{10}\left(\frac{1}{G} + 2\frac{P_{ASE}}{Gh\nu B_0}\right) \tag{4.5}$$
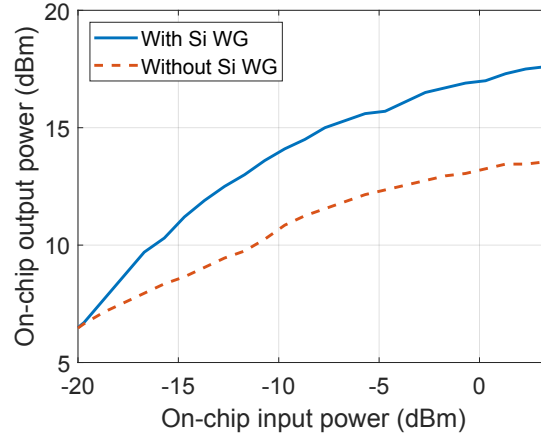
Figure 4.9: The on-chip optical output power of a 1.1 mm long optical amplifier without waveguide underneath and a 1.45 mm long optical amplifier with silicon waveguide underneath versus the on-chip optical input power.

where h is the Planck constant and ν is the photon frequency. We find that the noise figure of both the 1.45 mm and 1.2 mm SOA is approximately 9 dB for high input powers (> 0 dBm on-chip). This was measured using a injection current of 4.9 kA/cm^2 corresponding to 237 mA for the 1.45 mm SOA and 175 mA for the 1.2 mm SOA. For input powers lower than -15 dBm (on-chip) the noise figure becomes smaller than 8 dB for both devices. Both noise figures where determined for an input wavelength of 1575 nm. This NF is comparable to, but lower than, the on-chip noise figure (>10 dB) reported for a high-gain III-V-on-silicon amplifier [13].

4.7 Comparison to III-V waveguide amplifier

To further investigate the influence of the silicon waveguide underneath the III-V gain waveguide several amplifiers with an all-III-V gain waveguide were fabricated on the same chip. These amplifiers have a design almost identical to the ones in described in [17], apart from the gain waveguide width that is widened to 4 μm. An amplifier with a total length (including tapers) of 1.1 mm and a waveguide width of 4 μm was found to have a small-signal gain of 29 dB. This makes it comparable in terms of small-signal gain to the 1.45 mm long high-output-power amplifier with silicon waveguide underneath. The higher small-signal gain of the III-V amplifier is due to the higher confinement. The on-chip optical output power of the amplifier with and without silicon waveguide underneath as a function of
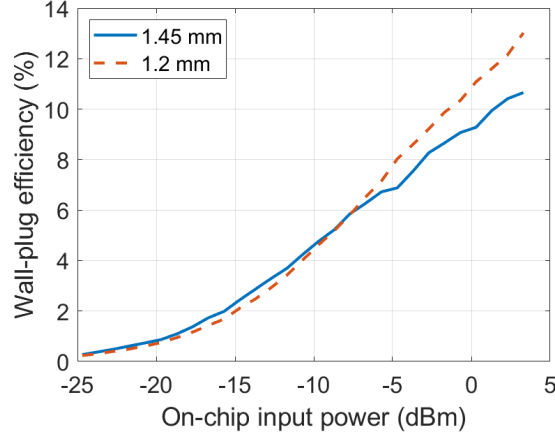
Figure 4.10: The measured wall-plug efficiency of the 1.2 mm and 1.45 mm long SOAs as function of the on-chip optical input power.

on-chip optical input power is shown in Fig. 4.9. It is clear that the silicon waveguide underneath greatly improves the fully saturated output power. For an on-chip input power of 3.5 dBm the amplifier with silicon waveguide underneath has on-chip output power of 17.5 dBm compared to 13.5 dBm for all III-V amplifier. We measured the transparency current density of the all-III-V amplifier and found it to match that of the amplifiers with the waveguide underneath. This confirms that the improved power saturation is achieved due to the design and not processing variations.

4.8   Wall-plug efficiency

Another interesting figure of merit for an optical amplifier is the Wall-Plug Efficiency (WPE). The WPE is determined by the ratio of optical output power to electrical input power and is defined [12] as

$$WPE(\%) = 100x(P_{out}P_{in})/(I_{bias}V_{bias}). \tag{4.6}$$

We measured the the WPE for both the 1.2 mm long and 1.45 mm long SOA, using the same injection current as was used to obtain the measurement results shown in Fig. 4.5. The WPE as function of on-chip optical input power is shown in Fig. 4.10. A WPE exceeding 10 % is found for on-chip input powers higher than 0 dBm.

4.9   Conclusion

In summary, we demonstrated a III-V-on-silicon SOA with a small-signal gain of 27 dB and a gain saturation power of approximately 17.2 dBm. 17.5 dBm waveguide-coupled output power is recorded, for a power consumption of 540 mW. This high output power is achieved by reducing the mode confinement in the active region, using a low-loss Si waveguide. This type of SOA can be integrated with advanced laser sources such as high-speed directly modulated lasers on the same PIC using the same epitaxial material. This device can therefore be of interest in several applications requiring high optical output power, including high-speed optical transceivers, microwave photonic systems and optical beamforming applications.

References

[1] K. Van Gasse, R. Wang, and G. Roelkens. *27 dB gain IIIV-on-silicon semiconductor optical amplifier with > 17 dBm output power.* Optics Express, 27(1):293, jan 2019.

[2] C. V. Poulton, A. Yaacobi, D. B. Cole, M. J. Byrd, M. Raval, D. Vermeulen, and M. R. Watts. *Coherent solid-state LIDAR with silicon photonic optical phased arrays.* Optics letters, 42(20):4091–4094, 2017.

[3] J. C. Hulme, J. K. Doylend, M. J. R. Heck, J. D. Peters, M. L. Davenport, J. T. Bovington, L. A. Coldren, and J. E. Bowers. *Fully integrated hybrid silicon two dimensional beam scanner.* Opt. Express, 23(5):5861–5874, 2015.

[4] J. Hulme, M. J. Kennedy, R.-L. Chao, L. Liang, T. Komljenovic, J.-W. Shi, B. Szafraniec, D. Baney, and J. E. Bowers. *Fully Integrated Microwave Frequency Synthesizer On Heterogeneous Silicon-III/V.* Opt. Express, 25(3):2422–2431, feb 2017.

[5] D. T. Spencer, T. Drake, T. C. Briles, J. Stone, L. C. Sinclair, C. Fredrick, Q. Li, D. Westly, B. R. Ilic, A. Bluestone, and Others. *An optical-frequency synthesizer using integrated photonics.* Nature, 557(7703):81–85, 2018.

[6] M. L. Davenport, S. Skendzic, N. Volet, J. C. Hulme, M. J. R. Heck, and J. E. Bowers. *Heterogeneous Silicon/IIIV Semiconductor Optical Amplifiers.* IEEE Journal of Selected Topics in Quantum Electronics, 22(6):78–88, nov 2016.

[7] C. Cox, E. Ackerman, G. Betts, and J. Prince. *Limits on the performance of RF-over-fiber links and their impact on device design.* IEEE Transactions on Microwave Theory and Techniques, 54(2):906–920, feb 2006.

[8] P. W. Juodawlkis, J. J. Plant, W. Loh, L. J. Missaggia, F. J. O'Donnell, D. C. Oakley, A. Napoleone, J. Klamkin, J. T. Gopinath, D. J. Ripin, and Others. *High-power, low-noise 1.5-μm slab-coupled optical waveguide (SCOW) emitters: physics, devices, and applications.* IEEE Journal of Selected Topics in Quantum Electronics, 17(6):1698–1714, 2011.

[9] K. Morito, S. Tanaka, S. Tomabechi, and A. Kuramata. *A broadband MQW semiconductor optical amplifier with high saturation output power and low noise figure.* IEEE photonics technology letters, 17(5):974–976, 2005.

[10] M. Smit, X. Leijtens, H. Ambrosius, E. Bente, J. van der Tol, B. Smalbrugge, T. de Vries, E.-J. Geluk, J. Bolk, R. van Veldhoven, L. Augustin, P. Thijs, D. D'Agostino, H. Rabbani, K. Lawniczuk, S. Stopinski, S. Tahvili, A. Corradi, E. Kleijn, D. Dzibrou, M. Felicetti, E. Bitincka, V. Moskalenko, J. Zhao, R. Santos, G. Gilardi, W. Yao, K. Williams, P. Stabile, P. Kuindersma, J. Pello, S. Bhat, Y. Jiao, D. Heiss, G. Roelkens, M. Wale, P. Firth, F. Soares, N. Grote, M. Schell, H. Debregeas, M. Achouche, J.-L. Gentner, A. Bakker, T. Korthorst, D. Gallagher, A. Dabbs, A. Melloni, F. Morichetti, D. Melati, A. Wonfor, R. Penty, R. Broeke, B. Musk, and D. Robbins. *An introduction to InP-based generic integration technology*. Semiconductor Science and Technology, 29(8):83001, 2014.

[11] F. M. Soares, M. Baier, T. Gaertner, M. Feyer, M. Möhrle, N. Grote, and M. Schell. *High-Performance InP PIC Technology Development based on a Generic Photonic Integration Foundry*. In Optical Fiber Communication Conference, pages M3F—-3. Optical Society of America, 2018.

[12] S. Cheung, Y. Kawakita, K. Shang, and S. J. B. Yoo. *Theory and design optimization of energy-efficient hydrophobic wafer-bonded III-V/Si hybrid semiconductor optical amplifiers*. Journal of Lightwave Technology, 31(24):4057–4066, 2013.

[13] P. Kaspar, G. de Valicourt, R. Brenot, M. A. Mestre, P. Jennevé, A. Accard, D. Make, F. Lelarge, G. Duan, N. Pavarelli, M. Rensing, C. Eason, P. O'Brien, S. Olivier, S. Malhouitre, C. Kopp, C. Jany, and S. Menezo. *Hybrid III-V/Silicon SOA in Optical Network Based on Advanced Modulation Formats*. IEEE Photonics Technology Letters, 27(22):2383–2386, nov 2015.

[14] W. Qiang and Others. *Semiconductor optical amplifiers*. World scientific, 2013.

[15] A. Abbasi, J. Verbist, J. Van Kerrebrouck, F. Lelarge, G.-H. Duan, X. Yin, J. Bauwelinck, G. Roelkens, and G. Morthier. *28 Gb/s direct modulation heterogeneously integrated C-band InP/SOI DFB laser*. Optics express, 23(20):26479–26485, 2015.

[16] G. Roelkens, A. Abassi, P. Cardile, U. Dave, A. De Groote, Y. De Koninck, S. Dhoore, X. Fu, A. Gassenq, N. Hattasan, and Others. *III-V-on-silicon photonic devices for optical communication and sensing*. In Photonics, volume 2, pages 969–1004. Multidisciplinary Digital Publishing Institute, 2015.

[17] G. Roelkens, A. Abassi, P. Cardile, U. Dave, A. de Groote, Y. de Koninck, S. Dhoore, X. Fu, A. Gassenq, N. Hattasan, Q. Huang, S. Kumari, S. Keyvaninia, B. Kuyken, L. Li, P. Mechet, M. Muneeb, D. Sanchez, H. Shao, T. Spuesens, A. Subramanian, S. Uvin, M. Tassaert, K. van Gasse, J. Verbist, R. Wang, Z. Wang, J. Zhang, J. van Campenhout, X. Yin, J. Bauwelinck, G. Morthier, R. Baets, and D. van Thourhout. *III-V-on-silicon photonic devices for optical communication and sensing.* Photonics, 2(3), 2015.

[18] D. Vermeulen, Y. De Koninck, Y. Li, E. Lambert, W. Bogaerts, R. Baets, and G. Roelkens. *Reflectionless grating couplers for Silicon-on-Insulator photonic integrated circuits.* Optics express, 20(20):22278–22283, 2012.

[19] B. B. Bakir, A. V. de Gyves, R. Orobtchouk, P. Lyan, C. Porzier, A. Roman, and J. . Fedeli. *Low-Loss ($>$1 dB) and Polarization-Insensitive Edge Fiber Couplers Fabricated on 200-mm Silicon-on-Insulator Wafers.* IEEE Photonics Technology Letters, 22(11):739–741, 2010.

[20] N. Volet, A. Spott, E. J. Stanton, M. L. Davenport, L. Chang, J. D. Peters, T. C. Briles, I. Vurgaftman, J. R. Meyer, and J. E. Bowers. *Semiconductor optical amplifiers at 2.0-μm wavelength on silicon.* Laser & Photonics Reviews, 11(2):1600165, 2017.

[21] L. F. Tiemeijer, P. J. A. Thijs, J. J. M. Binsma, and T. V. Dongen. *Direct measurement of the transparency current and valence band effective masses in tensile and compressively strained InGaAs/InP multiple quantum-well laser amplifiers.* Applied physics letters, 60(5):554–556, 1992.

[22] D. M. Baney, P. Gallion, and R. S. Tucker. *Theory and measurement techniques for the noise figure of optical amplifiers.* Optical fiber technology, 6(2):122–154, 2000.

[23] M. Movassaghi, M. K. Jackson, V. M. Smith, and W. J. Hallam. *Noise figure of erbium-doped fiber amplifiers in saturated operation.* Journal of lightwave technology, 16(5):812, 1998.

Chapter 5

III-V-on-silicon photonic transceivers for Radio-over-Fiber links

In this chapter we present the experimental demonstration of an analogue photonic link based on a III-V-on-silicon directly modulated DFB laser and a waveguide-coupled germanium photodiode. The material presented in this chapter has in part been published in reference [1].

5.1 Introduction

We are on the brink of a fully connected society, where everyone and everything is constantly exchanging information. Two pillars of this future society are the fifth generation wireless network (5G) and the Internet of Things. The goals for the 5G network are incredibly ambitious: delivering 10 Gb/s connections to users, seamless connectivity, low-latency and a total data traffic increase of a 1000-fold. To achieve these ambitious goals, radio access networks (RANs) will need to be rethought. Future RANs will need to incorporate small cells, use of higher carrier frequencies and massive multiple-input multiple-output (MIMO). Especially in a cloud-RAN configuration, where the small cells are coordinated by a centralized base-station, radio-over-fiber (RoF) links can play an essential role [2]. Given the large number of links that would be needed in such a cloud RAN, a low-cost and scalable transceiver solution is needed. Integrated microwave photonics (IMWP) is the ideal technology to realize this [3].

Many promising IMWP functions and sub-systems have been demonstrated such as tunable delays, tunable filters and beamforming networks

[4, 5]. Most of these photonic integrated circuits (PICs) were realized in passive photonic technologies, using external active components. In a recent demonstration a monolithic integrated photonic microwave filter was realized on the InP platform [6], including the integration of laser sources, optical modulators and photodetectors, which is an important milestone. As a hybrid approach, III-V-on-silicon photonic integrated circuits can also be used for integrated microwave photonics, combining the low loss of silicon / silicon nitride waveguide circuits with the active functionality implemented in III-V semiconductors. This technology has shown promising results for agile microwave signal generation [7, 8] and highly linear modulators [9].

While different IMWP functions have been demonstrated, the important functionality of integrated analogue RoF transmitters (Tx) and receivers (Rx) remains to be demonstrated. In this chapter, we demonstrate the use of a III-V-on-silicon transmitter and silicon photonic receivers for RoF links. A III-V-on-silicon distributed feedback (DFB) laser [10] is used at the Tx side. These lasers have the great advantage that they can be heterogeneously integrated on a 200mm or 300mm wafer-scale in the silicon photonics process, which makes this approach very scalable [11]. For RoF links it is interesting to use a directly modulated laser instead of a continuous wave laser and a Mach-Zehnder Modulator (MZM), as the insertion loss of the external modulator is eliminated this way and the component count is reduced. At the receiver side high-bandwidth waveguide-coupled Ge-on-Si photodetectors are used, integrated with a linear SiGe BiCMOS transimpedance amplifier (TIA). The scalability and cost-effectiveness of such Tx and Rx PICs make them a great candidate for mass deployment in future RANs. We perform two link experiments using these silicon photonic transceivers, showcasing their potential for various waveforms. In a first experiment we transmit a high-spectral-efficiency LTE-type 64 quadrature amplitude modulation (64-QAM) orthogonal frequency division multiplexing (OFDM) signal over 5 km single mode fiber at 3.5 and 5 GHz carrier frequency. The quasi error free performance of these links attests to the linearity and low noise of the Tx and Rx. In a second experiment, using the same transmitter but a higher bandwidth receiver, we transmit a broadband 16 Gb/s 16-QAM data signal on a 20 GHz carrier over a 5 km single mode fiber link, demonstrating that high bitrate transmission can be obtained using these integrated devices.

The remainder of this chapter is divided in three main sections. In the first section we describe the use of the III-V-on-silicon laser transmitter and Ge-on-silicon waveguide photodiode receiver (with integrated TIA) for the LTE link at 3.5 GHz and 5 GHz carrier frequency. The positive impact of using the Ge-on-Si photodiode in avalanche mode is discussed. In the

second section we describe the use of the same III-V-on-silicon transmitter together with a higher bandwidth silicon photonic waveguide-coupled Ge-on-Si lateral p-i-n photodetector receiver (again with integrated TIA) for 16 Gb/s 16-QAM data transmission at 20 GHz carrier frequency. These 16-QAM results are an extension of the content presented in [12]. In the final section the results are summarized and a conclusion is presented.

5.2 A 3.5 GHz and 5 GHz 64-QAM OFDM Radio-over-Fiber link

5.2.1 III-V-on-silicon transmitter

The transmitter is a directly modulated III-V-on-silicon DFB laser. The laser is fabricated by divinylsiloxane-bis-benzocyclobutene (DVS-BCB) adhesive wafer bonding of an InP/AlGaInAs multi-quantum-well (MQW) epitaxial stack to a silicon photonic integrated circuit [13]. The gain section is defined in the bonded III-V material by contact lithography followed by a combination of wet and dry etching. The silicon PIC contains 400 nm thick silicon ridge waveguides etched 180 nm deep, planarized down to the silicon device layer using SiO_2. Underneath the III-V gain material a DFB grating (grating period 245 nm, grating duty cycle of 50%, 340 μm length) is defined in the silicon waveguide. The light is coupled from the InP gain section to the passive Si waveguide by a two-step tapering structure. In the first part of the structure both the InP and Si waveguide are tapered over a length of 180 μm, in the second part the light is fully confined in the III-V and tapered over a length of 50 μm. Both a schematic sideview of the laser and a detailed top view of the taper structure are shown in Fig. 5.1b. The laser shown in Fig. 5.1b was fabricated by Dr. Amin Abbasi. By slowly narrowing the width of the III-V waveguide and widening the Si waveguide underneath, a linear adiabatic taper is created. This structure ensures that no light is lost due to coupling to higher order modes. Using a narrow III-V taper tip (500 nm) and silicon-on-insulator taper tip (200 nm) the reflections can be minimized as well. In between the InP-to-Si taper and the laser cavity there is a 50 μm long tapered III-V waveguide section. In this section the mode is fully confined in the III-V and the waveguide width is adiabatically widened from 1.5 μm to 3 μm.

As shown in Fig. 5.1b, the III-V to silicon waveguide taper is not part of the laser cavity that is formed by the etched silicon grating. Consequently, it has a different frequency response from the laser cavity, only supporting efficient modulation at low frequencies. To prevent a distortion of the laser modulation response, the III-V taper is electrically isolated from the main

III-V gain section. This is achieved by locally etching away the p-doped InGaAs/InP contact layer. By electrically isolating the tapers they can be dc biased (still required to pump the gain section to transparency), making sure they do not influence the frequency response of the laser. In the following experiments the taper was dc biased at 5 mA.

The III-V-on-silicon DFB laser is first characterized on a temperature-controlled stage and contacted using electrical probe needles. The series resistance of the device is 7 Ohm. The threshold current is 20 mA and the output power coupled to the silicon waveguide is approximately 3 mW for 100 mA bias current. The light is coupled from the Si waveguide into a cleaved single mode fiber with a fiber-to-chip grating coupler with a coupling efficiency of -7 dB. The laser shows excellent single mode behavior at 1570 nm, with a side mode suppression ratio of 40 dB. To determine the laser frequency response a small signal measurement is performed using a Keysight PNA-X 67 GHz network analyzer. In Fig. 5.1c the response of the laser is shown for three different bias currents. It is clear that the bandwidth increases with increasing bias current, due to the shift of the relaxation oscillation resonance frequency. At an injection current of 100 mA a bandwidth above 10 GHz is obtained, this is sufficient for the demonstrations in this work. Furthermore, III-V-on-Silicon DFB lasers with a bandwidth of 34 GHz have been demonstrated [14] and can be used in future demonstrations.

5.2.2   Ge-on-Si Receiver with integrated TIA

The Rx consists of a 14 μm long Ge-on-Si waveguide-coupled avalanche photodetector (APD) on a silicon photonic integrated circuit co-integrated with a TIA. The photodetector was developed by Dr. Hongtao Chen and the cross-section is shown in Fig. 5.2a.

The photodetector consists of a 400 nm thick and 1000 nm wide Ge slab epitaxially grown on top of a n-doped Si waveguide. The Ge is p-doped and contacted with tungsten plugs. Due to this geometry and by optimizing the doping profile very high electrical fields are created at low voltages in the germanium, allowing for avalanche operation at low bias voltages. A gain-bandwidth product of 100 GHz is achieved [15]. The avalanche mechanism is an appealing way to improve the link gain with low power expenditure, however a precise bias voltage control is needed, and this over a wide temperature range when used in uncooled conditions, which is not trivial. The PIC is co-integrated with the TIA on a printed circuit board using wire bonding. The TIA is designed in 0.13 μm SiGe Bipolar CMOS (BiCMOS) technology and is designed for linear operation with an APD [16]. It consumes 200 mW in operation. The receiver has variable
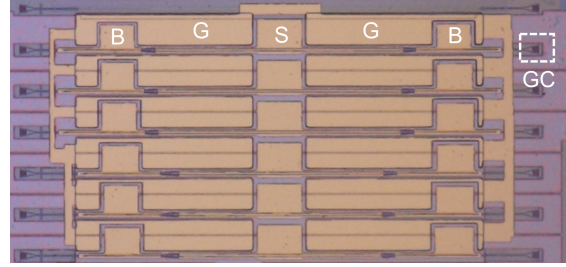
(a)
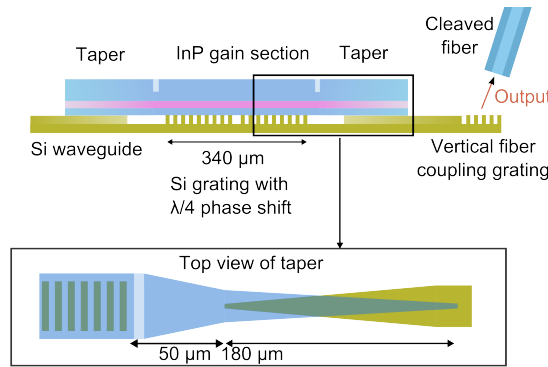
(b)
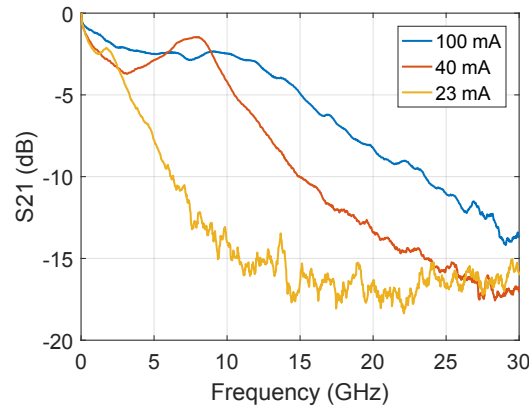
(c)

Figure 5.1: (a) Microscope image of the Tx PIC showing an array of III-V-on-silicon DFB lasers. The vertical grating coupler is indicated with GC. The contact pads for the RF probe are indicated with G (Ground) and S (Signal). The contact pads for the tapers are indicated with B (Bias). (b) Schematic side-view of the III-V-on-silicon laser and top view of the taper.(c) Small-signal response of the laser for different bias currents.

(a)   (b)
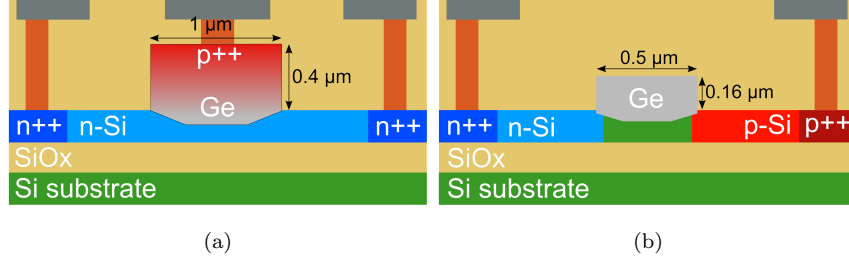
Figure 5.2: (a) Cross section of the Ge-on-Si avalanche photodetector. (b) Cross section of the Ge-on-Si lateral p-i-n photodetector.

gain settings and the entire amplifier chain is designed for high linearity (no internal hard decisions) over the whole operating range. Further details on the design of the receiver fall outside the scope of this work and can be found in [16].

5.2.3   Link characterization

While this Tx/Rx combination was previously used for 10 Gb/s non-return-to-zero digital data reception [17], the linearity or the influence of the avalanche gain on the complex modulation formats used in an analogue RoF link was not yet investigated. For the characterization of the link the III-V-on-silicon DFB laser is mounted on a temperature-controlled stage, kept at a constant temperature of 20 °C. The laser is contacted using a 40 GHz bandwidth Cascade radio frequency (RF) probe. The laser is biased using a bias-T and a stable current source. An Anritsu MS2692A is used as both a data signal generator (SG) and analyzer. The output of the SG is amplified by a 50 GHz bandwidth SHF amplifier with 14 dB gain. The laser diode did not have a 50 Ohm matching network and therefor part of the input signal is reflected to the amplifier. The optical output of the laser is -3 dBm in the fiber at 100 mA bias current due to the 7 dB loss of the grating coupler. To compensate these losses and to be able to vary the input power on the receiver without adjusting the laser bias current, a Keopsys Erbium Doped Fiber Amplifier (EDFA) and Santec OTF-350 optical filter are used. The EDFA is used in active current control to adjust the power output. The tunable optical filter (with an insertion loss of 4 dB) is used to filter out the ASE. The optical signal is coupled onto the receiver PIC containing the Ge-on-Si PD, again incurring 7dB loss. A schematic of the measurement setup is shown in Fig. 5.3. It is important to note that the EDFA is only necessary to investigate the signal quality as a function of
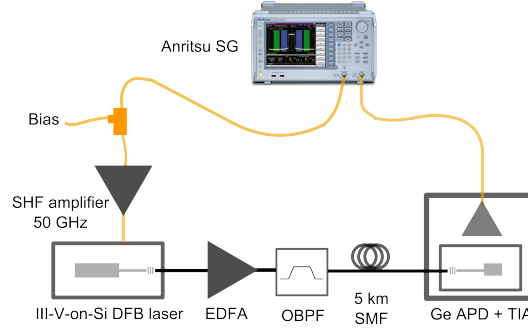
Figure 5.3: Overview of the LTE link experiment setup.

optical input power for the receiver. As will be discussed below, no optical amplification is needed to achieve an rms EVM lower than 1.5%.

First, the linearity of the link is measured using a two-tone third-order intercept point (IP3) measurement. This measurement is performed using the Anritsu MS2692A both as SG and spectrum analyzer. The bias current of the laser is 100 mA. The waveguide-coupled optical power received by the Ge photodiode is -9 dBm. The measurement is performed with two tones spaced 5 MHz at both 3.5 and 5 GHz. The measurement results are presented in Fig. 5.4. For a carrier frequency of 3.5 GHz we find a spurious free dynamic range (SFDR) of 90.2 dB · Hz$^{2/3}$, while for 5 GHz the SFDR degrades slightly by 1.4 dB which is consistent with the low-frequency roll-off shown in Fig. 5.1c. This is worse than current state-of-the-art MZM based links [18]. However, the link experiment discussed below proves that the linearity is sufficient for error-free LTE-signal transmission. At 3.5 and 5 GHz carrier frequencies, the third-order input intercept point (IIP3) occurs for 19.5 dBm and 22 dBm of input power respectively.

In a first transmission experiment a 20 MHz bandwidth 120 Mbit/s 64-QAM OFDM signal, which corresponds to a LTE compliant test signal, is transmitted on a 3.5 GHz carrier. Measurements are done both in an optical back-to-back configuration and using a 5 km standard single mode fiber (SMF) link. The photodiode is used in p-i-n mode using 2 V reverse bias. An electronic back-to-back measurement, without electro-optic conversion gives a rms error vector magnitude (EVM) of 0.6 %. The rms EVM was normalized to the maximum amplitude of the constellation. When the signal is transmitted over 50 m of optical fiber the rms EVM degrades to 1.4 %. When the length of the fiber span is increased to 5 km the EVM degrades further to 1.7 %. This still corresponds to error-free operation. At 5 GHz carrier frequency, an electric back-to-back measurement gave an rms EVM of
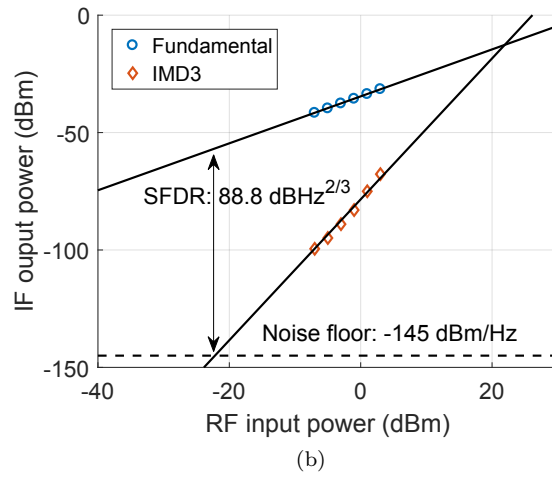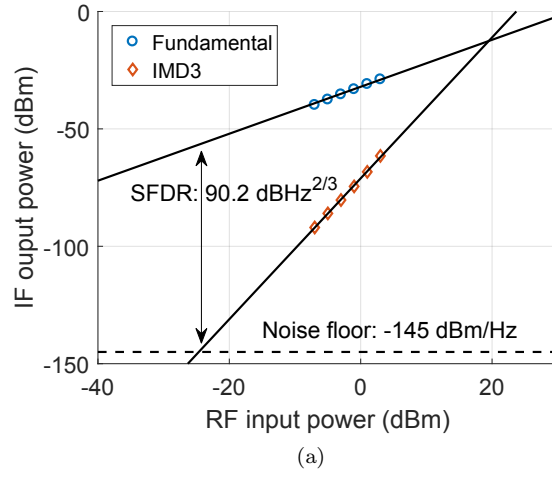
Figure 5.4: IP3 measurement of the link for a carrier frequency of (a) 3.5 GHz and (b) 5 GHz. The IF output power refers to the signal power at the output of the TIA. NF: noise floor, IM3: intermodulation, IIP3: input intercept point.
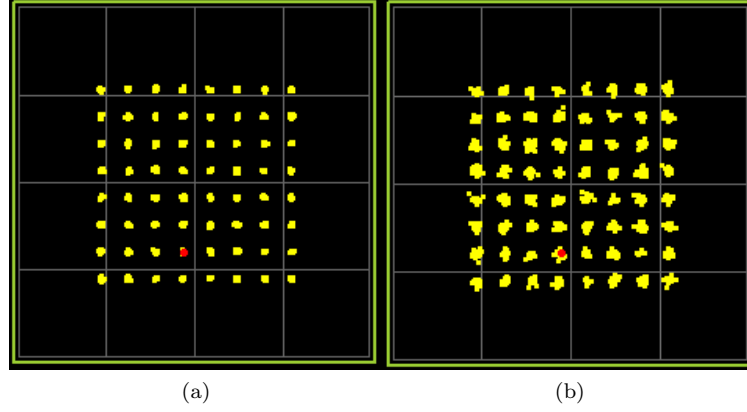
Figure 5.5: Received constellation diagrams of a 64-QAM OFDM signal (of a representative subcarrier) for a carrier frequency of (a) 3.5 GHz and (b) 5 GHz.

0.6 %. Optical transmission over 5 km of SMF showed a good signal quality, however the EVM degraded to 3.7 % (resulting in a BER of approximately 10^{-8}). The 64-QAM constellations of both signals (for a representative sub-carrier) can be found in Fig. 5.5.

To analyze the impact of using the photodetector in avalanche mode, we studied the photocurrent and EVM as a function of the reverse bias on the photodetector for a 5 km link length. At 2 V reverse bias the PD functions as a standard p-i-n detector with a responsivity of 0.6 A/W. To achieve avalanche amplification a reverse bias greater than 4 V is needed. Maximum amplification (M = 2.7) is found for a reverse bias of 6.2 V. From the graph in Fig. 5.6 (using an average optical input power on the detector of -11.5 dBm) we see strong increase in the photocurrent beyond 4 V reverse bias. At the same time the EVM decreases, which means that the signal is amplified without the excess noise deteriorating the signal quality. Since the increase in reverse bias only causes a minute increase in power consumption compared to the power consumption of the laser or an optical amplifier, it provides a very power-efficient gain mechanism, allowing longer amplifier free link-spans.

In a second measurement, we study the signal quality as a function of optical input power, for the PD in p-i-n and APD mode. The RF power provided by the SG is in this case fixed to -16 dBm, and the link length is 5 km. We see that for higher optical input powers the signal quality improves and the EVM drops below 3 %, corresponding to error-free operation. For low optical input power the signal quality is substantially better in APD mode. As the optical power increases the rms EVM of the p-i-n and APD
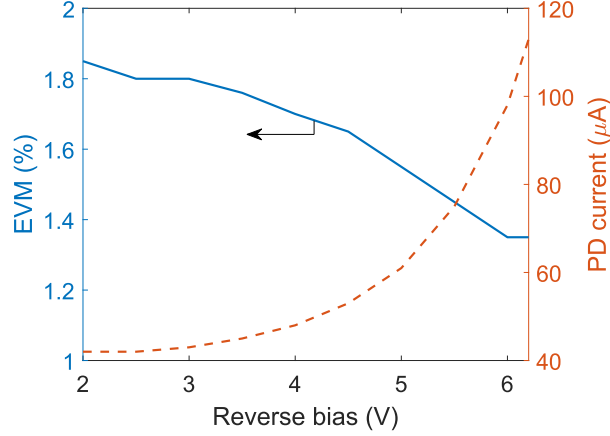
Figure 5.6: The rms EVM and APD current of a 3.5 GHz carrier 64-QAM OFDM signal transmitted over 5 km SMF as a function of the reverse bias of the APD.

mode converge. This shows that we can improve the sensitivity of the receiver by using the APD mode without compromising the performance at higher input power levels. This also illustrates that an EDFA is not necessary to achieve error-free transmission, even using the non-optimized fiber-to-chip grating couplers implemented in the Tx and Rx. Without EDFA (resulting in -10 dBm received optical power) a 4 dB (7 dB) margin is obtained in p-i-n (APD) mode. Using high-efficiency fiber-chip interfaces, e.g. edge couplers with 1 dB insertion loss [19], the link budget would be further increased allowing passive optical splitting in antenna arrays without optical amplification. Even though a substantial link margin can be achieved using only the APD, an EDFA could be used to further increase the margin. In practical systems for 5G fronthaul it is envisioned that there will be an EDFA in the system, in order to share the same optical infrastructure of the current access network, such as passive optical networks. Furthermore, we investigate the signal quality as a function of the RF input power provided by the SG, using the photodetector in avalanche mode (-6.2 V) and using an average optical input power on the detector of 70 μW (link length of 5 km). This measurement shows we have a wide range of RF input powers delivering an EVM below 5 %. When the driving signal is too low in power the SNR becomes insufficient. The dramatic increase in EVM at higher driving powers (the EVM increases from 5 % to 23 % when the RF input power increases from 2 to 4 dBm) is caused by clipping of the amplifier chain in the TIA.
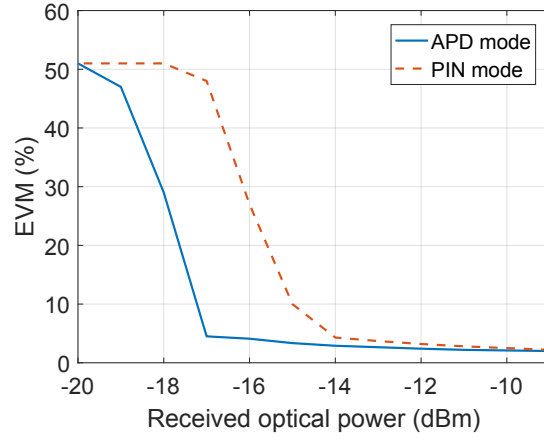
Figure 5.7: The rms EVM as a function of the optical power received by the Ge-on-Si PD. The RF power at the SG is kept constant at -16 dBm.
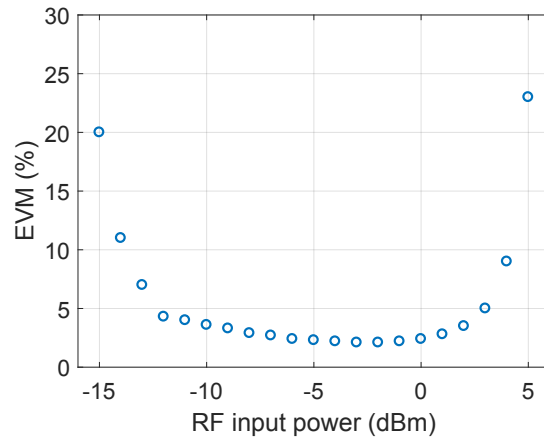
Figure 5.8: The rms EVM as a function of the RF power applied to the laser. The optical power received by the Ge-on-Si PD is -11.5 dBm and the PD is operated in APD mode at 6.2 V reverse bias.

5.3   16 Gb/s 16-QAM link at 20 GHz carrier frequency

5.3.1   III-V-on-silicon transmitter

The same III-V-on-silicon transmitter as in the LTE experiment is used for the link at 16 Gb/s 16-QAM link at 20 GHz carrier frequency. The laser is biased at 100 mA. While the carrier frequency is beyond the 3dB modulation bandwidth of the laser, still good signal transmission can be obtained, through proper equalization (partly by the peaking of the receiver response and by using a finite impulse response (FIR) equalizer), as will be demonstrated below.

5.3.2   Ge-on-Si Receiver with integrated TIA

Similar to the LTE experiment a waveguide-coupled Ge-on-Si photodetector co-integrated with a SiGe BiCMOS TIA is used as receiver. However, in this receiver a 14 μm long lateral p-i-n photodetector is used [20]. The photodetector was developed by Dr. Hongtao Chen and the cross-section is shown in Fig. 5.2b. The photodetector consists of a 0.5 μm wide and 0.16 μm thick germanium slab epitaxially grown on top of a 220 nm thick Si waveguide. A lateral p-i-n structure is defined with the p-contact and n-contact both on the silicon. To achieve optimal coupling between the Si waveguide and Ge absorber, a poly-Si optical taper is used. The responsivity for a bias voltage of -1 V and a wavelength of 1550 nm is 0.72 A/W. The small-signal bandwidth of the device at a -1 V bias exceeds 50 GHz. The TIA is fabricated using a 0.13 μm SiGe BiCMOS process. It consumes approximately 180 mW from a 2.5 V supply. A more detailed description of the TIA can be found in [21]. Wirebond-based co-integration is used. A microscope picture of the silicon photonic receiver co-integrated with the TIA on a high-speed printed circuit board is shown in Fig. 5.9. The small signal electro-optical response of the receiver is shown in Fig. 5.10, for -2dBm of waveguide-coupled optical power. The response shows slight peaking and a 3 dB bandwidth of approximately 20 GHz. This peaking is designed in order to partially compensate for the limited bandwidth of the III-V-on-silicon laser. The bandwidth is fully determined by the TIA as the Si-on-Ge PD has a flat response up to 50 GHz. To asses the linearity of the receiver an IP3 measurement is performed at 20 GHz using the small-signal set-up. The PNA-X is used to generate two tones spaced 5 MHz centered around 20 GHz and the strength of the intermodulation distortion ($2f_1 - f_2$ tone) is measured. The result of the IP3 measurement is shown in Fig. 5.11. The SFDR is 81 dB $\cdot$ Hz$^{2/3}$ for a photocurrent of 450 μA.
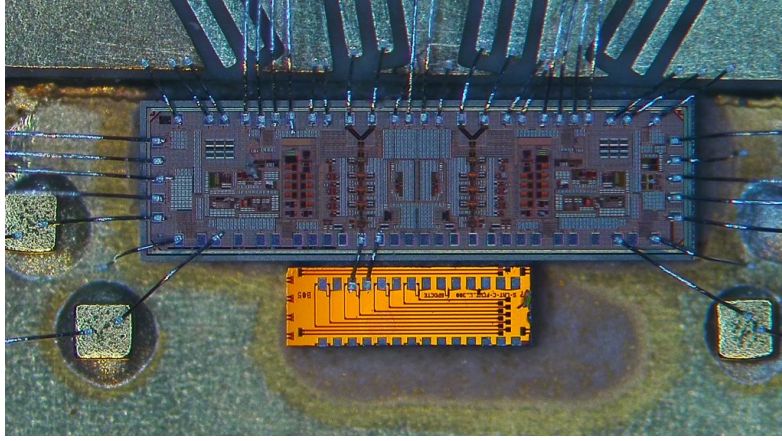
Figure 5.9: A microscope image of the silicon photonic receiver: the Ge-on-Si photodetector (small die) wirebonded to the SiGe BiCMOS TIA (large die). [12]
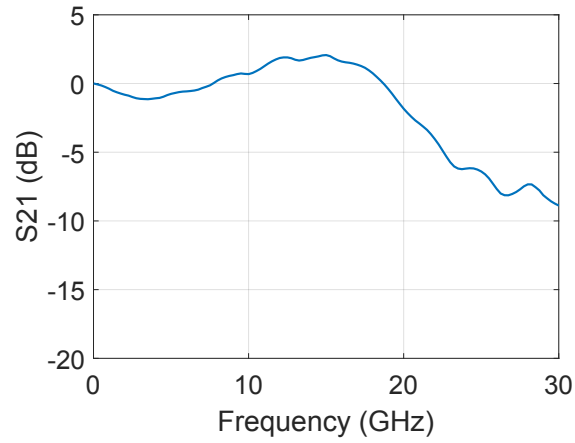
Figure 5.10: Small-signal frequency response of the receiver (Ge receiver and SiGe BiCMOS TIA on a high-speed printed circuit board). [12]
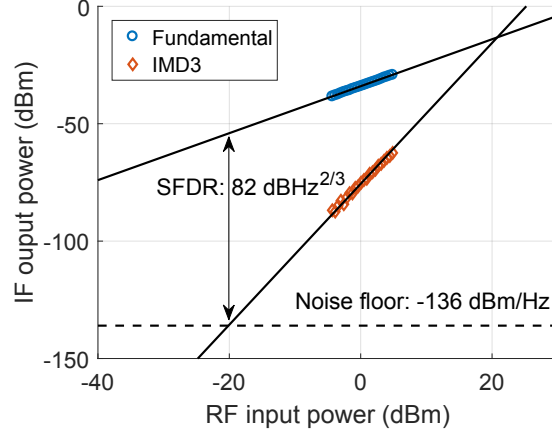
Figure 5.11: IP3 measurement of the Ge-on-Si lateral p-i-n photodiode with TIA. The dots represent measured values, the full lines are extrapolated values. NF: noise floor, IM3: intermodulation, IIP3: input intercept point.

5.3.3 RoF Link demonstration

A carrier frequency of 20 GHz is chosen in this experiment because it was the highest frequency at which a high data-rate 16-QAM signal could be transmitted. Since both Tx and Rx are bandwidth limited, the link gain drops at higher frequencies (beyond 20 GHz) degrading the SNR. The equalization is only implemented to counter the roll-off in the transmission band, but does not alter the SNR. As with the LTE link, the III-V-on-silicon laser is placed on a temperature-controlled stage and kept at a constant temperature of 20 °C. As in the previous system experiments the laser was biased at 100 mA. The Rx PD receives an optical power of approximately -3 dBm, creating a photocurrent of 300 μA. It is again contacted with a 40 GHz Cascade RF probe and biased using a Keithley current source and bias-T. To generate the high bandwidth data signal a Keysight M8195A Arbitrary Waveform Generator is used. Again the output of the laser is amplified with an EDFA to compensate the chip-to-fiber coupling losses. In this experiment 5 km standard SMF is used, before coupling to the silicon photonic receiver. The output of the receiver is captured by a 80 GSa/s real-time oscilloscope (Keysight DSAZ634A). An overview of the measurement set-up is shown in Fig. 5.12. A series of transmission experiments is performed, where the symbol rate of a 16-QAM signal at 20 GHz carrier frequency is increased from 1 to 5 Gbaud. For each transmission a $2^9 - 1$ symbols long pseudo random bit sequence (PRBS) is used. The received 1 GBd signal is equalized online and found to have an error vector magnitude (EVM) of
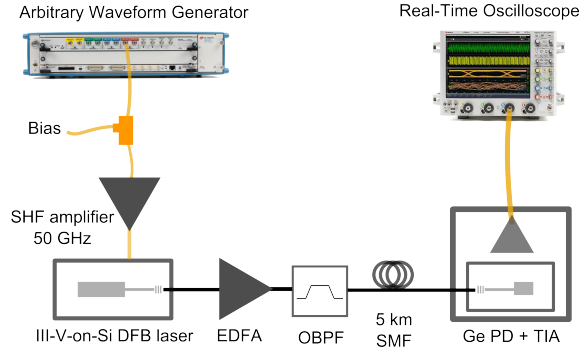
Figure 5.12: Schematic of the 20 GHz carrier transmission measurement set-up.

5.7%. The EVM is also determined online using the native vector signal analysis (VSA) software. To determine the BER, the unequalized waveform of 10^7 symbols is saved and loaded into Matlab. There the measured single carrier signal is directly down mixed to a baseband I/Q signal. To obtain the symbol sample time of the I/Q signal, the Gardner algorithm is used [22]. A finite impulse response equalizer is implemented using MAT-LAB by ir. Joris Van Kerrebrouck to reduce the Inter Symbol Interference (ISI). A constellation of the equalized 1 Gbaud (4 Gb/s) signal, based on 10^6 received symbols, is shown in Fig. 5.13b.

The equalized transmission is found to be error free for a series of 10^7 symbols, resulting in a BER below $2.5 \cdot 10^{-8}$. When no equalization is used, a BER of $5 \cdot 10^{-5}$ is found. We then further investigate the evolution of the online determined EVM as a function of the symbol rate of the 16-QAM signal on a 20 GHz carrier. This is shown in Fig. 5.14. A steady increase of the EVM up to 4 GBd is observed, after which it sharply increases to 10 % at 5 GBd. An offline analysis of the BER for 2 and 4 GBd is also performed by error counting. This gives a BER of $6 \cdot 10^{-7}$ for the 2 GBd data and $3 \cdot 10^{-6}$ for the 4 GBd data. The constellation of the 2 and 4 GBd transmission is also shown in Fig. 5.13b and 5.13c respectively. As a reference the constellation of an electrical 4 GBd back-to-back measurement is shown in Fig. 5.13a.

These results show that the silicon photonic Tx and Rx can also be used to transmit a high data-rate complex modulation format signal on a high-frequency carrier. Operation in the 28 GHz frequency window - which is a frequency band of great interest for 5G wireless networks [23]- is within reach, as higher bandwidth TIAs (or narrow-bandwidth TIAs which peak at 28 GHz) are definitely feasible [24] and even recently developed by ir.

(a) 16 Gb/s (B2B)

(b) 4 Gb/s (5 km)

(c) 8 Gb/s (5 km)

(d) 16 Gb/s (5 km)
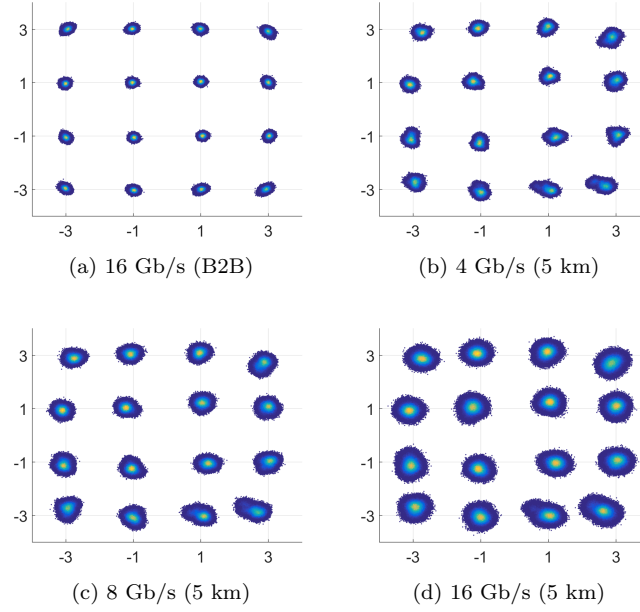
Figure 5.13: Constellation diagrams of 10^6 16-QAM symbols on a 20 GHz carrier transmitted (a) electrically back-to-back and (b-d) over 5 km of SMF.
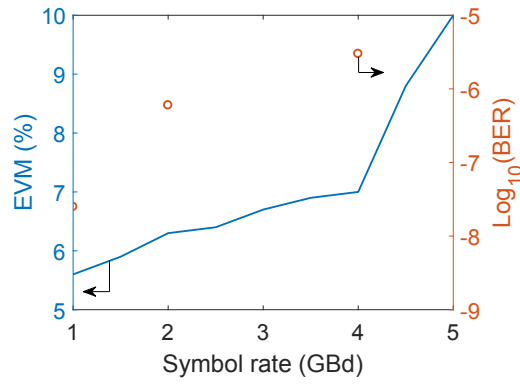
Figure 5.14: The EVM and Bit Error Rate BER as a function of the symbol rate, for a 16-QAM signal on a 20 GHz carrier. The BER was determined by offline error counting.

Laurens Bogaert at IDlab. Furthermore, III-V-on-Silicon DFB lasers with a bandwidth of 34 GHz have been demonstrated [14]. Further integrating the laser with a matching circuit or dedicated driver could improve the channel quality.

5.4 Conclusion

We demonstrate that silicon photonic transceivers are usable for analogue radio-over-fiber links. Both a scenario in which a high spectral efficiency LTE signal is to be transmitted (requiring sufficient linearity of the link for transmitting the 64-QAM OFDM signal) and a scenario in which a high bitrate (16 Gb/s 16-QAM) signal is transmitted is discussed. In both cases a directly modulated III-V-on-silicon laser is used, which simplifies the transmitter architecture. The use of silicon photonics provides the possibility of scaling, very much needed in the wireless communication networks of the future.

References

[1] K. Van Gasse, J. Van Kerrebrouck, A. Abbasi, J. Verbist, G. Torfs, B. Moeneclaey, G. Morthier, X. Yin, J. Bauwelinck, and G. Roelkens. *III-V-on-Silicon Photonic Transceivers for Radio-Over-Fiber Links*. Journal of Lightwave Technology, 36(19):4438–4444, oct 2018.

[2] C. Liu, J. Wang, L. Cheng, M. Zhu, and G.-K. Chang. *Key microwave-photonics technologies for next-generation cloud-based radio access networks*. Journal of Lightwave technology, 32(20):3452–3460, 2014.

[3] S. Iezekiel. *Integrated microwave photonics: a key enabling technology for radio-over-fiber*. In Broadband Access Communication Technologies XI, volume 10128, page 1012803. International Society for Optics and Photonics, 2017.

[4] D. Marpaung, C. Roeloffzen, R. Heideman, A. Leinse, S. Sales, and J. Capmany. *Integrated microwave photonics*. Laser & Photonics Reviews, 7(4):506–538, 2013.

[5] D. Pérez, I. Gasulla, and J. Capmany. *Integrated microwave photonics*. In Photonics Conference (IPC), 2016 IEEE, pages 5–6. IEEE, 2016.

[6] J. S. Fandiño, P. Muñoz, D. Doménech, and J. Capmany. *A monolithic integrated photonic microwave filter*. Nature Photonics, 11(2):124, 2017.

[7] J. E. Bowers, T. Komljenovic, J. Hulme, M. Davenport, and C. Zhang. *Integrated photonics for MWP*. In Photonics Conference (IPC), 2016 IEEE, pages 1–2. IEEE, 2016.

[8] J. C. Hulme, J.-W. Shi, M. Kennedy, T. Komljenovic, B. Szafraniec, D. Baney, and J. E. Bowers. *Fully integrated heterodyne microwave generation on heterogeneous silicon-III/V*. In Microwave Photonics (MWP), 2016 IEEE International Topical Meeting on, pages 336–339. IEEE, 2016.

[9] C. Zhang, P. A. Morton, J. B. Khurgin, J. D. Peters, and J. E. Bowers. *Ultralinear heterogeneously integrated ring-assisted Mach–Zehnder interferometer modulator on silicon*. Optica, 3(12):1483–1488, 2016.

[10] S. Keyvaninia, S. Verstuyft, L. Van Landschoot, F. Lelarge, G.-H. Duan, S. Messaoudene, J. Fedeli, T. De Vries, B. Smalbrugge, E. Geluk, et al. *Heterogeneously integrated III-V/silicon distributed feedback lasers*. Optics letters, 38(24):5434–5437, 2013.

[11] B. Szelag, K. Hassan, L. Adelmini, E. Ghegin, P. Rodriguez, S. Bensalem, F. Nemouchi, T. Bria, M. Brihoum, P. Brianceau, et al. *Hybrid III-V/Si DFB laser integration on a 220 mm fully CMOS-compatible silicon photonics platform.* In Electron Devices Meeting (IEDM), 2017 IEEE International, pages 24–1. IEEE, 2017.

[12] K. Van Gasse, J. Van Kerrebrouck, A. Abbasi, G. Torfs, J. Bauwelinck, and G. Roelkens. *16 Gbps RoF link at 20 ghz carrier frequency using a silicon photonics transmitter and receiver.* In Microwave Photonics (MWP), 2017 International Topical Meeting on, pages 1–4. IEEE, 2017.

[13] G. Roelkens, A. Abassi, P. Cardile, U. Dave, A. de Groote, Y. de Koninck, S. Dhoore, X. Fu, A. Gassenq, N. Hattasan, Q. Huang, S. Kumari, S. Keyvaninia, B. Kuyken, L. Li, P. Mechet, M. Muneeb, D. Sanchez, H. Shao, T. Spuesens, A. Z. Subramanian, S. Uvin, M. Tassaert, K. van Gasse, J. Verbist, R. Wang, Z. Wang, J. Zhang, J. van Campenhout, X. Yin, J. Bauwelinck, G. Morthier, R. Baets, and D. van Thourhout. *III-V-on-Silicon Photonic Devices for Optical Communication and Sensing.* Photonics, 2(3):969–1004, 2015.

[14] A. Abbasi, B. Moeneclaey, J. Verbist, X. Yin, J. Bauwelinck, G.-H. Duan, G. Roelkens, and G. Morthier. *Direct and Electroabsorption Modulation of a III-V-on-Silicon DFB Laser at 56 Gb/s.* IEEE Journal of Selected Topics in Quantum Electronics, 23(6):1–7, 2017.

[15] H. T. Chen, J. Verbist, P. Verheyen, P. D. Heyn, G. Lepage, J. D. Coster, P. Absil, X. Yin, J. Bauwelinck, J. V. Campenhout, and G. Roelkens. *High sensitivity 10Gb/s Si photonic receiver based on a low-voltage waveguide-coupled Ge avalanche photodetector.* Opt. Express, 23(2):815–822, Jan 2015.

[16] X. Yin, B. Moeneclaey, X.-Z. Qiu, J. Verbrugghe, K. Verheyen, J. Bauwelinck, J. Vandewege, M. Achouche, and Y. Chang. *A 10Gb/s APD-based linear burst-mode receiver with 31dB dynamic range for reach-extended PON systems.* Opt. Express, 20(26):B462–B469, Dec 2012.

[17] A. Abbasi, B. Moeneclaey, X. Yin, J. Bauwelinck, G. Roelkens, and G. Morthier. *10-/28-Gb Chirp Managed 20-km Links Based on Silicon Photonics Transceivers.* IEEE Photonics Technology Letters, 29(16):1324–1327, Aug 2017.

[18] S. Li, X. Zheng, H. Zhang, and B. Zhou. *Highly Linear Radio-Over-Fiber System Incorporating a Single-Drive Dual-Parallel MachZehnder*

Modulator. IEEE Photonics Technology Letters, 22(24):1775–1777, Dec 2010.

[19] B. B. Bakir, A. V. de Gyves, R. Orobtchouk, P. Lyan, C. Porzier, A. Roman, and J. . Fedeli. *Low-Loss (>1 dB) and Polarization-Insensitive Edge Fiber Couplers Fabricated on 200-mm Silicon-on-Insulator Wafers.* IEEE Photonics Technology Letters, 22(11):739–741, June 2010.

[20] H. Chen, P. Verheyen, P. De Heyn, G. Lepage, J. De Coster, S. Balakrishnan, P. Absil, W. Yao, L. Shen, G. Roelkens, et al. *- 1 V bias 67 GHz bandwidth Si-contacted germanium waveguide pin photodetector for optical links at 56 Gbps and beyond.* Optics Express, 24(5):4622–4631, 2016.

[21] B. Moeneclaey, J. Verbrugghe, J. Lambrecht, E. Mentovich, P. Bakopoulos, J. Bauwelinck, and X. Yin. *Design and Experimental Verification of a Transimpedance Amplifier for 64-Gb/s PAM-4 Optical Links.* Journal of Lightwave Technology, 36(2):195–203, 2018.

[22] F. Gardner. *A BPSK/QPSK timing-error detector for sampled receivers.* IEEE Transactions on communications, 34(5):423–429, 1986.

[23] T. Haifeng, L. Wei, W. Tan, F. Jian, and F. Zhiyong. *The analysis on the candidate frequency bands of future mobile communication systems.* China Communications, 12(Supplement):140–149, 2015.

[24] I. G. López, P. Rito, A. Awny, M. Ko, D. Kissinger, and A. C. Ulusoy. *A DC-75-GHz Bandwidth and 54* dBΩ *Gain TIA With 10.9* dB$\sqrt{\text{Hz}}$ *in 130-nm SiGe:C BiCMOS.* IEEE Microwave and Wireless Components Letters, 28(1):61–63, 2018.

Chapter 6

EAM-based up-converter-transmitter

In this chapter we describe the design and characterization of a silicon photonic microwave photonic mixer and transmitter. This subsystem is based on GeSi EAMs placed in a MZI structure integrated on a silicon photonic integrated circuit. The material presented in this chapter has in part been published in reference [1].

6.1 Introduction

As discussed in the previous chapter, silicon photonics could play an enabling role in next generation (5G) Radio Access Networks (RANs). Silicon photonics has shown to be a very promising technology to implement IMWP systems such as filters [2], integrated microwave-frequency generators [3] and even programmable signal processing systems [4–7]. In the next generation mobile network (5G) the use of carrier frequencies ranging from 6 GHz to 65 GHz is envisioned [8] [9], which will require devices and systems with very high bandwidths and flexibility. In such 5G RANs, Analogue Radio-over-Fiber (ARoF) could play an important role to enable the ambitious performance goals of 5G.

Another advantage of ARoF, is that the microwave frequency up- or down-conversion stage can be implemented in the optical domain. The use of photonic up-conversion enables wide-band operation and can simplify the transmitter RF-chain. Photonic microwave frequency conversion using LiNbO$_3$ MZMs has been extensively studied in the recent years and has shown promising results [10–14]. Most of these approaches rely on the use of two parallel LiNbO$_3$ MZMs in a super MZM structure, where one MZM

receives the data on a IF or RF carrier and the other is driven with the LO signal. To optimize the conversion efficiency, the super MZM is biased at minimum transmission such that the optical carrier is suppressed. This approach ensures that the photodiode is not saturated by the optical carrier which does not contribute to the signal. In many of these architectures an EDFA is used at the output stage of the MZM to optimize the conversion gain.

Although these systems allow for very flexible and wide-band frequency-converters/transmitters, the implementation using discrete modulators limits the scalability and cost-efficiency of this solution. An interesting approach is to use IMWP to implement a similar architecture, but on a silicon photonic platform. A fully integrated photonic frequency down-converter was demonstrated using a custom InP platform [15]. However, this system was developed for RF radar front-ends up to 1 GHz and not applied to wireless communication systems. Currently it is still quite challenging to provide high frequency modulators in compact Photonic Integrated Circuits (PICs). Although carrier-depletion-based modulators can provide bandwidths up to 40 GHz, the needed voltage swing to drive them remains rather large [16]. A very appealing alternative to carrier-depletion MZMs, are GeSi Electro-Absorption Modulators (EAMs). They provide bandwidths exceeding 65 GHz, covering a substantial part of the mmWave spectrum. Furthermore, they can be fabricated on a wafer-scale in a (200 mm or 300 mm wafer) silicon photonic pilot line. Radio-over-Fiber links using EAMs have been investigated [17], as well as EAM ARoF with photonic up-conversion [18]. However these results were demonstrated with discrete InP EAMs and the up-conversion was realized using bulky circulators and other discrete components. Not only do the GeSi EAMs have the advantage of wafer-scale fabrication, they can easily be integrated in a PIC with low-loss and compact waveguides, splitters, MZIs and thermo-optic phase-shifters.

In this chapter we present an ARoF up-converter/transmitter implemented in a silicon PIC. In the remainder of the chapter we will first give a qualitative analysis of the system operation followed by simulation results. Then we give a detailed discussion of the silicon photonic up-converter/transmitter implementation and the proposed down-link architecture. In the next section we present the results of the GeSi EAM bandwidth measurement, the up-converter/transmitter linearity measurement and the 2 km fiber transmission experiment. In the final part we present a conclusion.

6.2 Mixer system analysis

In this section we will analyze the basic operation of a photonic up-converter-transmitter based on two parallel GeSi EAMs in a MZI structure. Given the non-analytical transfer function of an EAM, an exact quantitative analysis is not possible. However, using sufficient approximations a qualitative insight into the operation of the system can be obtained. These insights are complemented by simulations in the following section.

The EAM-based system is very similar to the MZM-based down-converter described in [10]. However, MZMs have an analytic transfer function and therefore allow a rigorous mathematical analysis. The transfer function of EAMs is strongly device and wavelength dependent and requires a function to be empirically fitted to measured data. For a given wavelength, an EAM transfer function can be well approximated as an ideal intensity modulator with empirical second- and third-order non-linearities [19]. The optical output of an EAM using such an approximation can be written as:

$$P_{out}(V) = P_{in}(a_0 + a_1 V + a_2 V^2 + a_3 V^3) \tag{6.1}$$

With V the applied signal voltage, and a_i the respective coefficients which depend on the bias voltage V_b.

To analyze our EAM-based mixer, we will first derive an expression for the gain of a single EAM RoF link with and without optical amplification. We then analyze the basic concept of mixing with two EAMs in series and finally qualitatively analyze the operation of the parallel EAM mixer. The different links are shown in Fig. 6.1.

6.2.1 EAM RoF link

As we are mainly interested in analyzing the operation principle and small-signal conversion gain, it suffices to approximate the EAM as a linear intensity modulator. The output power of the EAM as a function of voltage is then given by:

$$P_{out}(V(t)) \approx P_{in}(a_0 + a_1 V(t)) \tag{6.2}$$

If we modulate the EAM with a single RF tone, we can easily derive the current at the photodiode in the link:

$$
\begin{aligned}
i_{pd}(t) &\approx \mathcal{R} P_{in}(a_0 + a_1 V_0 \cos{(\omega_{RF}t)}) \\
&= \mathcal{R} P_{in}\alpha_{IL}(1 + \beta \cos{(\omega_{RF}t)})
\end{aligned}
\tag{6.3}
$$

Where $\mathcal{R}$ is the responsivity of the photodetector and we have explicitly noted a_0 as the dynamic insertion loss α_{IL}. The dynamic insertion loss
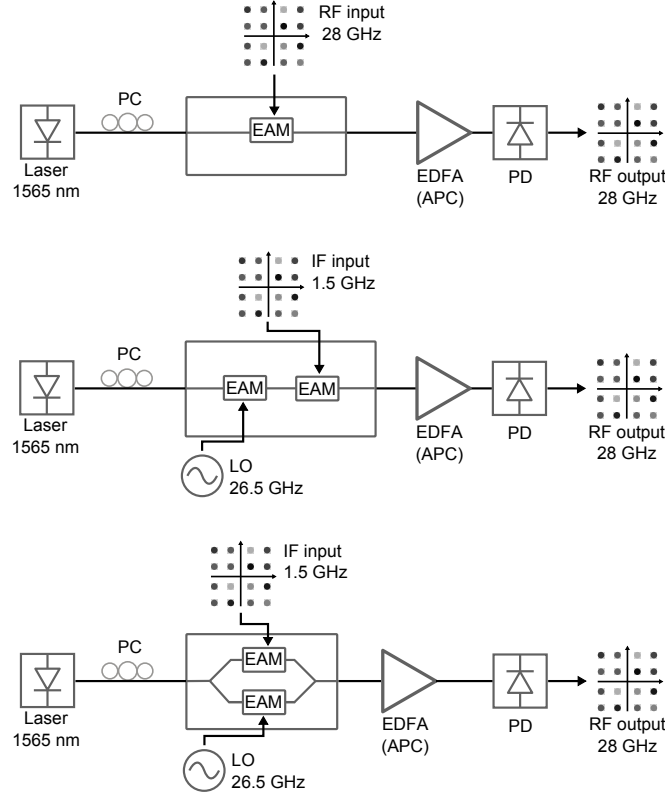
Figure 6.1: Overview of different EAM based RoF links.

corresponds to the loss when no modulation signal is applied. Furthermore we introduced the modulation factor $\beta = a_1 V_0 / \alpha_{IL}$. It is interesting to isolate the signal term and rewrite β as a function of the extinction ratio r:

$$i_{RF}(t) \approx \mathcal{R} P_{in} \alpha_{IL} \beta \cos(\omega_{RF} t) = \mathcal{R} P_{in} \alpha_{IL} \frac{r-1}{r+1} \cos(\omega_{RF} t) \qquad (6.4)$$

From this expression we see that the link gain is linearly dependent on the insertion loss α_{IL} and that the factor containing the extinction ratio asymptotically approaches 1 for increasing extinction ratios. It is clear that for a sufficiently high extinction ratio the insertion loss becomes the dominant factor in the link gain.

In an analogue link it is interesting to use an amplifier with a fixed output power rather than fixed gain, this because we want the photodiode in the link to always receive the maximum optical power it can handle.

An example of such an amplifier is an EDFA with Active Power Control (APC) which are widely available. Currently commercially available EDFAs can provide gain up to 40 dB with noise figures in the order of 4 dB. To analyze the influence of such an amplifier on the link gain we make a simple approximation for an amplifier with fixed output power:

$$G_{EDFA} = \frac{P_0}{\langle P_{input} \rangle} \tag{6.5}$$

With $\langle P_{input} \rangle$ the averaged input power of the EDFA and P_0 the set-point output power. This approximation is valid if the input power is sufficiently high so that the gain of the EDFA is not exhausted. If we assume the EAM is modulated by a single RF frequency and amplified by an EDFA in APC mode, we can write the optical output after the EDFA as:

$$\begin{aligned} P_{EDFA} &= G_{EDFA} P_{in} \alpha_{IL} (1 + \beta \cos{(\omega t)}) \\ &= P_0 (1 + \beta \cos{(\omega t)}) \end{aligned} \tag{6.6}$$

Combing equation Eq. 6.4 and equation Eq. 6.6 we can write the current output from the photodetector into a load as:

$$\begin{aligned} i_{pd} &= \mathcal{R} P_0 \big(1 + \beta \cos(\omega_{RF} t) \big) \\ &= i_0 \big(1 + \frac{r-1}{r+1} \cos(\omega_{RF} t) \big) \end{aligned} \tag{6.7}$$

From this equation it becomes clear that for a system where the optical power on the photodiode is constant the useful signal is limited only by the extinction ratio of the modulator and independent of the insertion loss. Unlike in Eq. 6.4, a modulator with higher extinction ratio will offer a better link gain independent of the insertion loss. For example, when using a MZM a better link gain can be achieved by using a bias point closer to the minimum transmission point.

6.2.2   Serial EAM mixer

To explain the microwave photonic mixing approach using parallel EAMs, it is instructive to first analyze a less complex topology. If we use two EAMs and optically connect them in series we can up- or down-convert a microwave signal [20]. A schematic of this approach is shown in Fig. 6.1 (middle). Using the previously derived expression for the transfer function of a single EAM we can formulate the transfer function of two EAMs in series, one driven by an IF signal and the other driven by an LO signal. If we assume that there is data $d(t)$ amplitude modulated on the IF carrier,

the expression for the output power of the serial mixer becomes:

$$P_{mixer}(t) = P_{in}\alpha_{IL}^2 \left[1 + \beta_{IF}d(t)\cos\left(\omega_{IF}t\right)\right]\left[1 + \beta_{LO}\cos\left(\omega_{LO}t\right)\right]$$
$$= P_{in}\alpha_{IL}^2 \left\{1 + \beta_{IF}d(t)\cos\left(\omega_{IF}t\right) + \beta_{LO}\cos\left(\omega_{LO}t\right)\right.$$
$$+ \frac{\beta_{IF}\beta_{LO}}{2}d(t)\cos\left((\omega_{IF} - \omega_{LO})t\right)$$
$$\left. + \frac{\beta_{IF}\beta_{LO}}{2}d(t)\cos\left((\omega_{IF} + \omega_{LO})t\right)\right\} \tag{6.8}$$

From this expression it is clear that both a down- and up-converted carrier with data will be generated when the light is received by a photodetector. The up-converted signal generated at the photodiode now simply becomes:

$$i_{up}(t) = \mathcal{R}P_{in}\alpha_{IL}^2 \frac{\beta_{IF}\beta_{LO}}{2}d(t)\cos\left((\omega_{IF} + \omega_{LO})t\right) \tag{6.9}$$

As expected the conversion gain depends quadratically on the insertion loss as we pass through two EAMs. To optimize the conversion gain we can again use an EDFA with fixed output power. The useful signal at the photodiode then becomes:

$$i_{up}(t) = \mathcal{R}P_0 \frac{\beta_{IF}\beta_{LO}}{2}d(t)\cos\left((\omega_{IF} + \omega_{LO})t\right) \tag{6.10}$$

As expected, the conversion gain of the mixer is proportional to the product of two EAM analogue links.

Finally we also see that the LO signal generated at the photodetector is always stronger than the up-converted signal:

$$\frac{i_{up}}{i_{LO}} = \frac{i_0 \frac{\beta_{IF}\beta_{LO}}{2}}{i_0\beta_{LO}} = \frac{\beta_{IF}}{2} < \frac{1}{2} \tag{6.11}$$

Which means that the unwanted LO signal is twice as strong at the photodiode as the wanted up-converted signal.

6.2.3 Parallel EAM mixer

We have shown that two EAMs connected in series can be used as microwave photonic mixer. However to analyze a structure were the two EAMs are placed in a MZI we need to have an approximation for the amplitude modulation of the electrical field inside the EAM and not the intensity modulation. A first approximation of the EAM transfer function can be made by assuming it is just the square root of the intensity modulation without any phase modulation.

$$t_{EAM}(V) = \frac{E_{out}}{E_{in}}(V) = \sqrt{a_0 + a_1 V} \tag{6.12}$$

Using this approximation and assuming a perfect MZI (biased at zero transmission) we can approximate the output from two parallel EAMs in a MZI configuration:

$$E_{out}(t) = \frac{E_{in}}{2}(\sqrt{a_0 + a_1 V_{IF}(t)} + e^{i\pi}\sqrt{a_0 + a_1 V_{LO}(t)})$$

$$= \frac{E_{in}\sqrt{a_0}}{2}\left\{\sqrt{1 + \frac{a_1}{a_0}V_{IF}(t)} - \sqrt{1 + \frac{a_1}{a_0}V_{LO}(t)}\right\}$$

$$\approx \frac{E_{in}\sqrt{a_0}}{4}\left\{\frac{a_1}{a_0}\Big[V_{IF}(t) - V_{LO}(t)\Big]\right.$$

$$\left. - \frac{a_1^2}{4a_0^2}\Big[V_{IF}^2(t) - V_{LO}^2(t)\Big] + ...\right\} \qquad (6.13)$$

where we derived the last expression by using a Taylor expansion of the square root. Most importantly we see that the biasing eliminates the unmodulated electric field, which corresponds to the optical carrier.

Now we will show that a up-converted signal is generated by this approach. In first order the optical output of the mixer is then given by:

$$P_{out}(t) \approx \frac{P_{in}\alpha_{IL}}{16}\Big[d(t)\beta_{IF}\cos(\omega_{IF}t) - \beta_{LO}\cos(\omega_{LO}t)\Big]^2 \qquad (6.14)$$

To analyze the mixing terms we can omit the constants and study the mixing products:

$$P_{out}(t) \approx \frac{P_{in}\alpha_{IL}}{16}\Big\{d^2(t)\beta_{IF}^2\cos^2(\omega_{IF}t) + \beta_{LO}^2\cos^2(\omega_{LO}t)$$

$$- 2d(t)\beta_{IF}\beta_{LO}\cos(\omega_{IF}t)\cos(\omega_{LO}t)\Big\}$$

$$= \frac{P_{in}\alpha_{IL}}{32}\Big\{\beta_{LO}^2 + d^2(t)\beta_{IF}^2 + d^2(t)\beta_{IF}^2\cos(2\omega_{IF}t)$$

$$+ \beta_{LO}^2\cos(2\omega_{LO}t)$$

$$+ 2d(t)\beta_{IF}\beta_{LO}\cos[(\omega_{IF} - \omega_{LO})t]$$

$$+ 2d(t)\beta_{IF}\beta_{LO}\cos[(\omega_{IF} + \omega_{LO})t]\Big\} \qquad (6.15)$$

We find that the data $d(t)$ is indeed transferred on a carrier with the up-converted frequency $\omega_{IF} + \omega_{LO}$ together with a down-converted term $\omega_{IF} - \omega_{LO}$. Furthermore, we see that no LO term is present in the photodiode output.

For a quantitative analysis of this photonic mixer we must resort to numerical simulations as the approximations used do not allow for accurate results.

Serial EAM mixer
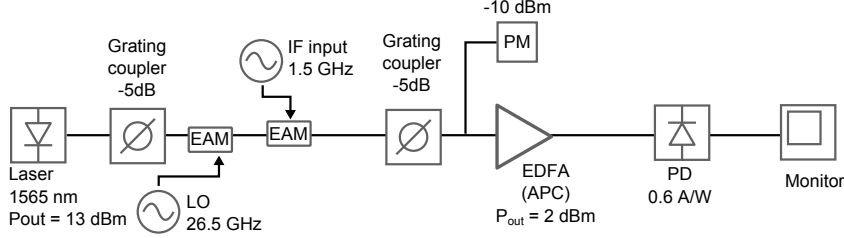
Parallel EAM mixer
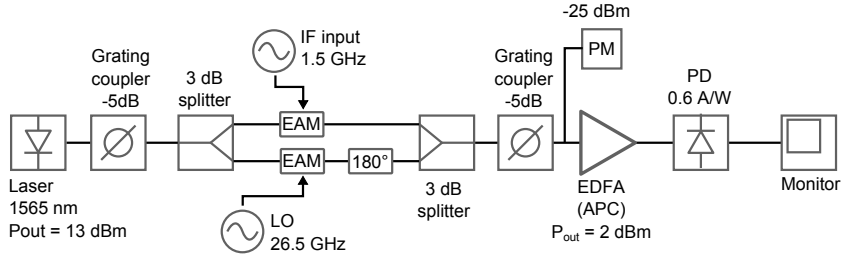
Figure 6.2: Overview of the models used in VPITransmissionmaker to simulate both the serial and parallel EAM mixers.

6.3 Simulation results

A simulation model was built using modules provided by VPITransmissionmaker software. We simulated both a serial EAM mixer as well as a parallel EAM mixer. This allows us to compare the performance and verify the analysis of the previous section with the results of the serial EAM. The equivalent circuits used in VPI to simulate the systems are shown in Fig. 6.2. For the EAMs we assumed that they have an insertion loss of 8 dB and an extinction ratio of 8 dB. These numbers are based on a previous measurement of 80 μm EAMs with a parallel 50 Ohm resistor driven with 2 V_{pp} or 10 dBm RF power. For the simulation in VPI we made a model to compare a serial EAM mixer and parallel EAM mixer. As described in Fig. 6.2 we used an ideal VPI laser module with 13 dBm of output power at a wavelength of 1565 nm. To incorporate the grating couplers we added 5 dB attenuators before and after the mixer PIC. The mixer consists of two ideal VPI EAM modules, that are modulated by a sine (10 dBm RF input power). The EAMs were approximated by the numerical formula:

$$P_{out} = P_{in}(0.159 + 0.115 \cos{(\omega t)}) \qquad (6.16)$$

The output of the mixer is amplified by an idealized EDFA with a fixed output power of 2 dBm and a noise figure of 4 dB. As a receiver, a pho-

todetector with a responsivity of 0.6 A/W was used. A monitor is used as electrical spectrum analyzer.

The result of the simulation is shown in Fig. 6.3. If we first inspect the serial mixer, we find that the generated RF signal at 28 GHz has a power of -28.4 dBm for an IF input power of 10 dBm. While the LO signal at 26.5 GHz had an output power of -19.4 dBm for an input power of 10 dBm. This corresponds to a conversion gain of -38.4 dBm and an LO throughput of -29.4 dB. This result can now be used to check our calculations of the previous section, for example if we calculate the RF to LO ratio using Eq. 6.11 we find:

$$\frac{P_{up}}{P_{LO}} = 20\log_{10}\left(\frac{\beta_{IF}}{2}\right) = 20\log_{10}\left(\frac{1}{2}\frac{r-1}{r+1}\right) \approx -8.8\text{dB} \qquad (6.17)$$

Which is an excellent match for the simulated value of -9 dB, validating our derivation of the EAM mixer.

The resulting spectrum of the parallel mixer is shown in Fig. 6.3(b). We see that the LO is strongly suppressed compared to the RF signal. The simulated RF signal output power is -17 dBm, while the LO output power is -36.4 dBm. This results in a conversion efficiency of -27 dB and an LO throughput of -46.4 dB. Compared to the serial mixer we have a conversion efficiency which is 11 dB higher. It is interesting to note that for this topology the RF signal is stronger than the LO throughput (+19.5 dB), which is an additional advantage when compared to the serial topology. Finally, the many spurious peaks are due to the inherent non-linearity of the EAM itself and will strongly depend on the actual device in real-life applications. Further investigation of the system would be needed to give a more insight into the spurious peaks.

The advantage of the parallel mixer becomes more apparent if the extinction ratio of the EAMs becomes smaller. For example, it is sometimes of interest to drive the EAMs with a smaller voltage to improve the linearity. For the EAM driven with the LO signal this is of no concern as the harmonics all fall out of band. For the IF EAM however this constraint can severely limit the applicable voltage swing. If we perform the same simulation, but now we drive the IF EAM with only half the voltage we find an ever greater improvement from serial to parallel configuration. The conversion gain of the serial mixer decreases to -44 dB, while the parallel conversion efficiency is only reduced by 2 dB to -29 dB. Finally it is important to note that all these simulations were done without TIA, therefor the final conversion gain could be further improved using suitable electronic components.
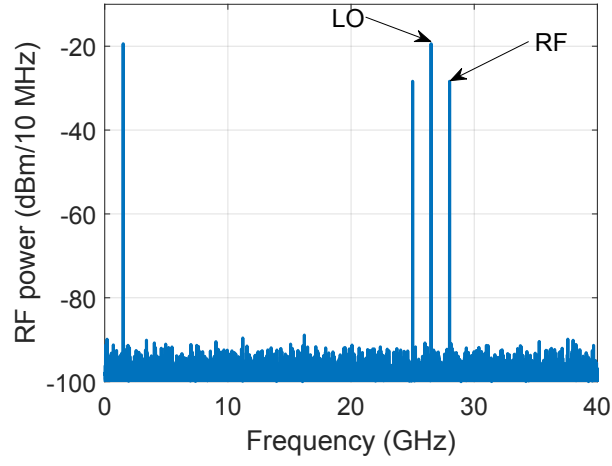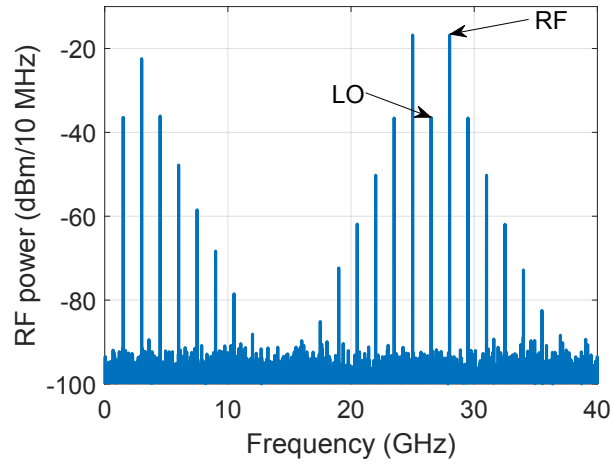
Figure 6.3: (a) Resulting electrical spectrum of the serial EAM mixer simulation for EAMs with an extinction ratio of 8 dB and an insertion loss of 8 dB. (b) Resulting electrical spectrum of the parallel EAM mixer using the same EAMs.
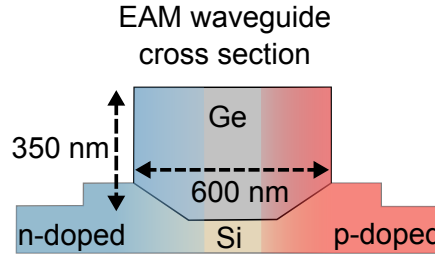
Figure 6.4: Cross section of the EAM waveguide.

6.4   Design and implementation

As we simulated in the previous section, an EAM mixer using an MZI structure biased at minimum transmission point has the highest conversion gain and lowest LO leakage. We chose to use this structure to design a PIC, using waveguide-coupled GeSi EAMs available on the iSiPP50G platform offered by imec. The mask design for this structure was executed by ir. Jochem Verbist and the device was designed by Dr. Ashwyn Srinivasan. The system design and characterization was performed by the author. In Fig. 6.4 the cross section of the EAM waveguide is shown. The key components of the PIC are two GeSi EAMs placed in a MZI structure. The MZI structure is created using passive silicon waveguides and 1 by 2 MMIs. One EAM is placed in the top MZI arm and is used to imprint the data (at IF frequency) on the optical carrier. The other EAM is placed in the bottom arm and is driven by the LO signal needed to up-convert the data to the wanted output RF frequency. The EAMs are connected with metal interconnects to an array of bondpads in G-S-G-S-G configuration with a 100 μm pitch (as shown in Fig. 6.5). An on-chip 70 Ohm resistor was included (in between G and S pads) to provide broadband matching, resulting in a return loss better than 10 dB from 10 MHz to 67 GHz (see Fig. 6.6). For narrow-band operation, a dedicated matching network could be used that would improve the conversion gain. The PIC contains two grating couplers which allow the PIC to be interfaced with cleaved single mode fiber (SMF). The MZI structure also contains a thermo-optic phase-shifter that is used to apply a static π phase-shift to the MZI structure. This static phase shift is needed to suppresses the optical carrier. This is important, because in this microwave photonic mixer architecture the optical carrier does not contribute to the output signal but can saturate the amplifier and receiver. Furthermore, by suppressing the carrier, the LO leakage at the receiver is
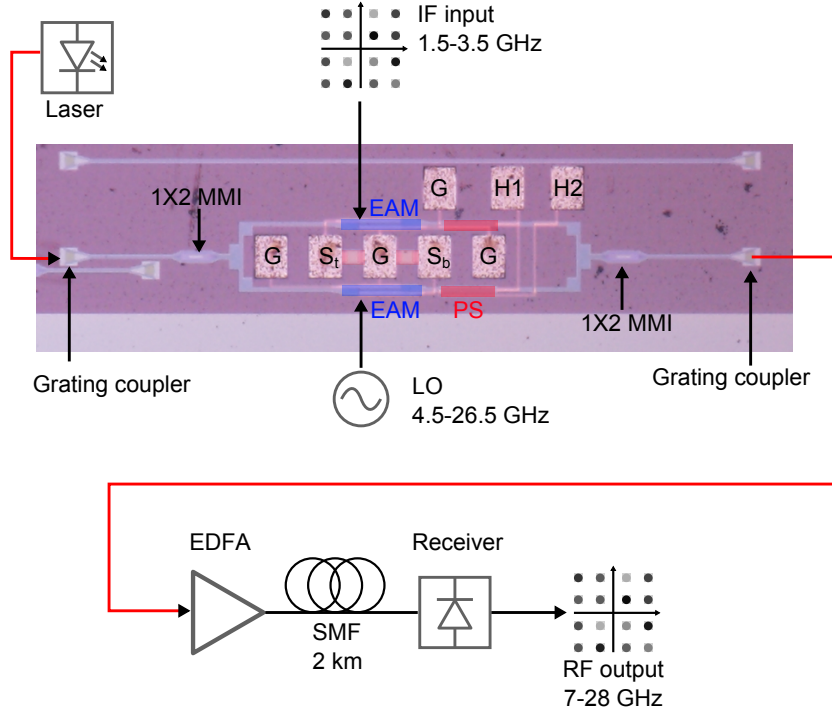
Figure 6.5: Overview of the full up-converter/transmitter link. EAM: Electro Absorption Modulator; MMI: Multi-Mode Interferometer; PS: Phase-Shifter; EDFA: Erbium Doped Fiber Amplifier; SMF: Single Mode Fiber.

also mitigated. This architecture closely resembles previously demonstrated photonic frequency-converters with LiNbO3 MZMs in each arm of a MZI structure [10]. In this implementation however, the amplitude modulators (MZMs) are replaced by intensity modulators (EAMs). As shown in Fig. 6.5 the envisioned down-link consists of a laser, the PIC, standard SMF, an optical amplifier and a PD. In this work the link was demonstrated with an external laser, but a fully integrated version of the PIC could be realized by the heterogeneous integration of a DFB laser onto the silicon PIC [21]. Similarly, the amplification stage at the PIC output was implemented with an EDFA in this work. However, depending on the system requirements a SOA could be heterogeneously integrated on the PIC [22]. Also on the receiver side a commercial device was used, however as we have demonstrated in the previous chapter a silicon PIC with GeSi photodiodes co-integrated with a TIA could also be used as receiver [23]. The GeSi EAMs have a bandwidth exceeding 65 GHz and therefore both the IF input and LO frequency can be extended to 60-70 GHz bands. This implies that the same structure can

also be used for photonic up-conversion and down-conversion of mmWave bands without any modification of the PIC. The carrier frequencies shown in Fig. 6.5 were used in the transmission experiment described in the following section and were limited by measurement equipment.

The EAMs have an extremely small footprint of 20 by 80 μm, which is an order of magnitude smaller than integrated silicon photonic MZMs. This implies that a large number of these mixers can be integrated on one PIC for wavelength multiplexing or space division multiplexing, as was shown for 896 Gb/s digital data transmission [24].
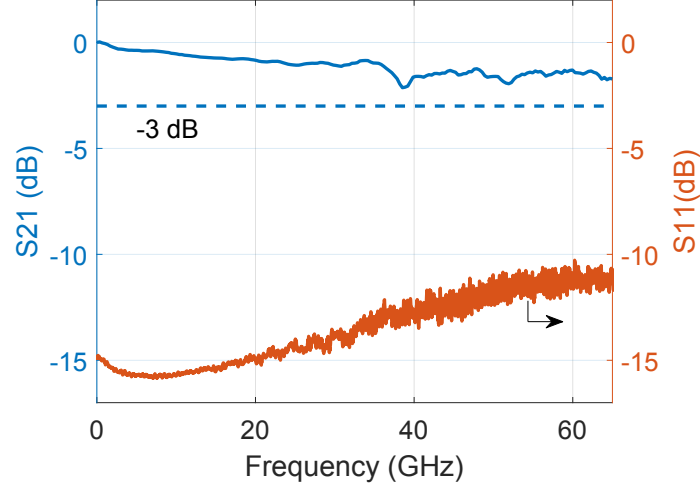
Figure 6.6: Small-signal frequency response and return loss of the GeSi EAM measured with a Keysight PNA-X vector network analyzer.

6.5   Measurement results

Before characterizing the up-conversion/transmitter we first carried out a small-signal measurement of a single EAM to determine the bandwidth and ripple. For this purpose we used a PNA-X vector network analyzer together with a u^{2}t 50 GHz XPDV2320R photodiode. To accurately determine the small-signal response up to 65 GHz, the frequency response of the photodiode was de-embedded. A measurement of the frequency dependent response of a GeSi EAM shows less than 1 dB ripple and a 3 dB bandwidth beyond 65 GHz. The result of this measurement is shown in Fig. 6.6.

To characterize the GeSi EAM up-converter/transmitter, the PIC was placed on a temperature-controlled chuck and kept at 20°C. The optical input and output were provided using a cleaved SMF. The layout of the measurement set-up is shown in Fig. 6.7. A tunable laser is used with an output power of 10 dBm at a wavelength of 1565 nm. The EAMs were contacted using a G-S-G-S-G RF probe with 100 μm pitch. Each EAM was reverse biased with 0.8 V and a heater was used to bias the MZI structure at minimum transmission point. The dynamic insertion loss of the EAM at a reverse bias of 0.8 V is approximately 8 dB. The LO EAM was driven with a Rhode and Schwarz signal generator (RS SG). This EAM could be driven with high power (10 dBm) without danger of compromising the linearity as the generated harmonics are out-of-band.
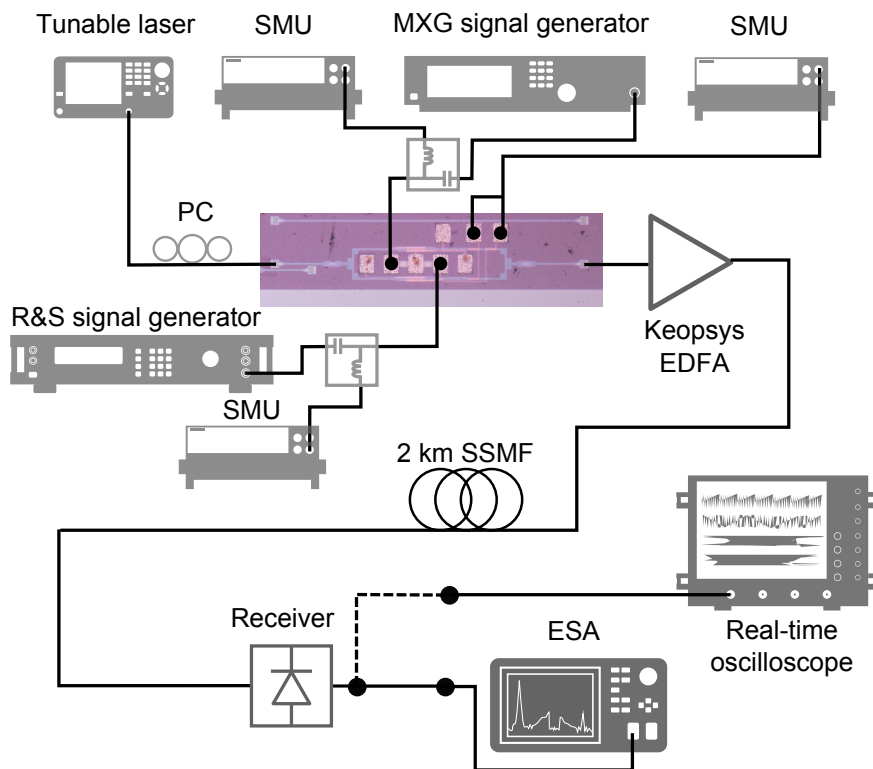
Figure 6.7: Layout of the measurement set-up for the 10 MBd 64-QAM signal over 2 km of standard SMF transmission experiment. SMU: Source Measure Unit; PC: Polarization Controller; SSMF: Standard Single Mode Fiber; EDFA: Erbium Doped Fiber Amplifier, ESA: Electrical Spectrum Analyzer.
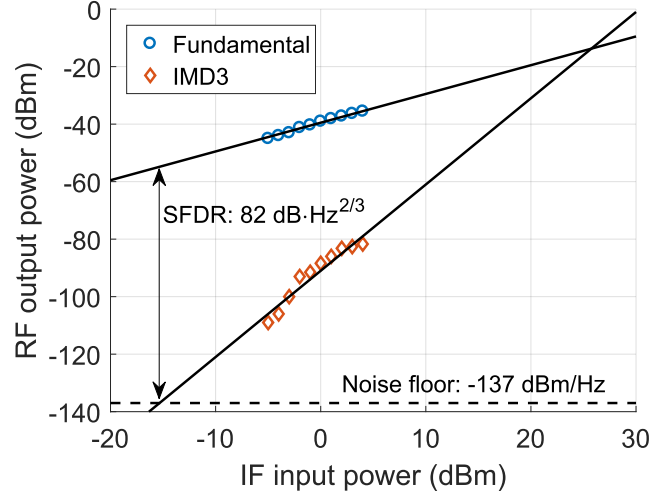
Figure 6.8: Results of the linearity (IP3) measurement as a function of the IF input power, with a fixed LO power of 10 dBm. The output power was measured at the photodiode output stage. SFDR: Spurious Free Dynamic Range; IMD3: third-order Inter-Modulation Distortion.

To determine the linearity of the mixer, the IF EAM was driven with a Keysight MXG signal generator (MXG SG). The MXG SG was used to generate a two-tone signal for an IP3 linearity measurement, with the tones centered at 1.5 GHz and spaced by 0.2 MHz. The IF input power was varied while the LO power was kept constant at 10 dBm.

To determine the inter-modulation distortion (IMD3) and the resulting up-converted signal, the signal power at 26000.1 MHz and the inter-modulation power at 26000.3 MHz were measured. The result of the measurement is shown in Fig. 6.8. The measured Spurious Free Dynamic Range (SFDR) exceeds $82 \text{ dB} \cdot \text{Hz}^{2/3}$, and the input third order intercept point (IIP3) occurs at 25 dBm of IF input power. The SFDR is comparable to earlier work on EAM based RoF links [17, 25] and could be further improved by lowering the noise floor.

To characterize the photonic system as transmitter with photonic up-conversion, we performed a transmission experiment over 2 km of SMF as described in Fig. 6.7. In a first transmission experiment a 10 MBd 64-QAM signal was generated on a 1.5 GHz IF carrier using the MXG SG. At the output of the PIC a Keopsys EDFA (CEFA-HG) is used to amplify the optical signal power to approximately -4 dBm. Although in mmWave frequency bands higher baud rates are of interest, in this experiment we
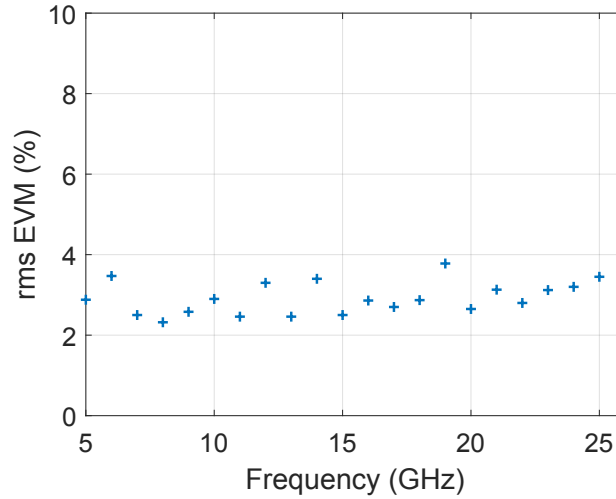
Figure 6.9: The rms EVM of a received 10 Mbd 64-QAM signal as a function of the received carrier frequency. The IF had a frequency of 1.5 GHz and an input power of 0 dBm, and LO input power of 10 dBm.

were limited by the bandwidth of the equipment. The 64-QAM signal was used to drive the IF EAM, while the LO EAM was driven using the R&S SG with a frequency varying from 4.5 to 24.5 GHz (10 dBm). In this experiment a linear PIN-TIA optical receiver (Discovery DSC-409) was used and the output of the receiver was analyzed using a Keysight MXA electrical signal analyzer (MXA SA). The LO frequencies were chosen to up-convert the IF signal to the >6 GHz bands, while the maximum RF carrier frequency was limited by the MXA SA. As shown in Fig. 6.6 the EAM bandwidth allows up-conversion to carrier frequencies larger than 65 GHz with less than 3 dB penalty. The rms EVM of the received 64-QAM signal was determined online using the native software of the MXA SA, without the use of equalization. The rms EVM was normalized to the maximum amplitude of the constellation. The rms EVM of 1000 symbols for the 64-QAM 10 MBd signal as a function of the received carrier frequency is shown in Fig. 6.9. Although the specifications for 5G RANs are not defined, the 3GPP defined a maximum rms EVM for current LTE RANs of 8 % for transmitted 64-QAM signals and 3.5 % for 256-QAM signals.

To investigate the transmission of higher baud rates, an in-house programmed FPGA signal generator (by Haolin Li) was used to create a 218 MBd 64-QAM signal on a 3.5 GHz carrier. Because the MXA SA is limited to 25 MBd signals, we used a Keysight real-time oscilloscope (DSA-Z 634A) to
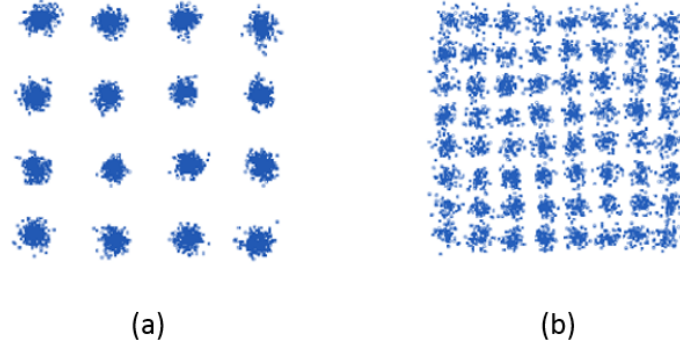
Figure 6.10: (a) Constellation diagram of the received 218.75 MBd 16-QAM data on a 28 GHz carrier with an rms EVM of 5 %. (b) Constellation diagram of the received 218.75 MBd 64-QAM data on a 28 GHz carrier with an rms EVM of 5.4 %.

analyze the received signal. Again, native software on the oscilloscope was used to determine the online rms EVM of the received signal. This time the RF carrier frequency was limited due to the oscilloscope to 28 GHz, which corresponded to an LO frequency of 24.5 GHz. A constellation diagram of both a 16-QAM and a 64-QAM received signal, transmitted over 2 km of SMF, are shown in Fig. 6.10. The rms EVM of the received data was 5.4 % for 1.3125 Gb/s 64-QAM data on a 28 GHz carrier.

We then investigated the conversion gain as a function of the LO frequency when an IF tone without data is used. The IF EAM was driven with a 0 dBm and 1.5 GHz tone, while the LO frequency was swept between 4.5 an 24.5 GHz with a constant power of 10 dBm. The result of the measurement is shown in Fig. 6.11. The ripple of the conversion gain is attributed to the probe contact and the cables, as the transmitter was not de-embedded and the response of the EAM should have less than 1 dB ripple according to Fig. 6.6.

6.6   Conclusions

In summary, we demonstrated a microwave photonic up-converter-transmitter implemented in silicon photonics. We showed that the EAM has a 3 dB bandwidth exceeding 65 GHz and a ripple smaller than 1 dB. Furthermore,
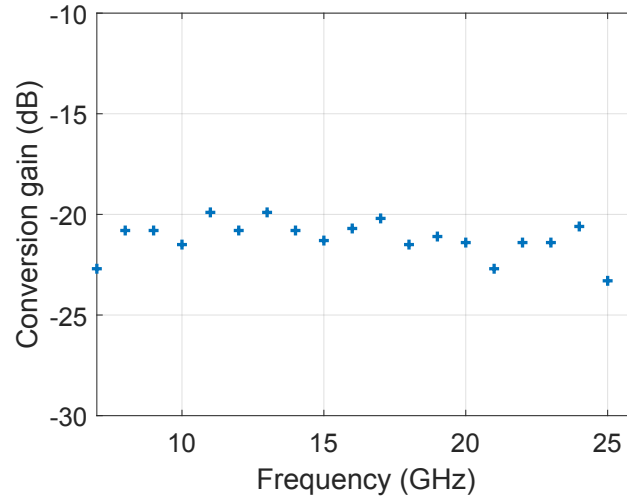
Figure 6.11: Conversion gain as a function of the carrier output frequency for an LO input power of 10 dBm.

we demonstrated the up-conversion of a 1.5 GHz IF to a frequency range of 7 to 26 GHz with less than 2 % rms EVM variation over the entire frequency range. This was done for a 64-QAM 10 MBd signal, where both the maximum carrier frequency and baud rate were limited by the measurement equipment. We then also demonstrated the transmission and up-conversion of a 1.3 Gb/s 64-QAM signal. In future PICs the external laser and amplifier could be heterogeneously integrated. In this work we presented the system as a transmitter and up-converter, but the PIC could also be used as a photonic microwave down-converter. Finally, due to the very compact footprint of the EAM many of these up-converter/transmitters can be combined and multiplexed on a single chip.

References

[1] K. Van Gasse, J. Verbist, H. Li, G. Torfs, J. Bauwelinck, and G. Roelkens. *Silicon Photonics Radio-Over-Fiber Transmitter Using GeSi EAMs for Frequency Up-Conversion.* IEEE Photonics Technology Letters, 31(2):181–184, jan 2019.

[2] W. Zhang and J. Yao. *On-chip silicon photonic integrated frequency-tunable bandpass microwave photonic filter.* Optics letters, 43(15):3622–3625, 2018.

[3] W. Zhang and J. Yao. *Silicon Photonic Integrated Optoelectronic Oscillator for Frequency-Tunable Microwave Generation.* Journal of Lightwave Technology, 2018.

[4] D. Pérez, I. Gasulla, L. Crudgington, D. J. Thomson, A. Z. Khokhar, K. Li, W. Cao, G. Z. Mashanovich, and J. Capmany. *Multipurpose silicon photonics signal processor core.* Nature communications, 8(1):636, 2017.

[5] W. Zhang and J. Yao. *A fully reconfigurable waveguide Bragg grating for programmable photonic signal processing.* Nature communications, 9(1):1396, 2018.

[6] Y. Xie, Z. Geng, L. Zhuang, M. Burla, C. Taddei, M. Hoekman, A. Leinse, C. G. H. Roeloffzen, K.-J. Boller, and A. J. Lowery. *Programmable optical processor chips: toward photonic RF filters with DSP-level flexibility and MHz-band selectivity.* Nanophotonics, 7(2):421–454, 2017.

[7] L. Zhuang, C. G. H. Roeloffzen, M. Hoekman, K.-J. Boller, and A. J. Lowery. *Programmable photonic signal processor chip for radiofrequency applications.* Optica, 2(10):854, oct 2015.

[8] S. Ek, T. Påahlsson, C. Elgaard, A. Carlsson, A. Axholt, A.-K. Stenman, L. Sundström, and H. Sjöland. *A 28-nm FD-SOI 115-fs Jitter PLL-Based LO System for 24-30-GHz Sliding-IF 5G Transceivers.* IEEE Journal of Solid-State Circuits, 2018.

[9] J. Lota, S. Sun, T. S. Rappaport, and A. Demosthenous. *5G Uniform Linear Arrays With Beamforming and Spatial Multiplexing at 28, 37, 64, and 71 GHz for Outdoor Urban Communication: A Two-Level Approach.* IEEE Transactions on Vehicular Technology, 66(11):9972–9985, 2017.

[10] E. H. W. Chan and R. A. Minasian. *Microwave photonic downconverter with high conversion efficiency.* Journal of Lightwave Technology, 30(23):3580–3585, 2012.

[11] T. Jiang, R. Wu, S. Yu, D. Wang, and W. Gu. *Microwave photonic phase-tunable mixer.* Optics express, 25(4):4519–4527, 2017.

[12] Y. Wang, J. Li, T. Zhou, D. Wang, J. Xu, X. Zhong, D. Yang, and L. Rong. *All-Optical Microwave Photonic Downconverter With Tunable Phase Shift.* IEEE Photonics Journal, 9(6):1–8, 2017.

[13] W. Zhai, A. Wen, W. Zhang, Z. Tu, H. Zhang, and Z. Xiu. *A Multichannel Phase Tunable Microwave Photonic Mixer With High Conversion Gain and Elimination of Dispersion-Induced Power Fading.* IEEE Photonics Journal, 10(1):1–10, 2018.

[14] T. Li, E. H. W. Chan, X. Wang, X. Feng, B.-O. Guan, and J. Yao. *Broadband Photonic Microwave Signal Processor With Frequency Up-/Down Conversion and Phase Shifting Capability.* IEEE Photonics Journal, 10(1):1–12, feb 2018.

[15] S. Jin, L. Xu, V. Rosborough, J. Klamkin, and Y. Li. *RF Frequency Mixer Photonic Integrated Circuit.* IEEE Photonics Technology Letters, 28(16):1771–1773, aug 2016.

[16] D. Patel, S. Ghosh, M. Chagnon, A. Samani, V. Veerasubramanian, M. Osman, and D. V. Plant. *Design, analysis, and transmission system performance of a 41 GHz silicon photonic modulator.* Optics express, 23(11):14263–14287, 2015.

[17] B. Hraimel, X. Zhang, W. Jiang, K. Wu, T. Liu, T. Xu, Q. Nie, and K. Xu. *Experimental demonstration of mixed-polarization to linearize electro-absorption modulators in radio-over-fiber links.* IEEE Photonics Technology Letters, 23(4):230–232, 2011.

[18] C. S. Park, C. K. Oh, C. G. Lee, D.-H. Kim, and C.-S. Park. *A photonic up-converter for a WDM radio-over-fiber system using cross-absorption modulation in an EAM.* IEEE photonics technology letters, 17(9):1950–1952, 2005.

[19] B. G. Kim, S. H. Bae, H. Kim, and Y. C. Chung. *RoF-based mobile fronthaul networks implemented by using DML and EML for 5G wireless communication systems.* Journal of Lightwave Technology, 36(14):2874–2881, 2018.

[20] G. Gopalakrishnan, W. Burns, and C. Bulmer. *Microwave-optical mixing in LiNbO₃ modulators*. IEEE Transactions on Microwave Theory and Techniques, 41(12):2383–2391, 1993.

[21] J. Zhang, B. Haq, J. O'Callaghan, A. Gocalinska, E. Pelucchi, A. J. Trindade, B. Corbett, G. Morthier, and G. Roelkens. *Transfer-printing-based integration of a III-V-on-silicon distributed feedback laser*. Optics express, 26(7):8821–8830, 2018.

[22] M. L. Davenport, S. Skendzic, N. Volet, J. C. Hulme, M. J. R. Heck, and J. E. Bowers. *Heterogeneous Silicon/IIIV Semiconductor Optical Amplifiers*. IEEE Journal of Selected Topics in Quantum Electronics, 22(6):78–88, nov 2016.

[23] K. Van Gasse, J. Van Kerrebrouck, A. Abbasi, J. Verbist, G. Torfs, B. Moeneclaey, G. Morthier, X. Yin, J. Bauwelinck, and G. Roelkens. *III-V-on-Silicon Photonic Transceivers for Radio-Over-Fiber Links*. Journal of Lightwave Technology, 36(19):4438–4444, oct 2018.

[24] P. De Heyn, V. I. Kopp, S. A. Srinivasan, P. Verheyen, J. Park, M. S. Wlodawski, J. Singer, D. Neugroschl, B. Snyder, S. Balakrishnan, and Others. *Ultra-dense 16×56Gb/s NRZ GeSi EAM-PD arrays coupled to multicore fiber for short-reach 896Gb/s optical links*. In 2017 Optical Fiber Communications Conference and Exhibition (OFC), pages 1–3. Ieee, 2017.

[25] K. K. Loi, J. H. Hodiak, X. B. Mei, C. W. Tu, W. S. C. Chang, D. T. Nichols, L. J. Lembo, and J. C. Brock. *Low-loss 1.3-μm MQW electroabsorption modulators for high-linearity analog optical links*. IEEE Photonics Technology Letters, 10(11):1572–1574, 1998.

Chapter 7

III-V-on-silicon photonic sampler

In this chapter we present the theory, design and implementation of a fully integrated photonic sampler based on a III-V-on-silicon mode-locked laser. This sub-sampler combines a mode-locked laser, dual-drive Mach-Zehnder modulator, semiconductor optical amplifier and photodiode on a single III-V-on-silicon photonic integrated circuit. Furthermore, we investigated the application of this integrated sub-sampler for the use in communication satellites. This was done in the framework of the Electro-Photonic Frequency Converter (EPFC) project in collaboration with the European Space Agency and Antwerp Space. The EPFC was designed in such a way that an incoming signal on a carrier in the Ka-band (27.25-29.75 GHz) is down-converted to the L-band in a single step (1.5 GHz). The material presented in this chapter has in part been published in reference [1].

7.1 Introduction

The use of short optical pulses to sample high-frequency electrical signals has been investigated for numerous applications. For example in frequency metrology, schemes based on optical sampling have been used to create sub-femtosecond optical-microwave phase detectors [2]. Mode-locked lasers can generate pulse-trains with extremely low timing jitter, which are ideally suited for photonic sampling ADCs [3]. A flexible and high-performance radar system based on a pulsed laser source and photonic ADC was demonstrated in [4]. The use of an optical pulse train is also of interest for microwave photonic frequency conversion. In [5] a millimetre-wave OFDM signal is up-converted from 5 GHz to 60 GHz by the external modulation of

a 55GHz quantum dashed mode-locked laser. Furthermore, ultrawideband RF down-conversion and disambiguation has been demonstrated using a subsampled analogue photonic link [6]. This disambiguation is based on dithering the repetition rate of the mode-locked laser, allowing to identify the original frequency of the subsampled signals. Finally, by using a mode-locked laser microwave photonic down-conversion can be combined with microwave photonic filtering in a single link [7].

In this chapter we develop microwave photonic down-conversion based on a mode-locked laser and modulator using integrated photonics. Previously demonstrated optical sampling schemes relied on fiber or solid state pulsed lasers. Such solutions are not suitable for scalable deployment in a wireless communication scenario. Thanks to the development of high-performance mode-locked lasers in III-V-on-silicon, together with phase shifters and amplifiers, this technology allows us to develop a fully integrated optical sampling PIC.

7.2   System design

In general, optical sampling relies on using an electro-optic modulator which imprints the RF signal, to be sampled, on an optical pulse train. As reported in [8], a single PIC containing lasers, modulators and photodiodes can be realized in III-V-on-silicon. As we have demonstrated in Chapter 2 also high-performance mode-locked lasers can be be realized in III-V-on-silicon. Using this technology it is possible to realize a full optical sampling circuit on a single PIC.

A schematic of such a PIC is shown in Fig. 7.1(a), while in Fig. 7.1(b) a system where one MLL PIC is shared to sub-sample several RF signals in parallel is shown. Using this approach it is also easy to remote the IF signal, as shown in Fig. 7.1(c). The remoting is especially interesting if the system is used for up-conversion in radio-over-Fiber links [5]. In the rest of the chapter we will discuss the development of this PIC with goal of implementation as a photonic sub-sampler in communication satellites. However, the fabricated PICs are multi-purpose and could be used for Radio-over-Fiber up-conversion or RF signal disambiguation [6]. Before we elaborate on the implementation in communication satellites and chip design, we first give a short analytical analysis in the next section.

7.3   System analysis

In this section we will clarify the operational principle of the III-V-on-silicon photonic sampler. As detailed before, the link is based on a mode-locked
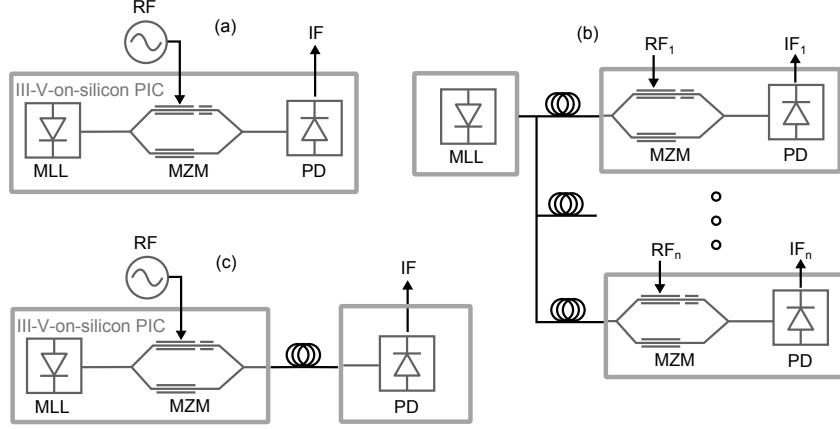
Figure 7.1: Schematic overview of a III-V-on-silicon integrated photonic sampling circuit. (a) Photonic sampler with all components integrated on a single PIC. (b) Photonic sampler system with shared MLL PIC serving several mixing PICs. (c) Photonic sampler-based Radio-over-Fiber link where the sampling can be used for up-conversion.

laser, MZM and photodiode. Since the MZM has an analytic transfer function that is not device dependent (except for limited parasitic effects) we can give a detailed analysis and estimate the conversion gain of the system.

7.3.1 Microwave photonic frequency-conversion

Many frequency conversion systems using MZMs have been studied. One of the first approaches using two MZMs in series was analyzed in [9]. A more efficient approach using a dual-parallel MZM (DPMZM), two MZM placed in a super MZI structure, was published in [10]. Later even more complex systems, with for example a fiber Sagnac loop, where explored [11]. Furthermore, using a DPMZM a frequency-converter with control of the output IF phase was achieved in [12]. Also more complex modulator systems such as dual-polarization DPMZMs have been used to achieve frequency-conversion with phase shifting functionality [13]. An appealing low-complexity approach is based on a Dual-Drive MZM as was proposed in [14] and more recently analyzed in detail in [15].

In a Dual-Drive MZM (DDMZM) architecture a single MZI structure is used, but each arm contains an independently addressable phase shifter. Such a device is sometimes used as a QPSK modulator. The main advantage of the DDMZM is the low complexity and ease of implementation
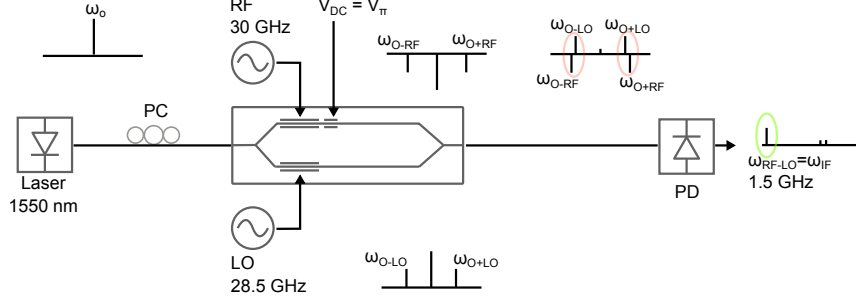
Figure 7.2: Schematic of a DDMZM-based microwave photonic frequency down-conversion link. In this schematic a Ka-band tone (30 GHz) is down-converted to a L-band carrier (1.5 GHz) in a single step using a high-frequency LO. A representative spectrum is shown in several stages of the system. The optical frequencies leading to the wanted IF beat-note are circled.

in a photonic circuit. To clarify the operation of this microwave photonic frequency-converter approach, we study the output of a DDMZM with a CW optical carrier as input. A schematic example of how a DDMZM-based microwave photonic frequency-converter works is shown in Fig. 7.2. The system is very similar in operation when compared to the EAM-based mixer, however now each arm contains a phase modulator instead of an intensity modulator. If one phase-shifter is modulated with a RF signal (a single RF tone for simplicity) and the other with a LO signal, the optical output of the DDMZM can be written as:

$$E(t) = \frac{E_{in}}{2}e^{j\omega_o t}\left(e^{j\beta_{RF}\cos(j\omega_{RF}t)} + e^{j\phi}e^{j\beta_{LO}\cos(\omega_{LO}t)}\right) \qquad (7.1)$$

$$= \frac{E_{in}}{2}e^{j\omega_o t}\Bigg\{ \sum_{n=-\infty}^{\infty} j^n J_n(\beta_{RF})e^{jn\omega_{RF}t}$$

$$+ e^{j\phi} \sum_{m=-\infty}^{\infty} j^m J_m(\beta_{LO})e^{jn\omega_{LO}t}\Bigg\}. \qquad (7.2)$$

Where E_{in} is the amplitude of the incident optical field, ω_o is the optical carrier angular frequency, ω_{RF} is the angular frequency of the RF tone, ω_{LO} is the angular frequency of the LO tone. In the last equation the Jacobi-Anger expansion was used to simplify the phase modulation terms. The modulation amplitude β is proportional to the ratio of the modulation voltage amplitude $V_{RF,LO}$ and the single-drive half-wave voltage V_π of the modulator:

$$\beta_{RF,LO} = \pi\frac{V_{RF,LO}}{V_\pi}. \qquad (7.3)$$

If the modulation amplitudes are sufficiently small we can approximate phase modulation with a single tone as:

$$\sum_{m=-\infty}^{\infty} j^m J_m(\beta) e^{jn\omega} \approx J_0(\beta) + 2j J_1(\beta) \cos(\omega t). \qquad (7.4)$$

This corresponds to only taking the first order optical side-bands into account and neglecting all harmonics. When using this photonic frequency-conversion approach the optical carrier does not contribute to the useful signal, while the optical carrier can saturate any amplifier or photodiode in the link and thus limit the conversion gain. Therefore, we use the DDMZM biased at the carrier-suppression operation point which corresponds to $\phi = \pi$ in Eq. 7.2. To give an analytic expression for the output signal of the photodiode $i_{PD}(t)$, we first need to calculate the optical intensity $P(t) = |E|^2$. If we use the approximation given in Eq. 7.4 to simplify Eq. 7.2 and put $\phi = \pi$, we can formulate the optical intensity at the output of the DDMZM as:

$$
\begin{aligned}
P(t) = \frac{P_{in}}{4} \Big\{ &J_0^2(\beta_{RF}) + J_0^2(\beta_{LO}) - 2J_0(\beta_{RF})J_0(\beta_{LO}) \\
&+ 4J_1^2(\beta_{RF}) \cos^2(\omega_{RF}t) + 4J_1^2(\beta_{LO}) \cos^2(\omega_{LO}t) \\
&- 8J_1(\beta_{LO})J_1(\beta_{RF}) \cos(\omega_{RF}t) \cos(\omega_{LO}t) \Big\}. \qquad (7.5)
\end{aligned}
$$

From this expression the photo-current can be easily calculated if the responsivity $\mathfrak{R}$ of the photodiode is known. It is clear from this expression that the output signal from the photodiode will contain several frequencies originating from the different beating frequencies.

$$i_{PD}(t) = \mathfrak{R}P(t) = i_{dc} + i_{2LO}(t) + i_{2RF}(t) + i_{RF+LO}(t) + i_{RF-LO}(t) \quad (7.6)$$

This expression is valid as long as the approximation in Eq. 7.4 is valid. When harmonics are taken into account, more terms have to be added. Furthermore, due to limited extinction ratios of real MZIs parasitic LO and RF frequency terms can appear. The full expression for the different

contributions is given by:

$$i_{dc} = \frac{P_{in}\mathfrak{R}}{4}\bigg\{ J_0^2(\beta_{RF}) + J_0^2(\beta_{RF}) - 2J_0(\beta_{RF})J_0(\beta_{RF})$$

$$+ 2J_1^2(\beta_{RF}) + 2J_1^2(\beta_{LO}) \bigg\} \qquad (7.7)$$

$$i_{2LO} = \frac{P_{in}\mathfrak{R}}{2} J_1^2(\beta_{LO}) \cos(2\omega_{LO}t) \qquad (7.8)$$

$$i_{2RF} = \frac{P_{in}\mathfrak{R}}{2} J_1^2(\beta_{RF}) \cos(2\omega_{RF}t) \qquad (7.9)$$

$$i_{RF+LO} = P_{in}\mathfrak{R}J_1(\beta_{RF})J_1(\beta_{LO}) \cos\big((\omega_{RF} + \omega_{LO})t\big) \qquad (7.10)$$

$$i_{RF-LO} = P_{in}\mathfrak{R}J_1(\beta_{RF})J_1(\beta_{LO}) \cos\big((\omega_{RF} - \omega_{LO})t\big) \qquad (7.11)$$

The last two equations correspond to up- and down-conversion respectively. To further examine the down-conversion case it is convenient to introduce a constant α_o, which takes any optical gain and losses in the system into account. Now we can express the output microwave power at the wanted IF:

$$P_{IF} = \langle i_{RF-LO}^2 \rangle Z_{out} = \frac{P_{in}^2 \mathfrak{R}^2 \alpha_0^2}{2} J_1^2(\beta_{RF}) J_1^2(\beta_{LO}) Z_{out}. \qquad (7.12)$$

To have a clear expression for the system gain we can express the RF input-power into the DDMZM in terms of the modulation amplitude V_{RF}:

$$P_{RF} = \frac{\langle V_{RF}^2 \rangle}{Z_{in}} = \frac{\beta_{RF}^2 V_\pi^2}{2\pi^2 Z_{in}}. \qquad (7.13)$$

If we now define the system gain as the ratio of P_{IF} and P_{RF} we find that:

$$G_{IF} = \frac{\langle i_{RF-LO}^2 \rangle}{\langle V_{RF}^2 \rangle} Z_{in} Z_{out}$$

$$= P_{in}^2 \mathfrak{R}^2 \alpha_0^2 \frac{\pi^2 J_1^2(\beta_{RF}) J_1^2(\beta_{LO})}{\beta_{RF}^2 V_\pi^2} Z_{out} Z_{in} \qquad (7.14)$$

If one assumes that β_{RF} is small enough so that $J_1(\beta_{RF}) \approx 0.5\beta_{RF}$, the last expression can be further simplified to:

$$G_{IF} = P_{in}^2 \mathfrak{R}^2 \alpha_0^2 \frac{\pi^2 J_1^2(\beta_{LO})}{4 V_\pi^2} Z_{out} Z_{in}. \qquad (7.15)$$

This expression is valid both for up- and down conversion, as the amplitude in Eq. 7.10 and Eq. 7.11 are equal. This expression is identical to the one derived in [15] for a link with fixed optical loss and gain. From this equation we find that the gain is maximal if $J_1(\beta_{LO})$ is maximal, this happens when
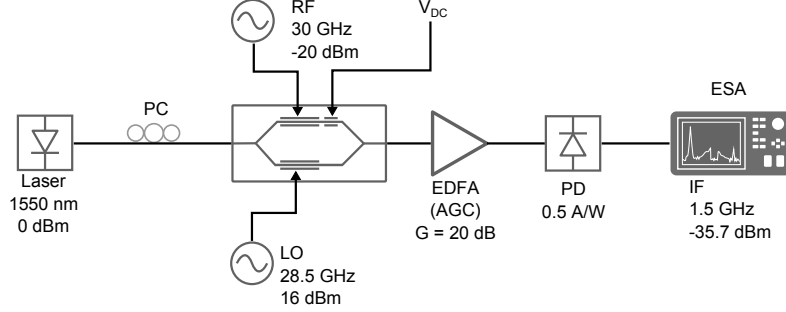
Figure 7.3: Schematic of an example microwave photonic down-conversion link with realistic values for the components. The LO is driven with a power corresponding to maximum conversion gain.

$\beta_{LO} = 1.84$ ($J_1(\beta_{LO}) \approx 0.58$). If an output power controlled EDFA is used, this expression is not instructive however as the factor α_0 also becomes a function of β_{RF} and β_{LO}.

At this point it is interesting to calculate the gain for a realistic down-conversion link with fixed optical loss. We assume a scenario where a signal in the Ka-band (30 GHz) with a signal strength of -20 dBm is down-converted to the L-band using a high-frequency LO (28.5 GHz). For a typical LiNb0$_3$ DDMZM (e.g. Fujitsu FTM7937EZ) the single ended V_π equals 3.5 V, which translates into an optimal LO driving amplitude of 2.05 V ($\beta_{LO} = 1.84$) or 16 dBm in a 50 Ω system. In Fig. 7.3 an example of such a down-conversion system is shown. In this system a laser with 0 dBm optical output power is used and the DDMZM is assumed to have an optical insertion loss of 6 dB. Furthermore, we consider the EDFA to have a gain of 20 dB and the PD to have a responsivity of 0.5 A/W. Using formula Eq. (7.15) we find a calculated down-conversion gain of -15.7 dB, or for an RF input power of -20 dBm an IF output power of -35.7 dBm. However, the LO power of 16 dBm used in this example is rather high and will require a powerful oscillator or high-frequency amplifier. From Eq. (7.15) it is also clear that the optical power contributes quadratically to the conversion gain, this means that it is sufficient to increase the optical power at the photodiode with 8 dB to achieve positive conversion gain. Therefore, it is interesting to use a high-gain high-power optical amplifier and a high-saturation power photodiode.

7.3.2 Mode-locked-laser-based microwave photonic frequency-conversion

In the previous section we described how a single CW laser and a DDMZM can be used to down-convert an RF signal. In this section we clarify how this can be combined with a mode-locked laser to create a photonic sub-sampler based frequency converter. To give a clear insight how this can be achieved with a MLL, we first investigate how frequency conversion can be achieved using optical heterodyning. Optical heterodyning is a technique based on the fact that two lasers with a slightly different wavelength incident on a photodiode produce a RF beatnote. For example, this approach has been used to create a tunable microwave synthesizer on a single PIC using III-V-on-silicon devices [16]. Not only is this technique used to generate high-frequency RF carriers, one can create a THz transmitter by modulating one or both of the optical carriers with data [17]. The generation of an RF signal by optical heterodyning can be explained starting from the expression for the field of two ideal single wavelength lasers:

$$E_{tot} = E_1 e^{j\omega_1 t} + E_2 e^{j\omega_2 t}. \tag{7.16}$$

When the combined light of these two lasers is incident on a photodiode, with sufficiently high bandwdith, the generated photocurrent can be expressed using the responisivity $\mathfrak{R}$:

$$
\begin{aligned}
i_{PD}(t) &= \mathfrak{R}\left(E_1 e^{j\omega_1 t} + E_2 e^{j\omega_2 t}\right)\left(E_1 e^{-j\omega_1 t} + E_2 e^{-j\omega_2 t}\right) \\
&= \mathfrak{R}\left[E_1^2 + E_2^2 + 2E_1 E_2 \cos\left((\omega_1 - \omega_2)t\right)\right] \\
&= i_{dc} + 2\mathfrak{R}\sqrt{P_1 P_2}\cos(\Delta\omega t)
\end{aligned}
\tag{7.17}
$$

Where we assumed E_1 and E_2 to be real. From the last equation it is clear that an electrical signal, with the difference frequency of the two optical carriers, is generated at the photodiode output. A schematic of this technique is shown in Fig. 7.4a. One of the advantages of this approach of microwave signal generation is the frequency tunability. Tuning one of the incident lasers by 1 nm at 1550 nm changes the RF frequency by more than 100 GHz. To achieve frequency conversion one or both of the optical signals need to be modulated with the RF input signal. To simplify the following analysis of the system, we will assume the MZM biased at quadrature functions as a perfect amplitude modulator with response $H(V) = (1 + V)/2$. Using this approximation we can express the modulated dual-wavelength signal as:

$$E_{mod} = \frac{1}{2}(1 + s(t))(E_1 e^{j\omega_1 t} + E_2 e^{j\omega_2 t}) \tag{7.18}$$

Where $s(t)$ is the signal modulated on the optical carriers. When incident on a photodiode the generated photocurrent can be expressed as:

$$i_{PD} = \frac{1}{4}(1 + 2s(t) + s^2(t)) \left[i_{dc} + 2\Re\sqrt{P_1 P_2} \cos(\Delta\omega t) \right] \qquad (7.19)$$

If the signal $s(t)$ is a single RF tone and we use $i_b = 2\Re\sqrt{P_1 P_2}$, this expression can be further simplified:

$$
\begin{aligned}
i_{PD} =& \frac{1}{8}(3 + 2cos(\omega_{RF}t) + cos(2\omega_{RF}t)) \left[i_{dc} + i_b \cos(\Delta\omega t) \right] \\
=& \frac{3}{8}i_{dc} + \frac{i_{dc}}{4}cos(\omega_{RF}t) + \frac{i_{dc}}{8}cos(2\omega_{RF}t) \\
& + \frac{i_b}{16}cos((2\omega_{RF} + \Delta\omega)t) + \frac{i_b}{16}cos((2\omega_{RF} - \Delta\omega)t) \\
& + \frac{i_b}{8}cos((\omega_{RF} + \Delta\omega)t) + \frac{i_b}{8}cos((\omega_{RF} - \Delta\omega)t) \qquad (7.20)
\end{aligned}
$$

The last two terms of this expression correspond to the up- and down-converted RF tone respectively. Now assume that we want to down-convert a RF signal consisting of a high-frequency RF carrier modulated with 64-QAM data. In this case the RF signal can be represented as an amplitude and phase modulated cosine $s(t) = d(t)cos(\omega_{RF}t + \phi_d(t))$. If we insert this in Eq. 7.19 and only retain the terms relevant for the wanted down-converted term we find:

$$
\begin{aligned}
i_{down} =& \frac{i_b}{2}d(t)cos(\omega_{RF}t + \phi_d(t)) \cos(\Delta\omega t) \\
=& \frac{i_b}{4}d(t)cos((\omega_{RF} - \Delta\omega)t + \phi_d(t)) \qquad (7.21)
\end{aligned}
$$

From the last expression it is clear that the result is the original RF signal down-converted to the wanted IF ($\omega_{RF} - \Delta\omega$) by optical heterodyning. Two possible examples of optical-heterodyning-based frequency-conversion are shown in Fig. 7.4b and Fig. 7.4c. In Fig. 7.4b down-conversion of a RF signal on a 61.5 GHz carrier to a 1.5 GHz carrier is shown. Up-conversion with optical heterodyning is an appealing way to generate THz carriers with complex modulated data [17]. One of the challenges of this approach is the mutual stability between the two optical carriers. When two separate lasers are used to generate a beat note, both lasers will drift due to local environmental variations such as temperature.

An interesting alternative is to use a mode-locked laser. In a mode-locked laser one single cavity is used with different lasing modes locked to each other. Because the modes are locked to each other, the generated beat-note by such a MLL is very stable. This can be achieved in several ways and many MLLs have been demonstrated based on fiber lasers, solid-state

lasers, VECSEls or PICs. Furthermore an RF reference can be used to lock the MLL to a fixed repetition rate. Using this approach the MLL can be used to generate many multiples of the reference signal.

As described in the introduction of this chapter, up-conversion of an OFDM QPSK signal to 60 GHz using a semiconductor quantum dash mode-locked laser with 55 GHz repetition rate is demonstrated in [5]. The same team later also achieved up-conversion by direct modulation of the same MLL [18]. A schematic representation of the MLL based frequency conversion is shown in Fig. 7.5.

We can make a similar derivation as was done for the optical hetero-dyning. We can approximate the output of a MLL as a sum of individual optical modes which have a fixed frequency spacing and fixed phase:

$$E_{tot} = \sum_{n=1}^{N} E_n e^{j(\omega + n\Delta\omega)t + \phi_n}. \tag{7.22}$$

In a first approximation we assume the mode-locked laser consists of three longitudinal modes with identical amplitude and no phase offset. The signal generated by a photodiode receiving this pulse train can be expressed:

$$\begin{aligned}
i_{pd}(t) &= |E(e^{j(\omega - \Delta\omega)t} + e^{j\omega t} + e^{j(\omega + \Delta\omega)t})|^2 \\
&= P(1 + 2\cos{(\Delta\omega t)})^2 \\
&= P(3 + 4\cos{(\Delta\omega t)} + 2\cos{(2\Delta\omega t)}) \tag{7.23}
\end{aligned}$$

If we now substitute this into Eq. 7.19 we have a similar expression:

$$i_{pd}(t) = i_0 \frac{1}{4}(1 + 2s(t) + s^2(t))[3 + 4\cos(\Delta\omega t) + 2\cos(2\Delta\omega t)] \tag{7.24}$$

This leads to a similar expression as derived in Eq. 7.20, the main difference is that there is now a up and down-conversion term proportional to twice the repetition rate. This derivation was done for three longitudinal modes but can be expanded for any number of modes. For a quantitative calculation the exact spectral shape of the MLL pulse is needed. However for quantitative results it is interesting to use numerical simulations, as will be presented later in this chapter.

(a)

(b)

(c)
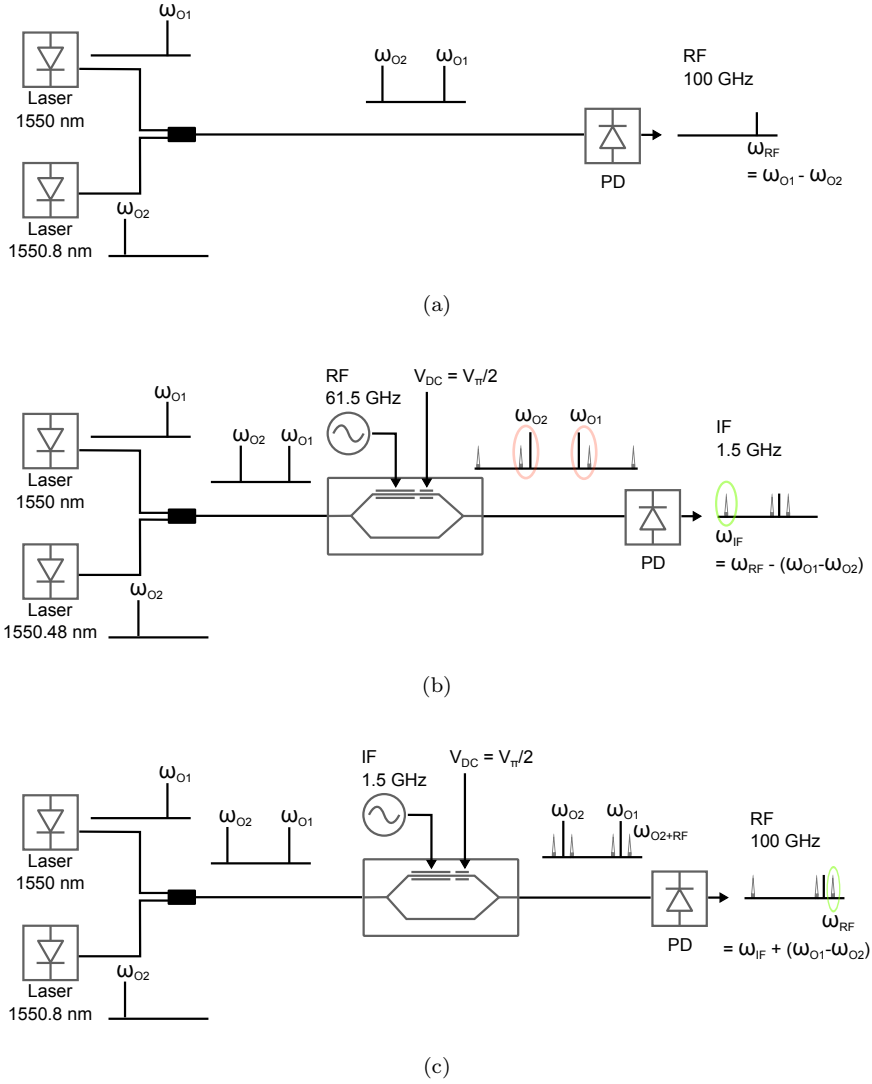
Figure 7.4: (a) Microwave photonic frequency generation by heterodyning two single mode lasers. (b) Schematic of a microwave photonic down-conversion system, where the frequency-conversion is achieved by optical heterodyning of two lasers. In this example an incoming signal on a 60 GHz carrier is down-converted to 1.5 GHz. (c) Schematic of a similar up-conversion system.

(a)

(b)
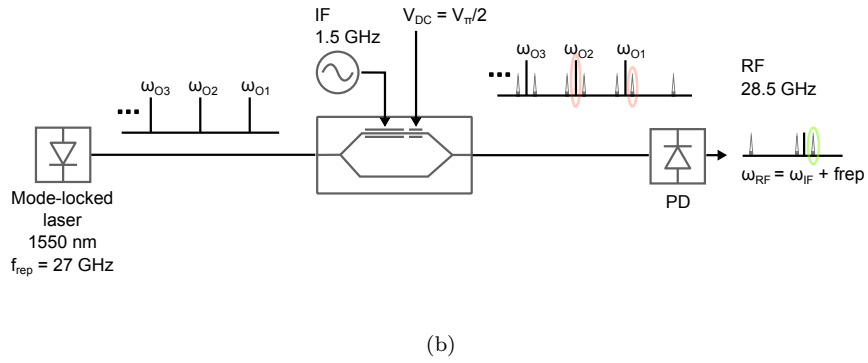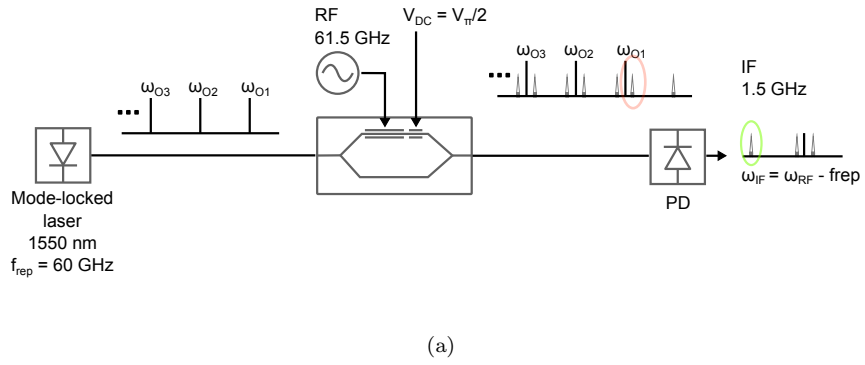
Figure 7.5: (a) Schematic of a microwave photonic down-conversion system, where the frequency-conversion is achieved by optical sampling by the mode-locked laser pulse train. In this example an incoming signal on a 60 GHz carrier is down-converted to 1.5 GHz. (b) Schematic of a similar up-conversion system.

7.4 Photonic sub-sampling frequency converters in communication satellites

7.4.1 Introduction

Frequency conversion is an important aspect of wireless communication, even more so in satellites, where signals are received and transmitted in many diferent frequency bands, as schematically illustrated in Fig. 7.6. In communication satellites large numbers (> 20) of channels have to be down-converted, from for example the Ka-band to a suitable IF, in parallel. This is a demanding part of the receiver and requires a well-designed down-conversion link with several amplifiers, mixers and local oscillators. Furthermore, if a single down-conversion step is wanted each channel requires its own dedicated high-frequency LO with low phase noise. Alternatively, one could use a centralized LO distributed to the individual components. However, the distribution of high-frequency signals using coax or waveguides can dramatically increase size, weight and power (SWaP). An attractive alternative is the use of optical fiber to distribute the LO, as this would considerably reduce the size and weight compared to coax or radio frequency (RF) waveguides. The optical distribution of LO signals in telecommunication satellites has been extensively studied by Thales Alenia Space (TAS) [19]. In this work, optical LO distribution was studied as part of a microwave photonic payload. Recently, a study was presented in which it was estimated that using microwave photonic payloads for communication satellites could save in terms of mass, number of devices and power consumption [20]. In the work of TAS [19], microwave photonic mixing is used to down-convert received Ka-band signals. Up- or down-converting RF signals in the optical domain is a well-studied technique [21–23]. Microwave photonic techniques have also been investigated for RF filtering in communication satellites [24]. Both the work in [19] and [24] was done using discrete opto-electronic components with promising results. It would be very interesting to implement such systems using photonic integrated circuits (PICs), as this would further reduce size and weight while increasing the system reliability.

7.4.2 System implementation

The use of photonic down-sampling to achieve down-conversion is ideally suited for narrow-band signals on high-frequency carriers, as the data can be directly down-converted to a low-frequency IF. Both the single PIC and distributed MLL schemes described in Fig. 7.1 are interesting solutions to down-convert an incoming signal in the Ka-band as shown in Fig. 7.6.
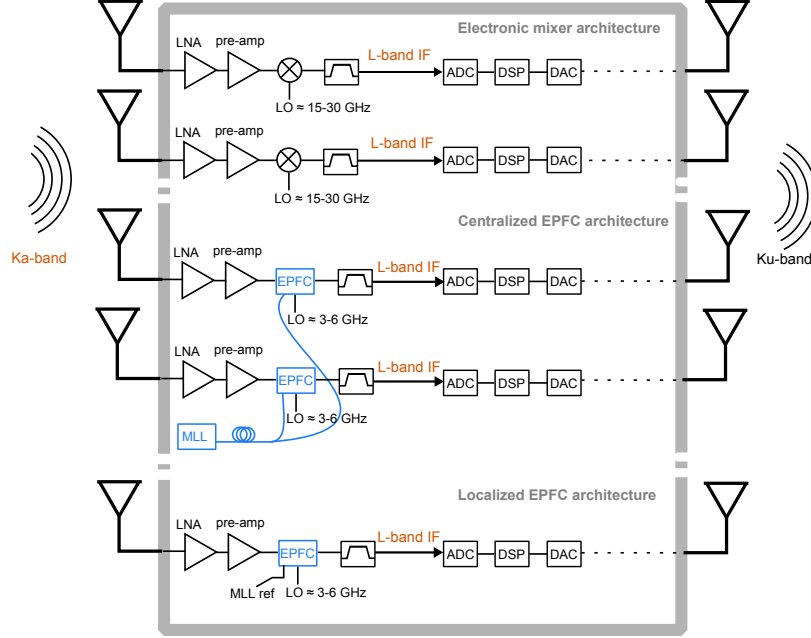
Figure 7.6: Schematic of a communication satellite receiving signals with frequencies in the Ka-band and transmitting signals in the Ku-band. Three different architectures are shown. At the top, an approach using a (subharmonic) MMIC mixer is shown. The other two architectures show an approach using an electro-photonic frequency converter. The centralized architecture uses only one chip-based MLL. The output of the MLL can be distributed using light-weight optical fiber to all the EPFCs. The localized EPFC uses an on-chip MLL, which functions as an optical LO

Modulators with high modulation efficiency have been shown in III-V-on-silicon [25], making the III-V-on-silicon optical sampler approach ideally suited for this down-conversion approach. Moreover, radiation studies performed on silicon photonic transceivers and InP MZMs for the use in particle colliders have shown promising results [26–28], defining a clear path for the use of these photonic integrated circuits in space. In Fig. 7.6 a possible schematic implementation of the integrated photonic sub-sampling PICs in a communication satellite is shown. This implementation was then developed in the framework of the European Space Agency's ARTES Electro-Photonic Frequency Converter (EPFC) project. In this project we designed and fabricated the PICs described before to meet several specifications for realistic implementation in a satellite. The target was to down-convert an incoming Ka-band signal to the L-band. The signal has a bandwidth of 500 MHz and can be received in five different channels with a center frequency

of 27.75, 28.25, 28.75, 29.25 and 29.75 GHz. However, the system should be able to down-convert each channel to the same IF of 1.5 GHz. This additional complexity can be solved in an elegant way by using a MZM with two independently addressable phase shifters. A detailed description of the III-V-on-silicon down-converting optical sub-sampler is given in the next section.

7.4.3 EPFC design

The system architecture is shown in Fig. 7.7 and is almost identical to the mode-locked laser down-conversion scheme described in Fig. 7.5. However in this approach a dual drive MZM is used that allows to implement a channel selection scheme. This channel selection scheme is based on the microwave photonic mixing approach shown in Fig. 7.2. The combination of optical sampling with a MZM-based photonic mixer using commercial discrete components was already demonstrated in [7]. In this approach the optical frequency comb output from the mode-locked laser was also used in combination with dispersive fiber to create a photonic tap filter, which allows to achieve both down-conversion and filtering in the optical domain.

The basic operation principle of the scheme is as follows. The RF signal to be down-converted drives one arm of the DD-MZM while a LO signal drives the other [10]. The optical pulse train generated by the mode-locked laser samples both signals and mixes them on the photodiode. In Fig. 7.7, an input RF signal with a frequency of 29.25 GHz (Ka-band) is down-converted to an IF of 1.5 GHz (L-band). The repetition rate of the mode-locked laser is chosen together with the frequency of the LO to achieve the wanted IF frequency, in this case 15.95 and 4.15 GHz, respectively. The optical output spectrum of the mode-locked laser can be represented as an optical frequency comb separated by the repetition rate of the MLL, as shown in Fig. 7.7. The optical sub-sampling of the RF signal can be represented in the frequency domain by a frequency comb, where every comb tooth has side bands. The spacing between the sidebands and the comb teeth corresponds to the frequency of the sampled signal. The resulting spectra after modulation with the RF and LO signal are shown in Fig. 7.7. In one of the arms of the DD-MZM, a static π-phase shift is applied, such that when both optical signals are combined, the carriers are cancelled. This results in the case of ideal suppression of the carriers, in an optical spectrum shown in Fig. 7.7. When this signal is incident on the photodetector, the beating of the different lines creates different RF signals, of which one is the wanted IF output. Because the output of the photodiode produces several beat notes, a bandpass filter is needed to isolate the IF. All the generated beat notes can be written as a combination of the MLL repetition rate, the RF, and
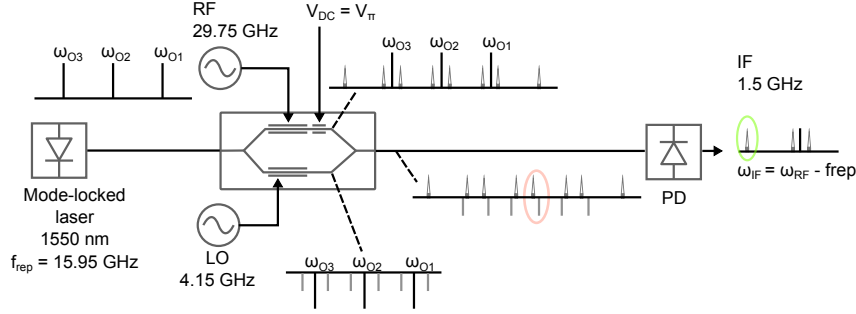
Figure 7.7: Overview of the EPFC system. The optical spectrum is shown in several essential steps of the down-conversion scheme, together with the electrical spectrum at the output.

LO frequency:

$$f_{IF} = k \cdot f_{rep} - l \cdot f_{LO} - m \cdot f_{RF} \quad k, l, m \in \mathbb{Z} \tag{7.25}$$

The wanted IF frequency in our chosen frequency plan is created by the beat note,

$$f_{IF} = 2 \cdot f_{rep} - f_{LO} - f_{RF} \tag{7.26}$$

The choice of the MLL repetition rate and LO frequency is non-trivial, as it should be possible to down-convert all five channels to the same IF without introducing any unwanted mixing products in the passband. To accommodate the down-conversion of these five Ka-band channels a frequency plan was devised. The down-conversion of the five channels in the Ka-band with a bandwidth of 500 MHz at center frequencies 27.75, 28.25, 28.75, 29.25, and 29.75 GHz was achieved using a MLL repetition of 15.95 GHz. The matching LO frequencies for down-conversion to 1.5 GHz IF are 5.65, 5.15, 4.65, 4.15, and 3.65 GHz respectively. This frequency plan allows all channels to be down-converted without creating any spurious beat note in a 500 MHz band around the IF. However, a narrow-band IF bandpass filter is needed to suppress the out-of-band spurs. Furthermore, a filter at the RF input is also needed to prevent unwanted signals being mixed down to the IF band. This system has the benefit that a different channel can be chosen by changing the LO frequency (in the few GHz range).
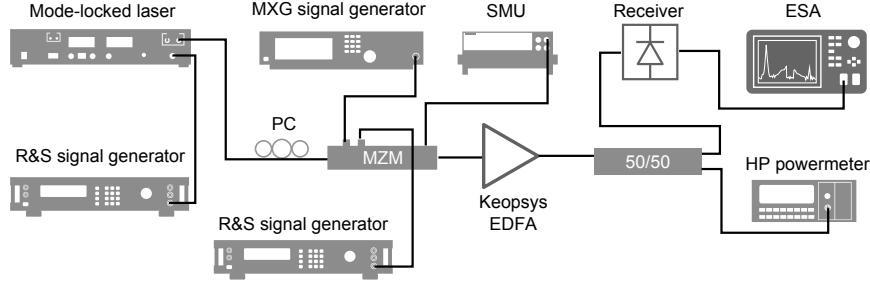
Figure 7.8: Overview of the measurement setup used for the breadboard demonstration of the EPFC system (Mode-locked laser: Calmar PSL-10-TT MLL; Receiver: Discovery semiconductor DSC-10)

7.5 Breadboard demonstration

As a first validation of the EPFC system, a breadboard demonstration was performed with commercial table-top equipment. An overview of the measurement setup is shown in Fig. 7.8. As optical source, a Calmar picosecond (PSL-10-TT) MLL was used with a pulse width of 3 picoseconds and a repetition rate of 10.3 GHz. Because the repetition rate of the MLL could not be tuned to the wanted 15.95 GHz, the frequency scheme was changed to:

$$f_{IF} = 3 \cdot f_{rep} - f_{LO} - f_{RF} \qquad (7.27)$$

The MLL repetition rate was locked to the 0 dBm output of a Rhode and Schwarz RF signal generator. The output of the laser was sent through an optical isolator and polarization controller, after which it was coupled into a Fujitsu FTM7937EZ LiNbO$_3$ dual-drive MZM. The modulator was biased at the minimum transmission point. The phase shifters of the modulator were driven by the input RF signal and the LO signal. The LO signal was fixed at 1 dBm and a frequency of 4.15 GHz. The RF power of the input signal was fixed at −10 dBm and a frequency of 28.25 GHz, corresponding to the second Ka-band channel. At the output of the MZM, an EDFA with APC was placed with a fixed output power of 0 dBm. The photodiode was a Discovery Semiconductor DSC10 with 40 GHz bandwidth and 0.5 A/W responsivity. The output of the photodiode was analyzed with an Agilent electrical spectrum analyzer (ESA) with 44 GHz bandwidth. The RF spectrum obtained at the output of the photodiode is shown in Fig. 7.9(a). A clear signal was observed at 1.5 GHz with a power of −30 dBm, which means that the total system has a conversion efficiency of −20 dB. No electrical amplification was used after the photodiode, but in a realistic implementation a TIA would be used to improve the performance of the link.

Fig. 7.9(b) shows a zoom-in of the IF band, when sweeping the RF input signal over a 800 MHz span around the channel center frequency of 28.25 GHz (−20 dBm RF input power). It can be seen that the response shows no
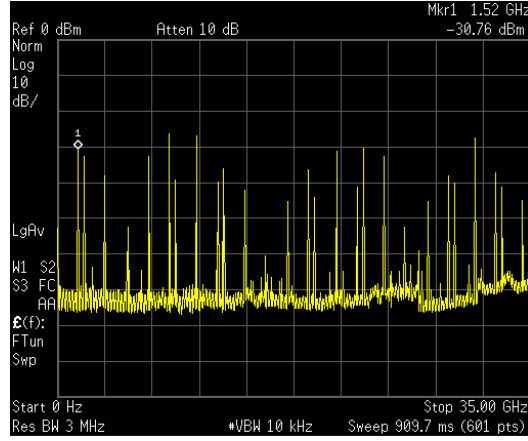
(a)
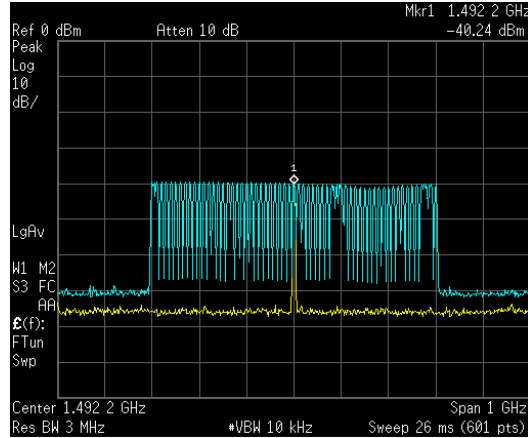
(b)

Figure 7.9: (a) Electrical output spectrum after the photodiode from 0 to 35 GHz. (b) IF output of Channel 2 swept 800 MHz in frequency for an RF input signal of -20 dBm

more than 1.5 dB ripple. The ripple is caused by the non-flat response of the DD-MZM, and can be equalized in baseband after down-conversion using digital signal processing. The 1-dB compression point was −2 dBm (RF input power). The experiment was repeated for all five channels by changing the LO frequency in steps of 500 MHz, showing similar results.

7.6 Design of photonic integrated circuit

In the previous section we validated the EPFC system using commercial components. Furthermore, the implementation of the system in a communications satellite was detailed in Fig. 7.6. In this section we will elaborate on the detailed chip design of the devices proposed in Fig. 7.1(a) and (b).

7.6.1 Single chip

As detailed in the previous section a DDMZM is required for the implementation. High performance phase-shifters can be implemented in III-V-on-silicon using a MQW AlGaInAs layer stack which was demonstrated in [25]. This material has a high phase shifting efficiency because a combination of effects is used, namely the Pockels effect, carrier-depletion and band-filling. Because of all these mechanisms working together a $V_\pi L_\pi$ of 2.4 Vmm could be achieved.

To statically bias the DDMZM at the minimum transmission operation point, a thermo-optic phase shifter is preferred as it is simple to fabricate and has negligible insertion loss. This thermo-optic phase-shifter can be realized using a thin layer of Ti-Au and can be easily incorporated in the III-V-on-silicon process flow. In the breadboard demonstration an EDFA was used to boost the conversion gain. An on-chip amplifier can be used to replace the EDFA. For the IF output stage, a photodiode realized in the same InGaAsP material used for laser and amplifier can be used (under reverse bias). We can then combine all these elements on one III-V-on-silicon PIC with two different types of InP materials, InGaAsP material for the MLL, SOA and PD and AlGaInAs material for the phase-shifters. Since this system will contain several different elements it is interesting to add optical testing ports, such that the individual devices can be tested. By using a 2 by 2 MMI for the DDMZM input and output, an optical test input and output port can be added without hindering the system performance. In Fig. 7.10 a schematic layout of the III-V-on-silicon localized EPFC is shown. As shown in the figure, a ring MLL has two optical outputs and one of them can be used to characterize the MLL without passing through the MZM. The MZM test input in combination with the MZM test output-port can be used to characterize the AlGaInAs phase-shifters or the thermo-optic phase shifter. The MZM test input can be used in combination with the thermo-optic phase shifter to test the SOA and PD.
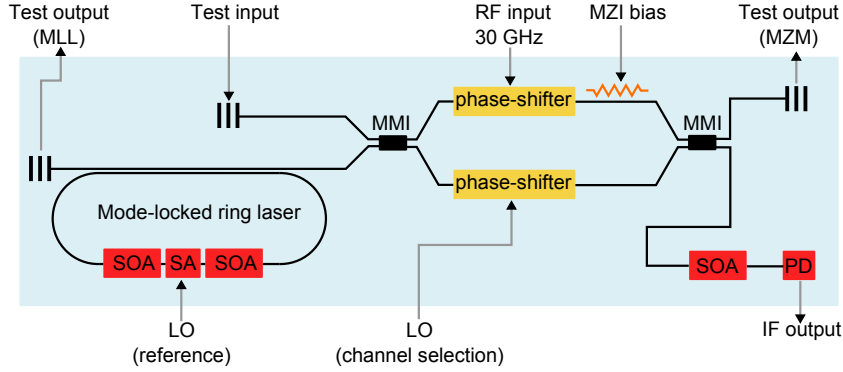
Figure 7.10: Schematic layout of the proposed localized EPFC implemented in a III-V-on-silicon PIC.

7.6.2   Distributed MLL design

As shown in Fig. 7.6 the centralized configuration requires a seperate PIC for the MLL and the mixer-receiver part of the system. In this case the mixer-receiver consists of a DDMZM, photodiode and a gain element. To overcome the fiber-to-chip coupling losses it is interesting to include a SOA on the MLL PIC to compensate these losses. As an SOA can be realized in the same material as the MLL gain section this does not dramatically increase the fabrication complexity, which is important to achieve a high yield. Although in a final version the mixer-receiver could be a separately designed chip, with some clever design the localized EPFC can be used as mixer receiver by using the test-input as input for the MLL input. The proposed system architecture is shown in Fig. 7.11. One of the main advantages of this scheme is the ability to distribute a high frequency LO to several mixers using single mode fiber. In a final design we look toward extending the used technology by using a iSiPP25G sampling chip. In this case the MZM is realized using carrier-depletion phase-shifters and the PD is realized using a waveguide-coupled Ge-on-Si Avalanche Photodetector (APD). A lay-out of this scheme is shown in Fig. 7.12.
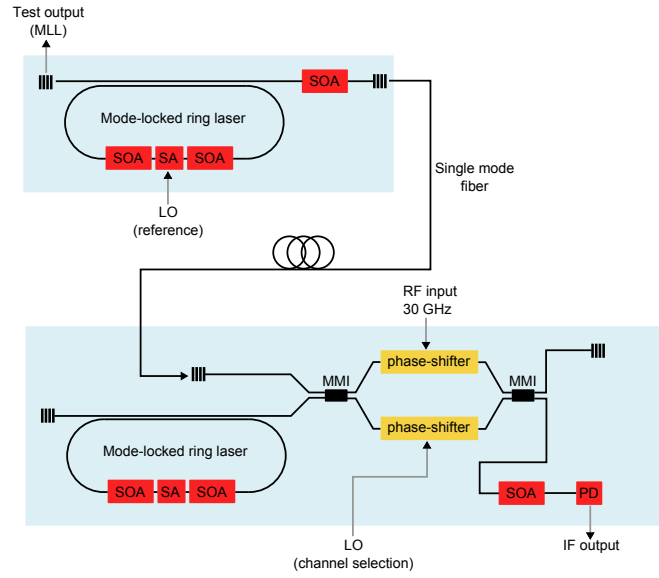
Figure 7.11: Schematic layout of the proposed centralized EPFC implemented in a III-V-on-silicon PIC.
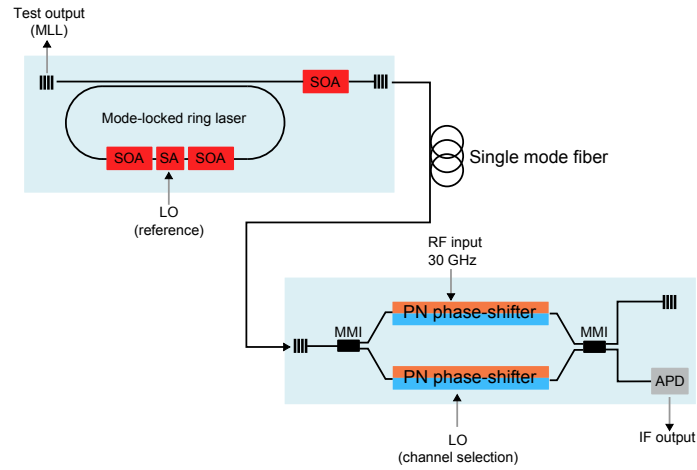
Figure 7.12: Schematic layout of the proposed centralized EPFC implemented with an advanced silicon photonic mixer-receiver.

7.6.3   Multiple die-to-wafer bonding

To fabricate the chip shown in Fig. 7.10 using multiple die-to wafer bonding the design has to be adjusted. As the dies have to be manually bonded for the prototype, the InP dies need to have a minimum size of 5 by 5 mm for handling. Furthermore, the dies need to be spaced at least 1 mm apart for practical alignment and bonding. This implies that the PIC needs to be designed in such a way that all InGaAsP-based devices are on one side and the AlGaInAs phase shifters on the other side. In Fig. 7.13 the design using two different InP materials is shown. Due to the many etching steps involved
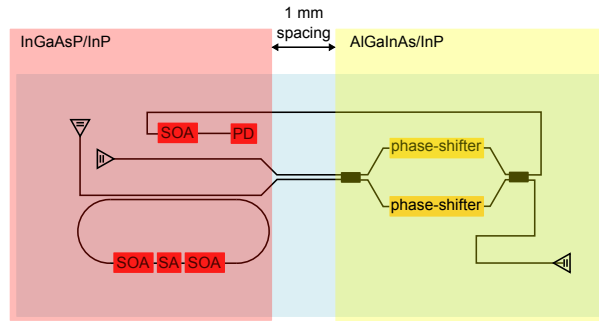
Figure 7.13: Layout of the localized EPFC PIC taking into account the double die-to-wafer bonding fabrication limitations. The red zone indicates the area covered by the InGaAsP/InP material and the yellow zone indicates the area covered by the AlGaInAs/InP material.

in the fabrication, it is imperative that the silicon waveguides and gratings are protected during the processing. This can be achieved by covering the waveguides and passive components with the InP dies during fabrication. However, when using two different dies it is impossible to fully cover the passive waveguides because of the 1 mm spacing between the dies. Therefor, extra processing steps need to be introduced to protect the waveguides during fabrication. However, it is possible to place all grating couplers underneath the InP materials such that they are maximally protected during fabrication.

7.6.4   Electrical contact design

Not only does the PIC design have to be compatible with fabrication, it also has to be electrically and optically probed for testing and packaging. Given the large amount of devices that have to be interfaced this is a non-trivial design challenge. Furthermore, we designed several PICs in parallel that all need to be packaged. To have a practical packaging solution we decided

to use a single PCB which could be used for all PICs. Using these design constraints a final layout for the devices and bondpads was determined. A schematic layout of the PCB and the different PICs is shown Fig. 7.14. Except for the bondpad layout, the dimensions of the different PICs also had to be coordinated such that an identical PCB could be used. The final size of the PIC was 0.73 by 7.25 mm.

(a)

(b)

(c)
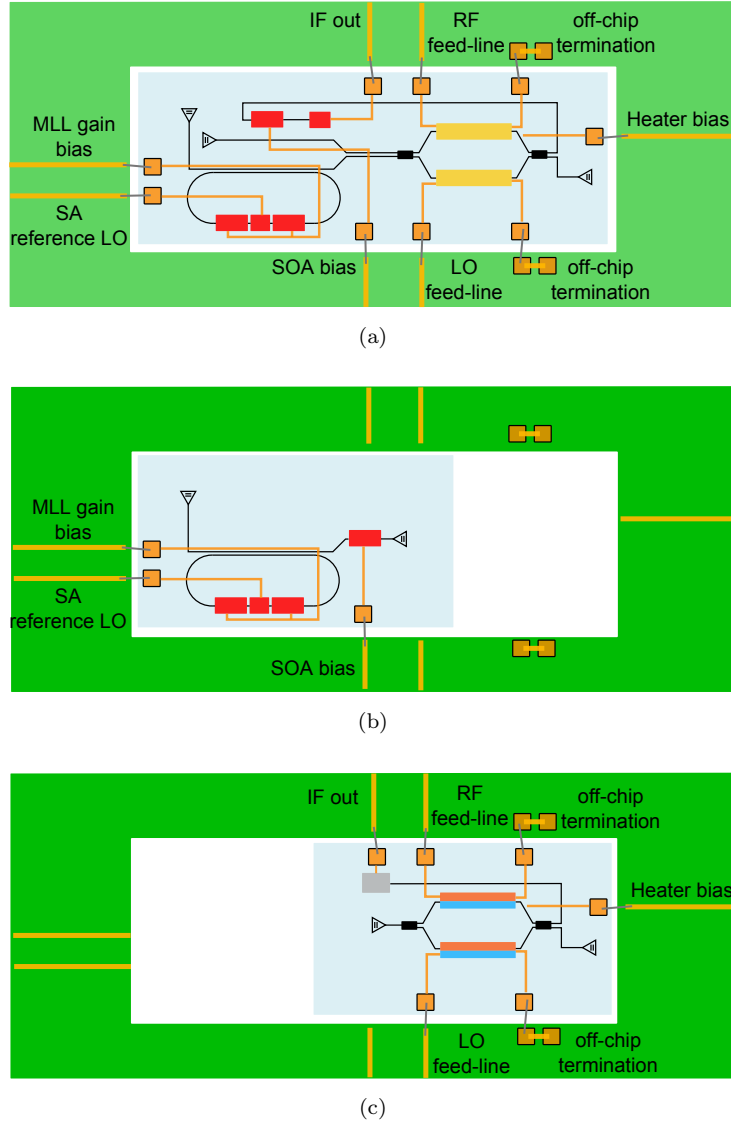
Figure 7.14: (a) Schematic overview of the localized EPFC PIC mounted on the PCB with the contacting scheme. The traces on the PCB are connected to bond pads on the PIC using wire-bonds. (b) Schematic overview of the MLL PIC used in the centralized EPFC system. The bondpad and contacting scheme is identical to the one used for the localized EPFC PIC, except of course for the unused connections. (c) Schematic overview of the silicon sampling integration.

7.7 III-V-on-silicon mixer fabrication

As was discussed in a previous section (7.6), the localized EPFC PIC requires the heterogeneous integration of two types of InP-based materials on a single silicon chip. As discussed before this introduces increased processing complexity but also restrictions on the chip-design. To maximize the amount of devices realized per fabrication run a large passive silicon PIC was designed containing 18 localized EPFC circuits. The lay-out file of the fabricated PIC with a colorized overlay indicating the bonded III-V materials is shown in Fig. 7.15. The passive silicon chip with waveguides measures 18.6 mm by 7.1 mm and needs three III-V dies to be bonded on top of it. By putting the phase-shifting material in a central position it can be shared by two circuits horizontally.

The fabrication of the chip was performed by Dr. Zhechao Wang while the masks were designed by the author. To fabricate the chip, three III-V dies were bonded simultaneously to the passive silicon PIC using a thin layer of DVS-BCB. One of the challenges of the fabrication process is to protect the passive waveguides in between the III-V dies during processing. To achieve this, a 1 μm thick layer of SiO$_2$ was deposited on top of the sample after the die bonding. To access the III-V material while protecting the waveguides, the sample was mechanically grinded to remove the layer of oxide on top of III-V material while leaving an oxide layer on top of the passive waveguides. Then the substrate of both the InP/InGaAsP and InP/AlGaInAs material was removed by etching with diluted HCl. To define the III-V waveguides, a SiN hard mask is deposited followed by an Inductively Coupled Plasma (ICP) etch of the top InGaAsP layer. Without removing the hardmask, the p-doped InP cladding is wet-etched using diluted HCl. This wet-etching step creates a V-shape in the waveguide allowing to define narrow taper tips with a width smaller than 500 nm. Once the p-doped layer is fully etched, a new SiN hardmask is deposited to etch the active QW layers. Once the hardmask is deposited, the InP/AlGaInAs material is covered with photoresist and the InGaAsP QWs are wet etched using H$_2$SO$_4$:H$_2$O$_2$:H$_2$O. Then the InP/InGaAsP material is covered and the AlGaInAs QWs are wet etched. After this step both III-V materials can be processed together. The next step is to define metal contacts on the n-contact layer. This is done by depositing Ni/Ge/Au on the n-doped InP. To isolate the separate devices, the n-doped InP layer is wet-etched in between individual amplifiers and phase shifters. To planarize the sample it is spin-coated with a thick DVS-BCB layer. Finally, vias for both the p-contacts and n-contacts are etched in the DVS-BCB and a Ti/Au contact layer is deposited using a lift-off process. A process flow of the full fabri-
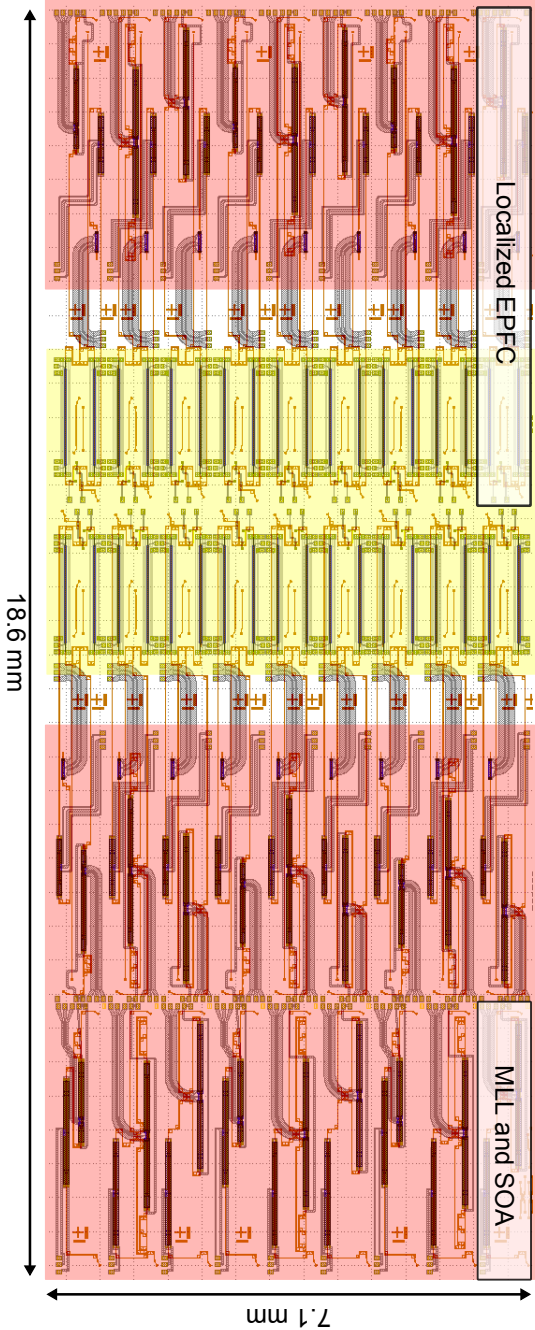
Figure 7.15: Overview of the full PIC design in gds file format. The full PIC contains 18 localized EPFCs with varied MLL designs. Furthermore, the PIC also contains (on the right) 9 stand-alone MLLs with additional output SOAs for the centralized design. The red overlay indicates the area covered by the InP/InGaAsP III-V material, while the yellow overlay indicates the area covered by the phase shifter InP/AlGaInAs material.

cation is shown in Fig. 7.16. To insure the chips are not damaged during
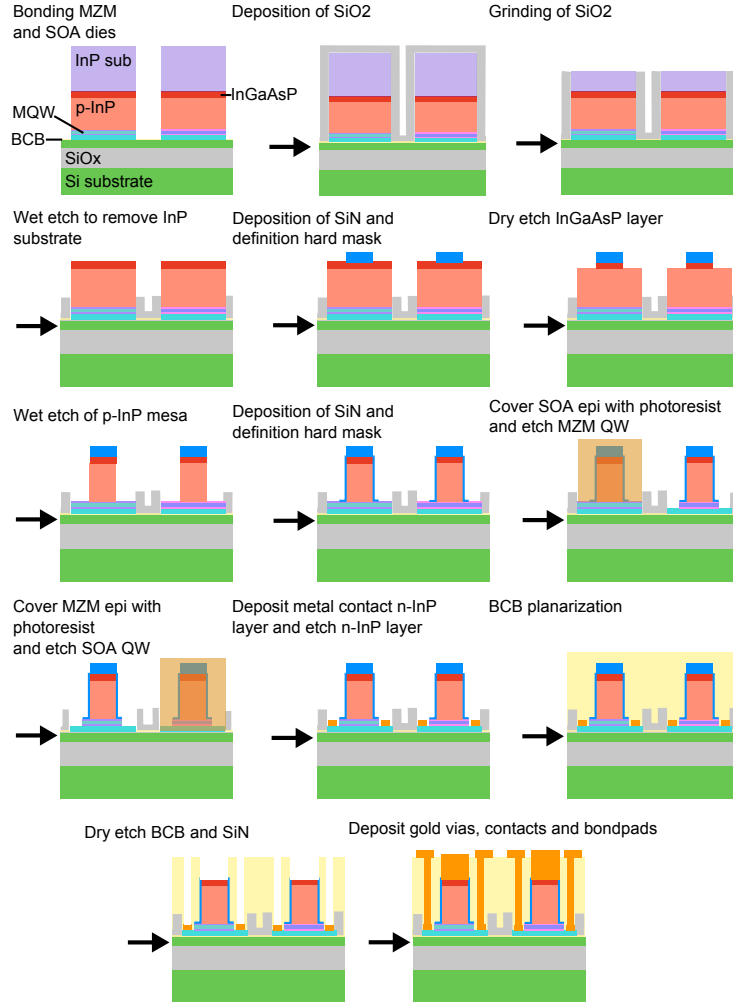
Figure 7.16: Process flow of the fabrication of the multiple-die III-V-on-silicon EPFC PIC.

dicing, the DVS-BCB was etched away in the dicing streets. This ensures that the dicing blade can directly cut the silicon without cracking the DVS-BCB planarization layer. The gds of an individual EPFC circuit is shown in Fig. 7.17 together with a finalized and diced EPFC PIC.
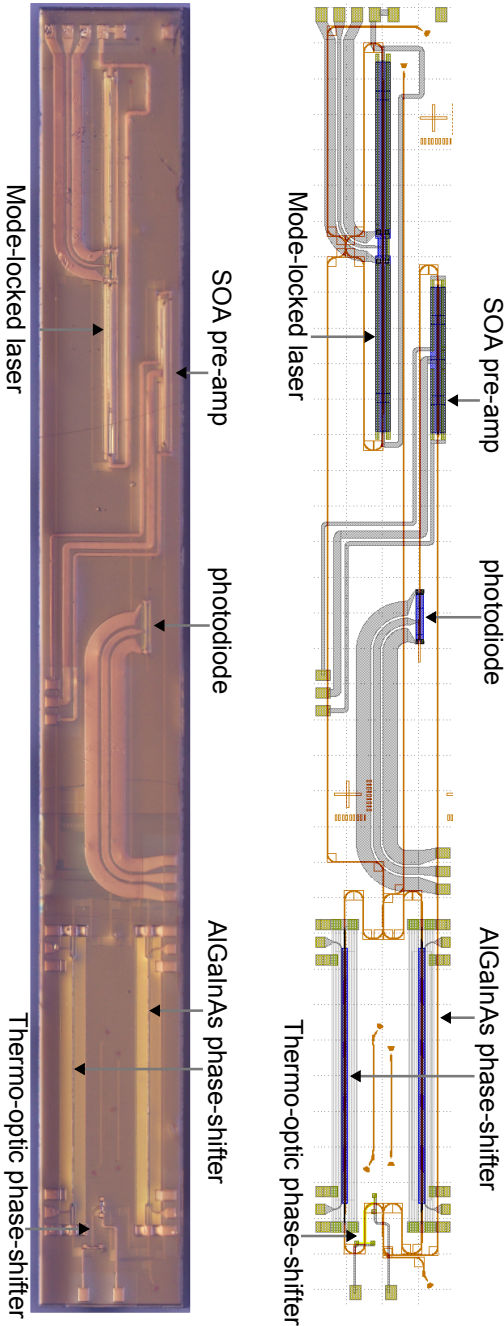
Figure 7.17: (top) A detailed design schematic of a single localized EPFC PIC. (bottom) Micrograph of a single diced-out localized EPFC PIC.

7.8 Integrated photonic devices demonstration

A first demonstration of the sub-sampling circuit was performed using a centralized LO configuration. A separate MLL PIC and MZM PIC were used, where the MLL PIC contained only a mode-locked laser and the MZM was part of a fully integrated EPFC system. A schematic lay-out of the experiment is shown in Fig. 7.18. Both chips were placed on a temperature
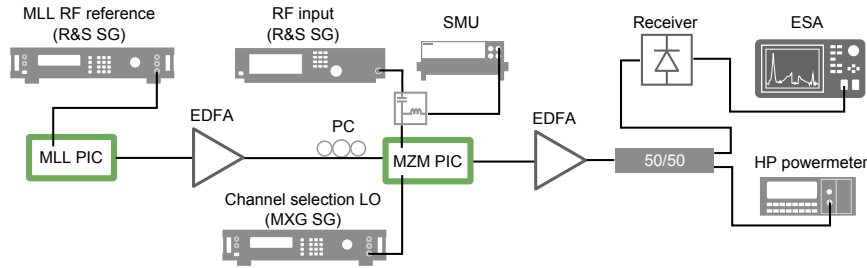
Figure 7.18: Overview of the measurement set-up used to characterize the microwave photonic down-conversion system using a MLL and MZM PIC.

controlled chuck and kept at a temperature of 20°C during the entire experiment. The MLL used in this experiment has the same design as the MLL described in Chapter 2, but has a shorter cavity and thus a higher repetition rate of 2.5 GHz. To achieve a repetition rate as close as possible to the desired frequency of 15.95 GHz, the laser was locked to the sixth harmonic. This harmonic locking was achieved by driving the saturable absorber section with 14 dBm of RF power at a frequency of 15.6 GHz. The RF spectrum generated by the laser, for both fundamental and harmonic operation, is shown in Fig. 7.19a. The MLL was contacted using a custom made RF probe, allowing to bias the gain section and deliver a high-frequency signal to the saturable absorber at the same time. The average optical output power of the mode-locked laser was approximately 2 mW in the waveguide for a gain current of 95 mA and a saturable absorber bias of -0.83 V. and the chip-to-fiber coupling induced a loss of approximately 10 dB. To compensate for the grating coupler losses an EDFA with 17 dB of gain was inserted between the MLL and MZM chip. The light is then coupled into the MZM PIC, also using a cleaved SMF and fiber-to-chip grating couplers. The MZM used in this experiment corresponds to the III-V-on-silicon device described in Chapter 3 and has a V_{π} of approximately 2 V. The small-signal response of the modulator is shown in Fig. 7.19b. Given that the bandwidth is limited it is interesting to calculate the effective V_{π}

(a)   (b)
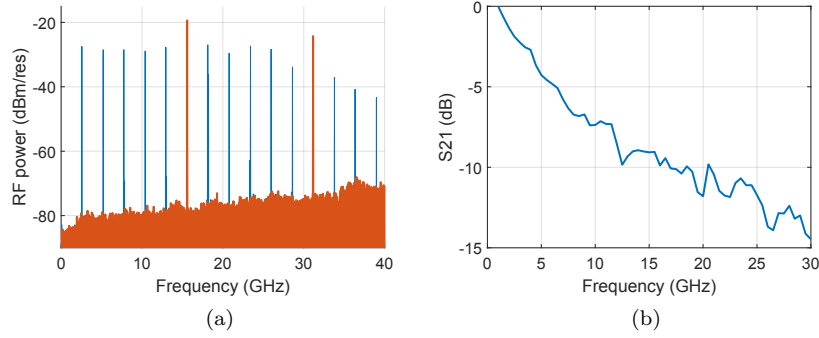
Figure 7.19: (a) The RF spectrum (62 kHz RBW) generated by the pulse train of the integrated mode-locked laser. The thin blue line represents the RF spectrum of fundamental operation, the thick orange line shows the harmonically (sixth harmonic) locked spectrum. (b) The small-signal modulation response of the III-V-on-silicon MZM.

at the frequencies of interest. For the channel-selection LO the frequencies of interest are centered at approximately 5 GHz where the effective V_π corresponds to approximately 3.2 V. However, for the Ka-band signal the small-signal response has deteriorated by -13 dB and the effective V_π is approximately 9 V. The two independent phase shifters of the MZM are driven by the LO (10 dBm) and the RF (0 dBm) input signal. Two RF probes and two fiber probes where needed to contact the MZM PIC. Because of space limitations we were unable to add another probe to contact the thermo-optic phase shifter. This prevented us from providing a static bias for the MZM using the thermo-optic phase shifter. In a packaged version this issue will no occur since all contacts can be easily wire-bonded to a PCB. Therefore, the phase shifters were DC-biased differently for a minimum transmission of the MZM. Because the grating couplers of the MZM PIC also have 10 dB loss, an additional EDFA was placed at the output. A Santec optical tunable filter (OTF-350) was placed after the EDFA to filter out the ASE. The average optical power incident on the PD was 0 dBm. To boost the electrical output signal, a photodetector with trans-impedance amplifier (TIA) was used. The receiver has a gain of 150 V/W. In the experiment, all five Ka-band channels (0 dBm input power) were successfully down-converted to an IF of 1.5 GHz. In Fig. 7.20 two of the down-converted channels are shown, where the input was swept over 700 MHz. Again a flat frequency response is obtained.

To further analyze these results, a simulation model of the system was developed using VPITransmissionmaker software. Mode-locked laser pulses
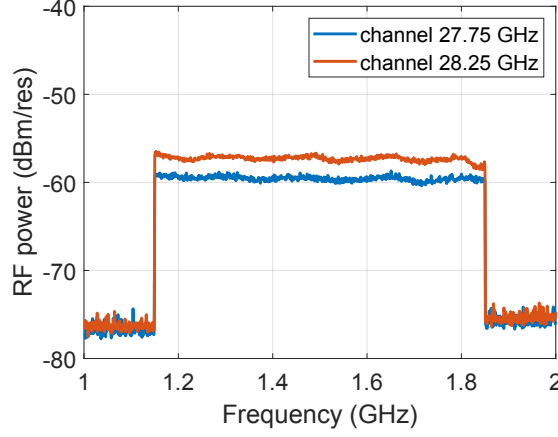
Figure 7.20: Output of the receiver measured using an electrical spectrum analyzer (max hold trace) while the IF input is swept over 700 MHz. Both channels are directly down-converted to 1.5 GHZ IF while the RF was changed from 27.75 GHz to 28.25 GHz. The channel selection was achieved using the LO phase-shifter.

with a FWHM of 3 ps are assumed, as was measured for an identical device with different repetition rate. The EDFAs were modeled using the standard VPI model. The MZM was modeled with an existing MZM model available in the software and the parameters measured for the MZM PIC were implemented. In Fig. 7.21, the measured electrical output spectrum for Channel 2 (28.25 GHz input center frequency) is shown by the blue full line. The simulated spectrum is overlapped in the same graph with orange open circles. Excellent agreement between simulation and measurement is found. That validation of this simulation model allows us to design the system implementation of the fully integrated EPFC prototype with localized LO. Although this experiment demonstrates that the fabricated PICs are capable of performing the targeted down-conversion, the performance is not yet optimized as this was a proof-of-concept demonstration.
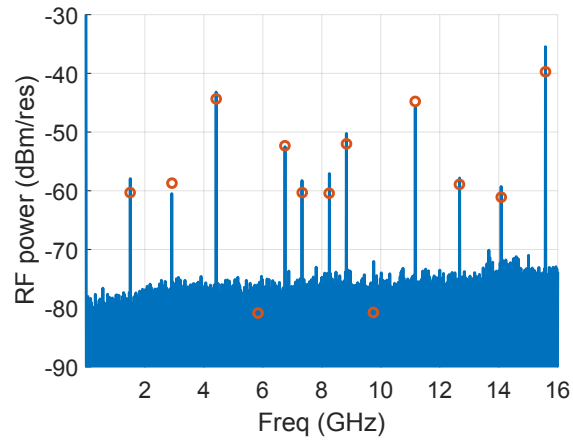
Figure 7.21: Output of the receiver measured using an electrical spectrum analyzer showing all mixing products up to the sampling frequency. The spectrum generated by the VPITransmissionmaker simulation is plotted on top of the measured results with orange circles.

7.9 Design and simulation of fully integrated EPFC

Based on the VPITransmissionmaker model developed in the previous section, we made a simulation model of the fully integrated EPFC. Based on the quantitative results of this model the surrounding system can be designed, with electrical amplification where needed. The fully integrated EPFC PIC is shown in Fig. 7.17 together with a schematic lay-out. The parameters of the MLL and MZM were determined in the previous section. The on-chip photodiode consists of a reversed biased InGaAsP waveguide-coupled gain section. A similar photodiode on a separate PIC was characterized and an analogue 5 GHz bandwidth and a responsivity of 0.5 A/W was found. The fully integrated PIC also contains an on-chip SOA at the MZM output, which is necessary to achieve a high conversion gain. The SOA was also modeled using an available parameterized model in VPI. The estimated V_π of the AlGaInAs phase-shifter at 30 GHz is approximately 10 V. Therefore, it was decided to implement a LNA at the RF input in the system design. The LNA was also inserted in the VPI model using an available building block combined with the specifications provided by the manufacturer (LNA type CGY2128UH/C1). An overview of the envisioned integrated EPFC is shown in Fig. 7.22(a). First we investigated the performance of the PIC without LNA at the input. The simulated IP3 linearity characteristic of the system is shown in Fig. 7.22(b). Finally the conversion gain of the system, including LNA, is shown in Fig. 7.22(c). We note a conversion gain of -4 dB for a LO input power of 0 dBm. Furthermore, we find that positive conversion gain is achieved for LO input powers exceeding 5 dBm. Although these are encouraging results, this simulation is of course a first approximation. In the final system the packaging will strongly influence the final behaviour. For a full quantitative analysis the losses of the RF connectors, PCB transmission lines and bond wires have to be taken into account. It is important to note that explanation given here is given for the situation when a single RF channel at a time is received by the antenna. When the system is deployed, it is possible several channels will be incident upon the antenna at the same time. In this case bandpass filters will have to be added at the input stage of the system such that the different incoming channels do not interfere with each other.

7.10 Packaging and assembly

To demonstrate the system, a PCB was designed including transmission lines, bias-T and terminations for the phase-shifters. The PCB design and

(a)

(b)   (c)
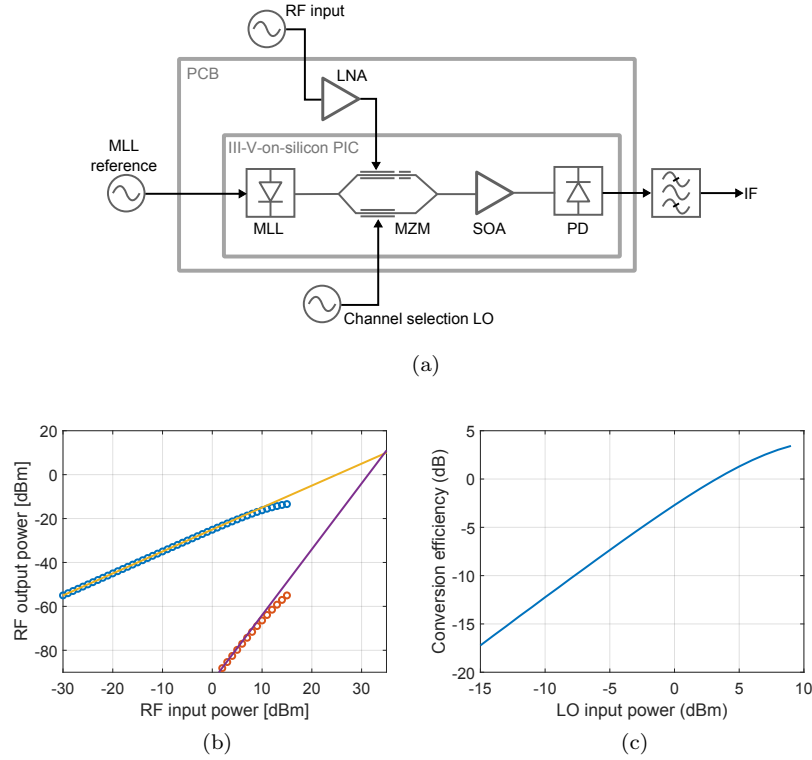
Figure 7.22: (a) System design of the fully integrated EPFC system. A simulation model of this system was developed with VPITransmissionmaker. (b) Simulated (two-tone) IP3 linearity characteristic of the PIC only, for an RF input frequency of 27.75 GHz. (c) Simulated conversion gain of the full system as a function of the LO input power.

manufacturing was done by Antwerp Space. To accommodate the placement of the PIC a recess was made in the PCB. This allows the wire-bonds to be as short as possible without thinning the PIC. The short wire-bonds reduce parasitic inductance and losses for the high-frequency signals. The PCB and PIC are mounted on a metal carrier and housing. In a final product the housing would be fully closed, however for test purposes the housing is half-open. A photograph of the full assembly in the metal housing is shown in Fig. 7.23. A microscope image of the PIC integrated on the PCB is shown in Fig. 7.24. In this figure the PIC shown in Fig. 7.17 can be recognized. All wire-bonds were covered with a protective epoxy to make them less vulnerable against mechanical stress during handling. Furthermore, in Fig. 7.24 the termination for the phase shifters can be clearly seen. One of the main challenges encountered during the assembly was the wire-bonding of the
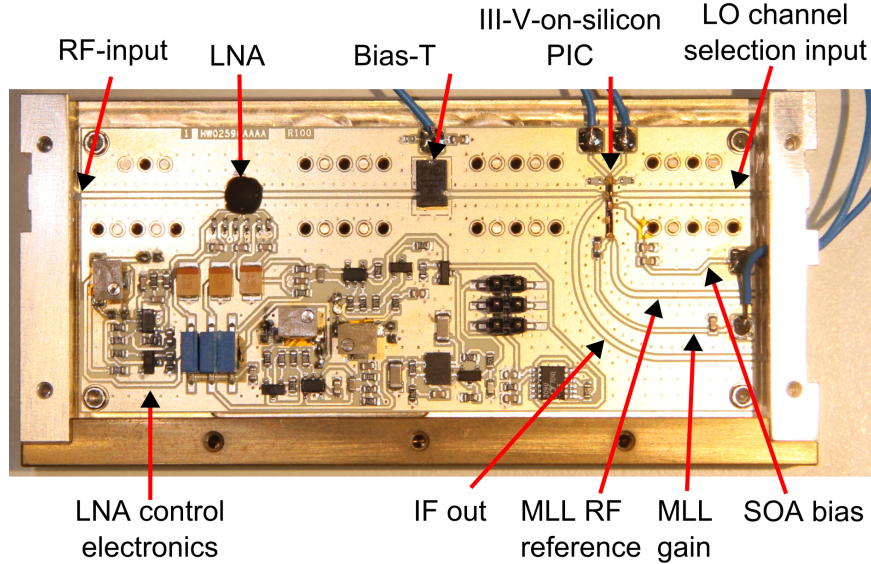
Figure 7.23: Photograph of the fully assembled EPFC prototype. All individual components and traces are indicated.

PIC. The bondpads of the PIC are Ti-Au on DVS-BCB and this type of bondpads tend to delaminate from the DVS-BCB while wirebonding. This was remedied by using a double gold deposition and a DVS-BCB coverage of the sides of the bondpads. In total three assemblies were made each containing a full III-V-on-silicon photonic sampler PIC. All components on the individual PICs were tested after dicing and before assembly and confirmed to all be functional. In a first step the PIC was glued to the metal carrier using a conductive epoxy and cured at 120^oC. Then the PCB was mounted on the metal housing. The assembly was then brought to the Eindhoven University of Technology where all bondpads were successfully wire-bonded to the traces on the PCB. A top-view photograph of the assembly with the indication of the different components is shown in Fig. 7.23. However, for testing additional connectors and mechanical matching structures had to be added to the assembly. It was found that during handling the wire-bonds broke because of mechanical stress. This was only discovered during testing and two assemblies were irreparably damaged. From further inspection it appears that the PCB can show warping and bending during handling, as it is only attached by four screws to the metal carrier. The PIC on other hand is directly glued to the metal carrier. Therefore we suspect that deformation of the PCB relative to the PIC during the attachment of connectors caused
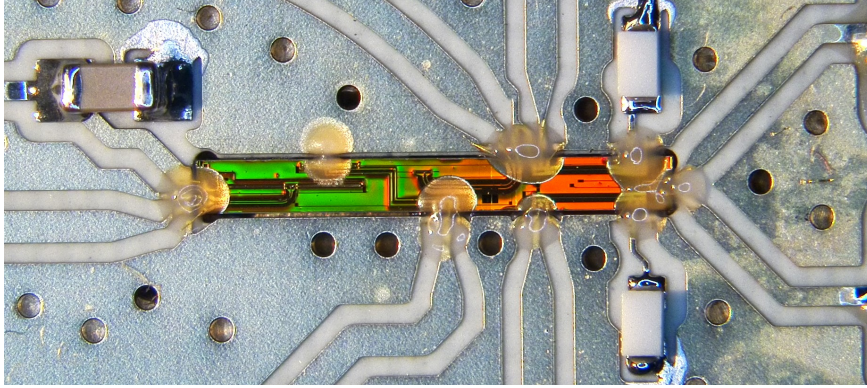
Figure 7.24: Microscope image of the EPFC PIC assembled on the PCB. The wire-bonds are encapsulated by a protective polymer.

the wire-bonds to break. In following iterations it would be advisable to use a protective epoxy to fixate the wire-bonds and provide additional rigidity for the PCB.

One assembly remained undamaged and the wire-bonds were covered with a protective epoxy as can be seen in Fig. 7.24. It was not possible to implement any further changes to the assembly as the PIC and PCB were already mounted and wire-bonded. To avoid damaging the wire-bonds a new approach for the mounting of connectors was developed. After adding the final connections the full assembly could be tested.

7.11   Final demonstration

With the full assembly ready, we first inspected the electrical characteristics of all photonic devices. All components showed the expected behaviour, except for the SOA which seemed to be open circuit. Because of the protective epoxy, it was not possible to inspect the bond-wires for fractures. To ascertain the origin of the broken contact, it was desirable to circumvent the wire-bonds and test the SOA on-chip using probing needles. However, the PIC was covered using a protective DVS-BCB layer on top of the contacting tracks and the bondpads were covered with protective epoxy. It was therefor impossible to contact the SOA with needles without removing the top DVS-BCB layer. Laser ablation was used to remove the DVS-BCB on top of the SOA contact tracks. This allowed us to directly contact the SOA use DC probing needles. When contacted this way the SOA showed the expected diode behaviour. From which we deduce that indeed the wire-bonds broke during handling before the protective epoxy could be applied. The

contacted PIC with the top DVS-BCB layer ablated is shown in Fig. 7.25. However, upon testing if the photodiode was responsive to the ASE output of the SOA no signal was found. From this we deduced that the optical waveguides were damaged during the laser ablation process. As the photodiode could not be used and the optical test outputs were covered by the bond-wire epoxy the full assembly could unfortunately not be characterized.
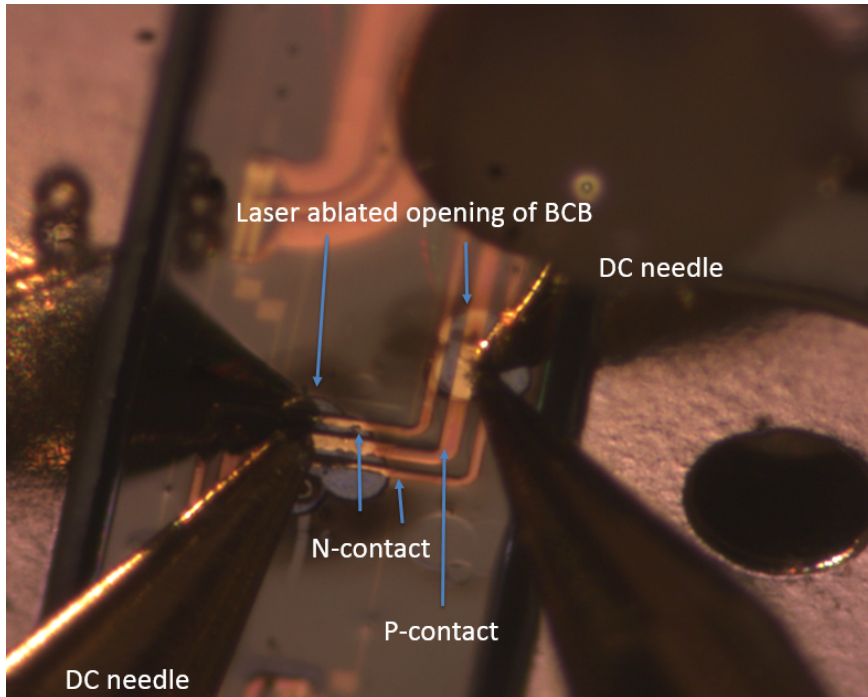
Figure 7.25: Microscope image of the EPFC PIC after laser ablation while being electrically probed with micro needles.

7.12 Conclusion

In summary, we have designed, validated, fabricated and characterized an integrated photonic sampling circuit using III-V-on-silicon PICs. The proposed design is novel because we combine a high-performance MLL on the same chip as a DDMZM. Furthermore, using the channel selection LO allows to increase the flexibility of the sampler. Although the fully integrated circuit on a PCB was not successfully demonstrated the different devices were separately validated. Furthermore, we believe that the wire-bonding is one

of the main bottle-necks in the successful full assembly. In a following itera-
tion it would be advised to create a mechanical dummy PIC to validate a full
assembly with the PCB before mounting a functional PIC. The presented
results were part of the ESA - ARTES project EPFC - Electro-Photonic
Frequency Converter. The extensive development of photonic components
and subsystems were the first steps in the integrated microwave photonics
development for communication satellites.

References

[1] K. Van Gasse, Z. Wang, S. Uvin, B. De Deckere, J. Mariën, L. Thomassen, and G. Roelkens. *Ka-band to L-band frequency down-conversion based on IIIV-on-silicon photonic integrated circuits.* CEAS Space Journal, 9(4), 2017.

[2] J. Kim, F. X. Kärtner, and F. Ludwig. *Balanced optical-microwave phase detectors for optoelectronic phase-locked loops.* Optics Letters, 31(24):3659, dec 2006.

[3] J. Kim, M. J. Park, M. H. Perrott, and F. X. Kärtner. *Photonic sub-sampling analog-to-digital conversion of microwave signals at 40-GHz with higher than 7-ENOB resolution.* Optics Express, 16(21):16509, oct 2008.

[4] P. Ghelfi, F. Laghezza, F. Scotti, G. Serafino, A. Capria, S. Pinna, D. Onori, C. Porzi, M. Scaffardi, A. Malacarne, V. Vercesi, E. Lazzeri, F. Berizzi, and A. Bogoni. *A fully photonics-based coherent radar system.* Nature, 507(7492):341–345, 2014.

[5] M. Huchard, B. Charbonnier, P. Chanclou, F. Van Dijk, F. Lelarge, G.-H. Duan, C. Gonzalez, and M. Thual. *Millimeter-wave photonic up-conversion based on a 55GHz quantum dashed mode-locked laser.* In 2008 34th European Conference on Optical Communication, pages 1–2. IEEE, 2008.

[6] S. R. Harmon and J. D. Mckinney. *Precision Broadband RF Signal Recovery in Subsampled Analog Optical Links.* IEEE Photonics Technology Letters, 27(6):620–623, mar 2015.

[7] J. Liao, X. Zheng, S. Li, H. Zhang, and B. Zhou. *High-efficiency microwave photonic harmonic down-conversion with tunable and reconfigurable filtering.* Optics Letters, 39(23):6565, dec 2014.

[8] J. Hulme, M. J. Kennedy, R.-L. Chao, L. Liang, T. Komljenovic, J.-W. Shi, B. Szafraniec, D. Baney, and J. E. Bowers. *Fully Integrated Microwave Frequency Synthesizer On Heterogeneous Silicon-III/V.* Opt. Express, 25(3):2422–2431, feb 2017.

[9] G. Gopalakrishnan, W. Burns, and C. Bulmer. *Microwave-optical mixing in LiNbO/sub 3/ modulators.* IEEE Transactions on Microwave Theory and Techniques, 41(12):2383–2391, 1993.

[10] E. H. W. Chan and R. A. Minasian. *Microwave photonic downconverter with high conversion efficiency.* Journal of Lightwave Technology, 30(23):3580–3585, 2012.

[11] Y. Gao, A. Wen, X. Wu, Y. Wang, and H. Zhang. *Efficient photonic microwave mixer with compensation of the chromatic dispersion-induced power fading.* Journal of Lightwave Technology, 34(14):3440–3448, 2016.

[12] Y. Wang, J. Li, T. Zhou, D. Wang, J. Xu, X. Zhong, D. Yang, and L. Rong. *All-Optical Microwave Photonic Downconverter With Tunable Phase Shift.* IEEE Photonics Journal, 9(6):1–8, 2017.

[13] T. Li, E. H. W. Chan, X. Wang, X. Feng, B.-O. Guan, and J. Yao. *Broadband Photonic Microwave Signal Processor With Frequency Up-/Down Conversion and Phase Shifting Capability.* IEEE Photonics Journal, 10(1):1–12, feb 2018.

[14] Z. Tang, F. Zhang, D. Zhu, X. Zou, and S. Pan. *A photonic frequency downconverter based on a single dual-drive Mach-Zehnder modulator.* In Microwave Photonics (MWP), 2013 International Topical Meeting on, pages 150–153. IEEE, 2013.

[15] B. M. Haas and J. D. McKinney. *Characterization of a Downconverting, Phase-Modulated RF-Over-Fiber Link With a Single Modulator.* IEEE Photonics Journal, 10(4):1–7, 2018.

[16] J. Hulme, M. Kennedy, R.-L. Chao, L. Liang, T. Komljenovic, J.-W. Shi, B. Szafraniec, D. Baney, and J. E. Bowers. *Fully integrated microwave frequency synthesizer on heterogeneous silicon-III/V.* Optics Express, 25(3):2422, feb 2017.

[17] G. Ducournau, P. Szriftgiser, A. Beck, D. Bacquet, F. Pavanello, E. Peytavit, M. Zaknoune, T. Akalin, and J.-F. Lampin. *Ultrawide-Bandwidth Single-Channel 0.4-THz Wireless Link Combining Broadband Quasi-Optic Photomixer and Coherent Detection.* IEEE Transactions on Terahertz Science and Technology, 4(3):328–337, may 2014.

[18] M. Huchard, P. Chanclou, B. Charbonnier, F. van Dijk, G.-H. Duan, C. Gonzalez, F. Lelarge, M. Thual, M. Weiss, and A. Stohr. *60 GHz radio signal up-conversion and transport using a directly modulated mode-locked laser.* In 2008 International Topical Meeting on Microwave Photonics jointly held with the 2008 Asia-Pacific Microwave Photonics Conference, pages 333–335. IEEE, sep 2008.

[19] M. Sotom, M. Aveline, R. Barbaste, B. Benazet, A. Le Kernec, J. Magnaval, and M. Picq. *Flexible photonic payload for broadband telecom satellites: from concepts to system demonstrators.* In International Conference on Space OpticsICSO 2016, volume 10562, page 105621Y. International Society for Optics and Photonics, 2017.

[20] P. M. P. A. S. M. Salvatore V. Feudale M. *Road map for future payloads using photonic technology.* In Workshop on Advanced Telecom Payloads, Noordwijk, The Netherlands, 2016.

[21] B. Cabon, Y. L. Guennec, M. Lourdiane, and G. Maury. *Photonic Mixing in RF Modulated Optical Links.* In LEOS 2006 - 19th Annual Meeting of the IEEE Lasers and Electro-Optics Society, pages 408–409, 2006.

[22] T. Zhang, F. Zhang, X. Chen, and S. Pan. *A simple microwave photonic downconverter with high conversion efficiency based on a polarization modulator.* In Asia Communications and Photonics Conference, pages AF2E–4. Optical Society of America, 2014.

[23] Y. Le Guennec, G. Maury, J. Yao, and B. Cabon. *New optical microwave up-conversion solution in radio-over-fiber networks for 60-GHz wireless applications.* Journal of lightwave technology, 24(3):1277, 2006.

[24] M. A. Piqueras, M. Beltrán, J. García, P. Villalba, and O. Navasquillo. *Tunable and reconfigurable photonic rf filtering for flexible payloads.* In International Conference on Space OpticsICSO 2016, volume 10562, page 1056220. International Society for Optics and Photonics, 2017.

[25] H.-W. Chen, J. D. Peters, and J. E. Bowers. *Forty Gb/s hybrid silicon Mach-Zehnder modulator with low chirp.* Optics express, 19(2):1455–1460, 2011.

[26] M. Zeiler, S. Detraz, L. Olantera, S. S. El Nasr-Storey, C. Sigaud, C. Soos, J. Troska, and F. Vasey. *Radiation hardness evaluation and phase shift enhancement through ionizing radiation in silicon Mach-Zehnder modulators.* In Radiation and Its Effects on Components and Systems (RADECS), 2016 16th European Conference on, pages 1–4. IEEE, 2016.

[27] D. G. Underwood, G. Drake, W. S. Fernando, and R. W. Stanek. *Modulator-based, high bandwidth optical links for HEP experiments.* IEEE Transactions on Nuclear Science, 60(5):3497–3501, 2013.

[28] M. L. Chu, S. Hou, S.-C. Lee, R. S. Lu, D. S. Su, and P. K. Teng. *Radiation hardness of the 1550 nm edge emitting laser for the optical links of the CDF silicon tracker.* Nuclear Instruments and Methods in Physics Research Section A: Accelerators, Spectrometers, Detectors and Associated Equipment, 541(1-2):208–212, 2005.

Chapter 8

Conclusions and perspectives

8.1 Overview

The outset of this work was to develop the necessary components to realize integrated microwave photonic subsystems using III-V-on-silicon and all-silicon photonic circuits. The envisioned systems were mainly oriented towards microwave photonic mixing and analogue links. One of the main motivations was the excellent work in both passive silicon photonic circuits and InP monolithic circuits. III-V-on-silicon allows to pick and choose the ideal III-V materials for a specific component and combine them on a single PIC, while also offering low-loss waveguides. In this work we have explored several basic building blocks that are required for integrated microwave photonics. The mode-locked laser is a key component for the optical sampling, but is rather complex to engineer. Designing and fabricating a reliable pulsed laser component in a real world application will require further investigation and development. Several modulator structures were compared, ranging from advanced designs using carrier-depletion phase-shifters to III-V-on-silicon phase-shifters and GeSi EAMs. Furthermore, the use of a passive silicon waveguide underneath a III-V gain section has enabled to push the maximum output power of an InP/InGaAsP SOA on silicon. Being able to integrate a high-power optical amplifier in a photonic circuit opens a lot of possibilities. Not only can the need for an EDFA be eliminated in some cases, the optical power levels for coherent communication are within reach. Although one would assume that a monolithic InP platform could easily offer a high-power amplifier, this is often not the case. This is because the amplifiers needed for lasers are often high-gain high-confinement amplifiers

which have a low saturation power. Adding a new type of material for a high-power amplifier would require the regrowth of a new stack, making the manufacturing more complex. The added advantage of the silicon passive waveguide and III-V active waveguide combination is that the confinement can be tailored without changing the active layer composition. For example, using the same material used for the high-power amplifier a high-speed directly modulated DFB laser was fabricated. We showed that this laser could be used to transmit up to 16 Gb/s (16-QAM) on a 20 GHz carrier over 5 km of single mode fiber. Combining these components could lead to compact Radio-over-Fiber transmitters with high bandwidth and output power. Not only directly modulated DFB lasers are interesting components for analogue links. As we have demonstrated, waveguide-coupled GeSi EAMs can be used in high-performance analogue links. Finally we investigated the integration of mode-locked lasers, modulators, amplifier and photodiode on a single III-V-on-silicon PIC, showing again the flexibility and possibilities of the technology.

8.2   III-V-on-silicon mode-locked laser

The laser presented in Chapter 2 achieved a low repetition rate (small frequency spacing between the optical modes), having several beyond state-of-the-art properties.

- Repetition rate of 1 GHz

- Optical spectrum wider than 10 nm with over 1400 longitudinal modes.

- The linewidth of the fundamental RF tone is smaller than 1 kHz.

- The optical linewidth of the longitudinal modes is 250-400 kHz.

This mode-locked laser outperforms other fully integrated devices in terms of fundamental RF linewidth [1]. This is in correspondence with other III-V-on-silicon devices that systematically outperform all-active designs in term of RF linewidth. Also in terms of optical linewidth this laser outperforms other similar devices where the optical linewidth was reported [2]. Furthermore, it is the only mode-locked laser with a 1 GHz repetition rate that also has a 10 nm wide optical spectrum.

However, the pulse duration of the laser is several picoseconds. This indicates that the pulse is not transform limited, which is consistent with the optical spectrum showing a small bat-ear (indicating self-phase modulation). The shortest pulses that have been demonstrated by all-active

semiconductor mode-locked lasers with facet mirrors is approximately 300-500 fs. However, these very short pulse durations are only demonstrated by a limited amount of devices for very specific laser operation points. However, due to the absence of an on-chip external cavity the optical linewidth is much larger (1-10 MHz).

The optical output power of the laser is approximately 0.5 mW, corresponding to a pulse energy of 0.5 pJ. If the pulse was closer to the transform limit, for example 1 ps, the peak power would exceed 0.5 W. It is likely that the current amplifier and saturable absorber design do not support such high peak powers because of the high confinement in the active region and limited saturation power. The amplifier design used in the mode-locked laser had a small-signal gain of approximately 20 dB and a fully saturated output power of approximately 10 dBm. This explains why a strongly stretched and self-phase modulated pulse is supported. Replacing the amplifier by the one described in chapter 4 could already further increase the pulse energy and peak power. However, to further optimize the design a more detailed analysis of the amplifier and cavity would be needed.

Finally, it would be very interesting to combine the InP gain section with SiN waveguides which have extremely low losses and no non-linear absorption. SiN would also allow for dispersion engineering in the cavity, allowing to create advanced pulsed laser topologies used in fiber lasers. Replacing the quantum-well gain material by quantum dash or quantum dot material could also further improve the optical gain bandwidth and overall performance. To the best of our knowledge, no quantum dot or quantum dash pulsed laser with on-chip dielectric external cavity has been demonstrated. If the wide optical spectra of previously demonstrated lasers could be combined with narrow optical linewidths offered by SiN external cavities, a new generation of pulsed lasers could be designed.

8.3 Silicon photonic modulators

We studied several approaches to developing a suitable integrated modulator for analogue photonic links. The carrier-depletion based modulators have the appealing advantage that they are easily integrated on a silicon PIC, however the devices are less efficient compared to InP based phase shifters. Consequently, it would be of great interest to further develop high-performance III-V-on-silicon modulators designed for microwave photonic applications. To make integrated microwave photonic links the modulators need to have a low V_π and insertion loss, while supporting high modulation-frequencies. Although, system level design where the electronic driver is co-designed with the modulator will be essential to push the performance

to the next step.

8.4   III-V-on-silicon semiconductor amplifier

Semiconductor optical amplifiers are essential components of almost all active integrated photonic circuits. However, most photonic platforms offer amplifiers with high confinement and gain for lasers but lack amplifiers providing > 50 mW of output power. Especially in analogue optical links the optical power is one of the dominant factors for the conversion gain. Having a high output power amplifier on the transmitter chip eliminates the need for an EDFA. Having all optical amplification integrated on the transmitter chip would greatly reduce the link cost and receiver implementation/upkeep cost. Not only in analogue links but also in coherent links high optical output power is needed.

   The amplifier we reported in the corresponding chapter offers already an improvement over the currently existing III-V-on-silicon amplifiers and opens up possibilities for both analogue links and coherent communication links. The elegant solution of using a wide silicon waveguide underneath the amplifier allows a lot of design freedom, as a high and low-confinement amplifier can be fabricated on the same PIC with the same materials. Although the amplifier is ideally suited as a booster amplifier at the output stage of a transmitter, it is also interesting to create high-output power on-chip lasers, both pulsed and CW.

8.5   Silicon photonic analogue links

As we demonstrated in the III-V-on-silicon transceiver chapter, a Radio-over-Fiber link can be realized using both an integrated transmitter and receiver. This is an important advancement as this paves the way to multiplexing several transmitter on a single chip. As we have demonstrated, a III-V-on-silicon DFB laser is capable of transmitting analogue signals at high carrier frequencies. Furthermore, the imec platform offers waveguide-coupled Ge photodiodes with a 3 dB bandwidth exceeding 67 GHz making them ideally suited for high-frequency analogue links envisioned in 5G networks. In the demonstration in Chapter 5 a Ge avalanche photodiode with co-integrated TIA was used as receiver for a 3.5-5 GHz link. In the second demonstration 16 Gb/s (16-QAM) data on a 20 GHz carrier was transmitted using a Ge photodiode co-integrated with a high-bandwidth TIA, illustrating that co-integration of silicon photonics with co-designed electronics can provide low-power and compact receivers.

8.6 EAM-based up-converter-transmitter

A second interesting transmitter structure was demonstrated in the EAM-based mixer-transmitter chapter, where we transmitted 64-QAM data on a 28 GHz carrier over 2 km of single mode fiber using a GeSi-EAM-based up-converter-transmitter. Not only is the EAM by itself a very promising modulator, the large bandwidth and flat response make it an ideal component for a microwave photonic mixer.

8.7 III-V-on-silicon photonic sampler

In the final chapter we demonstrated the design, fabrication and characterization of several fully integrated photonic sampling subsystems. Furthermore, we oriented the final implementation towards the integration in a communications satellite. This required a custom design and frequency plan to fulfill the required specifications. We verified the system design using commercial components and achieved a conversion gain of -20 dB using a LiNbO$_3$ DDMZM. We then verified the system using III-V-on-silicon devices and successfully down-converted all Ka-band channels to the L-band. Using these results and a simulation model we designed a fully integrated sampler together with driving electronics and housing. This was fabricated in collaboration with Antwerp Space. Although the individual components were found to be working, we did not manage to assemble a fully functioning system. The main challenge to be tackled in the future is further optimization of the photonic-electronic co-integration and assembly. Finally, it would be interesting to use novel III-V-on-silicon integration approaches such as transfer printing to increase flexibility and design freedom.

References

[1] M. L. Davenport, S. Liu, and J. E. Bowers. *Integrated heterogeneous silicon/IIIV mode-locked lasers.* Photonics Research, 6(5):468, may 2018.

[2] S. Srinivasan, M. Davenport, M. J. R. Heck, J. Hutchinson, E. Norberg, G. Fish, and J. Bowers. *Low phase noise hybrid silicon mode-locked lasers.* Frontiers of Optoelectronics, 7(3):265–276, sep 2014.